

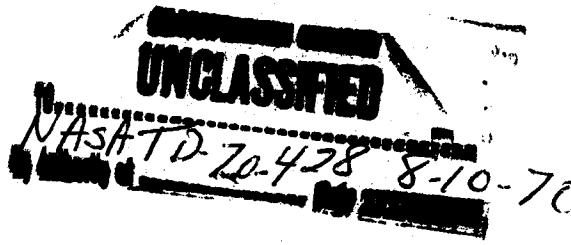
REF ID: A6191

CR-66354

STUDY OF THE INFLUENCE OF SIZE OF A MANNED LIFTING BODY ENTRY VEHICLE ON RESEARCH POTENTIAL AND COST

FINAL REPORT

Part III. Flight Performance



[REDACTED] DOCUMENT [REDACTED] UNCLASSIFIED

Declassified by authority of NASA
Classification Change Notices No. 105
Dated **-8-3170

Prepared by

N70-76650

MARTIN MARIETTA

for

NATIONAL AERONAUTICS AND SPACE ADMINISTRATION

UNCLASSIFIED: U.S. Government Agencies and
Contractors Only

REF ID: A67-4816
[REDACTED]

99
CR-66354

STUDY OF THE INFLUENCE OF SIZE OF A MANNED LIFTING BODY ENTRY VEHICLE ON RESEARCH POTENTIAL AND COST

FINAL REPORT

Part III. Flight Performance

May 1967

1-3

Distribution of this report is provided in the interest of information exchange. Responsibility for the contents resides in the author or organization that prepared it.

[REDACTED]
[REDACTED] DOCUMENT - [REDACTED] UNCLASSIFIED
[REDACTED]

Prepared Under Contract No. NAS 1-6209 by
MARTIN MARIETTA CORPORATION
Baltimore, Maryland 21203

for
NATIONAL AERONAUTICS AND SPACE ADMINISTRATION
Government Agencies and
Contractors Only

DECLASSIFIED

PRECEDING PAGE BLANK NOT FILMED.

FOREWORD

This document is a part of the final report on a "Study of the Influence of Size of a Manned Lifting Body Entry Vehicle on Research Potential and Cost," conducted by the Martin Marietta Corporation, Baltimore Division, for the National Aeronautics and Space Administration, Langley Research Center, under Contract NAS 1-6209 dated April 1966. The final report is presented in eight parts:

I. Summary	CR-66352
II. Research Program Experiments	CR-66353
III. Flight Performance	CR-66354
IV. Candidate Entry Vehicle Designs	CR-66355
V. Systems Integration	CR-66356
VI. Research Vehicle Size Selection and Program Definition	CR-66357
VII. Selected Entry Vehicle Design	CR-66358
VIII. Alternative Approaches	CR-66359

The study was managed at Martin Marietta by:

Robert L. Lohman--Study Manager

Rudolph C. Haefeli--Assistant Study Manager

The principal contributors to the study were James McCown, Robert Schwab, Ray Sorrell and James Vaeth; Mr. Louis Sheldahl also made a major contribution to the study as Study Manager during the first quarter.

000000000000
ER 14471

ABSTRACT (Total Study)

This study presents data—based upon a developed logic, task definitions, vehicle criteria, system analyses and design, and concepts of operation and implementation—with which the usefulness and cost of an entry flight research program can be evaluated.

The study defines 52 specific research tasks of value in developing operational lifting body systems, primarily for near-earth missions. Parametric design and performance data are evolved within a matrix of 5 vehicle sizes (with 1, 2, 4, 6 and 8 men) and 4 boosters (GLV, Titan III-2, Titan III-5 and Saturn IB) for all flight phases, from launch to landing. The design studies include vehicle arrangements, weight, aerodynamic heating and subsystem details. Systems integration analyses yield both design data, subsystem tradeoffs, and development and operations plans; and they lead, in turn, to cost effectiveness analyses which become the primary basis for vehicle and program selection.

A 25-foot long, 3-man vehicle weighing 12,342 pounds is selected for a research program of 9 manned (plus 2 unmanned) flights. This vehicle performs the maximum number of tasks and affords the highest research value per unit cost and the lowest cost per unit of payload in orbit; the estimated program cost is \$1 billion. A detailed preliminary design of this vehicle is accomplished, including layout drawings and descriptions of each subsystem to identify available hardware as well as future options. Modifications for secondary research objectives—rendezvous and docking and supercircular entry—are considered.

The study also includes a brief examination of 2 smaller unmanned vehicles as alternate approaches to reduce cost.

DECLASSIFIED
ER 14471
iv

~~DECLASSIFIED~~

CONTENTS

	Page
FOREWORD	iii
CONTENTS	v
LIST OF ILLUSTRATIONS	vii
SUMMARY	xix
I. INTRODUCTION	1
II. LIST OF SYMBOLS	3
III. AERODYNAMIC CHARACTERISTICS	7
A. Physical Characteristics	7
B. Aerodynamic Control Laws	7
C. Aerodynamics	8
IV. LAUNCH VEHICLE PERFORMANCE	13
A. Launch Vehicle Characteristics	13
B. Payload Insertion Capability	13
C. Location of the Orbit Insertion Point	14
D. Launch Trajectories	14
V. ORBIT CHARACTERISTICS	19
VI. DEORBIT CHARACTERISTICS	23
VII. ORBITAL ENTRY	27
A. Study Results--Nominal Entry Condition	29
B. Effect of L/D	30
C. Effect of Bank Angle	30
D. Footprint Variation During Entry	31
E. Entries at Steeper Than Nominal Angles	31
F. Effect of Wing Loading on Entry Performance	32
G. Entry from a Near Polar Orbit	34
VIII. ENTRIES AT SUPERCIRCULAR VELOCITIES	35
A. Control Logic	35
B. Entry Corridor	36
C. Study Results	36
IX. LANDING PERFORMANCE	39
X. ABORT ANALYSIS	41
A. Pad Abort	41
B. Launch Abort	42
C. Landing Envelopes	43
D. Effect of Wing Loading	43
E. Effect of L/D and Bank Angle on the Abort Parameters	44
F. Effect of Insertion Altitude on the Abort Parameters	44
G. Launch Abort with the Saturn 1-B	45

030000000000
ER 14471-8

	Page
H. Ascent Abort Entry with Pitch Angle Modulation	45
I. Booster Fall-Back	46
REFERENCES	49

DECLASSIFIED
ER 14471-3
vi

REF ID: A6512

LIST OF ILLUSTRATIONS

Figure	Title	Page
FIGURE 1.	HL-10 ENTRY VEHICLE WITH CANOPY.....	53
FIGURE 2.	HL-10 ENTRY VEHICLE WITHOUT CANOPY	53
FIGURE 3.	AERODYNAMIC SURFACE NOMENCLATURE	54
FIGURE 4.	TRIM LONGITUDINAL AERODYNAMICS	54
a)	$M = 0.35$	54
b)	$M = 0.5$	55
c)	$M = 0.6$	55
d)	$M = 0.95$	55
e)	$M = 1.0$	55
f)	$M = 1.1$	55
g)	$M = 1.2$	56
h)	$M = 1.5$	56
i)	$M = 1.8$	56
j)	$M = 6.8$	56
FIGURE 5.	TRIM ELEVON DEFLECTION VERSUS MACH NUMBER	57
FIGURE 6.	TRIM ANGLE OF ATTACK VERSUS MACH NUMBER	57
FIGURE 7.	TRIM LONGITUDINAL AERODYNAMICS VERSUS MACH NUMBER	58
FIGURE 8.	VISCOUS CORRECTIONS TO C_L AND C_D	58
FIGURE 9.	HYPersonic VISCOUS L/D	59
FIGURE 10.	HYPersonic VISCOUS LIFT COEFFICIENT	60
FIGURE 11.	HYPersonic VISCOUS DRAG COEFFICIENT	61

LIST OF ILLUSTRATIONS (continued)

Figure	Title	Page
FIGURE 12.	LAUNCH VEHICLE MINIMUM PAYLOAD CAPABILITY (DUE EAST ETR LAUNCH)	62
FIGURE 13.	PAYLOAD DEGRADATION DUE TO LAUNCH AZIMUTH	63
FIGURE 14.	ORBIT INSERTION POSITION	63
a)	100 N. MI. (185.2 KM) ORBIT	63
b)	EFFECT OF INJECTION ALTITUDE ON RANGE-TO-INSERTION	63
FIGURE 15.	GLV LAUNCH TRAJECTORY	64
FIGURE 16.	TITAN III-2 LAUNCH TRAJECTORY	65
FIGURE 17.	TITAN III-5 LAUNCH TRAJECTORY	66
FIGURE 18.	SATURN 1-B LAUNCH TRAJECTORY	67
FIGURE 19.	PEAK LAUNCH DYNAMIC PRESSURE (NOMINAL TRAJECTORY)	68
FIGURE 20.	INSERTION CONDITIONS USING TITAN III-2	68
FIGURE 21.	CROSSRANGE REQUIRED FOR FRC (EDWARDS AFB) LANDING	69
a)	ORBITS 1 THROUGH 6	69
b)	ORBITS 15 THROUGH 21	69
FIGURE 22.	CROSSRANGE REQUIRED FOR EGLIN AFB LANDING	70
a)	ORBITS 1 THROUGH 5	70
b)	ORBITS 13 THROUGH 21	70
FIGURE 23.	GROUND TRACES	71
a)	$\beta_L = 65.8^\circ$, 5 ORBITS	71
b)	$\beta_L = 110^\circ$, 15 ORBITS	71

LIST OF ILLUSTRATIONS (continued)

Figure	Title	Page
FIGURE 24. DEORBIT FROM CIRCULAR ORBITS		72
a) ENTRY ANGLE		72
b) INERTIAL GROUND RANGE FROM DEORBIT TO ENTRY ALTITUDE		73
c) TIME FROM DEORBIT TO ENTRY ALTITUDE		74
d) TOTAL INERTIAL VELOCITY AT ENTRY ALTITUDE		75
FIGURE 25. DEORBIT FROM ELLIPTICAL ORBITS		76
a) ENTRY ANGLE		76
b) INERTIAL GROUND RANGE FROM DEORBIT TO ENTRY ALTITUDE		77
c) TIME FROM DEORBIT TO ENTRY ALTITUDE . . .		78
d) TOTAL VELOCITY AT ENTRY ALTITUDE		79
FIGURE 26. DEORBIT ΔV FROM APOGEE ALTITUDE		80
a) -1.5° ENTRY ANGLE		80
b) -4.0° ENTRY ANGLE		80
FIGURE 27. AVAILABLE ENTRY ANGLES FOR FIXED DEORBIT ΔV		81
a) $\Delta V_{do} = 1000$ FPS (304.8 M/SEC)		81
b) $\Delta V_{do} = 520$ FPS (158.5 M/SEC)		81
FIGURE 28. DEORBIT NEAR APOGEE OF BASELINE ORBIT		82
a) INERTIAL GROUND RANGE FROM DEORBIT TO ENTRY ALTITUDE		82
b) TIME FROM DEORBIT TO ENTRY ALTITUDE . .		83
c) TOTAL INERTIAL VELOCITY AT ENTRY ALTITUDE		83
d) ENTRY ANGLE		83

0319 [REDACTED]

LIST OF ILLUSTRATIONS (continued)

Figure	Title	Page
FIGURE 29.	ENTRY DATA: $i = 35.7^\circ$, $\gamma = -1.5^\circ$, $W/S = 50 \text{ PSF}$ (2.39 KN/M^2)	84
a)	ENTRY FOOTPRINT	84
b)	R_c VERSUS R_d	84
c)	$q_{\text{MAX.}}$ VERSUS n_T _{MAX.}	85
d)	Q_{T_S} VERSUS \dot{q}_s _{MAX.}	85
e)	Q_{T_S} VERSUS R_c	86
f)	t VERSUS R_c	86
g-1)	h VERSUS V_R FOR L/D _{MAX.} ENTRIES	87
g-2)	h VERSUS R_d FOR L/D _{MAX.} ENTRIES	88
g-3)	h VERSUS t FOR L/D _{MAX.} ENTRIES	89
g-4)	GROUND TRACES FOR L/D _{MAX.} ENTRIES	90
g-5)	STRIP RECORDER OUTPUT FOR L/D _{MAX.} ENTRIES	91
h-1)	h VERSUS V_R FOR 88% L/D _{MAX.} ENTRIES	94
h-2)	h VERSUS R_d FOR 88% L/D _{MAX.} ENTRIES	95
h-3)	h VERSUS t FOR 88% L/D _{MAX.} ENTRIES	96
h-4)	GROUND TRACES FOR 88% L/D _{MAX.} ENTRIES	97
h-5)	STRIP RECORDER OUTPUT FOR 88% L/D _{MAX.} ENTRIES	98
i-1)	h VERSUS V_R FOR 75% L/D _{MAX.} ENTRIES	101
i-2)	h VERSUS R_d FOR 75% L/D _{MAX.} ENTRIES	102
i-3)	h VERSUS t FOR 75% L/D _{MAX.} ENTRIES	103
i-4)	GROUND TRACES FOR 75% L/D _{MAX.} ENTRIES	103

0319 [REDACTED]
DEPT. OF ER 14471-3 [REDACTED] ED
X

LIST OF ILLUSTRATIONS (continued)

Figure	Title	Page
i-5)	STRIP RECORDER OUTPUT FOR 75% L/D _{MAX.} ENTRIES	104
j-1)	h VERSUS V _R FOR L/D _{MIN.} ENTRIES	107
j-2)	h VERSUS R _d FOR L/D _{MIN.} ENTRIES	108
j-3)	h VERSUS t FOR L/D _{MIN.} ENTRIES	109
j-4)	GROUND TRACES FOR L/D _{MIN.} ENTRIES	109
j-5)	STRIP RECORDER OUTPUT FOR L/D _{MIN.} ENTRIES	110
k-1)	VARIATION OF R _c WITH L/D	113
k-2)	VARIATION OF R _d WITH L/D	113
k-3)	VARIATION OF q _s _{MAX.} WITH L/D	114
k-4)	VARIATION OF Q _{T_S} WITH L/D	114
k-5)	VARIATION OF q _{MAX.} WITH L/D	115
k-6)	VARIATION OF n _{T_S} _{MAX.} WITH L/D	115
l-1)	VARIATION OF R _c WITH BANK ANGLE	116
l-2)	VARIATION OF q _s _{MAX.} WITH BANK ANGLE	116
l-3)	VARIATION OF Q _{T_S} WITH BANK ANGLE	117
l-4)	VARIATION OF q _{MAX.} WITH BANK ANGLE	117
l-5)	VARIATION OF n _{T_S} _{MAX.} WITH BANK ANGLE	117
m)	FOOTPRINT VARIATION DURING ENTRY	118
FIGURE 30.	ENTRY DATA: i = 35.7°, γ = -2.0°, W/S = 50 PSF (2.39 KN/M ²)	119
a)	ENTRY FOOTPRINT	119
b)	R _c VERSUS R _d	119
c)	q _{MAX.} VERSUS n _{T_S} _{MAX.}	120

LIST OF ILLUSTRATIONS (continued)

Figure	Title	Page
	d) Q_{T_S} VERSUS $\dot{q}_{s_{MAX}}$	120
FIGURE 31.	ENTRY DATA: $i = 35.7^\circ$, $\gamma = -4.0^\circ$, W/S = 50 PSF (2.39 KN/M ²)	121
	a) ENTRY FOOTPRINT	121
	b) R_c VERSUS R_d	121
	c) $\dot{q}_{s_{MAX}}$ VERSUS $n_{T_{MAX}}$	122
	d) Q_{T_S} VERSUS $\dot{q}_{s_{MAX}}$	122
FIGURE 32.	VARIATIONS OF TRAJECTORY PARAMETERS WITH ENTRY ANGLE-- $i = 35.7^\circ$, W/S = 50 PSF (2.39 KN/M ²)	123
	a) R_c	123
	b) R_d	123
	c) $\dot{q}_{s_{MAX}}$ AT $\phi = 0^\circ$	123
	d) $\dot{q}_{s_{MAX}}$ AT $\phi = \pm 45^\circ$	123
	e) Q_{T_S} AT $\phi = 0^\circ$	124
	f) Q_{T_S} AT $\phi = \pm 45^\circ$	124
	g) q_{MAX} AT $\phi = 0^\circ$	124
	h) q_{MAX} AT $\phi = \pm 45^\circ$	124
	i) $n_{T_{MAX}}$ AT $\phi = 0^\circ$	125
	j) $n_{T_{MAX}}$ AT $\phi = \pm 45^\circ$	125
FIGURE 33.	ENTRY DATA: $i = 35.7^\circ$, $\gamma = -1.5^\circ$, W/S = 40 PSF (1.92 KN/M ²)	126
	a) ENTRY FOOTPRINT	126
	b) R_c VERSUS R_d	126

LIST OF ILLUSTRATIONS (continued)

Figure	Title	Page
	c) $q_{MAX.}$ VERSUS $n_{T_{MAX.}}$	127
	d) Q_{T_S} VERSUS $\dot{q}_{s_{MAX.}}$	127
FIGURE 34.	ENTRY DATA: $i = 35.7^\circ$, $\gamma = -1.5^\circ$, W/S = 60 PSF (2.87 KN/M^2)	128
	a) ENTRY FOOTPRINT	128
	b) R_c VERSUS R_d	128
	c) $q_{MAX.}$ VERSUS $n_{T_{MAX.}}$	129
	d) Q_{T_S} VERSUS $\dot{q}_{s_{MAX.}}$	129
FIGURE 35.	VARIATIONS OF TRAJECTORY PARAMETERS WITH WING LOADING-- $i = 35.7^\circ$, $\gamma = -1.5^\circ$	130
	a) R_c	130
	b) R_d	130
	c) $\dot{q}_{s_{MAX.}}$ AT $\phi = 0^\circ$	130
	d) $\dot{q}_{s_{MAX.}}$ AT $\phi = \pm 45^\circ$	130
	e) Q_{T_S} AT $\phi = 0$	131
	f) Q_{T_S} AT $\phi = \pm 45^\circ$	131
	g) $q_{MAX.}$	131
	h) $n_{T_{MAX.}}$	131
FIGURE 36.	ENTRY DATA: $i = 85^\circ$, $\gamma = -1.5^\circ$, W/S = 50 PSF (2.39 KN/M^2)	132
	a) ENTRY FOOTPRINT	132
	b) R_c VERSUS R_d	132

LIST OF ILLUSTRATIONS (continued)

Figure	Title	Page
c)	$q_{MAX.}$ VERSUS $n_{T_{MAX.}}$	133
d)	Q_{T_S} VERSUS $\dot{q}_{s_{MAX.}}$	133
FIGURE 37. ENTRY CORRIDOR AT $L/D_{MIN.}$, 0° BANK ANGLE . . .		134
FIGURE 38. ENTRY DATA: $V_I = 26\ 000$ FPS (7.93 KM/SEC) . . .		134
a)	$q_{MAX.}$ VERSUS $n_{T_{MAX.}}$	134
b)	Q_{T_S} VERSUS $\dot{q}_{s_{MAX.}}$	135
c)	R_c VERSUS R_d	135
d)	Q_{T_S} VERSUS R_c	136
e)	t VERSUS R_c	137
f-1)	h VERSUS V_R FOR $\gamma = -4.4^\circ$ AND $L/D_{MAX.}$. . .	138
f-2)	h VERSUS t FOR $\gamma = -4.4^\circ$ AND $L/D_{MAX.}$. . .	139
f-3)	h VERSUS R_d FOR $\gamma = -4.4^\circ$ AND $L/D_{MAX.}$. . .	139
g-1)	h VERSUS V_R FOR $\gamma = -4.4^\circ$ AND $L/D_{MIN.}$. . .	140
g-2)	h VERSUS t FOR $\gamma = -4.4^\circ$ AND $L/D_{MIN.}$. . .	141
g-3)	h VERSUS R_d FOR $\gamma = -4.4^\circ$ AND $L/D_{MIN.}$. . .	141
h)	STRIP RECORDER DATA-- $L/D_{MAX.}$, $\phi = 0^\circ$. . .	142
i)	STRIP RECORDER DATA-- $L/D_{MAX.}$, $\phi = 45^\circ$. . .	145
j)	STRIP RECORDER DATA-- $L/D_{MIN.}$, $\phi = 0^\circ$. . .	148
k)	STRIP RECORDER DATA-- $L/D_{MIN.}$, $\phi = 45^\circ$. . .	151
l-1)	VARIATION OF $q_{MAX.}$ WITH ENTRY ANGLE . . .	154
l-2)	VARIATION OF $n_{T_{MAX.}}$ WITH ENTRY ANGLE ..	154
l-3)	VARIATION OF $\dot{q}_{s_{MAX.}}$ WITH ENTRY ANGLE ..	154

~~DECLASSIFIED~~

LIST OF ILLUSTRATIONS (continued)

Figure	Title	Page
<i>t-4)</i>	VARIATION OF Q_{T_S} WITH ENTRY ANGLE	155
<i>t-5)</i>	VARIATION OF R_c _{MAX.} WITH ENTRY ANGLE .. .	155
<i>t-6)</i>	VARIATION OF R_d _{MAX.} WITH ENTRY ANGLE .. .	155
<i>t-7)</i>	VARIATION OF t _{MAX.} WITH ENTRY ANGLE.	155
FIGURE 39.	ENTRY DATA: $V_I = 30\ 000$ FPS (10.4 KM/SEC)	156
a)	q _{MAX.} VERSUS n_t _{MAX.}	156
b)	Q_{T_S} VERSUS \dot{q}_s _{MAX.}	156
c)	R_c VERSUS R_d	157
d)	Q_{T_S} VERSUS R_c	158
e)	t VERSUS R_c	159
f-1)	h VERSUS V_R FOR $\gamma = -6^\circ$ AND L/D _{MAX.}	160
f-2)	h VERSUS t FOR $\gamma = -6^\circ$ AND L/D _{MAX.}	161
f-3)	h VERSUS R_d FOR $\gamma = -6^\circ$ AND L/D _{MAX.}	161
g-1)	h VERSUS V_R FOR $\gamma = -6^\circ$ AND L/D _{MIN.}	162
g-2)	h VERSUS t FOR $\gamma = -6^\circ$ AND L/D _{MIN.}	163
g-3)	h VERSUS R_d FOR $\gamma = -6^\circ$ AND L/D _{MIN.}	163
h)	STRIP RECORDER DATA-- L/D _{MAX.} , $\phi = 0^\circ$. . .	164
i)	STRIP RECORDER DATA-- L/D _{MAX.} , $\phi = 45^\circ$. . .	167
j)	STRIP RECORDER DATA-- L/D _{MIN.} , $\phi = 0^\circ$. . .	170
k)	STRIP RECORDER DATA-- L/D _{MIN.} , $\phi = 45^\circ$. . .	173
<i>t-1)</i>	VARIATION OF \dot{q} _{MAX.} WITH ENTRY ANGLE	176
<i>t-2)</i>	VARIATION OF n_t _{MAX.} WITH ENTRY ANGLE .. .	176

03 [REDACTED] 00

LIST OF ILLUSTRATIONS (continued)

Figure	Title	Page
	<i>t</i> -3) VARIATION OF $q_{s_{MAX}}$ WITH ENTRY ANGLE	176
	<i>t</i> -4) VARIATION OF Q_{T_s} WITH ENTRY ANGLE	177
	<i>t</i> -5) VARIATION OF R_c WITH ENTRY ANGLE	177
	<i>t</i> -6) VARIATION OF R_d WITH ENTRY ANGLE	178
	<i>t</i> -7) VARIATION OF t_{MAX} WITH ENTRY ANGLE	178
FIGURE 40.	ENTRY DATA: $V_I = 34,000$ FPS (10.4 KM/SEC).	179
a)	q_{MAX} VERSUS $n_{T_{MAX}}$	179
b)	Q_{T_s} VERSUS $q_{s_{MAX}}$	179
c)	R_c VERSUS R_d	180
d)	Q_{T_s} VERSUS R_c	181
e)	t VERSUS R_c	181
f-1)	h VERSUS V_R FOR $\gamma = -6.2^\circ$ AND L/D_{MAX}	182
f-2)	h VERSUS t FOR $\gamma = -6.2^\circ$ AND L/D_{MAX}	183
f-3)	h VERSUS R_d FOR $\gamma = -6.2^\circ$ AND L/D_{MAX}	183
g-1)	h VERSUS V_R FOR $\gamma = -6.2^\circ$ AND L/D_{MIN}	184
g-2)	h VERSUS t FOR $\gamma = -6.2^\circ$ AND L/D_{MIN}	185
g-3)	h VERSUS R_d FOR $\gamma = -6.2^\circ$ AND L/D_{MIN}	185
h)	STRIP RECORDER DATA-- L/D_{MAX} , $\phi = 0^\circ$	186
i)	STRIP RECORDER DATA-- L/D_{MAX} , $\phi = 45^\circ$	189
j)	STRIP RECORDER DATA-- L/D_{MIN} , $\phi = 0^\circ$	192
k)	STRIP RECORDER DATA-- L/D_{MIN} , $\phi = 45^\circ$	195

LIST OF ILLUSTRATIONS (continued)

Figure	Title	Page
I-1)	VARIATION OF $q_{MAX.}$ WITH ENTRY ANGLE	198
I-2)	VARIATION OF $n_{T_{MAX.}}$ WITH ENTRY ANGLE	198
I-3)	VARIATION OF $\dot{q}_{S_{MAX.}}$ WITH ENTRY ANGLE	198
I-4)	VARIATION OF Q_{T_S} WITH ENTRY ANGLE	198
I-5)	VARIATION OF $R_{c_{MAX.}}$ WITH ENTRY ANGLE	199
I-6)	VARIATION OF $R_{d_{MAX.}}$ WITH ENTRY ANGLE	199
I-7)	VARIATION OF $t_{MAX.}$ WITH ENTRY ANGLE	199
FIGURE 41. EFFECTS OF VARYING ENTRY VELOCITY		200
a)	$q_{MAX.}$	200
b)	$n_{T_{MAX.}}$	200
c)	$\dot{q}_{S_{MAX.}}$	201
d)	Q_{T_S}	201
e)	$R_{c_{MAX.}}$	202
f)	$R_{d_{MAX.}}$	202
g)	$t_{MAX.}$	203
FIGURE 42. TOUCHDOWN SPEEDS AT EDWARDS AFB		204
FIGURE 43. LANDING GEAR EFFECTS ON AERODYNAMICS		204
FIGURE 44. GROUND EFFECTS ON AERODYNAMICS		204
FIGURE 45. LANDING TRAJECTORY		205
a)	1.35-g PULL-UP	205
b)	2.0-g PULL-UP	206

LIST OF ILLUSTRATIONS (concluded)

Figure	Title	Page
FIGURE 46.	ASCENT ABORT MODES	207
FIGURE 47.	TYPICAL PAD ABORT TRAJECTORY	208
FIGURE 48.	ABORT ANALYSIS LAUNCH TRAJECTORIES	209
FIGURE 49.	ABORT ENVIRONMENT PARAMETERS	210
	a) $q_{MAX.}$	210
	b) $\dot{q}_{sMAX.}$	210
	c) $n_{TMAX.}$	211
FIGURE 50.	LANDING ENVELOPE	212
	a) $\Delta V = 0$ FPS (0 M/SEC)	212
	b) $\Delta V = 600$ FPS (183 M/SEC), POSIGRADE)	212
FIGURE 51.	EFFECT OF WING LOADING ON ABORT PARAMETERS	213
	a) $q_{MAX.}$	213
	b) $q_{sMAX.}$	213
	c) $n_{TMAX.}$	213
FIGURE 52.	ABORT ENTRY TIME HISTORIES	214
	a) DYNAMIC PRESSURE	214
	b) TOTAL LOAD FACTOR	214
FIGURE 53.	ABORT ENTRY TRAJECTORIES FOR MAXIMUM LOAD FACTOR	215
	a) TITAN III-2	215
	b) SATURN 1-B	216
FIGURE 54.	INSTANTANEOUS IMPACT POINTS, TITAN III-2	217

SUMMARY

This Part presents parametric flight performance analyses performed under NASA Contract NAS 16209 entitled "Study of the Influence of Size of a Manned Lifting Body Entry Vehicle on Research Potential and Cost." This study was aimed at examining the use of the HL-10 configuration for various entry research and development tasks related to future operational mission requirements. The complete research and operational program was to be developed, including mission descriptions specifically generated using performance characteristics of selected launch vehicles and of different sizes of the HL-10 entry vehicle.

The flight performance analyses provided data for mission planning and for vehicle design. These studies extensively examined launch, orbit, de-orbit, entry and landing performance. Various abort considerations were also analyzed. The unique maneuverability offered by the lifting body was used to develop the entry environment required for carrying out the research program, and to provide safe return of the crew with normal horizontal landing. The study approach, then, emphasized the important entry flight phase.

The entry analysis included extensive calculations of trajectories to provide parametrically the performance and environment of the entry vehicle. Initial conditions, vehicle characteristics and attitude programs were varied. For example, initial entry velocity ranged from 25 500 fps (7.8 km/sec) to 34 000 fps (10.4 km/sec), with entry vehicle wing loading from 40 psf (1.9 kN/m^2) to 60 psf (2.9 kN/m^2). Entry vehicle sizes ranged from a 1-man crew to an 8-man crew.

A precise, high-speed analog computer program was used to obtain most of the data, although a large amount of digital computer results were also obtained. The results included trajectory time histories, landing footprints, ground traces, and environmental data. The entry programs were related to realistic closed-loop guidance systems which were analyzed in parallel study activities.

The launch analyses provided performance characteristics and payload capabilities for four launch vehicles, GLV, Titan III-2, Titan III-5 and Saturn 1-B. Ascent trajectories were calculated for various launch azimuths and orbit insertion altitudes and speeds. A part of abort considerations included establishing system design requirements and entry vehicle trajectories following any launch vehicle failure.

Orbit analysis was performed for flight durations between 1 and 16 orbits. Emphasis was placed on integrating trajectory requirements using Cape Kennedy for launch and FRC (Edwards AFB) for landing. Performance aspects of de-orbit and return to the atmosphere were also defined and integrated into mission descriptions and vehicle design requirements.

This Flight Performance Volume presents the flight characteristics of all launch to landing flight phases. Part V, Systems Integration, presents specific mission profiles based on these data, and in addition presents selected detailed

performance data for the launch vehicle and entry vehicle in the recommended research program. Parts IV, "Candidate Entry Vehicle Designs," and VII, "Selected Entry Vehicle Design" present navigation and guidance analyses which describe closed-loop performance capabilities using specific guidance schemes. The present performance volume includes the longitudinal viscous, aerodynamic characteristics of the HL-10 used in this study.

DECEMBER 1970
ER 14471-3

I. INTRODUCTION

This Part of the final report on a "Study of the Influence of Size of a Manned Lifting Body Entry Vehicle on Research Potential and Cost" deals with the many flight performance characteristics of the launch vehicle and entry vehicle during all the mission phases. A vehicle matrix was selected for the study consisting of four launch vehicles (GLV, Titan III-2, Titan III-5, and Saturn 1-B) and five HL-10 entry vehicle sizes (1-, 2-, 4-, 6- and 8-man crews). Performance characteristics were needed for all of these to provide basis for selecting the most effective flight system for the entry research program. The goals of the performance studies were to define subsystem design criteria, to develop mission descriptions, and to establish entry conditions which provide the flight environments for specific research tasks.

At the start of the study, NASA provided fundamental guidelines and characteristics of candidate launch vehicles and the entry vehicle. The Gemini launch vehicle (GLV) was included because it might provide sufficient payload capability (8200 lb, 3.7 Mg) for the smallest size entry vehicle. The Titan III family provides capabilities from 17 000 pounds (7.7 Mg) to 36 000 pounds (16.3 Mg). Of this family, the Titan III-2 and III-5 were selected for this study to span the possible payload requirements range. They can launch payloads of 17 000 pounds (7.7 Mg) and 27 400 pounds (12.4 Mg), respectively. These two boosters consist of up-rated cores (Stages 1 and 2) with solid-propellant rocket motors (Stage 0) using 2- and 5-segments, respectively. The Titan transtage (Stage 3) is not included in these versions. Of the launch vehicles which were studied, the Saturn 1-B provides the largest capability, 35 300 pounds (16 Mg). All of these are assumed to be man-rated. Reliability and cost numbers for this study pertaining to the boosters were provided by NASA (inputs from the Air Force were provided to NASA for Titan III). Data was derived with these as guidelines for other phases of the study.

The flight performance of the launch phase is presented in this part for all these boosters. This includes analysis of payload capabilities launching from KSC (Kennedy Space Center) at various azimuth headings with direct insertion into orbit from 60-nautical mile to 150-nautical mile altitudes (111 and 278 km). Time histories of trajectory parameters are shown which include environmental data such as load factors and dynamic pressure. Considerations related to ascent abort are also presented here.

The HL-10 lifting body entry vehicle was selected by NASA for the present study objectives. It is typical of a medium L/D (lift-to-drag ratio) lifting body which provides a significant maneuverability during entry. It was felt that many of the general results of the study would apply if similar configurations, such as SV-5, M2-F2, or improved versions, were carried through the study. The aerodynamic configuration and wind tunnel test data of the HL-10 entry vehicle have been extensively developed and documented at NASA, Langley Research Center.

An analysis (described in Part IV, Candidate Entry Vehicle Designs) resulted in selection of the HL-10 configuration with Canopy-D for the research entry vehicle. This provides a subsonic L/D of 4.0 which is quite satisfactory for approach and landing. It also provides a hypersonic L/D of 1.14 (inviscid) for a crossrange maneuver potential of 800 nautical miles (1.5 Mm). The configuration and aerodynamics related to performance are summarized in this part (details of configurations are shown in Parts IV and VII). Corrections to the lift and drag for viscosity are presented as functions of Mach number, Reynolds number and angle-of-attack, and were used in performance calculations.

Many aspects of entry flight performance are presented in this part. Various entry conditions such as velocity, flight path angle, wing loading, and maneuver controls were used to provide environmental data and research mission characteristics. Return to the earth's atmosphere at speeds up to 34 000 fps (10.4 km/sec) was included as part of a secondary study objective to look into possibilities for research at supercircular speeds.

For the primary study objectives pertaining to entry at near-orbital speeds, comprehensive time history and summary data is presented for landings at the primary landing site, Edwards AFB. Trajectory data, including landing maneuver footprints, are shown for various levels of L/D. For these, the angle of attack was programmed, ranging from $L/D_{max.}$ to $C_{L_{max.}}$, to provide various maneuver ranges. The maximum practical crossrange occurs using an angle of attack for an L/D between $L/D_{max.}$ and 88% $L/D_{max.}$ and, as shown in Parts IV and VII, is 676 nautical miles (1.25 Mm) using the selected guidance approach.

The entry analyses presented here also include abort considerations in various phases of flight. During ascent, if a booster were to shut down, the subsequent trajectory of the entry vehicle may expose it to more extreme heating rate and deceleration conditions than are experienced during normal entry. Abort environmental data are therefore presented as a basis for design criteria.

The landing performance is also discussed, with some flare and float maneuvers selected on the basis of other lifting body simulation and HL-10 air launch-flight experience.

The entry vehicle launch is followed by orbit and deorbit flight phases. This report provides data for mission durations from 1 to 16 orbits, with special consideration to landing requirements for Edwards AFB and for a typical East Coast alternate site at Eglin AFB. The entry research mission in general is completed within three orbits. The deorbit analysis provides data for deorbit propulsion requirements and mission aspects of the descent to the entry altitude. Circular and elliptical orbits from 80 to 400 nautical miles (148 to 740 km) are included. The relations between deorbit conditions and initial entry conditions are shown.

The purpose of this Flight Performance part is to present parametric data pertaining to all flight phases and vehicle systems of the study. Specific data applying to the recommended D/3 entry vehicle are presented in Part V, Systems Integration, which also includes mission profiles, parachute recovery, and abort mode descriptions.

II. LIST OF SYMBOLS

C_D	Drag coefficient
\bar{C}_D	$d(C_D)/d\mu$
C_{D_f}	Coefficient of drag due to friction
C_f	Coefficient of friction
C_L	Lift coefficient
\bar{C}_L	$d(C_L)/d\mu$
C_{L_f}	Coefficient of lift due to friction
D	Drag
g	Acceleration of gravity
h	Altitude
i	Orbit inclination angle
J_0, J_1, J_2	Harmonic coefficients
L	Lift
L/D	Lift to drag ratio
M	Mach number
n_T	Aerodynamic load factor
Q_T, Q_{T_S}	Stagnation point total heating
q	Dynamic pressure
\dot{q}, \dot{q}_s	Stagnation point heat transfer rate

r	Radial distance from earth's center
R	Range
R_c	Crossrange
R_d	Downrange (measured from entry)
R_R	Inertial downrange from deorbit to entry
Re_l	Reynolds number based on length
R_\oplus	Equatorial earth radius
S	Reference area
(T-D)/W	Axial acceleration
t	Time
t_D	Time from deorbit to entry
U	Gravitational potential
V	Inertial velocity
V_{TD}	Touchdown velocity
V_R	Relative velocity
W	Weight
W/S	Wing loading
α	Angle of attack
α_{TD}	Angle of attack at touchdown
β_L	Launch azimuth
γ	Flight path angle
γ_0	Initial entry angle

DRAG COEFFICIENT

ΔC_D	Incremental change in drag coefficient
ΔC_L	Incremental change in lift coefficient
ΔP	Payload degradation due to launch azimuth
ΔV	Incremental change in velocity
ΔV_{do}	Incremental deorbit velocity
δ	Deorbit thrusting angle
δ_a	Aileron deflection angle
δ_e	Elevator deflection angle
δ_{ef}	Elevon flap deflection angle
δ_{if}	Tip fin inner flap deflection angle
δ_{of}	Tip fin outboard flap deflection angle
δ_r	Rudder deflection angle
θ	Pitch angle; included angle of rudder cross section (fig. 3)
λ	Longitude
μ	Viscous parameter $M^{618} / \sqrt{Re_l}$
μ_\oplus	Geocentric gravitational constant
ψ_I	Inertial heading angle
ϕ	Bank or roll angle; latitude

(This page unclassified)

ER 14471

RECEDING PAGE BLANK NOT FILMED.

III. AERODYNAMIC CHARACTERISTICS

The aerodynamics of the HL-10 lifting body have been obtained by NASA in an extensive series of wind tunnel tests. The current study utilized this data in performance, controls, stability, loads and heating analyses. The present section summarizes a part of this data, the longitudinal trim aerodynamics, which was then employed in the various flight performance analyses. Estimates of the viscous lift and drag coefficients are also included here.

An early part of the study involved analyzing characteristics of the HL-10 both with and without canopy-D. This canopy has been defined in the NASA references. The present data includes canopy and no-canopy aerodynamics. The configurations used in the size tradeoff analyses and in the recommended size (D/3) were all the HL-10 with canopy-D.

A. PHYSICAL CHARACTERISTICS

Three view drawings of the HL-10 canopy and no-canopy configurations are shown in figures 1 and 2, respectively, where dimensions are given as a function of body length (reference length). Physical characteristics related to aerodynamics are presented in table 1. The aerodynamic surface nomenclature is indicated in figure 3. Additional configuration details are presented in Section II of Part IV.

B. AERODYNAMIC CONTROL LAWS

The HL-10 has three aerodynamic control surfaces, the right and left elevons and the rudder, which provide pitch, yaw and roll control. Other movable surfaces are used to alter the configuration at subsonic and transonic speeds. These other surfaces include three-position elevon flaps and two-position tip-fin flaps which provide improved performance and longitudinal stability characteristics over the entire spectrum of flight speeds. The rudder, attached to the center fin, is split vertically; its surfaces may be deflected outward to serve as speed brakes or inward to reduce subsonic base drag. All of these surfaces are identified in table 2, together with a summary of their angular deflections. (It is possible that later detailed stability analyses and air-launch flights may result in a decision to delete some of these movable surfaces from the entry vehicle configuration.)

During a typical entry at hypersonic speeds, the fin and elevon flaps are undeflected; i.e., $\delta_{e_f} = \delta_{o_f} = \delta_{i_f} = 0^\circ$. They remain undeflected until deceleration to approximately Mach 1.2. Here the elevon flaps are extended ($\delta_{e_f} = 20^\circ$) and the inner-surface tip-fin flaps are extended ($\delta_{i_f} = 30^\circ$) to improve the transonic longitudinal characteristics. After further deceleration, at approximately Mach 0.6, the inner surface tip-fin flaps are re-

tracted ($\delta_{i_f} = 0^\circ$ and $\delta_{o_f} = -40^\circ$); the rudder surfaces are converged ($\theta = 12^\circ$), and the elevon flap is retracted ($\delta_{e_f} = -8^\circ$). This geometry increases the subsonic maximum trimmed L/D for the approach and landing phases. Pitching motion is obtained by deflection of the left and right elevons.

The elevon deflection is represented by:

$$\delta_e = \frac{\delta_e, \text{ right} + \delta_e, \text{ left}}{2}$$

Roll control is provided by differential deflection of the right and left elevons. Positive aileron deflection is defined as right elevon down giving negative rolling moments. The aileron deflection is represented by:

$$\delta_a = \delta_e, \text{ right} - \delta_e, \text{ left}$$

C. AERODYNAMICS

Aerodynamic data for the HL-10 configuration were obtained from wind tunnel test data of references 1 through 4, covering the speed range from $M = 0.35$ to $M = 6.8$. Trim longitudinal aerodynamic data are presented for both canopy and no canopy configurations. The data presented in figure 4 are representative of the subsonic through hypersonic speed range. Additional data for intermediate Mach numbers have been calculated. Summary curves for the canopy configuration presenting trim values of elevon deflection, angle of attack, lift and drag coefficient and lift to drag ratio are illustrated in figures 5 through 7. These characteristics are presented in the three flight modes of maximum lift-to-drag ratio, maximum lift and zero lift.

Viscous effects at hypersonic speeds are accounted for using the method described in reference 5. Briefly, this approach describes the vehicle as a complex set of flat plates and, using flat-plate boundary-layer analysis, generates the degradation to lift and drag due to friction. The expression for skin friction used in the analysis, based on the reference enthalpy method and Newtonian theory, is as follows:

$$C_f = 1.47 \mu \sin \alpha \cos^{3/2} \alpha \left(\frac{l}{s} \right)^{1/2} \left[1.0 + 1.7 \sin^2 \alpha + \frac{0.37 + \frac{T_w}{T_\infty}}{0.074 M_\infty^2} \right]^{-0.191}$$

where:

μ = viscous parameter = $M^{6.18} / \sqrt{Re_l}$

l = vehicle length

S = boundary layer growth length
 α = effective local angle of attack
 T_w/T_∞ = wall to free stream temperature ratio
 M_∞ = free stream Mach number

The viscous corrections to lift and drag are obtained using this friction coefficient, and may be written as

$$C_{L_f} = \mu \overline{C_L} \text{ and } C_{D_f} = \mu \overline{C_D}.$$

Here $\overline{C_L}$ and $\overline{C_D}$ simply represent the rate of change of C_L and C_D as μ varies; these are presented as functions of α in figure 8. Variations of the hypersonic viscous lift-to-drag ratio, lift coefficient and drag coefficient as a function of the viscous parameter and angle of attack are shown in figures 9 through 11, respectively. The use of these viscous coefficients should be terminated when the free-molecular flow value of the viscous parameter μ is attained. Since the theories for laminar skin friction and free molecular skin friction are separate, the value of μ where the continuum drag equals the free-molecular drag does not agree with its value where the continuum lift equals the free-molecular lift. However, because the dynamic pressure at either value is negligible (less than unity), the selection of either is suitable here since the difference will not affect the trajectory. The continuum drag equals the free-molecular flow drag when $\mu = 0.275$.

TABLE 1
AERODYNAMIC PHYSICAL CHARACTERISTICS

Reference length = l , length of body

Center of gravity location

X_{cg} at $0.53l$ (measured aft from station 0)

Y_{cg} at $0.0125l$ (measured down from horizontal reference line)

Z_{cz} at horizontal centerline of vehicle planform

Body (without fins)

Length	l
Height (maximum without canopy)	$0.2161 l$
Height (maximum with canopy-D)	$0.259 l$

30

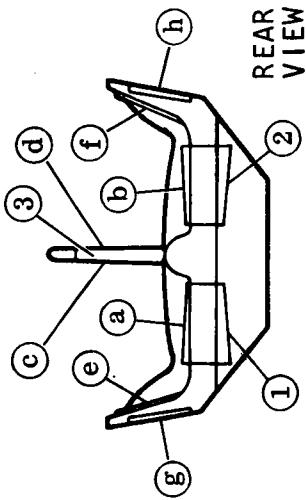
TABLE 1. --continued
AERODYNAMIC PHYSICAL CHARACTERISTICS

With (maximum at station 1.0 ℓ)	0.64506	ℓ
Projected planform area with elevons	0.357	ℓ^2
Leading edge radius (constant)	0.04275	ℓ
Center vertical fin with rudder, modified E_2		
Area (true, including rudder)	0.035153	ℓ^2
Leading edge radius	0.005	ℓ
Rudder area (aft of hinge)	0.009958	ℓ^2
Rudder base (normal)	0.00593	ℓ^2
Leading edge sweep (from vertical)	25°	
Root chord (water 0.0821 ℓ)	0.2035	ℓ
Tip chord (waterline 0.3201 ℓ)	0.0929	ℓ
Total wedge angle	6°	
Tip fin, modified I_4		
Area (true)	0.0340	ℓ^2
Leading edge radius, root	0.0167	ℓ
Leading edge radius, tip	0.0089	ℓ
Inner surface cant (from vertical, in station plane)	22.6°	
Outer surface cant (from vertical, in station plane)	11.7°	
Inner surface toe-in (to body centerline, in water-line plane)	7°	
Outer surface toe-in (to body centerline, in water-line plane)	11°	
Elevons		
Area (true, aft of hingeline)	0.01953	ℓ^2
Leading edge radius, root	0.0396	ℓ
Leading edge radius, tip	0.04823	ℓ
Total wedge angle	20.1°	
Hingeline sweep (forward from station line, in water-line plane)	17°	

TABLE 2

SUMMARY OF AERODYNAMIC CONTROLS AND MOVABLE SURFACES

No.	Designation	Type of control	Basic configuration			Subsonic $M < .6$
			Hypersonic $M > 1.2$	Transonic $1.2 \geq M \geq .6$	Control deflection	
<u>Control Surfaces</u>						
δ_e	{ 1. Left elevon 2. Right elevon }	Variable, + down	+40°	-40°	+40°	+40°
δ_r	3. Rudder (*)	Variable, + left	-20°	+20°	-20°	+40°
<u>Other Movable Surfaces</u>						
δ_{e_f}	{ a. Left elevon flap b. Right elevon flap }	3 positions, + up	0	+20°	0	-8.3°
$\theta/2$	{ c. Left rudder surface d. Right rudder surface }		0	+20°	0	-8.3°
δ_{i_f}	{ e. Left tip fin inner flap f. Right tip fin inner flap }	2 positions, minus (-) toward fin	0	0	0	-6°
δ_{o_f}	{ g. Left tip fin outer flap h. Right tip fin outer flap }		0	30°	0	-6°
			0	30°	0	-40°
			0	0	0	-40°



(*) Split rudder (can be used as dive brake)

03 [REDACTED] 30
(This page unclassified)

DE [REDACTED] 30

ER 14471

IV. LAUNCH VEHICLE PERFORMANCE

Four launch vehicles were evaluated as potential candidates to meet the needs of the lifting body entry research program. Three of these vehicles, namely the GLV, the Titan IIIC, and the Saturn 1-B, were selected for consideration in this study by the NASA. This Contractor was given the option to select a fourth launch vehicle for consideration from the Titan III family. To assist in this selection, the Air Force and the Denver Division of Martin Marietta Corporation provided data for the Titan III family to NASA, Langley Research Center.

This data, contained in reference 6, describes eight launch vehicles, four with transtages and four without transtages (the transtage is the final stage (Stage 3) sometimes used for orbit insertion and subsequent maneuvers). The payload which could be inserted into near-earth orbit is always greater without transtage for low-earth orbits. Consequently, since the current primary objectives of entry research do not require a restartable upper stage for in-orbit maneuvers, and since launch vehicle cost is obviously reduced by deleting a stage, transtages were excluded. For the launch vehicles, then, the following nomenclature for Titan III was adopted. Titan III-C was named Titan III-5 which refers to a man-rated Titan III with an uprated core, a five-segment pair of solid-propellant rocket motors (SRM) having 120-inch (3.05-m) diameter, and no transtage. The launch vehicle Titan III-2 is the same except the SRM's have only two segments. The Titan III-2 was selected to be the fourth of the candidate launch vehicles for the initial tradeoff analyses, based on the need in this study for a launch vehicle which has a payload potential between GLV and Titan III-5.

A. LAUNCH VEHICLE CHARACTERISTICS

Weight and performance characteristics for the selected candidate launch vehicles were obtained from references 6 through 11. A summary of pertinent launch vehicle weight data is shown in table 3. Engine performance characteristics are summarized in table 4. Two of the candidate launch vehicles (GLV and Saturn 1-B) are two-stage vehicles. The other two (Titan III-2 and Titan III-5) are three-stage vehicles as a result of the addition of the 120-inch (3.05 m) SRM's.

B. PAYLOAD INSERTION CAPABILITY

Figure 12 summarizes the minimum payload capability for the candidate launch vehicles for easterly launches from the Eastern Test Range (ETR). Minimum payload capability is defined as the payload which normally can be carried to orbit insertion with a probability of occurrence at least equivalent to a three-sigma (standard deviation) value. For the Titan, this provides approximately three percent velocity margin relative to normal nominal performance. A payload correction for other (non-east) launch azimuths is shown in figure 13.

03 [REDACTED] 30

The baseline mission involves a launch at an azimuth heading of 65.8° east of north into an 80 nautical mile (148 km) perigee orbit. Insertion is terminated with an overspeed sufficient to result in an apogee altitude of 200 nautical miles (370 km). Figure 12 yields the payload corresponding to minimum ascent performance with a due east (90°) launch azimuth. This value is reduced by an increment (ΔP) from figure 13 to account for the non-east (65.8°) launch azimuth. A summary of the performance of the launch vehicles is given in table 5 for insertion into an 80/200 nautical mile (148/370 km) orbit.

C. LOCATION OF THE ORBIT INSERTION POINT

Trajectories for the launch phase (liftoff to orbit insertion) were computed for each of the candidate launch vehicles. Launch azimuth was varied from due north in eastward increments to due south. The launch vehicles were assumed to orbit the minimum performance payload for the specific launch azimuth. The insertion locations are summarized in figure 14. The data of figure 14 represents primarily an insertion altitude of 100 nautical miles (185 km).

For a 90° launch azimuth, a band is indicated which describes the spread of insertion points for a range of insertion altitudes between 60 nautical miles (111 km) and 150 nautical miles (278 km).

D. LAUNCH TRAJECTORIES

Figures 15 through 18 summarize the launch trajectories for the candidate launch vehicles. To enable direct comparisons, these data are presented for identical launch azimuths (due east from ETR) and identical insertion conditions (perigee insertion into an elliptical 80/200 nautical mile (148/370 km) orbit).

The variation of peak launch dynamic pressure with insertion altitude is shown in figure 19. The peak launch dynamic pressure generally decreases as the insertion altitude increases. Figure 19 also shows a variation among launch vehicles which is related to the thrust-to-weight differences of the first-stage propulsion systems.

TABLE 3
LAUNCH VEHICLE WEIGHT SUMMARY

		GLV		Titan III-2		Titan III-5		Saturn 1-B	
	lb	Mg	lb	Mg	lb	Mg	lb	Mg	
<u>Stage 0</u> (solids)									
Loaded weight	544	854	247.	141	1 036	764	470.	268	
Burnout weight	106	709	48.	402	158	952	72.	099	
Consumed weight	438	145	198.	739	877	812	398.	169	
<u>Stage 1</u>									
Loaded weight	266	019	120.	664	307	023	139.	263	992
Burnout weight	11	476	5.	205	17	991	8.	161	714
Consumed weight	254	543	115.	459	289	032	131.	102	450.
Dry weight	9	662	4.	383	16	635	7.	546	287
<u>Stage 2</u>									
Loaded weight	66	411	30.	123	76	744	76	744	46.
Burnout weight	5	829	2.	644	7	956	7	956	705
Consumed weight	60	582	27.	479	68	788	31.	201	889
Dry weight	5	050	2.	291	7	369	3.	343	747

TABLE 4

LAUNCH VEHICLE ENGINE PERFORMANCE SUMMARY

	GLV	Titan III-2	Titan III-5	Saturn 1-B
<u>Stage 0</u>				
Engine type	SRM	SRM	SRM	
Number of engines	2 (2 seg each)	2 (5 seg each)	2 (5 seg each)	
Propellant (Ox) (fuel)	None	Solid	Solid	None
Thrust (liftoff)	1 556 640 lb 6. 91 MN	2 018 914 lb (8. 96 MN)	2 018 914 lb (8. 96 MN)	
Propellant flow rate (liftoff)	6 978. 5 lb/sec (31 kN/sec)	8 813. 7 lb/sec (39 kN/sec)	8 813. 7 lb/sec (39 kN/sec)	
Specific impulse (liftoff)	233 sec	229 sec	229 sec	
<u>Stage 1</u>				
Engine type	YLR-87-AJ-5	YLR-87-AJ-5	YLR-87-AJ-5	H-1 uprated
Number of engines	2	2	2	8
Propellant (Ox) (fuel)	N ₂ O ₄	N ₂ O ₄	N ₂ O ₄	LO ₂
Thrust (liftoff)	50/50 UDMH 431,000 lb (1. 91 MN)	50/50 UDMH 510,000 lb (2. 26 MN)	50/50 UDMH 510,000 lb (2. 26 MN)	RP-1
Propellant flow rate (liftoff)	1 673 lb/sec (7. 44 kN/sec)	1 738. 1 lb/sec (7. 71 kN/sec)	1 738. 1 lb/sec (7. 71 kN/sec)	1 613 286 lb (7. 17 MN)
Specific impulse (liftoff)	257 sec	293 sec	293 sec	6 264 lb/sec (2. 78 kN/sec)
				257. 53 sec
<u>Stage 2</u>				J-2 uprated
Engine type	YLR-91-AJ-5	YLR-91-AJ-5	YLR-91-AJ-5	J-2 uprated
Number of engines	1	1	1	1
Propellant (Ox) (fuel)	N ₂ O ₄	N ₂ O ₄	N ₂ O ₄	LO ₂
Thrust (liftoff)	50/50 UDMH 100,000 lb (4. 45 MN)	50/50 UDMH 100,000 lb (4. 45 MN)	50/50 UDMH 100,000 lb (4. 45 MN)	LH ₂
Propellant flow rate (liftoff)	322. 1 lb/sec (1. 43 kN/sec)	322. 1 lb/sec (1. 43 kN/sec)	322. 1 lb/sec (1. 43 kN/sec)	225,000 lb (10. 0 MN)
Specific impulse (liftoff)	310 sec	310 sec	310 sec	531. 79 lb/sec (2. 36 kN/sec)
				423. 1 sec

ER 14471-3

TABLE 5
LAUNCH VEHICLE PERFORMANCE COMPARISON
(BASELINE MISSION)

Launch vehicle	Minimum payload, $\beta_L = 90^\circ$		ΔP for $\beta_L = 65.8^\circ$		Minimum payload, $\beta_L = 65.8^\circ$	
	Ib	Mg	Ib	kg	Ib	Mg
GLV	8 360	3.78	180	81	8 180	3.70
Titan III-2	17 240	7.83	300	136	16 940	7.69
Titan III-5	27 820	12.6	430	195	27 390	12.4
Saturn 1-B	36 040	16.3	730	331	35 310	16.0

03 [REDACTED] 00

(This page unclassified)

DECLASSIFIED

ER 14471

PRECEDING PAGE BLANK NOT FILMED

V. ORBIT CHARACTERISTICS

The basic research mission orbit altitude and launch azimuth were determined within the study constraints of altitudes of 80 to 400 nautical miles (148 to 741 km) and of a maximum in-orbit time period of 24 hours (16 orbits), with launch at KSC and entry at FRC.

The geographical data used in this analysis and throughout the study are based on an oblate, rotating earth with an equatorial radius of 20 925 640 feet (6.378 Mm) and a polar radius of 20 855 500 feet (6.356 756 Mm). The potential

function $U = \frac{\mu_{\oplus}}{r} \left[1 - \frac{J_2 R_{\oplus}^2}{2r^2} (3 \sin^2 \phi - 1) \right]$. Numeric values for the potential

function constants are:

$$\mu_{\oplus} = 1.407 639 \times 10^{16} \text{ ft}^3/\text{sec}^2 (399 \text{ Tm}^3/\text{sec}^2)$$

$$R_{\oplus} = 20 925 640 \text{ ft (6.38 Mm)}$$

$$J_0 = 1, J_1 = 0, J_2 = 1082.32 \times 10^{-6}$$

Orbit insertion conditions were obtained from trajectory data using a Titan III-2 booster launched from KSC. Insertion longitude, latitude and orbit inclination as a function of launch azimuth is presented in figure 20 for an orbital altitude of 100 nautical miles (185 km). Figure 14 shows the variation of the insertion point with insertion altitude. The choice of orbit altitude between 80 and 400 nautical miles (148 to 741 km) has negligible effect on orbit ground traces and crossrange maneuver requirements. Orbit results from launch azimuths from 58.3° to 125.5° were examined for their ability to sweep near the latitude of FRC (latitude 34.9° N, longitude 117.8° W), and to provide a maximum number of orbit passes near FRC. Orbit ground traces were generated using analog computations (ref. 12) and crossranges to FRC were calculated. Figure 21 presents these crossranges as a function of launch azimuth for orbits 1 through 6 and 15 through 21. This figure shows that the most functional launch azimuths for KSC to Edwards missions fall into two bands:

- (1) $50^\circ < \beta_L < 80^\circ$ for mission durations of four to six orbits
- (2) $100^\circ < \beta_L < 130^\circ$ for missions of two or less orbits and missions of 15 and 16 orbits.

Missions of 7 through 14 orbits are not feasible if the launch azimuth is to be maintained within normal range safety constraints ($\beta_L < 110$ deg) for KSC launches.

Figure 22 similarly shows the crossranges required for landings at an alternate East Coast site, Eglin AFB, Florida (latitude 30.47° N, longitude 86.5° W). Orbit one and two pass Eglin within the crossrange capability of the entry vehicle when the launch azimuth is less than 100° .

The number of orbits in the mission depends in part on requirements for in-flight preparations for the entry research experiments. Three orbits appear to allow ample time for such set-up and calibrations. Based on the data of figures 21 and 22, a launch azimuth of 65.8° East of North offers various trajectory and safety advantages for a three-orbit entry research mission. First, return to FRC on the third orbit does not require any cross-range maneuver. Even if the mission cannot be completed within three orbits, entry can be delayed until the fourth orbit, again without requiring crossrange, or until the fifth orbit with a crossrange of only 250 nautical miles (463 km). In the event of a premature mission abort, return to Eglin AFB is possible on the first orbit and into Edwards and Eglin AFB's on the second orbit, with medium crossrange maneuver requirements. Contingency landings can also be made at Eglin on the third and fourth orbits, well within the maneuverability of the HL-10. A landing may be made at Eglin even on the fifth orbit if the aerodynamics are as good as predicted by wind tunnel data. Orbit ground traces for this recommended launch azimuth are shown in figure 23a for the first five orbits.

Crossranges and landing times are presented in table 6 for both the primary (Edwards AFB) and the alternate (Eglin AFB) landing sites. For a launch time of 9:00 a.m. (local) at KSC, the normal and emergency landing times for each orbit are in daylight, providing a desirable measure of mission safety.

Longer missions with durations up to 16 orbits may be desirable. For a launch azimuth of 110° , landings may be made at FRC (Edwards AFB) on the 15th and 16th orbits. Contingency landings are then possible at Eglin AFB on the 13th and 14th orbits. All of these are well within the crossrange capability of the HL-10 configuration (figs. 21a and 21b). Orbit ground traces for the 110° launch azimuth are shown in figure 23b for 15 orbits. The 15th orbit, passing close to Edwards, is recommended to be the entry orbit for such a long duration mission. Landing times and crossranges to touchdown at selected sites are presented in table 7 for those orbits that come well within the crossrange capability of the entry vehicle (600 n. mi., 1.11 Mm). Landing times are shown in table 7 for a typical 3:00 p.m. (local) launch time.

Emergency landing sites are identified (fig. 23b and table 7) at Wheelus, Libya and in the Pacific south of Japan (30° N, 130° E) to provide a capability of landing on any of the first 17 orbits during daylight at a minimum number of sites. The Pacific location is presumed covered by a recovery ship which has terminal guidance capability. Similarly, if Wheelus is not available for land landing, an offshore recovery ship could provide for emergency recovery.

TABLE 6
BASIC RESEARCH MISSION RECOVERY PLAN

Landing site	Performance parameter	Orbit number				
		1	2	3	4	5
<u>Primary:</u> Edwards AFB, California	Crossrange n. mi.		250	10	10	250
	km		463	18.5	18.5	463
	Landing time hr:min.		9:26 a.m.	11:00 a.m.	12:34 p.m.	2:08 p.m.
<u>Alternate:</u> Eglin AFB, Florida	n. mi.	168	320	192	192	760
	km	311.1	592.6	355.6	355.6	
	Landing time hr:min.	10:06 a.m.	11:40 a.m.	1:14 p.m.	2:48 p.m.	

Launch from KSC at 9:00 a.m. with a 65.8° azimuth heading

Note: All times are local mean solar times (LMST)

TABLE 7
LONG DURATION MISSION RECOVERY PLAN

Landing site	Performance parameter	Orbit number																		
		1	2	3	4	5	6	7	8	9	10	11	12	13	14	15	16	17		
<u>Primary:</u> Edwards AFB, California	Crossrange n. mi.	145	480													80	118	410		
	km	268.5	880													148.5	218.8	760		
	Landing time hr:min.	1:52 p.m.	3:26 p.m.													11:48 a.m.	1:22 p.m.	2:56 p.m.		
<u>Alternate:</u> McKinley AFB, Florida	Crossrange n. mi.	450														210	95	50	355	
	km	834														389	176.3	389	92.7	638
	Landing time hr:min.	4:06 p.m.														9:20 a.m.	10:54 a.m.	12:28 p.m.	2:02 p.m.	3:36 p.m.
<u>Emergency:</u> Tunis, Libya	Crossrange n. mi.															524	100	69	46	423
	km															972	185.5	128	85.4	785
	Landing time hr:min.															8:50 a.m.	10:24 a.m.	11:58 a.m.	1:32 p.m.	3:06 p.m.
<u>Emergency:</u> Pacific Ship	Crossrange n. mi.	209	152	237	28	435														
	km	388	282	440	51.9	806														
	Landing time hr:min.		9:31 a.m.	11:05 a.m.	12:39 p.m.	2:13 p.m.	3:47 p.m.													

Launch from KSC at 3:00 p.m. with a 110° azimuth heading

Note: All times are local mean solar times (LMT)

ER 14471-3

VI. DEORBIT CHARACTERISTICS

Deorbit propulsion requirements and relationships with entry parameters were evaluated for orbit altitudes up to 400 nautical miles (740 km). These provided data for mission analysis for the flight phase which extends from initiation of deorbit to atmospheric entry at 400 000 feet (122 km). The results presented in this section were obtained from analog trajectory simulations with the following assumptions.

- (1) Spherical, non-rotating earth with a radius of 20 925 738 feet (6.38 Mm) and a gravitational constant of $1.407\ 639 \times 10^{16}\ ft^3/sec^2$ ($399\ Tm^3/sec^2$). This assumption was made (for this flight phase only) in order that the study results be independent of orbit inclination. The oblateness effects are, in general, negligible for present purposes. The rotational effects on ground range can be appropriately added, once the inclination is known, by desk calculations.
- (2) The deorbit velocity was applied impulsively (instantaneous velocity change) in the plane of the orbit and in a retrograde direction. The retrograde direction is essentially optimum for the present design considerations.

Figure 24 parametrically describes various entry conditions, including entry angle, entry velocity, range and time from deorbit to entry altitude, for deorbit maneuvers from circular orbits. Figure 25 is a similar presentation but for deorbit maneuvers originating at the apogee altitude of selected elliptical orbits.

Deorbit maneuvers from elliptical orbits would generally occur at or near apogee, particularly for a KSC launch with a perigee insertion into an elliptical orbit. The perigee insertion point and subsequent near-term perigees then occur in the northern hemisphere. Also, the desired landing sites such as Edwards and Eglin AFB are in the northern hemisphere at approximately the same latitude as insertion, and deorbit generally occurs about 180° of central angle prior to touchdown to minimize propulsion requirements.

The proposed entry research program can be performed adequately with a single entry angle such as -1.5° . However, some flexibility in entry angle is desirable. The velocity requirements to achieve a -1.5° and a -4.0° entry angle therefore were evaluated in detail, with the results displayed in figure 26. The minimum deorbit velocity requirement for entry angles from -1.5° to -4.0° occurs when the mission orbit is elliptical and the perigee altitude is lowest (80 nautical miles, 148 km). The deorbit velocities required to achieve a -4° entry angle are appreciably higher than for the -1.5° entry angle (fig. 26b). Altering the deorbit thrusting angle from retrograde ($\delta = -180^\circ$) to a line directed towards the center of the earth ($\delta = -90^\circ$) reduces the deorbit velocity requirement only for orbit altitudes less than 150 nautical miles (278 km). Even these velocity levels were 7 or 8 times greater than that required for a -1.5° entry angle.

These deorbit velocity requirements are nominal only. Safety considerations demand that some redundancy be added to the required levels. After a deorbit propulsion system is specified, variations in entry conditions can be achieved by varying flight parameters. This may be illustrated using figure 27. This graph presents entry angle as functions of deorbit thrusting angle and orbit altitude for specific deorbit velocities $\Delta V_{do} = 1\ 000$ fps (305 m/sec) and 520 fps (159 m/sec).

The following possibilities are then available for changing entry angle, if such is desired by an entry research requirement.

- (1) Change the launch insertion conditions to achieve a desired orbit altitude and eccentricity from which to initiate deorbit.
- (2) Adjust the deorbit thrusting angle. This technique is more effective at the higher orbit altitudes.
- (3) Allow for use of only a portion of the deorbit impulse capability. One approach is to provide multiple solid-propellant motors for deorbit, providing means thereby for maximum and minimum total impulses. With this technique, consideration must be given to safety requirements of backup deorbit capability.
- (4) Another method, not shown in figure 27, is to achieve the entry conditions by deorbiting from an elliptic orbit at a non-apogee point, as will be discussed later.

The 80/200 nautical miles (148/370 km) elliptic orbit is selected for the basic entry research program in part because it tends to minimize deorbit propulsion requirements, as indicated in figure 26a. For -1.5° entry angle, the velocity requirement is only 130 fps (39.6 m/sec). This is readily available from a single, spherical, solid-propellant motor. By providing two of these motors, a redundant capability and a total deorbit velocity of 260 fps (79.2 m/sec) are available. With two more motors of approximately the same size, the functions of both deorbit and ascent abort can be combined into a single system. This propulsion system provides a velocity potential in orbit of approximately 520 fps (158 m/sec) available in increments of 130 fps (39.6 m/sec). For the normal mission using a -1.5° entry angle, a quadruply redundant deorbit capability is therefore provided.

Some additional data related to such a deorbit versatility are presented in figure 28. For this data, an oblate rotating earth and the baseline 80/200 nautical miles (148/370 km) orbit were used to determine effects of deorbiting within $\pm 60^\circ$ of central angle about apogee using a retrograde thrust. Figures 28a and 28b show that the inertial range and time to entry altitude can be adjusted by selecting the deorbit location and by using one or more of the assumed motors. A range of entry angles from approximately -1.3° to -3.1° then can be achieved (fig. 28d). The inertial entry velocity is affected only by the deorbit impulse used (fig. 28c).

For normal deorbit, a velocity of 130 fps (39.6 m/sec) would be applied at or near apogee of the baseline orbit, to provide a -1.5° entry angle. This

DECLASSIFIED

normal deorbit impulse could be applied within a 60° central angle of the apogee point with negligible change in the entry angle and entry velocity (figs. 28c and 28d).

031400000000

(This page unclassified)

DECOMMISSIONED

ER 14471

PRECEDING PAGE BLANK NOT FILMED.

VII. ORBITAL ENTRY

A comprehensive parametric study of the performance of the HL-10 has been made for a return from near-earth orbits. Maneuver capability and the resulting entry environment have been obtained, including the effects of entry angle, wing loading, L/D, and bank angle. The results of these parametric analyses for entry at near-earth orbital speeds are presented in this section.

The entry trajectory computations were performed, in general, using an accurate, high speed analog computer simulation described in reference 12. An oblate, rotating earth and the ARDC 1959 atmosphere were used. The study dealt primarily with return from an orbit inclined 35.7°. This orbit inclination was emphasized in the entry calculations because of its use in the proposed 11-flight research program. The initial entry conditions at 400 000 feet (122 km) (velocity and entry angle) were obtained on the basis of an apogee deorbit from the baseline 80/200 nautical miles (148/370 km) orbit as functions of deorbit total impulse. The aerodynamic data of Section III of this Part, including viscous aerodynamic corrections, were programmed. Four angle-of-attack programs, functions of the viscous similarity parameter, $M^{\frac{6}{18}} \sqrt{Re_1}$, were selected to represent pitch control laws during entry. These

angles of attack varied during entry to correspond to four levels of viscous L/D as follows:

$L/D_{max.}$, 88% of $L/D_{max.}$, 75% of $L/D_{max.}$, and

$L/D_{min.} (C_L \text{ hypersonically})$.

The hypersonic angles-of-attack are on the backside of the L/D versus angle-of-attack curve (angle and lift greater than at $L/D_{max.}$).

The nominal touchdown point was assumed to be at FRC (Edwards AFB), California. The latitude and longitude of entry point (defined at 400 000 feet (122 km) altitude) were determined by using an iterative procedure with the analog simulation. First, the orbit inclination was predetermined, and entries were calculated using a 75% $L/D_{max.}$ angle-of-attack program, and no bank angle. Touchdown points were noted and the entry points were then corrected until the touchdown point had the coordinates for Edwards AFB. Table 8 is a summary of the initial conditions obtained in this manner. This part of study assumed open-loop programming of the angle-of-attack developed at one of the four L/D levels, and of a constant bank angle throughout entry. The bank angle was set at 0° when a 90° heading change was reached to improve crossrange. In addition to computing many entry trajectory parameters, stagnation point convective heating data were also determined based on using a 1.0 foot (0.305 m) nose radius.

TABLE 8
INITIAL CONDITIONS FOR ENTRY AT NEAR EARTH ORBITAL SPEEDS

Orbit inclination, deg	Inertial entry angle, γ, deg	Inertial entry velocity, V, fps (km/sec)	Entry latitude, deg	Wing loading		Weight, W, lbM (kg)	Length, l, ft (m)	Reference area, S, ft ² (m ²)
				Entry longitude, deg	(kN/m ²)			
* 35.7	-1.5	25 860(7.88)	2.1 S	166.0	E 50 (2.39)	10 200(463)	23.9(7.29)	204(19)
35.7	-2.0	25 780(7.86)	5.76 N	176.4	E 50 (2.39)	10 200(463)	23.9(7.29)	204(19)
35.7	-4.0	25 190(7.68)	19.68 N	198.5	E 50 (2.39)	10 200(463)	23.9(7.29)	204(19)
35.7	-1.5	25 860(7.88)	1.0 N	168.5	E 40 (1.92)	6 060(275)	20.6(6.28)	151.5(14.1)
35.7	-1.5	25 860(7.88)	2.0 S	163.2	E 60 (2.87)	15 500(704)	26.9(8.20)	258(24)
35.85	-1.5	25 860(7.88)	57.62 N	80.0	E 50 (2.39)	10 200(463)	23.9(7.29)	204(19)

*Considered the nominal condition for this study.

A. STUDY RESULTS--NOMINAL ENTRY CONDITION

Initial conditions described in table 8 were examined during this study. The condition indicated by the asterisk represents closely the entry condition later selected for the proposed flight test research program. The entry footprint for this condition ($\gamma = -1.5$, $i = 35.7^\circ$, $W/S = 50 \text{ psf} (2.39 \text{ kN/m}^2)$) is shown on figure 29a. This footprint is located over the North American continent as previously described so that a 75% L/D_{\max} entry with 0° bank angle provides a touchdown at Edwards AFB. The maximum footprint based on flying at L/D_{\max} throughout the entry includes most of the United States, and parts of Canada and Mexico. A maximum practical, or usable, footprint, however, is somewhat smaller depending on the status of L/D uncertainties and guidance tolerances. On figure 29a, the usable footprint for early flights of the HL-10 is more nearly described by the 88% L/D_{\max} contour. This contour still provides landing possibilities over most of the United States west of the Great Plain States.

The same footprint is shown on figure 29b in terms of downrange (R_d) and crossrange (R_c). Crossrange is defined as the distance perpendicular to the orbit trace of an orbit containing the state vector at the time of entry. Figure 29b shows that in accordance with this definition, a zero bank entry at 75% L/D_{\max} would develop a 70 nautical miles (130 km) crossrange to the left (or north). The maximum crossrange for this entry condition is approximately 800 nautical miles (1.48 Mm) to the left and 690 nautical miles (1.28 Mm) to the right. The environmental operating envelopes for this nominal entry condition are shown on figures 29c and 29d for bank angles up to 75° . Bank angles greater than 75° do not provide any performance improvements nor do they have any operational merit. Within the operating bounds of $\pm 75^\circ$ bank angle, and L/D_{\max} and L/D_{\min} , the following limitations can be assumed for the entry environment:

$$Q_{T_S}; 136\,000 \text{ Btu/ft}^2 (1.54 \text{ GJ/m}^2)$$

$$\dot{q}_s_{\max}; 196 \text{ Btu/ft}^2\text{-sec} (2.22 \text{ MW/m}^2)$$

$$q_{\max}; 550 \text{ psf} (26.3 \text{ kN/m}^2)$$

$$n_T_{\max}; 4 \text{ g}$$

The relationship between crossrange (R_c), total stagnation heat (Q_{T_S}), and entry time (t), is shown in figures 29e and 29f. The maximum total heat (Q_T) for this nominal entry condition is encountered in a maximum L/D entry with no bank angle. This type of entry also requires the maximum entry time

(2750 sec). Total stagnation heating is a strong function of entry time. Consequently, it can be reduced by any maneuver which reduces the entry time such as banking and lowering L/D level. This is true even though the peak stagnation heating rate (\dot{q}_S) occurs at L/D_{max} and increases with bank angle. This effect is also readily apparent in figure 29d.

Figures 29g-1 through 29g-5 show more details of the entry trajectory history at L/D_{max} , altitude, downrange, crossrange and velocity histories, along with a reproduction of the complete analog simulation strip recorder output for 0° and $\pm 45^\circ$ bank angle. Similar trajectory data is shown for 88% L/D_{max} entries on figures 29h-1 through 29h-5, for 75% L/D_{max} entries on figures 29i-1 through 29i-5, and for C_L_{max} entries on figures 29j-1 through 29j-5.

B. EFFECT OF L/D

The data for entries at $\gamma = -1.5^\circ$, and $W/S = 50 \text{ psf} (2.39 \text{ KN/m}^2)$, has been plotted on figures 29k-1 through 29k-6 as a function of L/D level to facilitate the evaluation of vehicle performance and entry environment at intermediate L/D levels. Increasing L/D improves the ranging capability, increases the heating environment, but relieves the peak dynamic pressure and total load factor environment. The peak values of dynamic pressure and load factor occur at a Mach number less than 2.4, where the entry is progressing to flight at smaller lift coefficients on the front side of the L/D vs angle-of-attack curves.

C. EFFECT OF BANK ANGLE

The effects due to varying bank angle during the nominal entry at $\gamma = -1.5^\circ$ and $W/S = 50 \text{ psf} (2.39 \text{ kN/m}^2)$ are presented on figures 29l-1 through 29l-5. Maximum crossranging capability occurs at a bank angle of 45° and is independent of L/D level used during entry. Peak stagnation heating rate increases with increasing bank angle primarily because banking reduces the vertical component of lift and, therefore, permits the vehicle to penetrate more deeply into the atmosphere at the higher velocities. Entry time is decreased by banking and for this reason total stagnation heating is reduced.

The effect of increasing bank angle on peak dynamic pressure is almost negligible at medium to low L/D levels (fig. 29l-4). The peak dynamic pressure, even with banking, continues to occur in the low supersonic flight regime and therefore is not affected by the increased altitude penetration to the first skip. The effect of bank angle on q_{max} is more noticeable at the higher L/D and bank angle levels.

Figure 29l-5 shows the effect of bank angle on maximum total load factor. No significant increase in n_T^{max} is noted for bank angles up to $\pm 50^\circ$. At

larger bank angles, the increase in n_T is more appreciable. Since maximum.

maximum crossrange capability is attained with a 45° bank angle, there appears to be little justification for entry flight at steeper than 45° bank angles.

D. FOOTPRINT VARIATION DURING ENTRY

An analysis was performed to evaluate the decrease in the size of the footprint that results if modulating to the extremes of L/D and bank angle were delayed until the entry was in progress. This would correspond to an operational situation where a decision to proceed to an alternate site is made after the entry is in progress. An entry trajectory at 75% L/D_{max} and 0° bank angle, landing at Edwards AFB was selected as a nominal. At preselected velocities along this trajectory, L/D and bank angle modulation was begun. The footprints resulting from this procedure are summarized on figure 29m.

The reduction in the footprint size is appreciable, even for the case where modulation is delayed only to the bottom of the first skip ($V_R = 24\ 000$ fps, 7.32 km/sec). The necessity to begin such maneuvers soon after entry is strongly illustrated.

E. ENTRIES AT STEEPER THAN NOMINAL ANGLES

An operational mission may require entering the earth's atmosphere with an entry angle greater than -1.5°. Therefore, two additional entry angles have been evaluated, -2° and -4°, for the nominal wing loading, W/S = 50 psf (2.39 kN/m²), and the nominal inclination, i = 35.7°.

Entry data, including footprints and envelopes describing the design environment, are shown in figures 30a through 30e for the -2° entry angle, and figures 31a through 31d for the -4° entry angle studies. These and other data have been combined in figures 32a through 32j to show parametrically the effects of steepening the entry angle.

In general, the effect of increasing the entry angle from -1.5° is to reduce the maneuver or performance potential of the HL-10, and to intensify the severity of the entry environment. These changes, however, are not linear with an increase in entry angle. Small increases in the entry angle, such as could result from a tolerance study of insertion, orbit decay, and deorbit would not appreciably affect the design parameters. Larger increases of the entry angle on the order of 2° or more have a marked effect on the magnitude of the design entry parameters, as illustrated in the following table.

<u>Entry Parameter</u>	Change in parameter from $\gamma = 1.5^\circ$ to . . .	
	-2°	-4°
γ		
R_c	-2.5%	-16.3%
R_d	-17.8%	-48.9%
\dot{q}_s _{max.}	+36%	+125%
Q_{T_s} _{max.}	-10.3%	-41.9%
$q_{max.}$	0	+89%
n_T _{max.}	+1.8%	+91.5%

F. EFFECT OF WING LOADING ON ENTRY PERFORMANCE

Size selection of the research vehicle had not been made at the time these parametric studies were being performed. The wing loading for vehicles A (one-man size) through E (eight-man size) ranged from about 40 psf (1.92 kN/m^2) to 60 psf (2.87 kN/m^2). Entry trajectories at these two levels of wing loading, and for a -1.5° entry angle, were simulated and evaluated.

The two extremes in wing loading were approximated as shown in table 8 by changing weight, vehicle length and vehicle reference area. In this way, the aerodynamic corrections due to viscosity, which are functions of Reynolds number, were properly simulated for the extreme wing loadings of 40 and 60 psf (1.92 and 2.87 kN/m^2).

Entry data summarizing performance and operating environment are shown in figures 33a through 33g for a wing loading of 40 psf (1.92 kN/m^2) and in figures 34a through 34d for a wing loading of 60 psf (2.87 kN/m^2). Since the nominal wing loading was assumed to be 50 psf (2.39 kN/m^2), sufficient data points are available to cross plot the effects of wing loading as shown in figures 35a through 35h.

The results of this analysis indicate that increasing wing loading generally increases all the entry performance and environment parameters except maximum load factor, as shown in the following table:

Effects of Wing Loading, W/S

Wing loading	$40 \text{ psf} \left(1.92 \frac{\text{kN}_2}{\text{m}} \right)$	$50 \text{ psf} \left(2.39 \frac{\text{kN}_2}{\text{m}} \right)$	$60 \text{ psf} \left(2.87 \frac{\text{kN}_2}{\text{m}} \right)$
Crossrange, R_c' to the left	790 n. mi. (1.46 Mm)	800 (1.48 Mm)	810 (1.50 Mm)
Downrange, R_d	6430 n. mi. (11.9 Mm)	6800 n. mi. (12.6 Mm)	7070 n. mi. (13.1 Mm)
Max. stag. heat rate, q_s max. ($\phi = 45^\circ$)	$134 \frac{\text{Btu}}{\text{ft}^2 - \text{sec}} \left(1.52 \frac{\text{MW}}{\text{m}^2} \right)$	$146 \frac{\text{Btu}}{\text{ft}^2 - \text{sec}} \left(1.66 \frac{\text{MW}}{\text{m}^2} \right)$	$154 \frac{\text{Btu}}{\text{ft}^2 - \text{sec}} \left(1.75 \frac{\text{MW}}{\text{m}^2} \right)$
Total stag. heat, Q_{rT_S} ($\phi = 0^\circ$)	$118 \ 500 \frac{\text{Btu}}{\text{ft}^2} \left(1.34 \frac{\text{GJ}}{\text{m}^2} \right)$	$136 \ 000 \frac{\text{Btu}}{\text{ft}^2} \left(1.54 \frac{\text{GJ}}{\text{m}^2} \right)$	$151 \ 000 \frac{\text{Btu}}{\text{ft}^2} \left(1.71 \frac{\text{GJ}}{\text{m}^2} \right)$
Max. dynamic pressure, q max.	$340 \text{ psf} \left(16.3 \frac{\text{kN}}{\text{m}^2} \right)$	$385 \text{ psf} \left(18.4 \frac{\text{kN}}{\text{m}^2} \right)$	$425 \text{ psf} \left(20.4 \frac{\text{kN}}{\text{m}^2} \right)$
Max. load factor, n_{rT} max. ($\phi = \pm 45^\circ$)	1.96 g	1.94 g	1.82 g

ER 14471-3

G. ENTRY FROM A NEAR POLAR ORBIT

Parametric data was also obtained for a return entry into Edwards AFB from an orbit inclined 85° to the equator. Only the approach from the north was examined. An entry angle of -1.5° and a wing loading of 50 psf (2.39 kN/m^2) were assumed. The results of this entry condition are summarized in figures 36a through 36d.

The entry footprint (fig. 36a) for this inclination appears to differ considerably from the footprint for a 35.7° inclination (fig. 29a). Actually, the differences are minor, but in this presentation are exaggerated because of the co-ordinate projection, especially across lines of longitude nearer the ear h's pole. A better understanding of the changes in the footprint is obtained by comparing plots of R_c vs R_d , figures 29b and 36b. The differences can be related to the increased relative velocity (with respect to the rotating earth atmosphere) of the 85° orbit as compared to the 35.7° orbit. This relative velocity increase manifests itself in a small increase in the maneuver capability, and a slightly more severe entry environment as shown below:

	<u>Orbit inclination</u>	
	<u>35.7°</u>	<u>85°</u>
Average crossrange, $(R_c \text{ left} + R_c \text{ right})/2$	745 n. mi. (1.38 Mm)	790 n. mi. (1.46 Mm)
$\dot{q}_s \text{ max.}$	$196 \frac{\text{Btu}}{\text{ft}^2 \text{ - sec}} \left(2.22 \frac{\text{MW}}{\text{m}^2} \right)$	$214 \frac{\text{Btu}}{\text{ft}^2 \text{ - sec}} \left(2.43 \frac{\text{MW}}{\text{m}^2} \right)$
Q_{T_S}	$136\ 000 \frac{\text{Btu}}{\text{ft}^2} \left(1.54 \frac{\text{GJ}}{\text{m}^2} \right)$	$154\ 000 \frac{\text{Btu}}{\text{ft}^2} \left(1.75 \frac{\text{GJ}}{\text{m}^2} \right)$
$q_{\max.}$	$550 \text{ psf} \left(23.6 \frac{\text{kN}}{\text{m}^2} \right)$	$550 \text{ psf} \left(23.6 \frac{\text{kN}}{\text{m}^2} \right)$
$n_T \text{ max.}$	4 g	4.18 g

DECLASSIFIED

VIII. ENTRIES AT SUPERCIRCULAR VELOCITIES

The entry flight of the HL-10 has been examined in the range of supercircular entry velocities up to and including 34 000 fps (10.4 km/sec). This range was selected because of the secondary objectives of the study to examine use of the manned lifting body entry research vehicle for supercircular velocity entries using typical launch vehicles. This analysis was performed using the analog trajectory simulation program.

The entries were initiated from equatorial orbits over a rotating, oblate earth and with an ARDC 1959 atmosphere. All entry conditions were initiated at 0° latitude and longitude with an easterly heading. Two levels of L/D were simulated, L/D_{max} and L/D_{min} . The latter corresponds to C_L_{max} .

during hypersonic flight. Attenuation of the flight path phugoid following entry into the atmosphere was accomplished by using bank angle modulation. Entry stagnation heating data was developed for a nose radius of one foot (0.305 m). An HL-10 canopy-D configuration weighing 6060 pounds (2.75 Mg), with a length of 20.6 feet (6.28 m), and a reference area of 151.5 ft^2 (14.1 m^2), $W/S = 40 \text{ psf}$ (1.92 kN/m^2), was assumed for the study. This is representative of an unmanned research vehicle such as described in Part VIII, Alternate Approaches. A manned vehicle such as the D/2 is longer (25 ft, 7.6 m) and has a higher W/S (53 psf, 2.6 kN/m^2).

A. CONTROL LOGIC

A simple control logic was selected for the supercircular entry calculations which use bank angle modulation with a constant altitude constraint. Initial values of angle-of-attack and bank angle are based on downrange and crossrange requirements. Entry proceeds with these values until the first pull-out where the local flight path angle has decreased to 0°. The bank angle is then increased to reduce the vertical component of lift to prevent a climb-out. As the speed decreases, the bank angle is reduced, maintaining constant altitude, until the angle reaches its initial value. Bank angle modulation is then discontinued and the entry proceeds essentially along an equilibrium glide path. When the turn angle reaches 90°, the bank angle is reduced to zero to improve the crossrange.

This control logic is used in this phase of the study to acquire parametric environmental data and to provide a basis for mission planning. The actual guidance logic recommended for the flight program uses a closed-loop scheme which includes modulation in pitch and roll angles. The recommended primary and backup guidance equipments are discussed in Part VII.

B. ENTRY CORRIDOR

Figure 37 describes the range of available entry angles for entry velocities between 26 000 and 34 000 fps (7.93 and 10.4 km/sec). The upper skip limit was determined based on an entry at $C_{L_{max}}$ using bank angle modulation.

The skip limit is defined as the minimum entry angle at which roll modulation to inverted flight (bank angle = 180°) could not limit the subsystem altitude transient below the entry altitude.

The lower limit of the entry corridor results from a load factor constraint for an entry at $C_{L_{max}}$. Lower limits are shown in figure 37 based on constraints on total deceleration of 6 and 8 g. The entry conditions of interest lie between the skip limit and g-limit constraints. Additional heating constraints, for example, might also be imposed. The specific entry conditions evaluated in this analysis are indicated in figure 37 and are tabulated for convenience in Table 9.

TABLE 9
ENTRY CONDITIONS AT SUPERCIRCULAR SPEED

Inertial entry velocity		Inertial entry angles, deg		
fps	km/sec	low	medium	high
26 000	7.93	-1.5	-4.4	-7.3
28 000	8.54	-3.3	-5.2	-7.2
30 000	9.15	-4.2	-6.0	-7.1
32 000	9.76	-4.9	-6.0	-7.1
34 000	10.4	-5.4	-6.2	-7.0

C. STUDY RESULTS

Presentations of trajectory data are included in this section for three entry velocities. Results from the analysis of the three velocities, 26 000, 30 000, and 34 000 fps (7.93, 9.15, and 10.4 km/sec) are typical for the entire range. The summary plots at the end of this section include data obtained from entries starting at these speeds, plus trajectories calculated for intermediate entry speeds of 28 000 fps (8.54 km/sec) and 32 000 fps (9.76 km/sec). Figures 38a through 38l-7 contain detailed data for entries

at 26 000 fps (7.93 km/sec). Figures 39a through 39l-7 contain data for entries at 30 000 fps (9.15 km/sec), and figures 40a through 40l-7 contain data for entries at 34 000 fps (10.4 km/sec). Figures 41a through 41g present summaries of the more pertinent design parameters throughout the entire entry velocity and entry angle regime analyzed.

Figure 41a shows the effect of entry velocity and entry angle on maximum dynamic pressure. Throughout the entry velocity range, flight at L/D_{max} at the steeper entry angles consistently developed the maximum dynamic pressure. An entry at 26 000 fps (7.93 km/sec), at L/D_{max} , with an entry angle close to an 8-g entry corridor pullup limit, will experience about a 1 000 psf (47.9 kN/m^2) peak dynamic pressure. This peak dynamic pressure diminishes to 740 psf (35.4 kN/m^2) for an entry using 34 000 fps (10.4 km/sec) at the 8-g entry corridor pullup limit. The trend indicated in figure 41a shows that for a given entry angle, increasing the entry velocity decreases the peak dynamic pressure.

An interesting reversal of these trends occurs for entries at the smaller entry angles (figures 38a, 39a and 40a). The critical flight condition for peak dynamic pressure then is $C_{L_{max}}$, and not L/D_{max} . This trend

reversal occurs because the critical point in the entry, at which peak dynamic pressure develops, shifts from a subsonic condition at low entry angles to a hypersonic condition at the higher entry angles. This effect is also clearly illustrated in the strip recorder data for an entry velocity of 30 000 fps (9.15 km/sec) in figures 39h through 39k.

Figure 41b shows the effect of entry velocity and entry angle on the peak load factor experienced during entry. The data on this figure is for $C_{L_{max}}$ entries. For any given entry angle and entry velocity, the critical condition always occurs during a $C_{L_{max}}$ entry (cf. figures 38a, 39a and 40a). For a given entry angle, the peak load factor experienced during the entry decreases as entry velocity increases.

Figures 41c and 41d show the effect of entry velocity and entry angle on the peak aerodynamic stagnation heating parameters. For entry at angles near the entry corridor of the skip limit, the peak stagnation heating rate and the total stagnation heating both increase as the entry velocity is increased. Figure 41g shows there is also a substantial decrease in the entry time as entry velocity increases. The shorter flight duration at the higher entry velocities results in the total heating increasing only about 10 percent while the peak stagnation heating rate increases almost 300 percent.

Entry vehicle performance in terms of downrange and crossrange maneuverability (figs. 41e and 41d) improve appreciably as entry velocity increases for a given entry angle. For example, a maximum crossrange of 1 080 nautical miles (1.93 Mm) is theoretically possible at an entry velocity of

03 [REDACTED] 30

34 000 fps (10.4 km/sec). The same configuration is capable of a maximum crossrange of only 800 nautical miles (1.48 Mm) at 26 000 fps (7.93 km/sec). The entry angle, however, cannot be maintained for any significant increase in entry velocity without approaching the skip limit of the entry corridor. To avoid skipping, the entry angle is increased as entry velocity increases. For this reason (cf. figure 41f), the maximum potential downrange for an entry at 34 000 fps (10.4 km/sec) could be reduced to one-third the maximum downrange at a 26 000 fps (7.93 km/sec) entry.

DECOMMISSIONED

IX. LANDING PERFORMANCE

The primary landing site, Edwards AFB, California, has a runway altitude 2300 feet (702 m) above sea level. Touchdown speeds at this altitude for a standard day density are shown in figure 42 for various wing loadings, W/S, assuming equilibrium glide flight. The representative lift coefficients here are for Mach 0.35, typical of approach and landing speeds.

The D/3 configuration has a wing loading of 55.1 psf (2.64 kN/m^2). Its landing gear is designed for tail clearance with the ground at touchdown at up to a 25° angle of attack. At a nominal 20° angle of attack, the touchdown speed for this vehicle is 217 knots (112 m/sec) (fig. 42). This speed is reduced to 189 knots (97 m/sec) at an angle of attack at touchdown of 25° .

Estimates of the incremental changes to aerodynamic lift and drag, due to landing gear extension and ground effects based on data for SV-5, are presented in figures 43 and 44, respectively. These estimates are included in the digital simulation of the landing maneuver. The complete extension of the landing gear was assumed to require 2 seconds (the design criterion, however, is 1 sec). The landing gear effects were varied in the simulation linearly with the gear extension. The ground effects were not included until the entry vehicle was within 10 feet (3.05 m) of the ground.

The landing maneuver is initiated by increasing angle-of-attack to a pre-determined pull-up load factor. This load factor is maintained until the rate of sink (R/S) has decreased to less than 13 fps (4 m/sec). The angle of attack is then reduced to terminate the pull-up maneuver and later increased as required during the float phase to maintain a rate of sink no greater than 13 fps (4 m/sec) until touchdown. The landing gear is deployed sometime during the last 10 seconds before touchdown.

Two landing trajectories are presented in figure 45 for different load factors during the pull-up, 1.35 and 2.0 g. The angle of attack at touchdown is 20° which ensures adequate tail clearance. The different load factors provide significant variations in the trajectory parameters. Table 10 summarizes data pertaining to the two landing trajectories.

Discussions with the flight test personnel of the current HL-10, M2-F2 air launch test program at FRC have indicated that pilot preference during the landing maneuver of these vehicles is to maintain an excess of kinetic energy for final flight path corrections. The pilots therefore prefer to initiate the flare from a relatively steep flight path angle of -30° , with an indicated airspeed in excess of 300 knots (154 m/sec). They prefer to develop 1.8 to 2.2 g during the flare with a subsequent float phase of at least 10 seconds. Gear extension is delayed until 1 to 5 seconds prior to touchdown. Trajectory (b) was computed to approximate a trajectory based on these pilot preferences.

30

TABLE 10
SUMMARY OF LANDING TRAJECTORY DATA

	Trajectory (a) fig. 45a	Trajectory (b) fig. 45b
<u>Start of flare</u>		
Altitude	5580 ft (1.7 km)	3860 ft (1.18 km)
Height above runway	3280 ft (1 km)	1560 ft (0.475 km)
Range from touchdown	2.4 n. mi. (4.44 km)	1.55 n. mi. (2.87 km)
Indicated airspeed	332 knots (171 m/sec)	331 knots (171 m/sec)
True airspeed	362 knots (186 m/sec)	351 knots (181 m/sec)
Flight path angle (relative)	-26.9°	-30.5°
Load factor	1.35 g	2.0 g
<u>End of flare (start of float)</u>		
Altitude	2376 ft (723 m)	2451 ft (747 m)
Height above runway	76 ft (23.2 m)	151 ft (46 m)
Range from touchdown	0.4 n. mi. (741 m)	0.79 n. mi. (1.46 km)
True airspeed	265 knots (136 m/sec)	288 knots (148 m/sec)
Speed lost in flare	97 knots (49.8 m/sec)	63 knots (32.4 m/sec)
Time in flare	23.2 sec	9 sec
<u>Touchdown</u>		
Angle of attack	19.5°	19.5°
True airspeed	226 knots (116 m/sec)	226 knots (116 m/sec)
Rate of sink	12 fps (3.66 m/sec)	12 fps (3.66 m/sec)
Time in float	5.82 sec	11 sec

These trajectories serve as a basis for preliminary considerations of visibility during the approach and landing, and of landing gear design characteristics. Pilot-in-the-loop analog simulations are required, however, to define in detail the landing maneuver.

X. ABORT ANALYSIS

Analyses of abort trajectories have been performed to determine the environment and guidelines for design of the entry vehicle and its abort propulsion system. Primary emphasis was placed on evaluation of the abort environment using a Titan III-2 launch vehicle from KSC on an azimuth of 65.8° to an insertion altitude of 80 nautical miles (148 km). Included is an evaluation of abort from on-the-pad and a study of the fall-back area of the spent booster parts. Additional analyses concern the effects on the launch trajectory due to altering the insertion altitude and changing the launch vehicle. Variations in the abort entry environment as affected by entry vehicle wing loading were also considered. The following sections present a discussion of the trajectory abort studies. The various abort modes are summarized in figure 46, and other design aspects are discussed in Parts IV, V, and VII.

A. PAD ABORT

The hazard environments due to an explosion on the pad of a Titan III or Saturn 1-B launch vehicle are indicated in Part IV. The limiting boundary of a pad-explosion fireball is shown for Titan III in figure 47 together with an envelope of heating rate which is critical to parachute material.

In a typical abort from the pad, two of the four solid-propellant motors provided for abort and deorbit functions would be ignited. At the same time the adapter separation is initiated, freeing the entry vehicle to begin a vertical rise away from the launch vehicle. At burnout of the abort motors, the entry vehicle is already outside the envelope of the ensuing fireball. At this time, the burned out abort motors are ejected and the two remaining solid propellant motors are ignited. Also, a 10°/sec pitch program is initiated to reach an angle of attack of 15° prior to thrust termination. This angle of attack corresponds to L/D_{max} at subsonic speeds. At thrusting termination, the spent motors and the remaining portion of the adapter are jettisoned. By this time the vehicle has reached a velocity of 320 fps (97.5 m/sec) and an altitude of 1000 feet (305 m) and continues along a ballistic trajectory until it reaches an apogee 13.1 seconds after liftoff. Here the vehicle is at an altitude of 2200 feet (671 m) and in an inverted (upside down) position. Sufficient aerodynamic roll control is available at this point ($V = 135$ fps, 41.2 m/sec) to roll the vehicle level. Seat ejection of the crew or complete vehicle recovery is then initiated. Normally a water landing and recovery would be made just offshore. The present concept does not provide for a normal horizontal landing because of the flight distance to a suitable landing strip.

B. LAUNCH ABORT

A launch trajectory for Titan III-2 and one for Saturn 1-B are shown in figure 48. These served as a basis for initiating abort trajectories assuming malfunctions at various ascent flight velocities. The subsequent entry vehicle flight environment was calculated to provide vehicle design criteria. These launch abort flight data are described in the following paragraphs. Figure 48 indicates the speeds at which subsequent abort flight provides critical load factors and stagnation point heating rates. These were calculated for the Titan III-2 with insertion at 80 nautical miles (148 km).

The velocity increment applied by the abort propulsion system was treated parametrically using increments up to 1000 fps (305 m/sec). Specific maneuvers (pitch programs) were selected for the flight of the entry vehicle following abort. Its angle of attack was increased to the level for $C_{L_{max}}$ and adjusted thereafter to maintain $C_{L_{max}}$.

Pertinent environmental parameters are presented in figure 49 as functions of the velocity at initiation of the abort maneuver. These data include the maximum values of dynamic pressure, stagnation point heating rate and load factor during the flight following abort for bank angles of 0° and 45° and for abort motor velocity increments of 0 and 600 fps (182 m/sec). The extremes which yield a basis for design criteria occur at the following ascent velocities:

Peak dynamic pressure, q_{max} . 1271 fps (388 m/sec)

Peak heat transfer rate, $\dot{q}_{s_{max}}$. 21 500 fps (6.56 km/sec)

Peak total load factor, $n_{T_{max}}$. 13 500 fps (4.13 km/sec)

The design abort condition for q_{max} depends upon the magnitude of the incremental velocity change that is delivered by the abort system. The effect of drag in reducing the abort motor velocity increment cannot be neglected. This would reduce q_{max} below 1200 psf (5.75 kN/m^2) for the abort speeds near 1000 fps (.3 km/sec). A second q_{max} peak occurs simultaneously with the peak load factor. This peak is not as sensitive to the magnitude of the abort velocity increment.

In summary, the abort design conditions from a Titan III-2 launch trajectory occur at a relative velocity of 13 500 fps (4.13 km/sec) and at 21 500 fps (6.56 km/sec) during the ascent trajectory to 80 nautical miles (148 km). These design conditions are as follows for an HL-10 abort entry at $C_{L_{max}}$, with wing loading of 50 psf (2.39 kN/m^2).

	Bank angle, deg	
	0	45
q_{\max} , psf (kN/m^2)	520 (24.9)	625 (30)
$n_T \max$, g	7.8	9.75
$q_s \max$, $\text{Btu}/\text{ft}^2\text{-sec}$ (MW/m^2)	155 (1.76)	170 (1.93)

The entry vehicle structure could meet the criteria for the 7.8 g and 9.75 g load factors. The crew, however, requires a limitation of 6 g. This limit can be met by modulation of the angle-of-attack to reduce lift. A discussion of the modulation technique follows later in this section.

C. LANDING ENVELOPES

The post-abort flight of the entry vehicle after separation from the launch vehicle provides an opportunity to maneuver to some selected landing position. If this maneuver is made at $C_L \max$ with bank angle limits of $\pm 45^\circ$, the

landing envelope areas are shown in figure 50. This figure in essence shows a set of footprint heels, since L/D levels other than $C_L \max$ were not considered at present because of the desire to relieve the abort design environment.

Bermuda is located within this landing envelope which is developed for a 65.8° launch azimuth. For this reason, Bermuda is potentially an ideal base in the west Atlantic on which to station and deploy recovery forces. Horizontal landings on Bermuda following a launch abort at relative velocities up to 13 500 fps (4.13 km/sec) may also be possible. Although it is not shown in figure 50, the availability of Bermuda could be further extended by using the abort velocity in a retrograde direction.

Grand Canary Island in the east Atlantic is another potential location on which to base a launch abort recovery operation as it is also located within the landing envelope of figure 50. It appears feasible that with proper guidance programming the HL-10 could be maneuvered to within a reasonable radius of either Bermuda or Grand Canary Island. An efficient recovery operation in the Atlantic might then need only these two bases.

D. EFFECT OF WING LOADING

Effects of varying wing loading (W/S) between 40 and 60 psf (1.91 and $2.87 \text{ kN}/\text{m}^2$) were investigated. The results are summarized in figure 51. Increasing W/S causes an appreciable increase in the magnitude of the abort design parameters, as summarized below for a no bank angle entry at $C_L \max$.

	Wing loading, W/S, psf(kN/m ²)		
	40 (1.91)	50 (2.39)	60 (2.87)
$q_{\max.}$, psf (kN/m ²)	345 (16.5)	520 (24.9)	595 (28.5)
$n_T^{\max.}$, g	6.8	7.8	10
$\dot{q}_s^{\max.}$, Btu/ft ² sec(MW/m ²)	145 (1.65)	155 (1.76)	170 (1.93)

E. EFFECT OF L/D AND BANK ANGLE ON THE ABORT PARAMETERS

The critical abort environment is less severe when the entry is made at $C_L^{\min.}$ ($L/D_{\min.}$) and zero bank angle. Some maneuvers, however, may require using the higher L/D capability of the entry vehicle. Increasing L/D from $L/D_{\min.}$ to 75% of $L/D_{\max.}$ increases $q_{\max.}$ by 11%, increases $\dot{q}_s^{\max.}$ by 6%, and increases $n_T^{\max.}$ by 1%. An entry using a 45° bank angle can increase $q_{\max.}$ by 22%, $\dot{q}_s^{\max.}$ by 9% and $n_T^{\max.}$ by 25% over entry values at zero bank angle.

F. EFFECT OF INSERTION ALTITUDE ON THE ABORT PARAMETERS

The ascent trajectory of a launch vehicle can change significantly for different orbit insertion altitudes (figure 48). The subsequent post-abort environment and criteria for design of the entry vehicle are therefore dependent on the specification of this trajectory. For the Titan III-2 ascent at an insertion altitude of 100 nautical miles (185 km) compared to 80 nautical miles (148 km), the abort design parameters increase about 11%, as summarized below for zero bank angle:

	Insertion altitude, n. mi. (km)	
	80 (148)	100 (185)
$q_{\max.}$, psf (kN/m ²)	520 (24.9)	560 (26.8)
$n_T^{\max.}$, g	7.8	8.8
$\dot{q}_s^{\max.}$, Btu/ft ² -sec(MW/m ²)	155 (1.76)	170 (1.93)

DECLASSIFIED

G. LAUNCH ABORT WITH THE SATURN 1-B

A Saturn 1-B launch trajectory to an 80 nautical mile (148 km) insertion altitude is considerably different from that of Titan III-2 (fig. 48). Abort trajectories of the entry vehicle were generated from the Saturn 1-B trajectory originating at the ascent velocities which were most critical for the Titan III. These calculations, summarized below, indicate a more critical entry flight environment than for Titan III, partly because the Saturn 1-B trajectory is almost everywhere higher in altitude.

	Launch vehicle	
	Titan III-2	Saturn 1-B
$q_{\max.}$, psf (kN/m^2)	520 (24.9)	670 (32.1)
$n_T^{\max.}$, g	7.8	10.15
$\dot{q}_s^{\max.}$, Btu/ $\text{ft}^2\text{-sec}$ (MW/m^2)	155 (1.76)	165 (1.87)

Prior abort studies (ref. 5) indicated that the critical abort velocities from the Saturn 1-B trajectories occur at lower ascent velocities. The abort environment from a Saturn 1-B is, therefore, more severe than shown in this table.

H. ASCENT ABORT ENTRY WITH PITCH ANGLE MODULATION

The angle-of-attack can be adjusted during the abort entry flight to limit the maximum load factor. As the flight progresses to lower altitudes and higher dynamic pressures, load factor control is obtained by reducing the pitch angle to decrease the lift coefficient. Some characteristics of this technique were evaluated for Titan III-2 and Saturn 1-B ascent trajectories with insertion at both 80 and 100 nautical miles (148 and 185 km). The abort entry trajectories were calculated using pitch modulation to limit peak acceleration to 6 g. Table 11 summarizes pertinent results from which the following observations are derived:

- (1) The abort condition for critical load factor from the Saturn 1-B occurs at a much lower ascent velocity than from the Titan III-2.
- (2) The maximum dynamic pressure encountered in a launch abort from a Saturn 1-B can be three times as severe as from a Titan III-2. Furthermore, this peak value exceeds the limiting design criterion of 1200 psf (57.5 kN/m^2). The Saturn 1-B trajectory could be reshaped to reduce the value, with a reduction in payload capability.
- (3) The time during which the peak 6 g acceleration is experienced for a Saturn 1-B abort is almost twice that for Titan III-2.

- (4) The angle of attack during the modulation maneuver following a Saturn 1-B launch abort reduces to as low as 16° . The angle of attack for maximum L/D, however, is approximately 27° . The entry vehicle therefore must be operated on the front side of the L/D curve for part of its flight. This complicates guidance and control, and some additional heat protection might be required on the upper surface.

Figure 52 shows the time histories of three types of entry trajectories from critical abort condition on a Titan III-2 launch trajectory to 80 nautical miles (148 km). The modulated angle-of-attack entry is compared to entries at $C_{L_{\max}}$ and at L/D_{\max} . Results are summarized in table 12. Down-

range, measured from launch abort to touchdown, and peak heating ratio are not significantly increased for the modulated entry.

Figure 53 presents trajectory parameters for the abort condition which results in the maximum load factor environment during entry. Data are shown for Titan III-2 and Saturn 1-B launch trajectories to an 80 nautical mile (148 km) insertion altitude.

I. BOOSTER FALL-BACK

The location of impact points for the Titan III-2 in the event of a malfunction and abort was examined. The instantaneous impact points were approximately computed using a vacuum trajectory, assuming that all external forces except gravity are removed at the time of abort. Results are presented in figure 54 for the Titan III-2 launched at an azimuth of 65.8° from KSC, to an altitude of 80 nautical miles (148 km).

The SRM's (Stage 0) are normally dropped 92.5 seconds after liftoff and impact at a position 28.7°N and 79.9°W . Burnout of Stage 1 occurs at 247.59 second and impact occurs at 32.08°N and 69.3°W . Stage 2 of the launch vehicle is inserted into orbit along with the payload. Coordinates for Bermuda are indicated in figure 54. Normal impact locations of the launch vehicle pose no threat to Bermuda.

TABLE 11
SUMMARY OF MODULATED ABORT RE-ENTRIES

<u>Launch vehicle</u>	<u>Insertion altitude, n. mi. (km)</u>	<u>Critical abort velocity (relative), fps (km/sec)</u>	<u>Peak dynamic pressure, psf (kN/m^2)</u>	<u>Peak load factor, g</u>	<u>Total time at 6 g, sec</u>	<u>Minimum during modulation, deg</u>
Titan III-2	80 (148)	13 000 (3.96)	565 (27)	6	23	39
Titan III-2	100 (185)	12 950 (3.95)	980 (46.9)	6	35.5	26.6
Saturn 1-B	80 (148)	9 850 (3.0)	1550 (73.2)	6	41	16

TABLE 12
COMPARISON OF MODULATED AND UNMODULATED ABORT ENTRIES

<u>Angle-of-attack modulation</u>	<u>L/D</u>	<u>Downrange, n. mi. (Mm)</u>	<u>Peak dynamic pressure, psf (kN/m^2)</u>	<u>Load factor, g</u>	<u>Peak heating rate, Btu/$\text{ft}^2\text{-sec}$ (MW/m^2)</u>
yes	Min.	775 (1.44)	565 (27.1)	6	75 (.852)
no	Min.	752 (1.39)	520 (24.9)	7.8	79 (.896)
no	Max.	926 (1.72)	1400 (67)	8.15	131 (1.48)

(This page unclassified)

RECEDING PAGE BLANK NOT FILMED

REFERENCES

1. Ladson, Charles L.: Effects of Various Canopies on the Aerodynamic Characteristics of a Manned Lifting Entry Vehicle at Mach 0.06 to 6.8. NASA TMX-1321, 1966 (C).
2. Campbell, James F.; and Grou, Josephine W.: Stability and Control Characteristics of a Manned Lifting Entry Vehicle at Mach Numbers from 1.50 to 2.16 Including Hinge Moment and Pressure Distribution Data. NASA TMX-1314, 1966 (C).
3. McShera, John T.; and Campbell, James F.: Stability and Control Characteristics of a Manned Lifting Entry Vehicle at Mach Numbers from 2.29 to 4.63. NASA TMX-1019, 1964 (C).
4. Ladson, Charles L.: Aerodynamic Characteristics of a Manned Lifting Entry Vehicle with Modified Tip Fins at Mach 6.8. NASA TMX-1158, 1965 (C).
5. Wing, L. D.; and Eillertson, W. H.: Research Studies and Analyses to Define Manned Lifting Entry Flight Environment. NASA CR-639, 1966 (C).
6. Titan III Boosters for Langley's Manned Lifting Body Entry Program (U). Report M-66-8, Martin Marietta Corporation, February 1966 (C).
7. Revised Saturn 1-B Preliminary Reference Trajectory for the A5-207 Mission. Technical Bulletin TB-AE-65-295, Chrysler Corporation, November 12, 1965 (C).
8. Saturn 1-B Launch Vehicle Supporting Technical Information for a Study of the Influence of Size of a Manned Lifting Body Entry Vehicle on Research Potential and Project Cost. Langley Research Center Information Note, May 1966 (C).
9. Saturn 1-B Launch Vehicle Design Data. Internal Note, IN-P and VE-V-63-1, Marshall Space Flight Center, August 8, 1963 (C).
10. Gemini Launch Program, GTA-9, Pre-Flight Test Report (U). Report LV-326-9, Martin Marietta Corporation, April 1966 (C).
11. Manned Orbiting Laboratory Titan III Pre-Phase I Study, Volume III-6 Payload Performance, Volume III-9 Payload Growth. Report SSD-TR-64-207, Air Force Systems Command, September 1964 (C).
12. Rubin, Arthur and Shepps, Lloyd: A General Purpose Analog Translational Trajectory Program for Orbiting and Re-entry Vehicles. Report ER-14258, Martin Marietta Corporation, June 1966.

(This page unclassified)

PRECEDING PAGE BLANK NOT FILMED

REF ID: A657030

ILLUSTRATIONS

031410307030
ER 14471-3

0317122A1030

DECOMMISSIONED

PRECEDING PAGE BLANK NOT FILMED

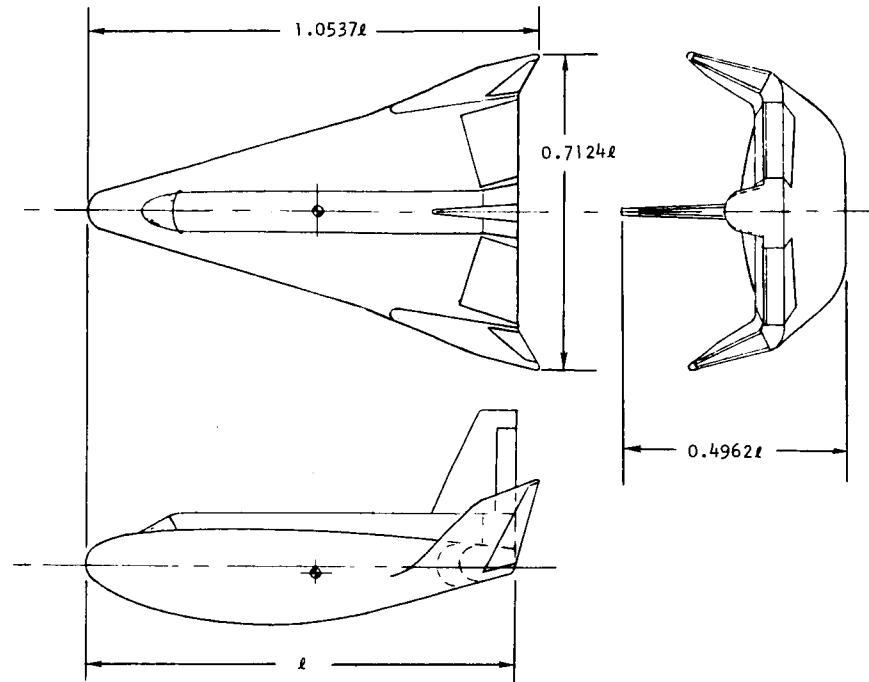


FIGURE 1. HL-10 ENTRY VEHICLE WITH CANOPY

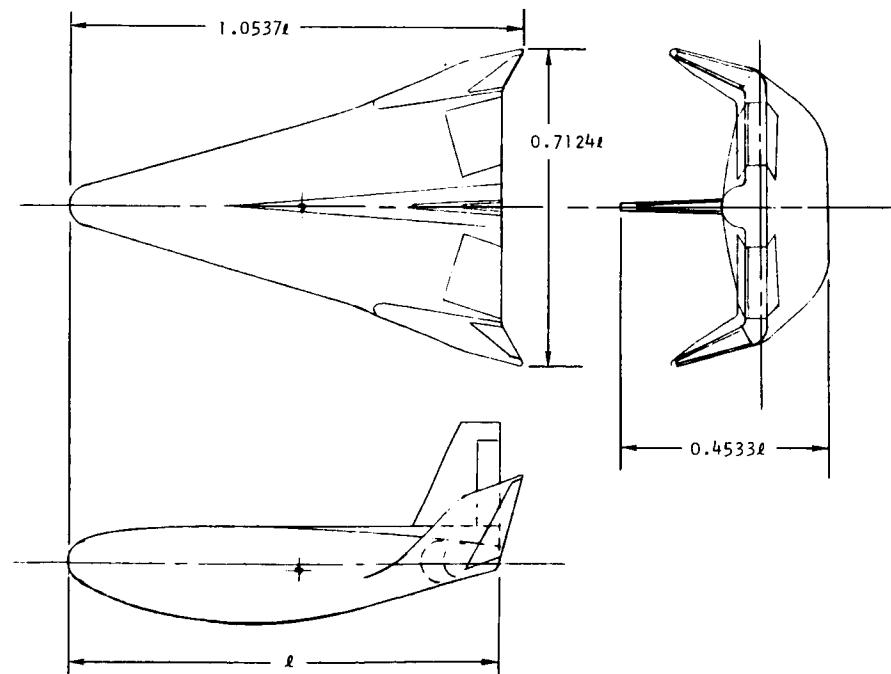


FIGURE 2. HL-10 ENTRY VEHICLE WITHOUT CANOPY

030
ER 14471-3

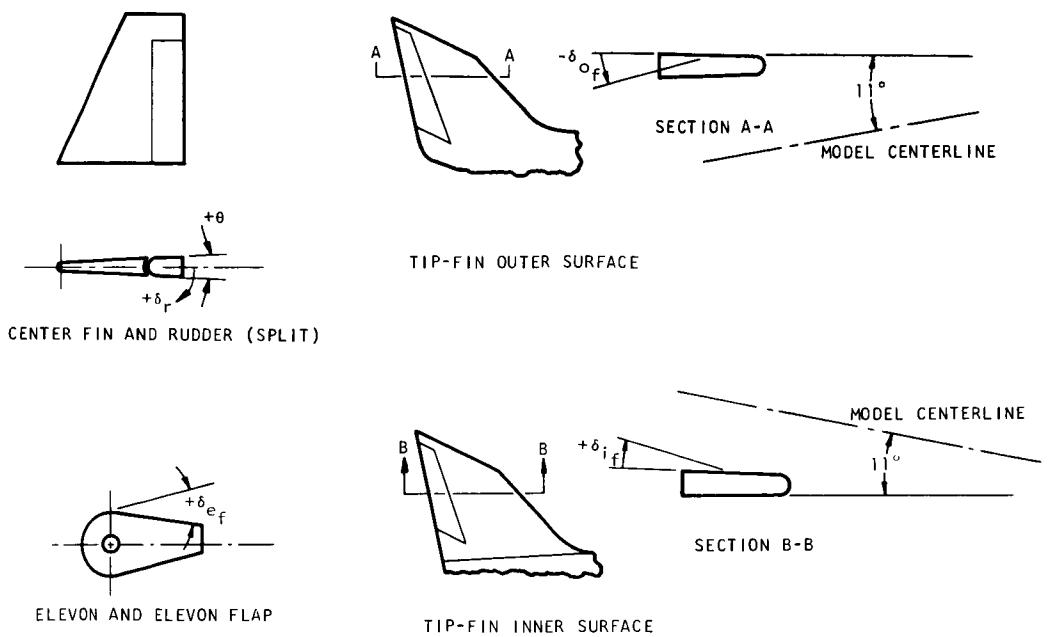
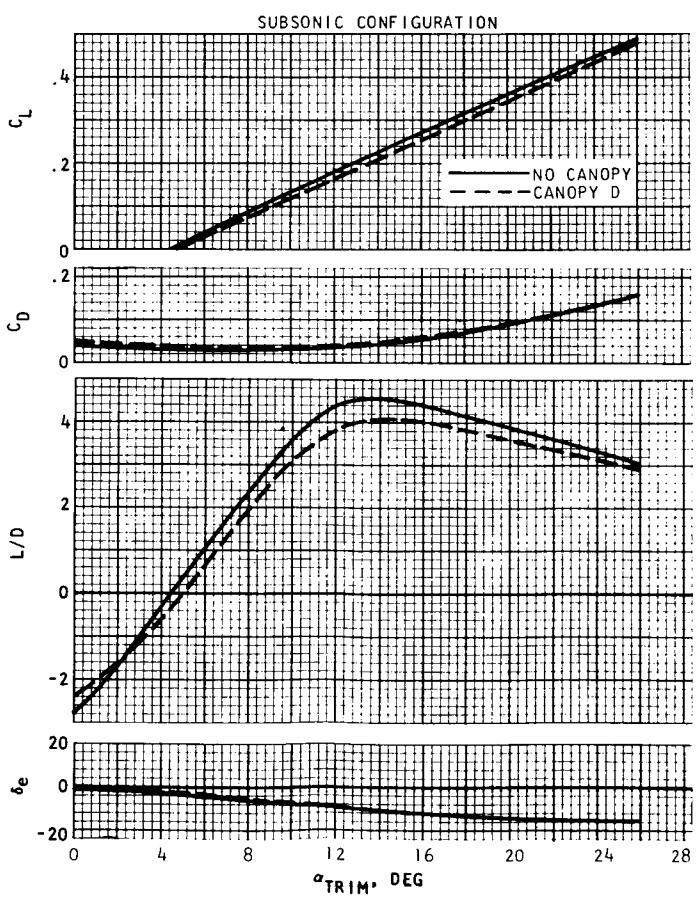


FIGURE 3. AERODYNAMIC SURFACE NOMENCLATURE

FOR SUBSONIC CONFIGURATION

$$\theta = 12^\circ, \delta_{of} = -40^\circ$$

$$\delta_{if} = 0^\circ; \delta_{ef} = -8.3^\circ$$



a) $M = 0.35$

FIGURE 4. TRIM LONGITUDINAL AERODYNAMICS

DECCLASSIFIED

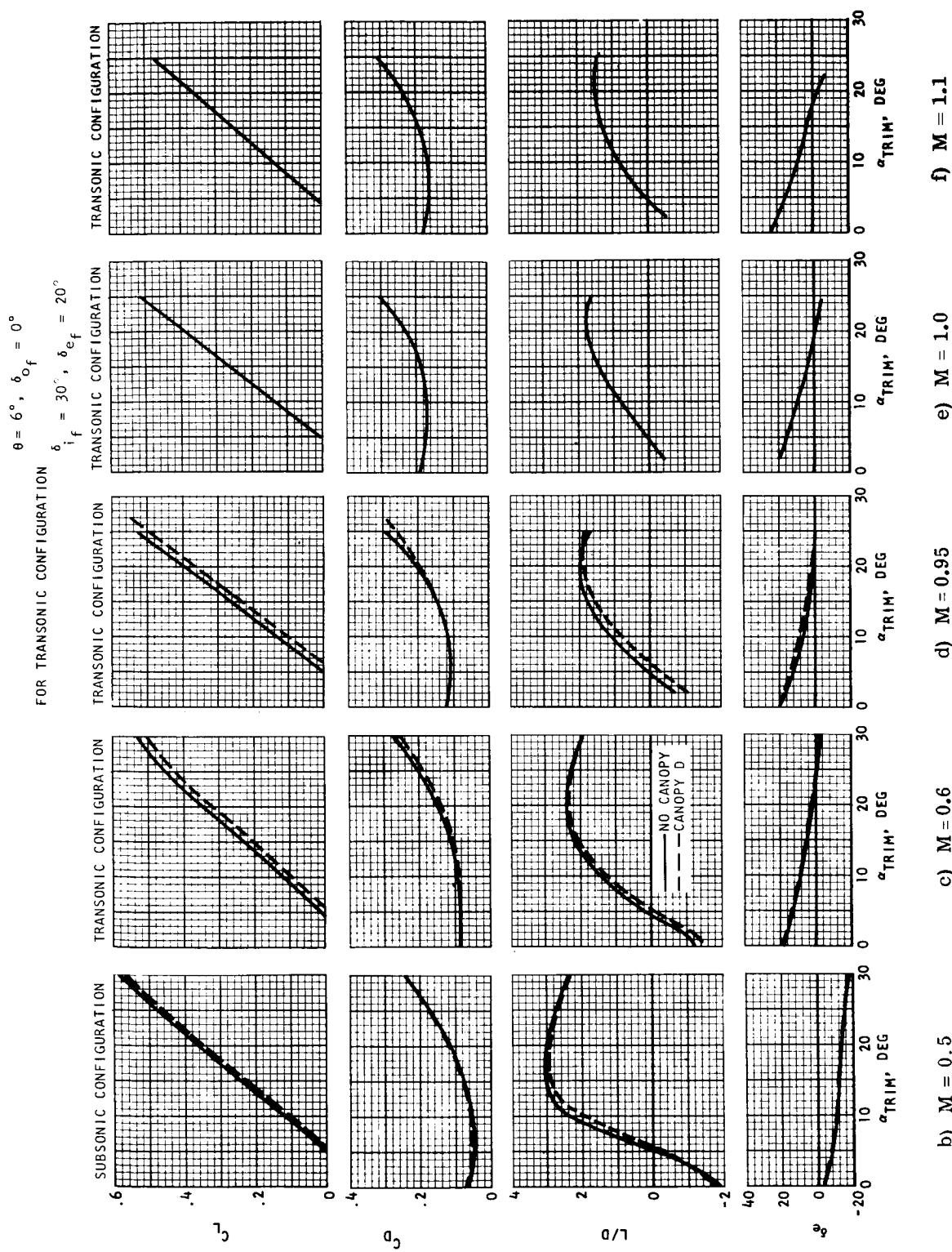


FIGURE 4.--CONTINUED

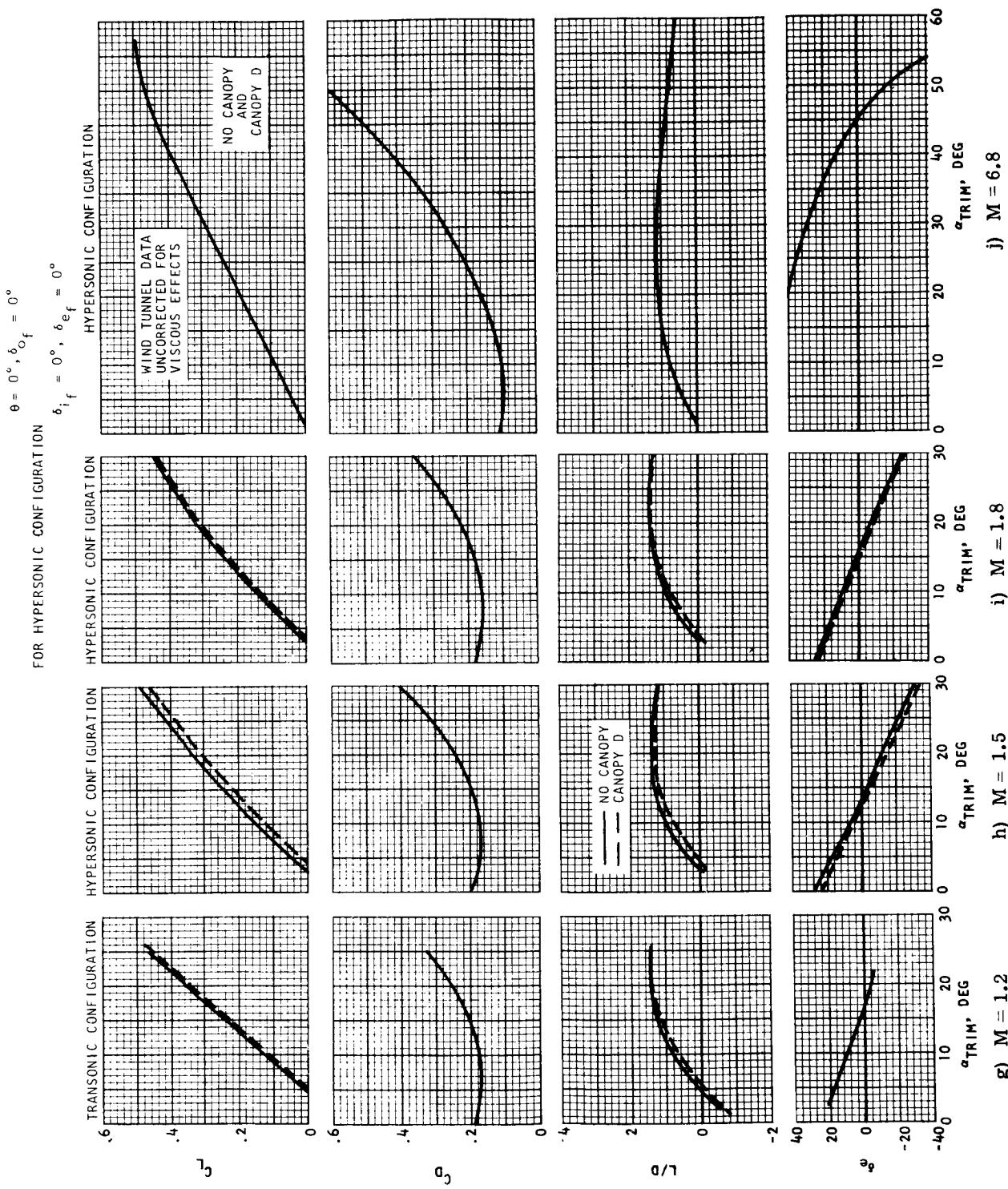


FIGURE 4.--CONCLUDED

ER 144713

DECLASSIFIED

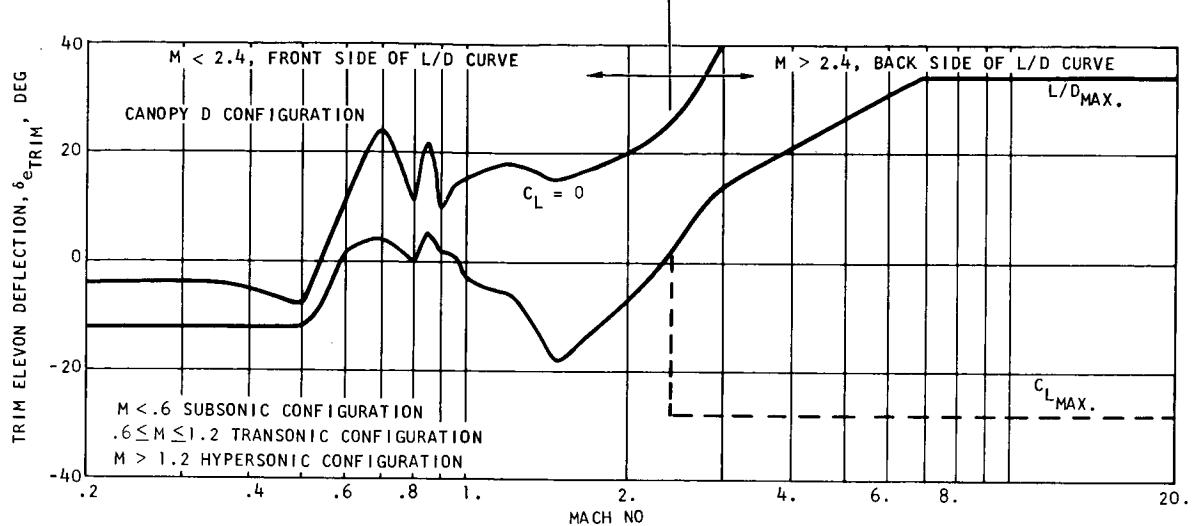


FIGURE 5. TRIM ELEVON DEFLECTION VERSUS MACH NUMBER

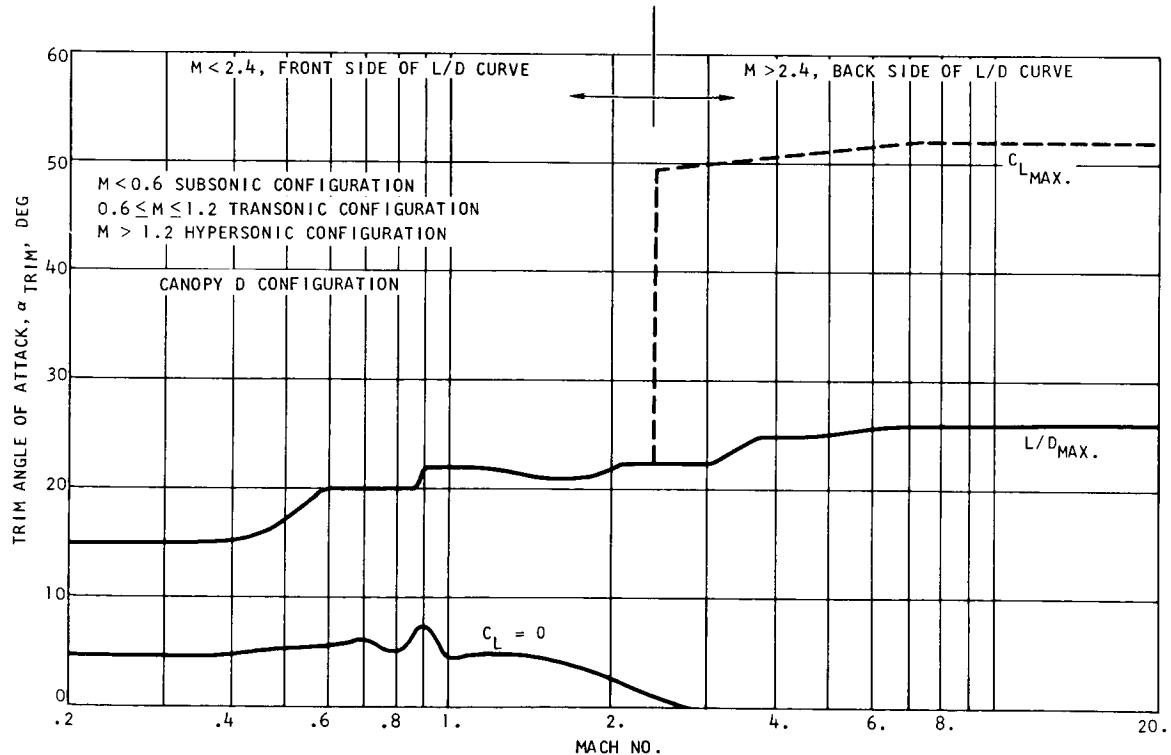


FIGURE 6. TRIM ANGLE OF ATTACK VERSUS MACH NUMBER

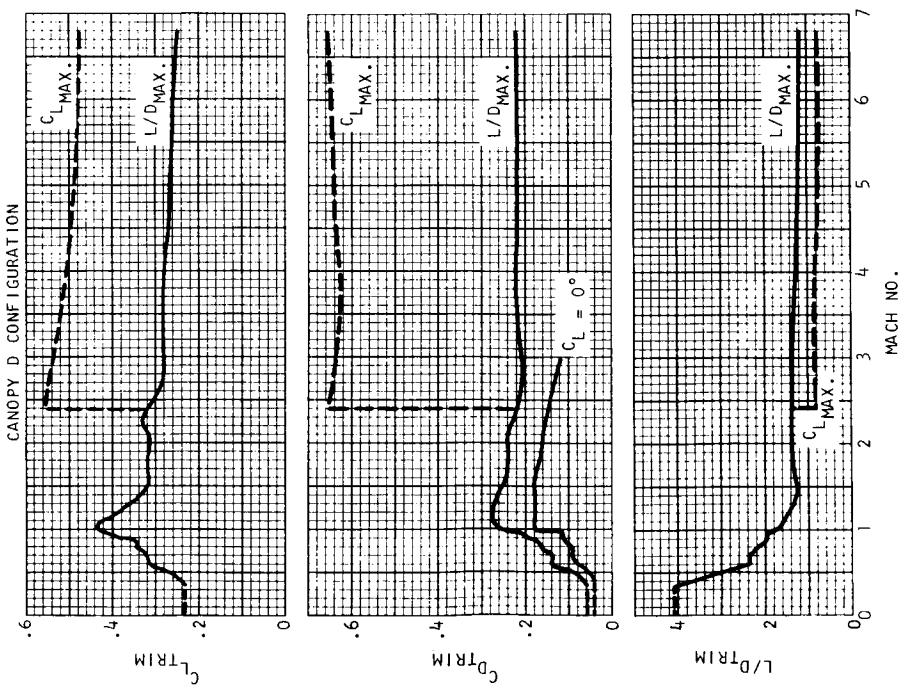


FIGURE 7. TRIM LONGITUDINAL AERODYNAMICS
VERSUS MACH NUMBER

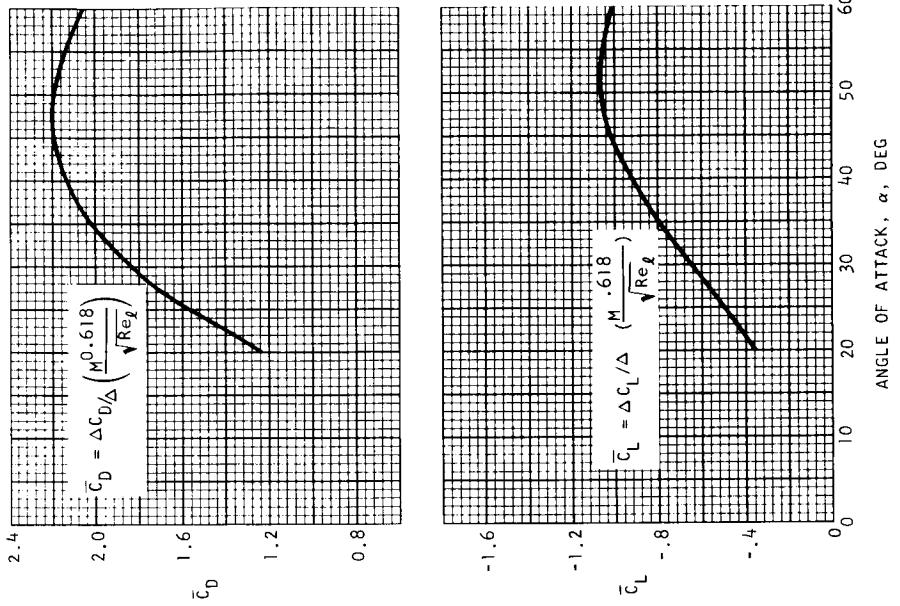


FIGURE 8. VISCOS CORRECTIONS TO C_L AND C_D

DECLASSIFIED

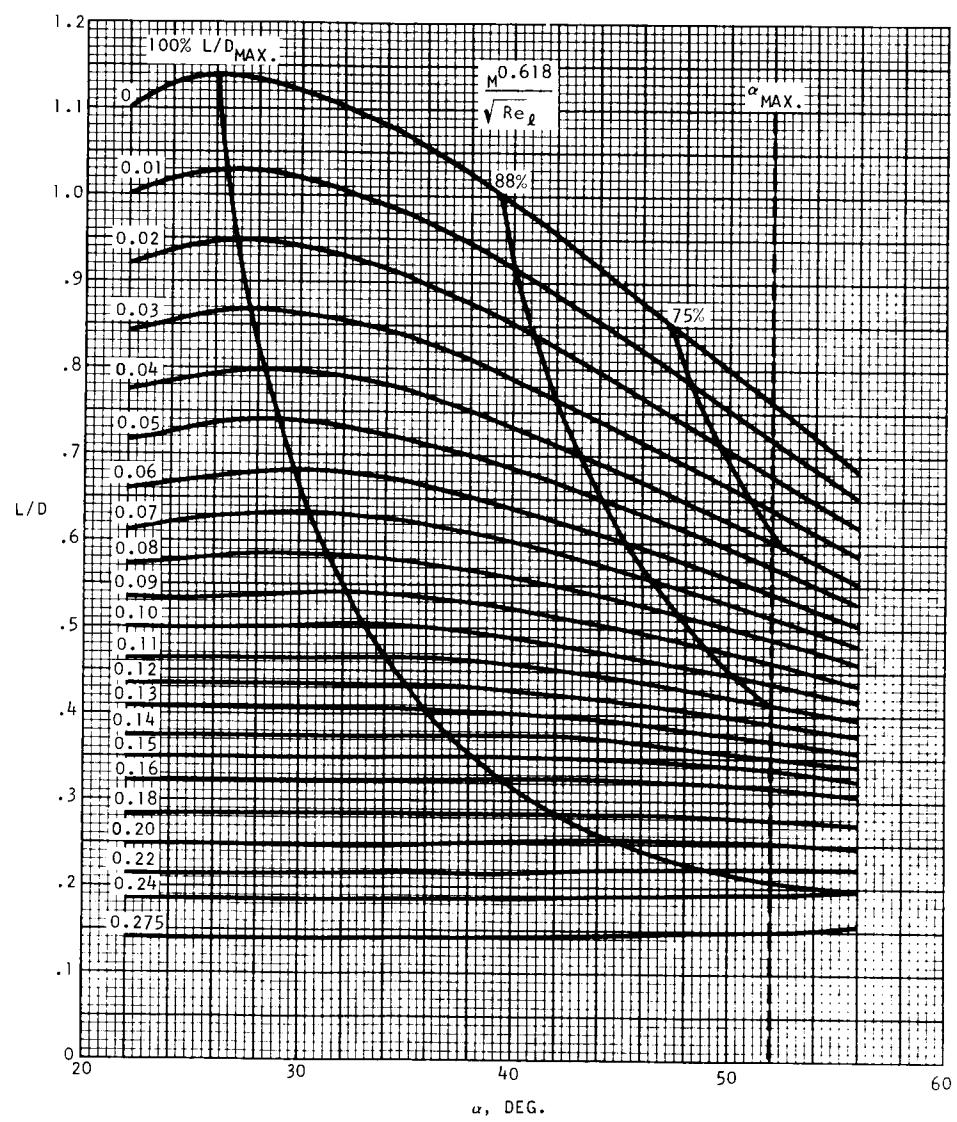


FIGURE 9. HYPERSONIC VISCOUS L/D

ER 14471-3

03000200 1000

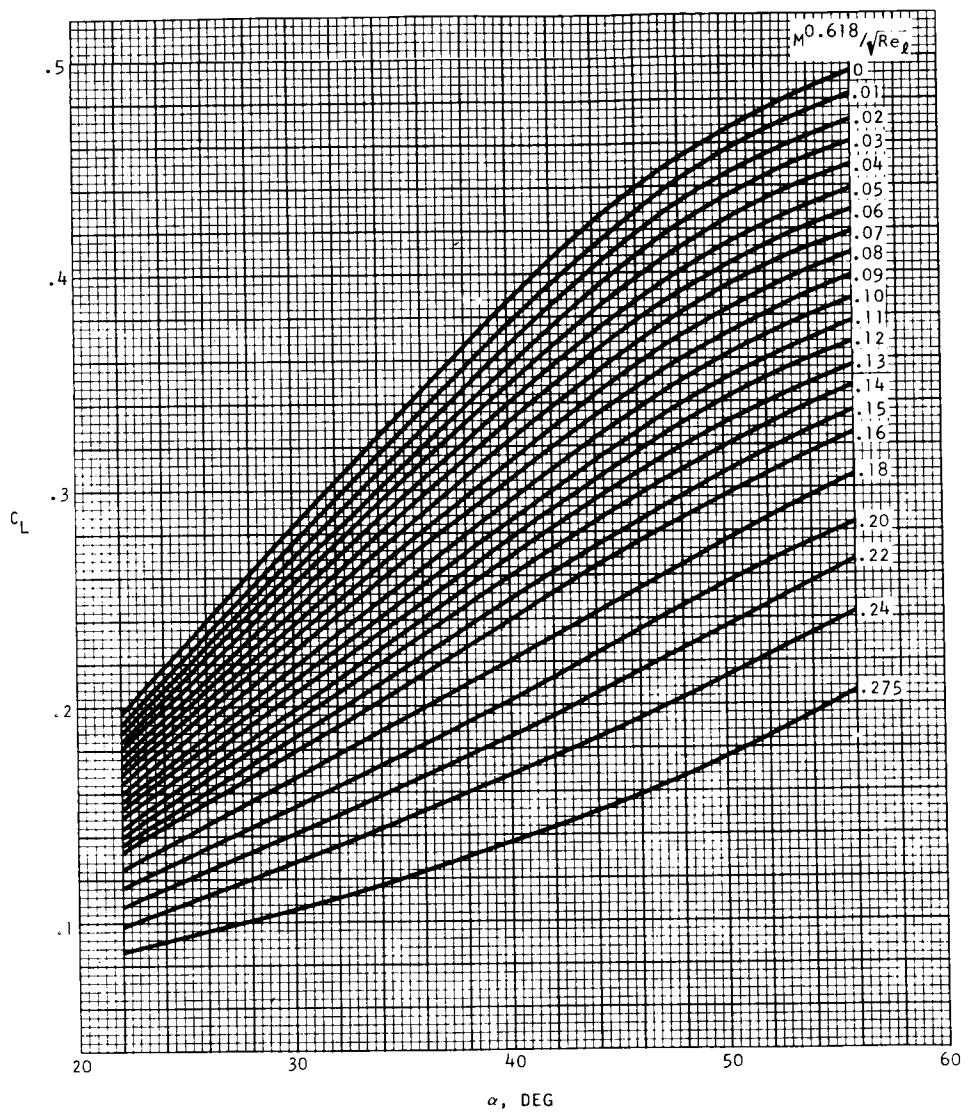


FIGURE 10. HYPERSONIC VISCOUS LIFT COEFFICIENT

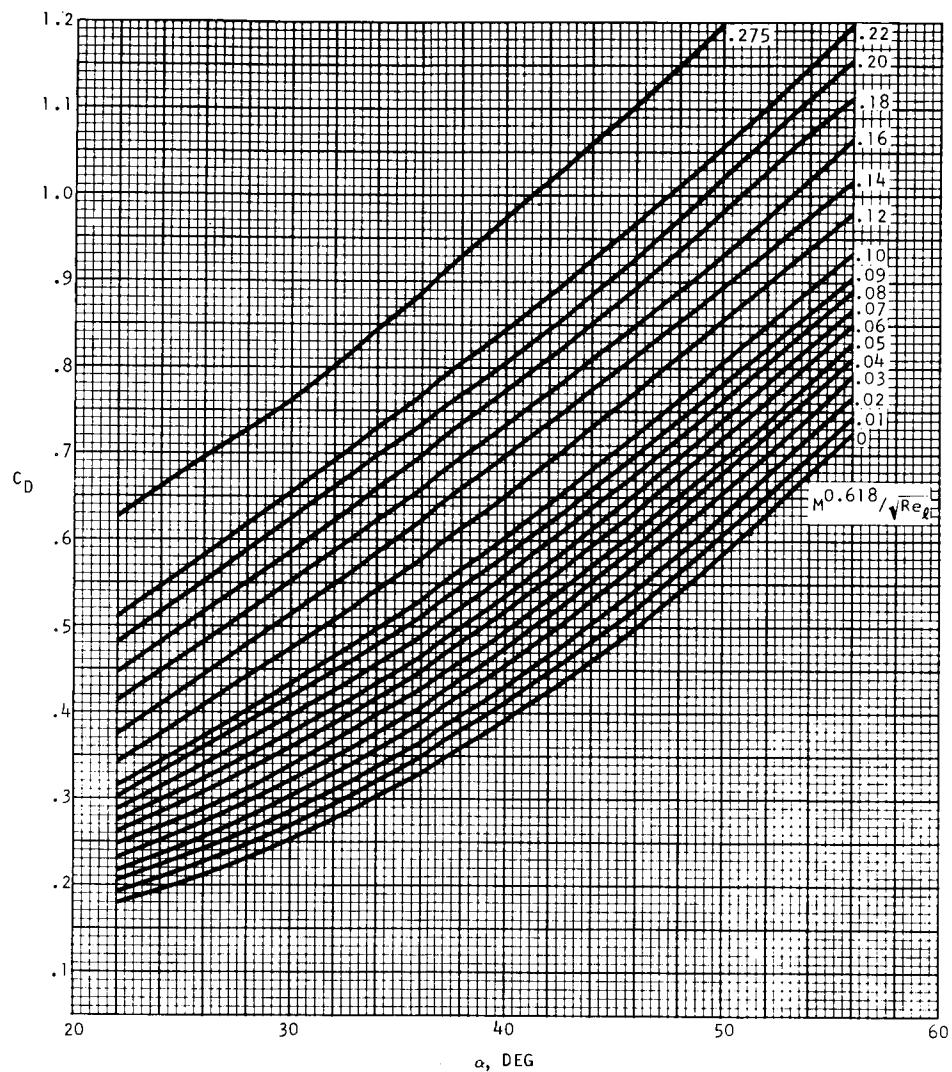


FIGURE 11. HYPERSONIC VISCOUS DRAG COEFFICIENT

PERIGEE ALTITUDE	
N. MI.	KM
A 60	111
B 80	148
C 100	185
D 120	222
E 140	259
F 150	279

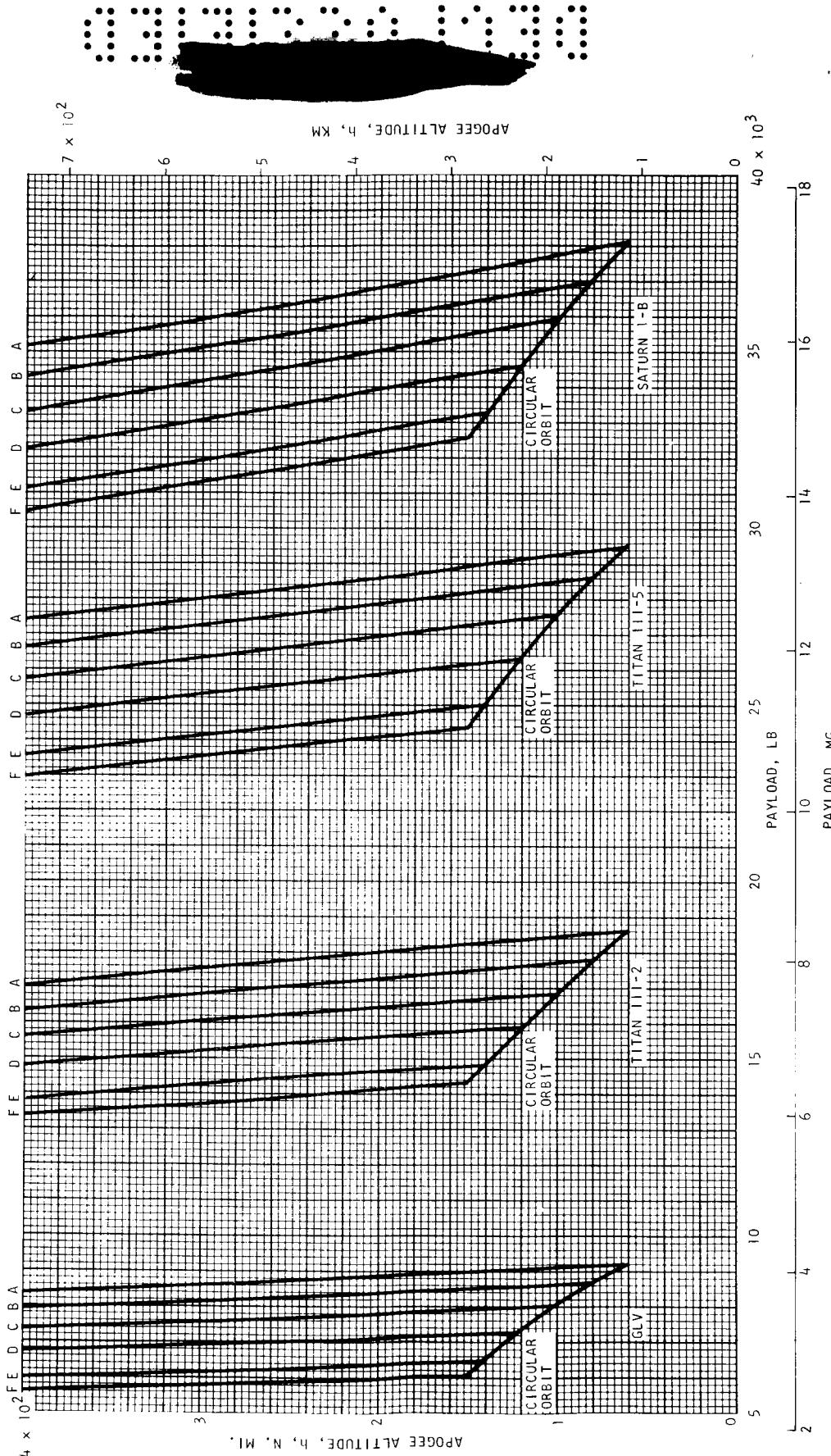


FIGURE 12. LAUNCH VEHICLE MINIMUM PAYLOAD CAPABILITY (DUE EAST ETR LAUNCH)

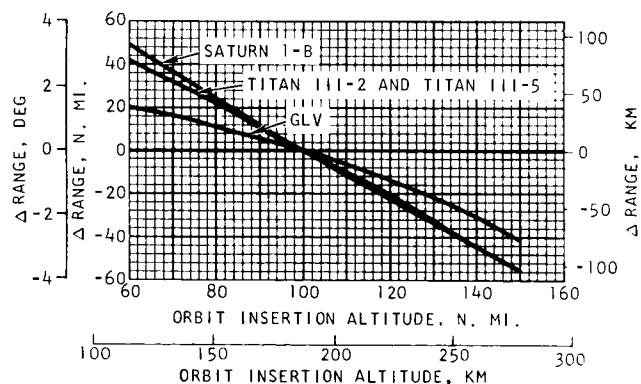
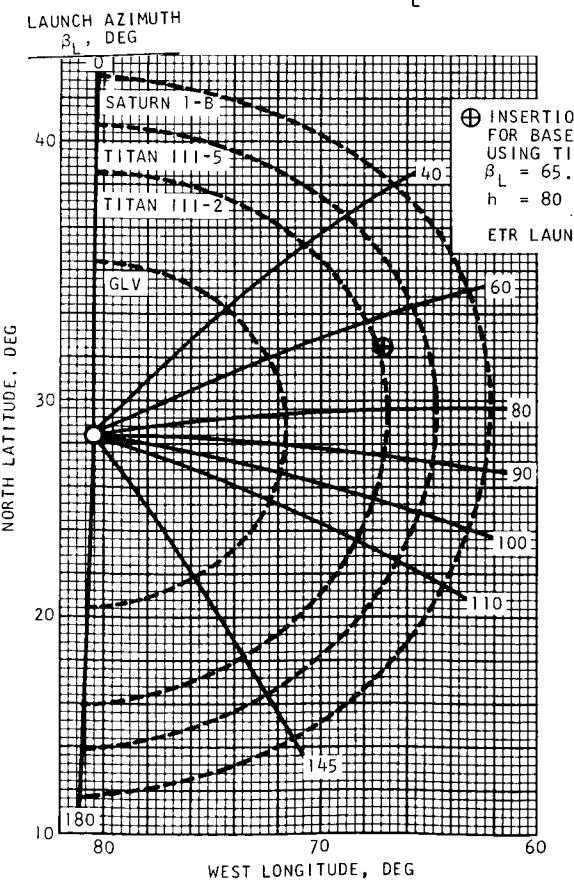
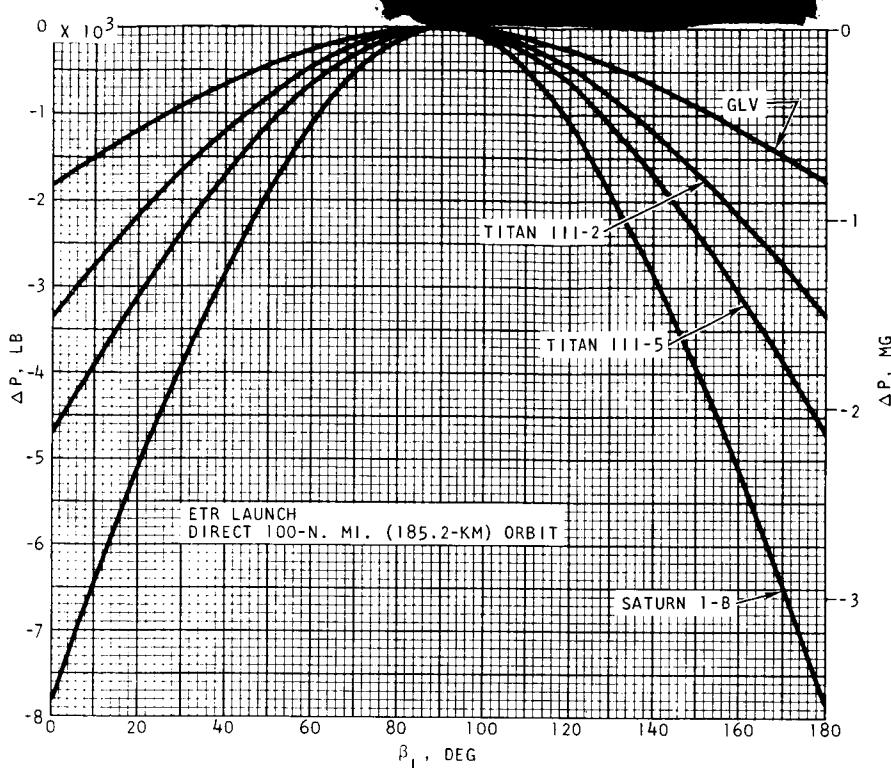


FIGURE 14. ORBIT INSERTION POSITION

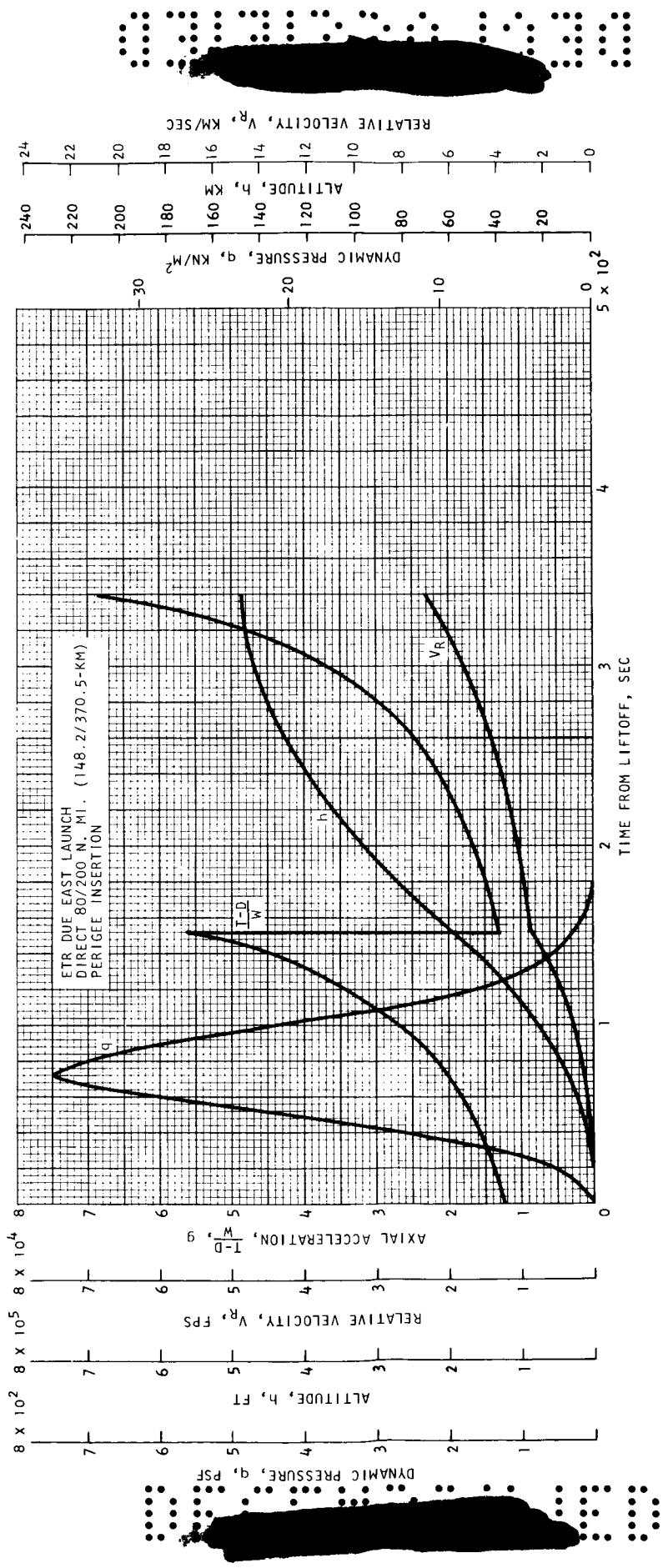


FIGURE 15. GLV LAUNCH TRAJECTORY

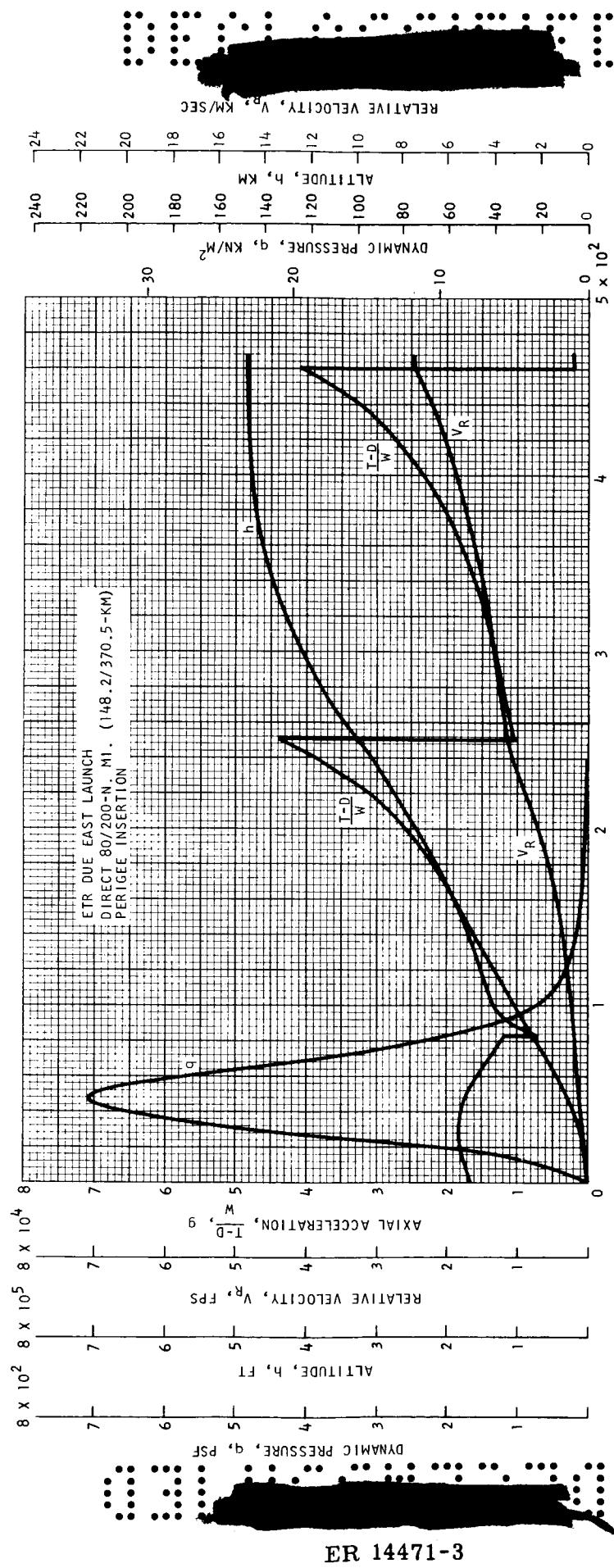


FIGURE 16. TITAN III-2 LAUNCH TRAJECTORY

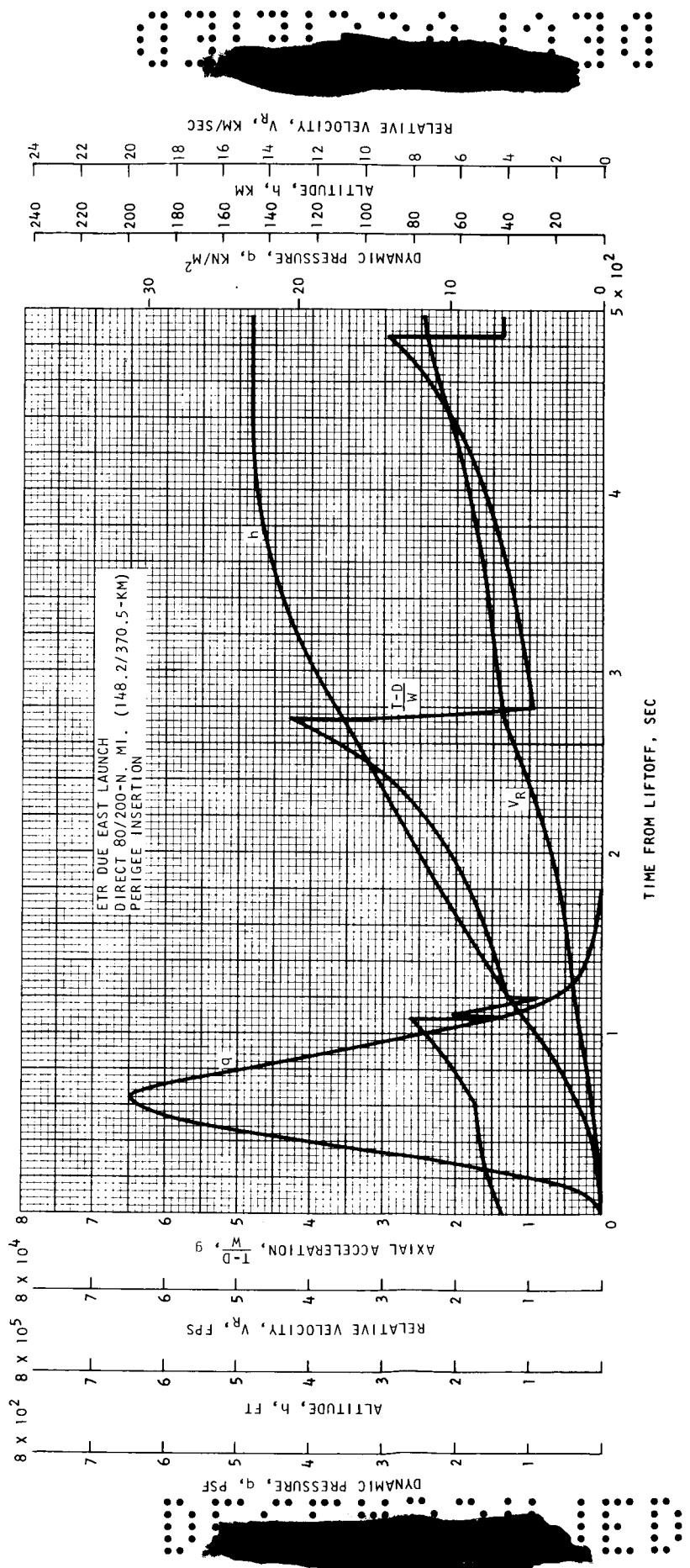


FIGURE 17. TITAN III-5 LAUNCH TRAJECTORY

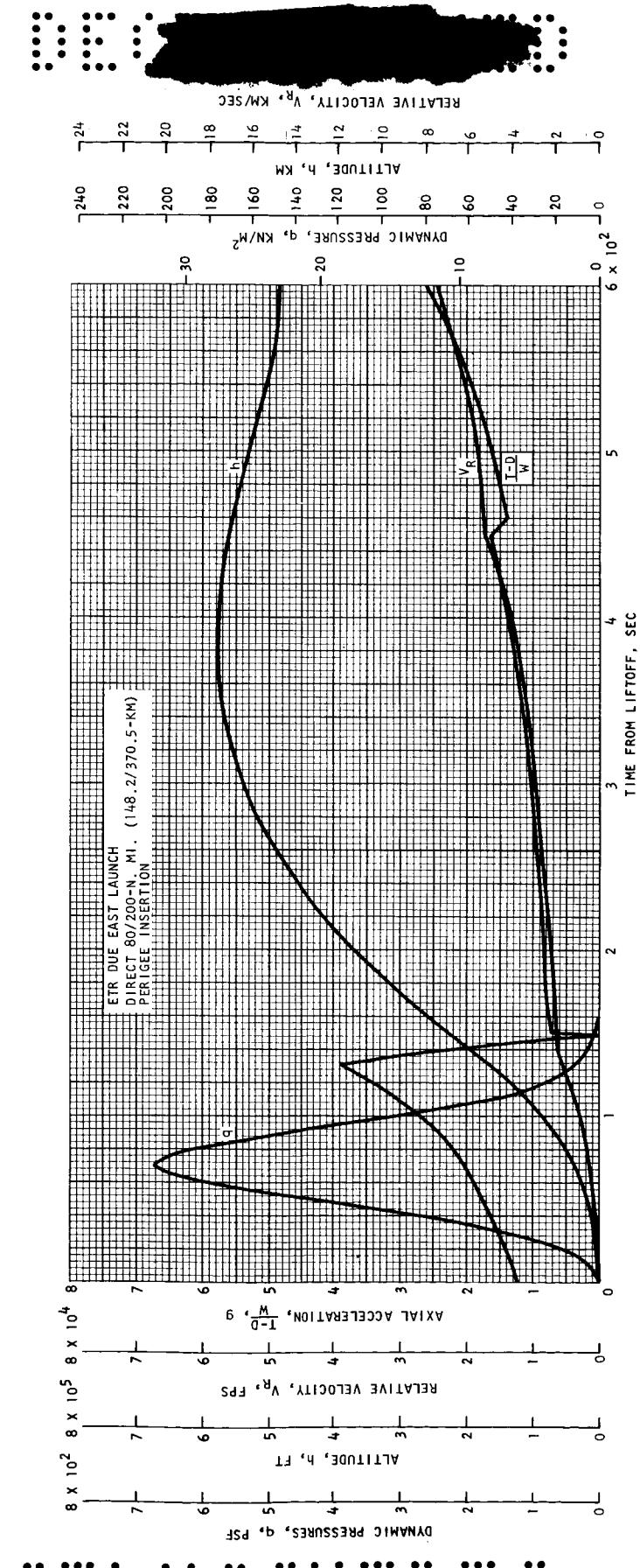


FIGURE 18. SATURN 1-B LAUNCH TRAJECTORY

q_{MAX.}, PSF

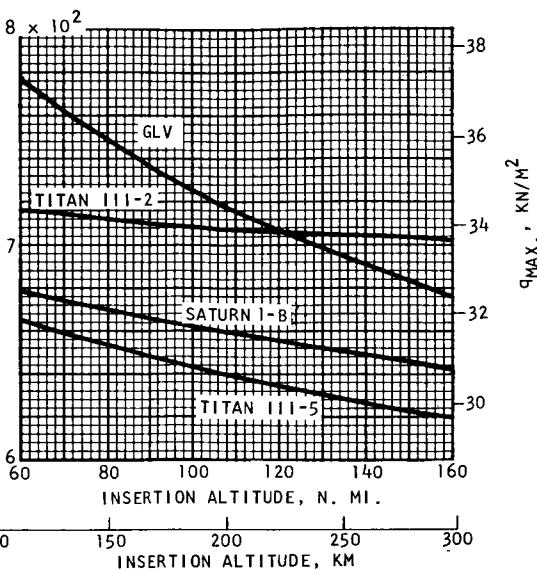


FIGURE 19. PEAK LAUNCH DYNAMIC PRESSURE (NOMINAL TRAJECTORY)

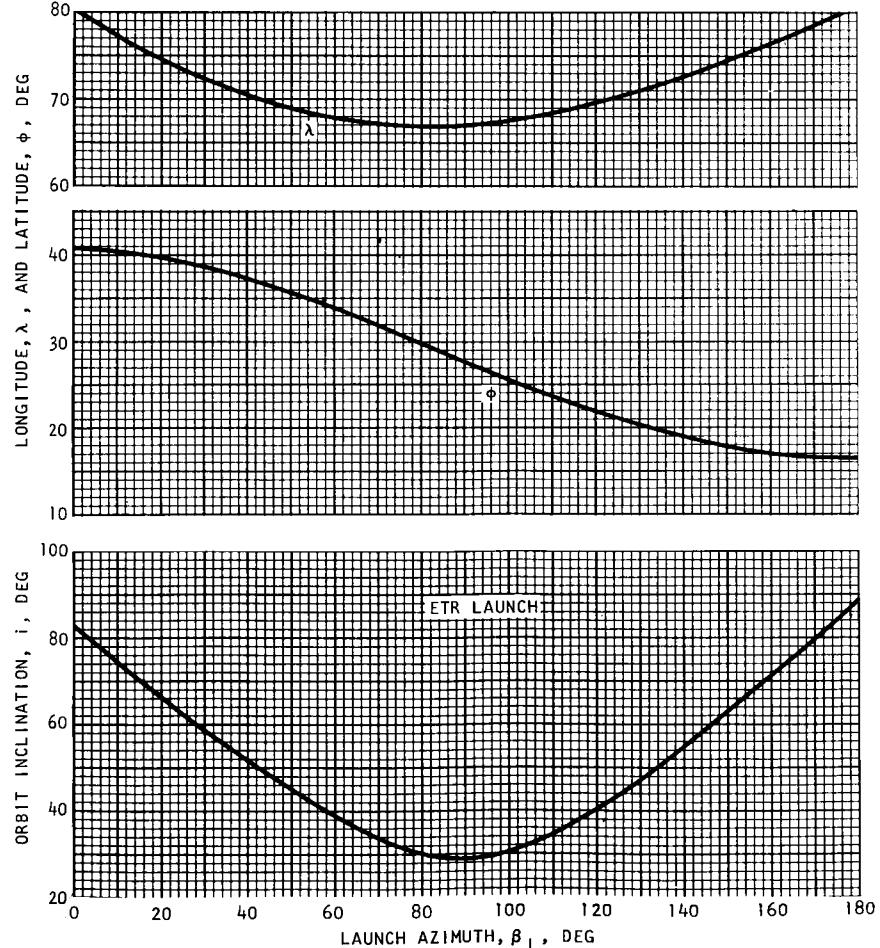
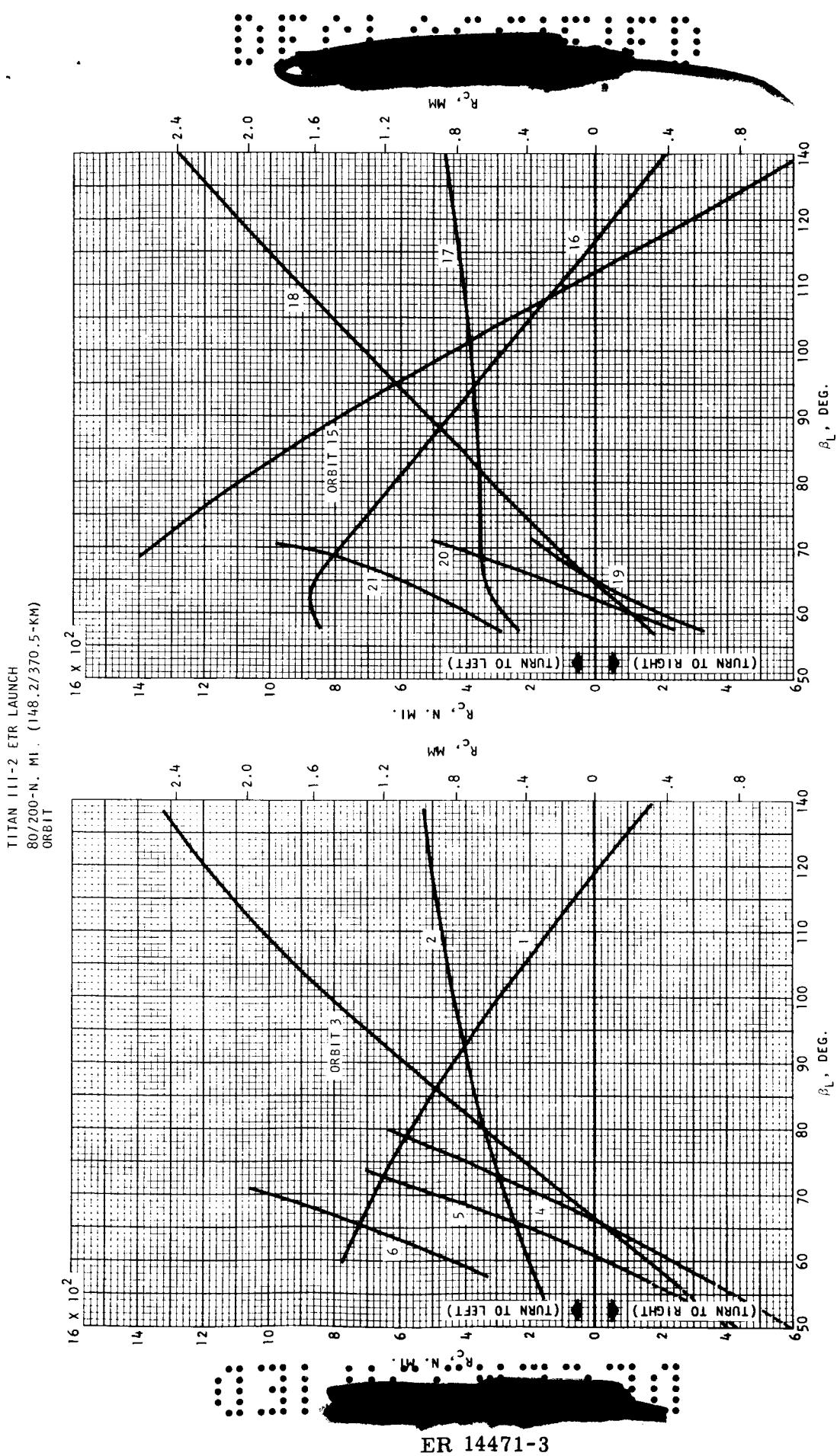


FIGURE 20. INSERTION CONDITIONS USING TITAN III-2

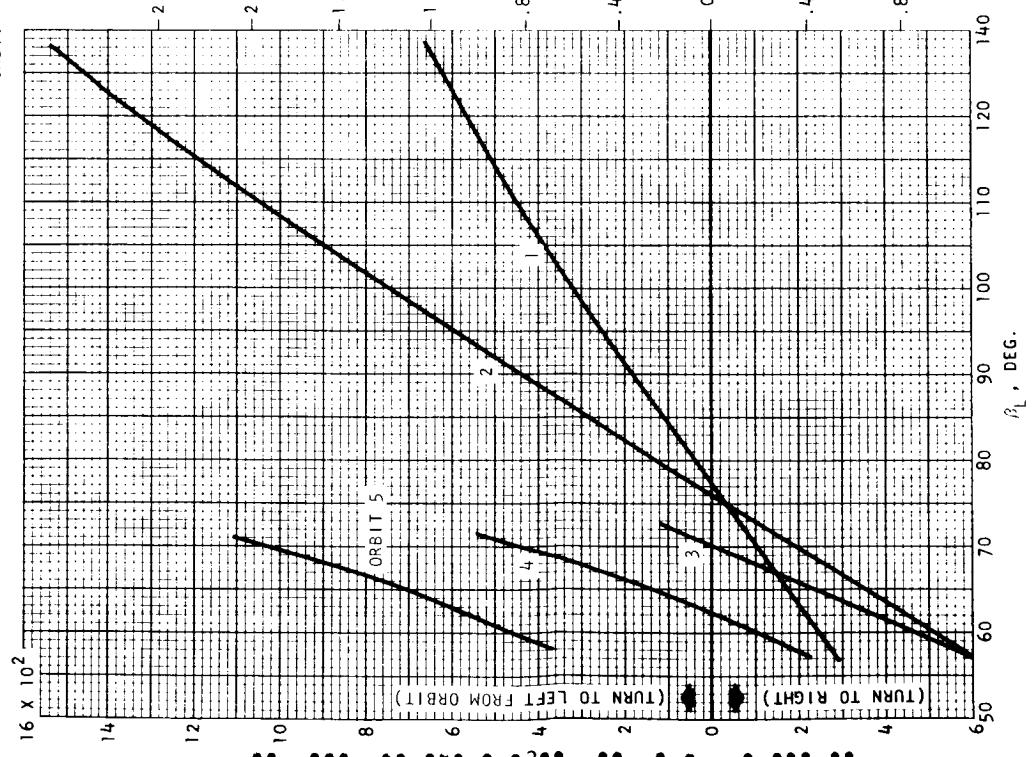


b) ORBITS 15 THROUGH 21

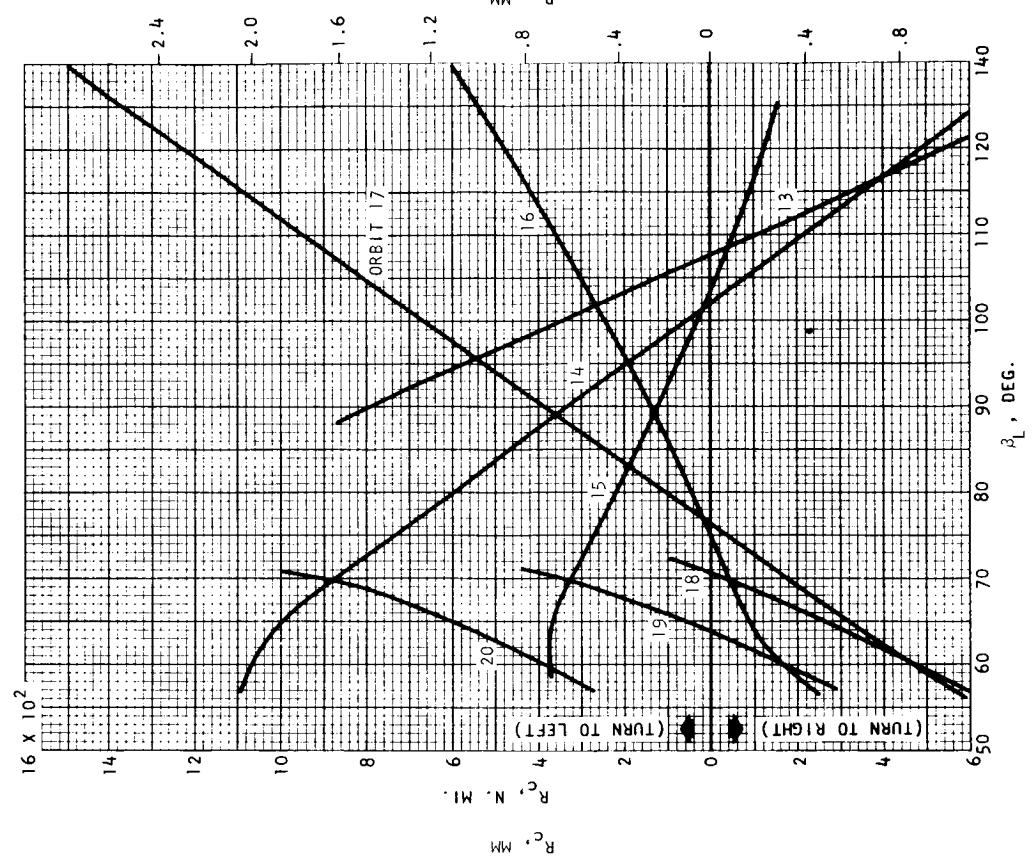
a) ORBITS 1 THROUGH 6

FIGURE 21. CROSSRANGE REQUIRED FOR FRC (EDWARDS AFB) LANDING

TITAN III-2 ETR LAUNCH
80/200-N. MI. (148.2/370.5-KM)

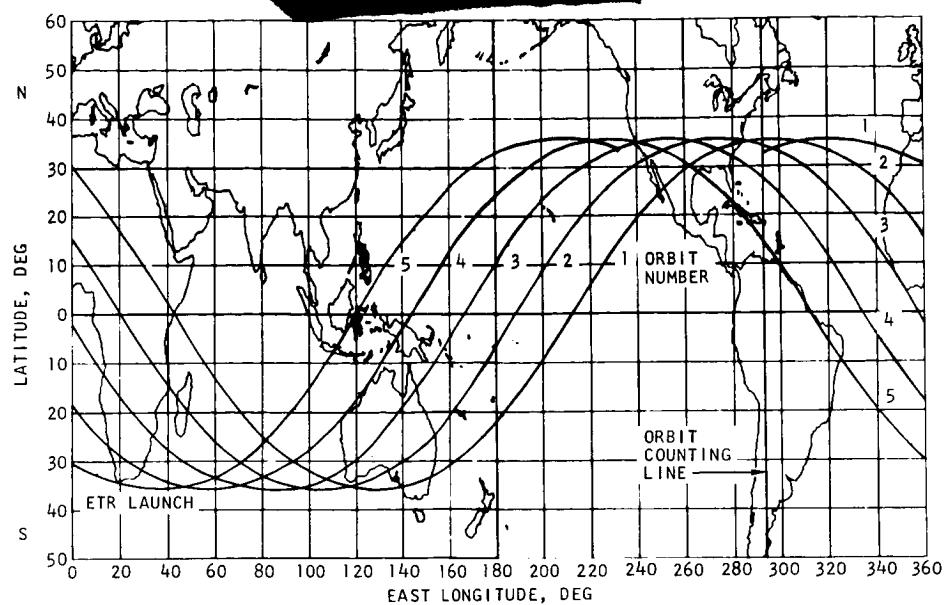


a) ORBITS 1 THROUGH 5

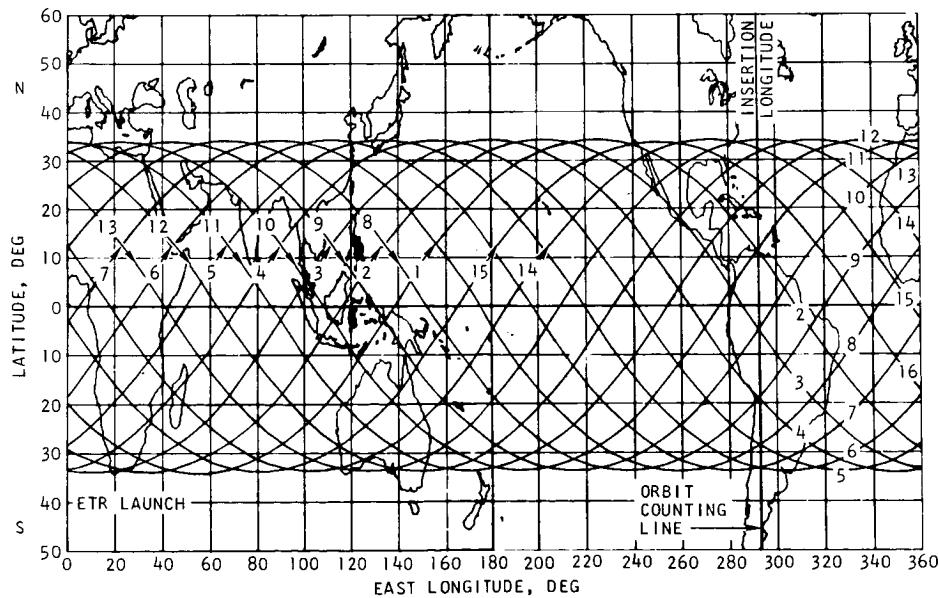


b) ORBITS 13 THROUGH 21

FIGURE 22. CROSSRANGE REQUIRED FOR EGLIN AFB LANDING



a) $\beta_L = 65.8^\circ$, 5 ORBITS



b) $\beta_L = 110^\circ$, 15 ORBITS

FIGURE 23. GROUND TRACES

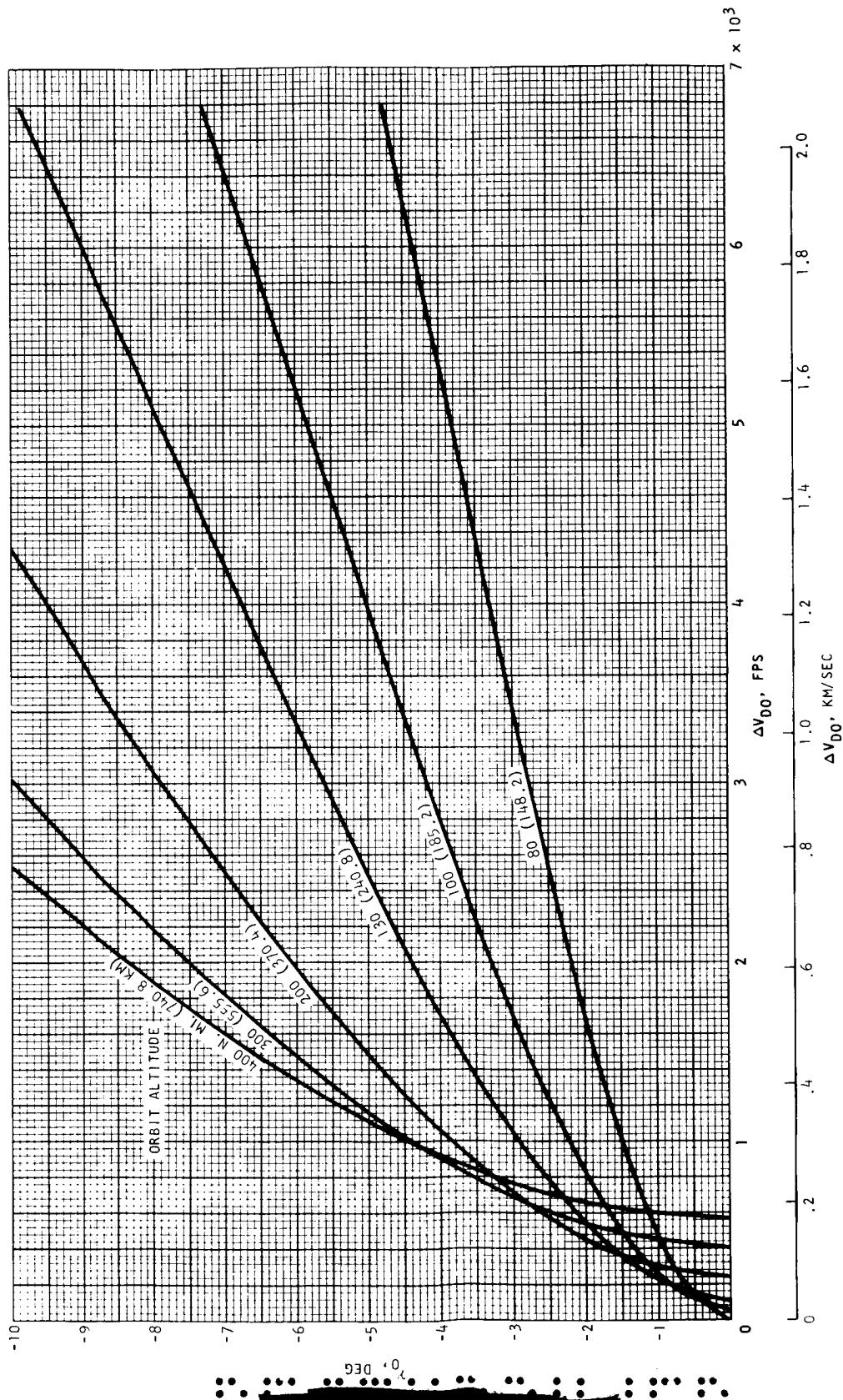
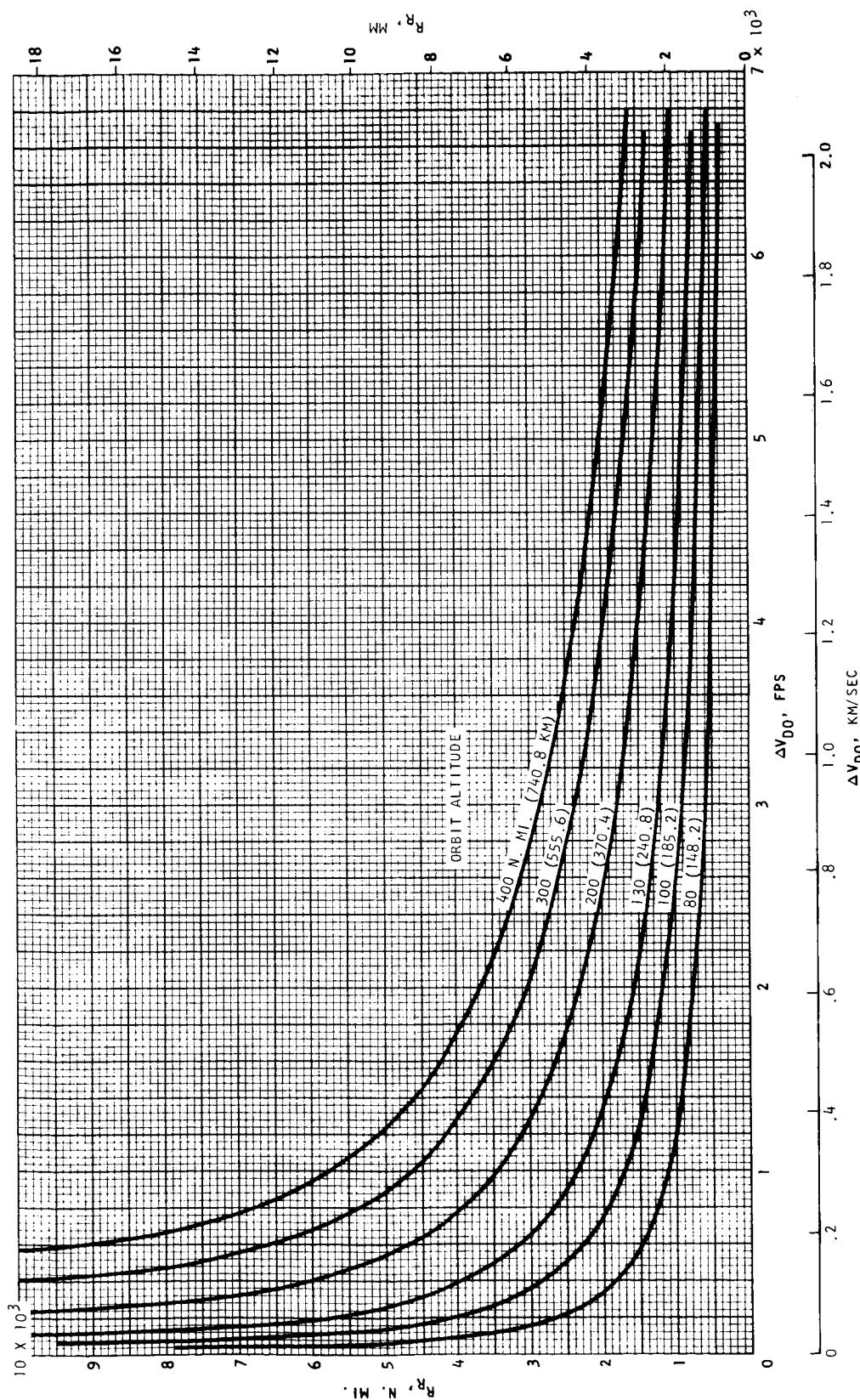
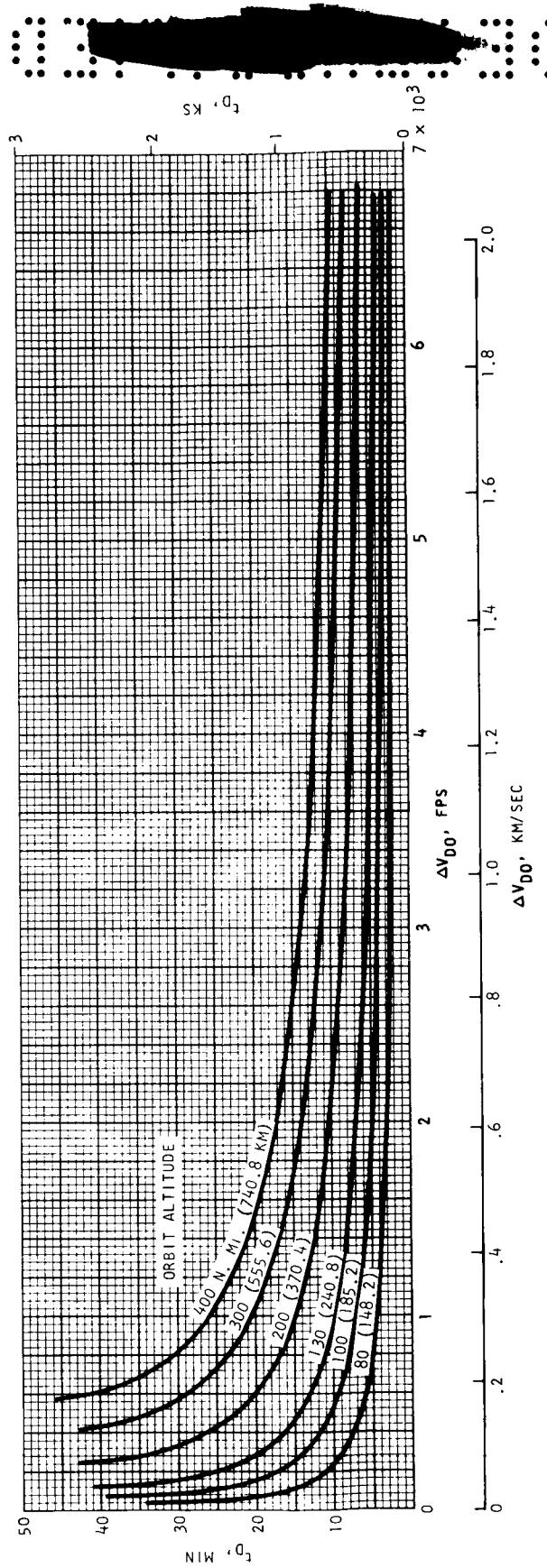


FIGURE 24. DEORBIT FROM CIRCULAR ORBITS
a) ENTRY ANGLE



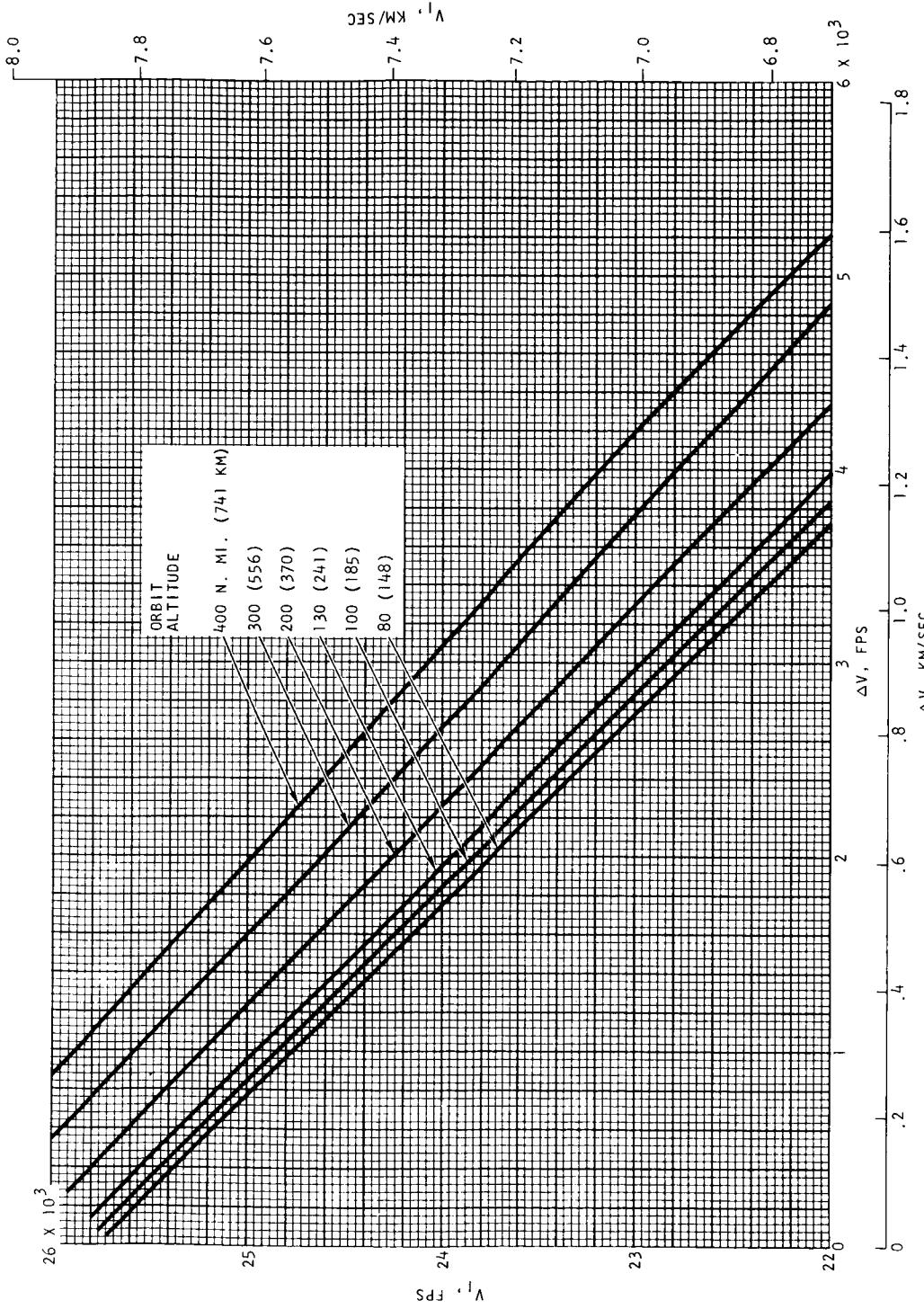
b) INERTIAL GROUND RANGE FROM DEORBIT TO ENTRY ALTITUDE

FIGURE 24.-CONTINUED

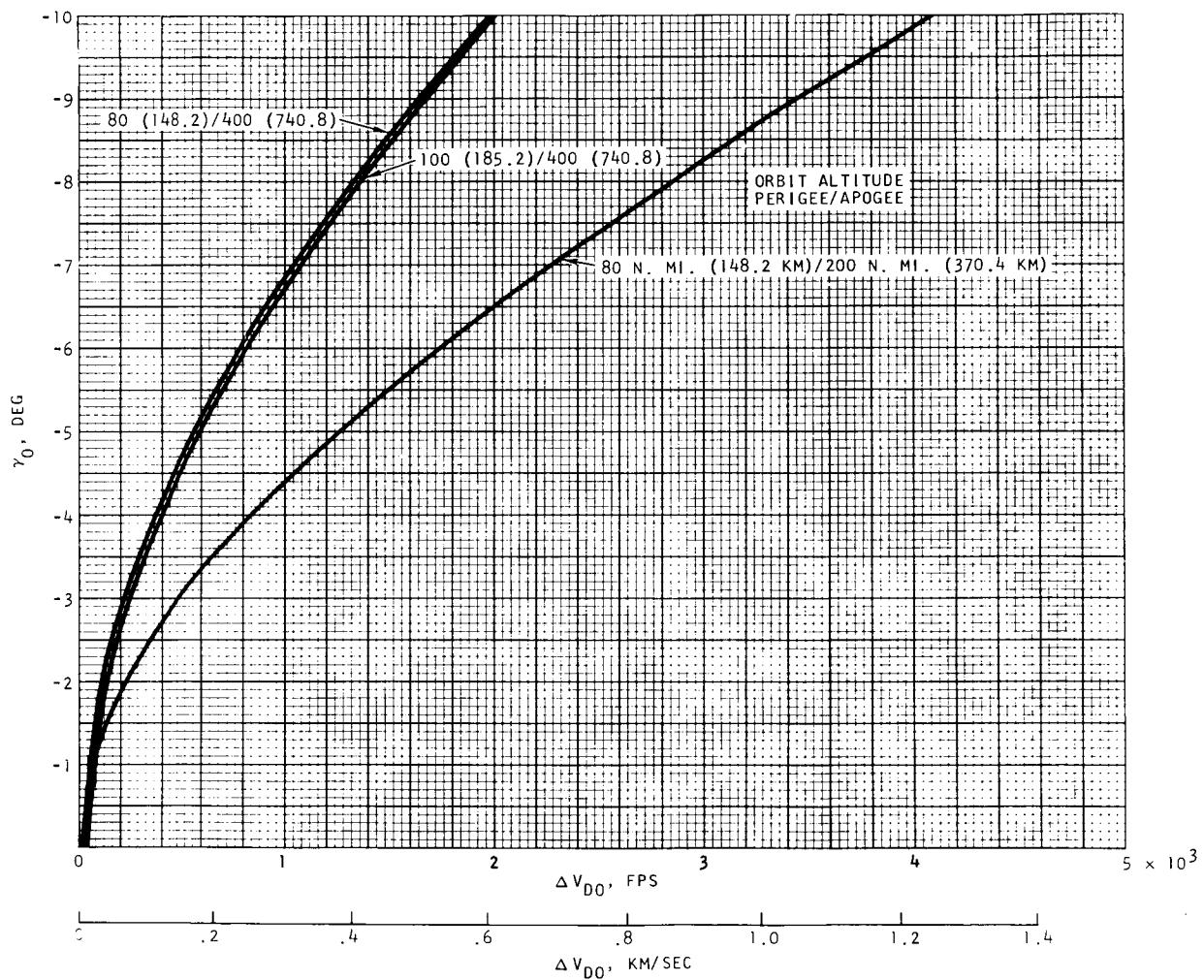


c) TIME FROM DEORBIT TO ENTRY ALTITUDE

FIGURE 24. --CONTINUED

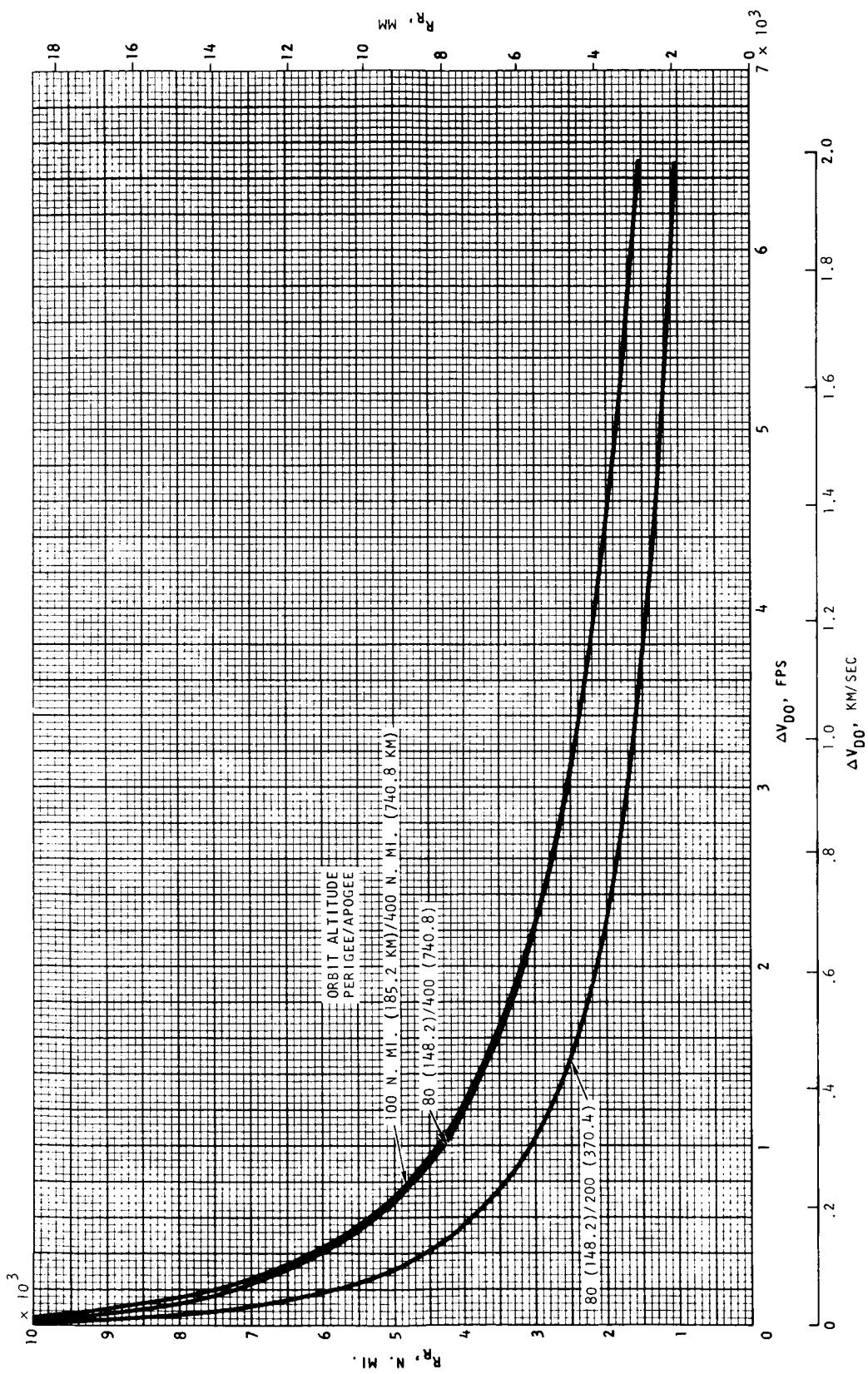


d) TOTAL INERTIAL VELOCITY AT ENTRY ALTITUDE
--CONCLUDED



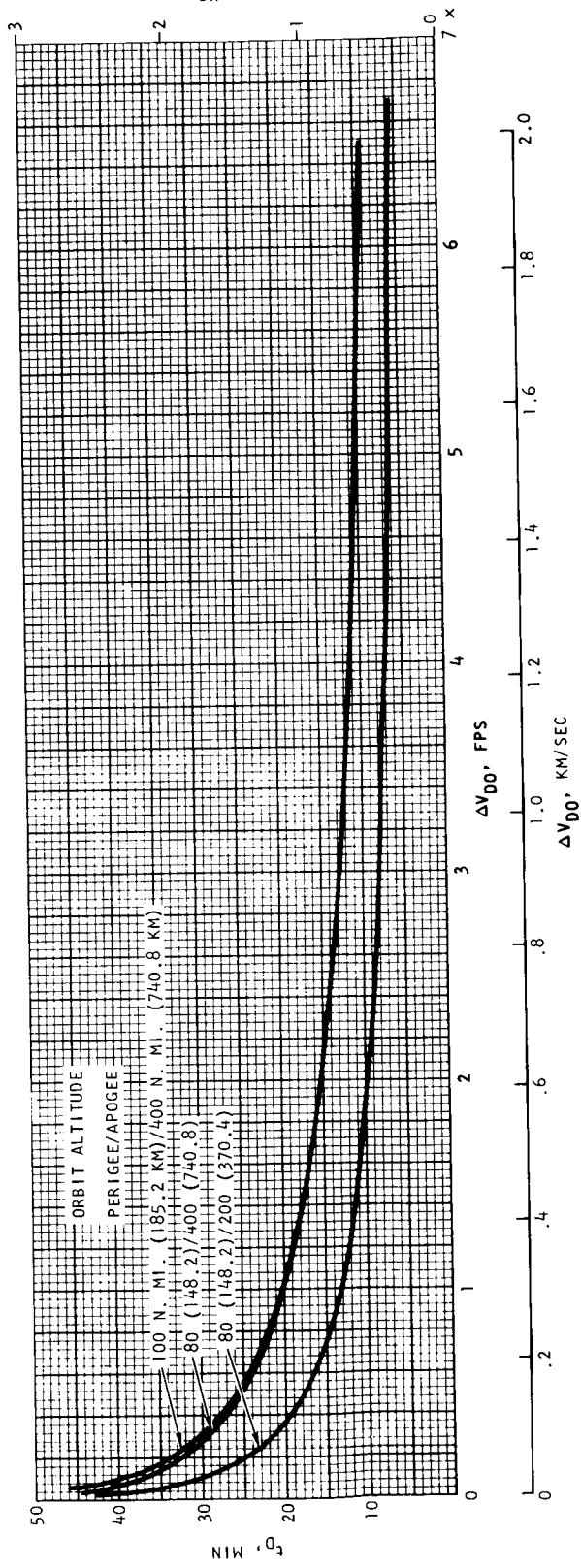
a) ENTRY ANGLE

FIGURE 25. DEORBIT FROM ELLIPTICAL ORBITS



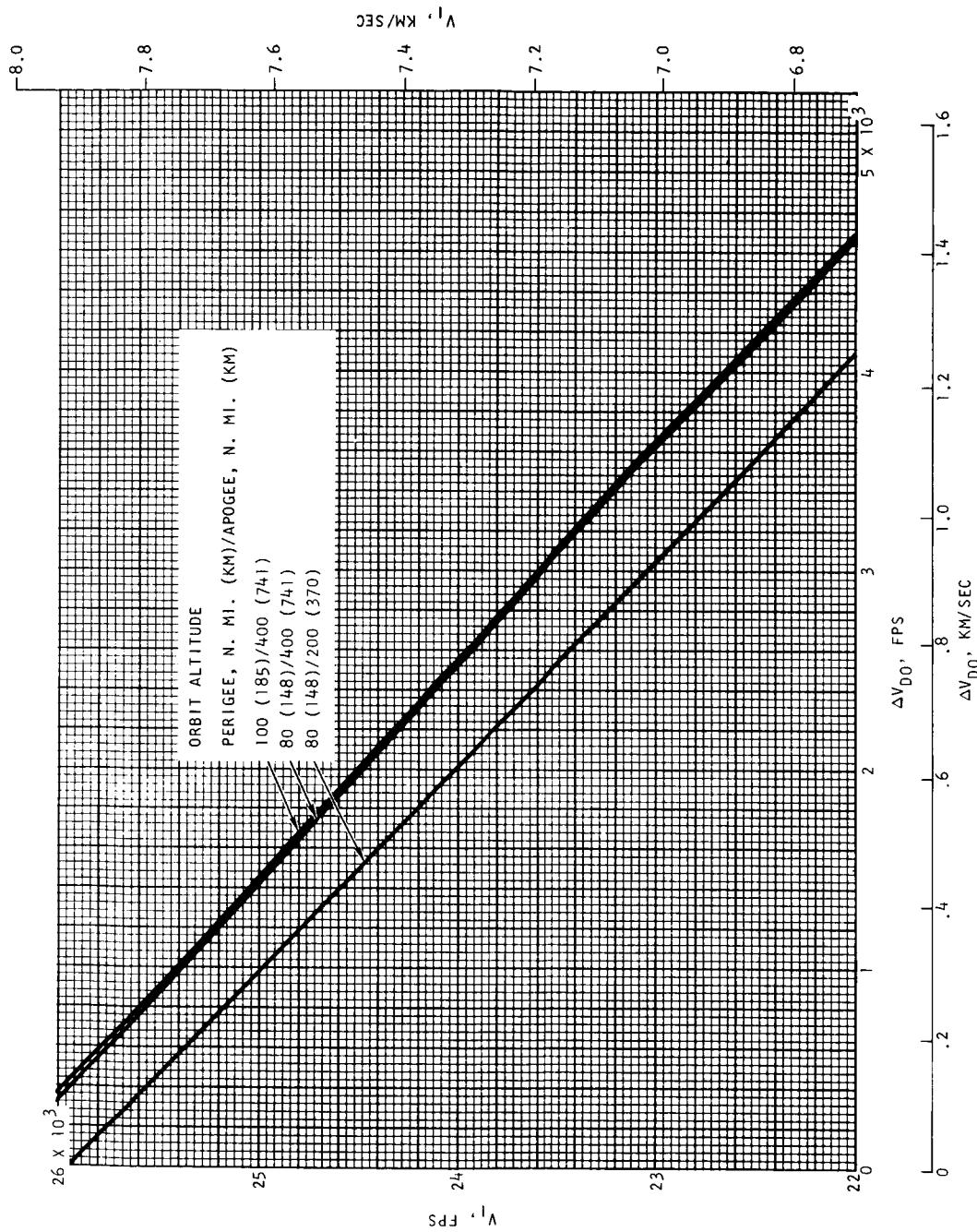
b) INERTIAL GROUND RANGE FROM DEORBIT TO ENTRY ALTITUDE

FIGURE 25. --CONTINUED



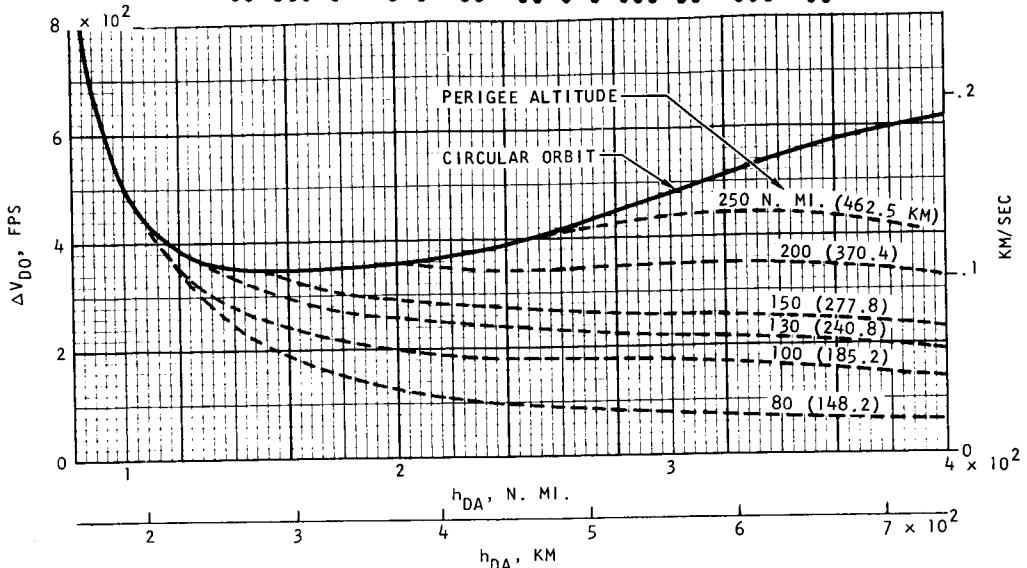
c) TIME FROM DEORBIT TO ENTRY ALTITUDE

FIGURE 25. --CONTINUED

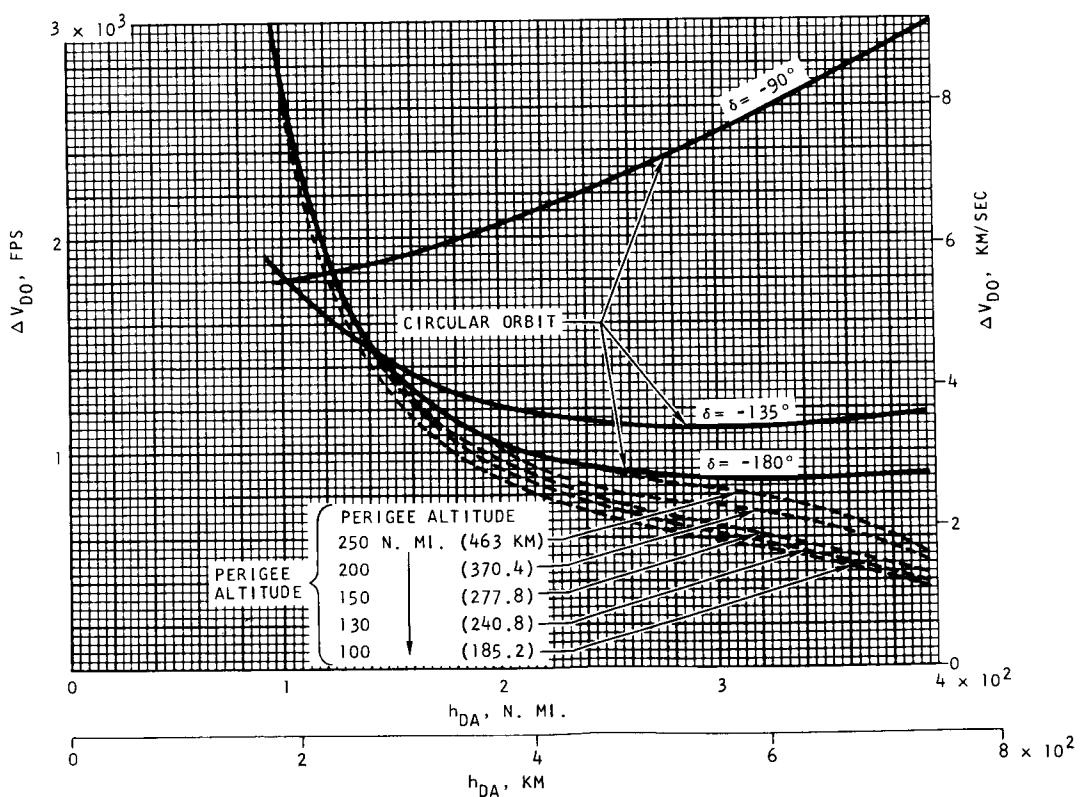


d) TOTAL VELOCITY AT ENTRY ALTITUDE

FIGURE 25.--CONCLUDED

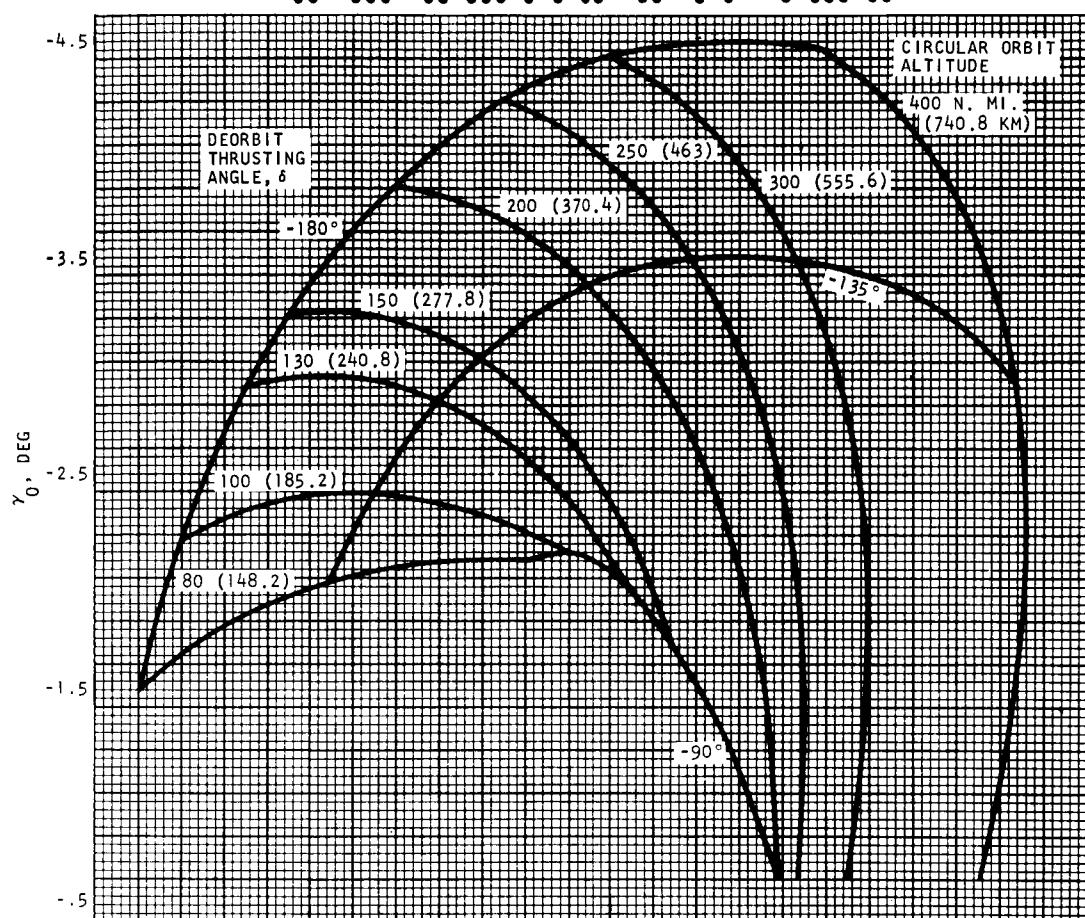


a) -1.5° ENTRY ANGLE

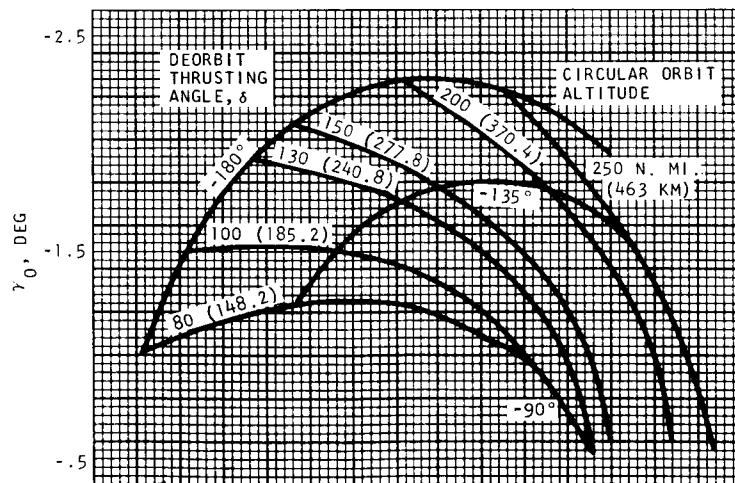


b) -4.0° ENTRY ANGLE

FIGURE 26. DEORBIT ΔV FROM APOGEE ALTITUDE

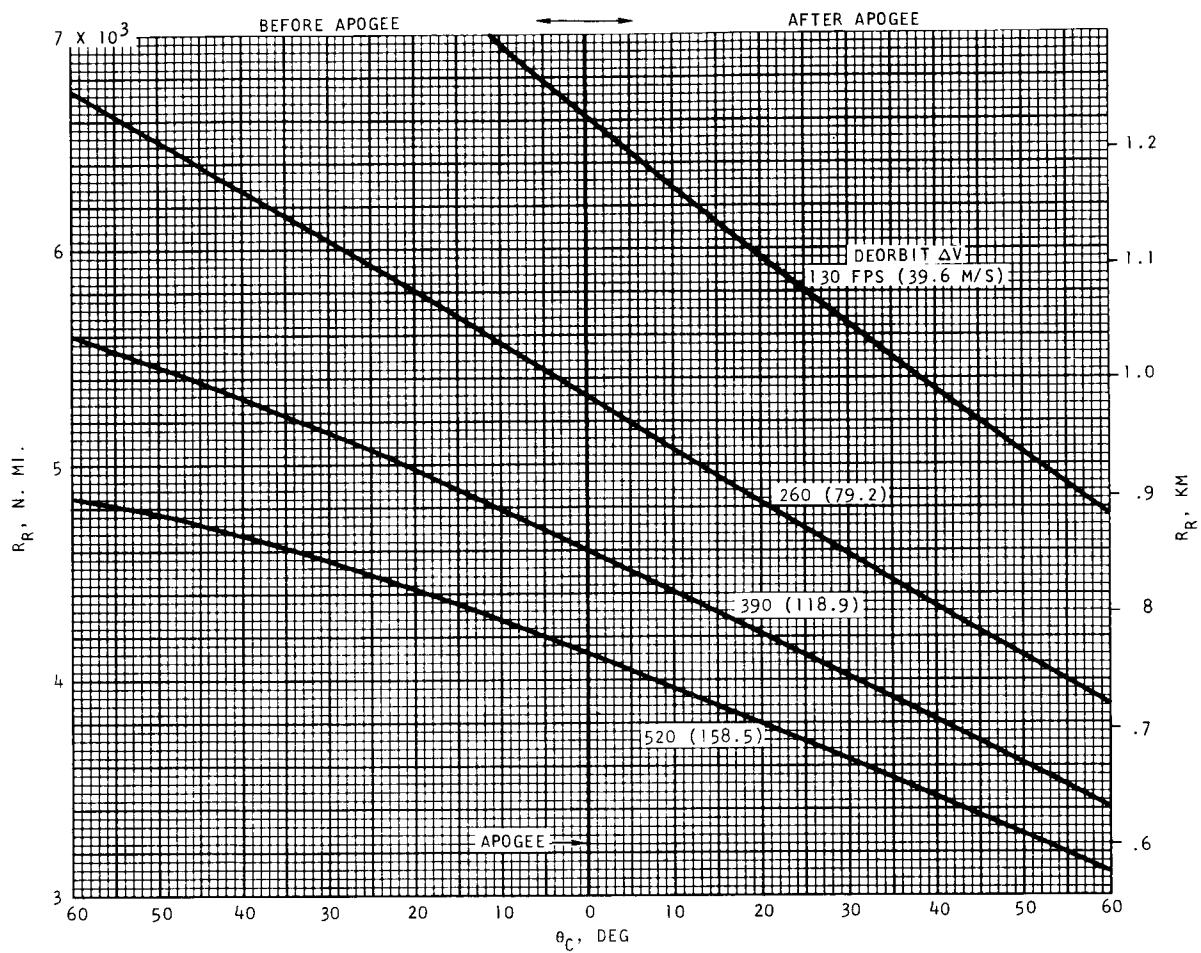


a) $\Delta V_{do} = 1000$ FPS (304.8 M/SEC)



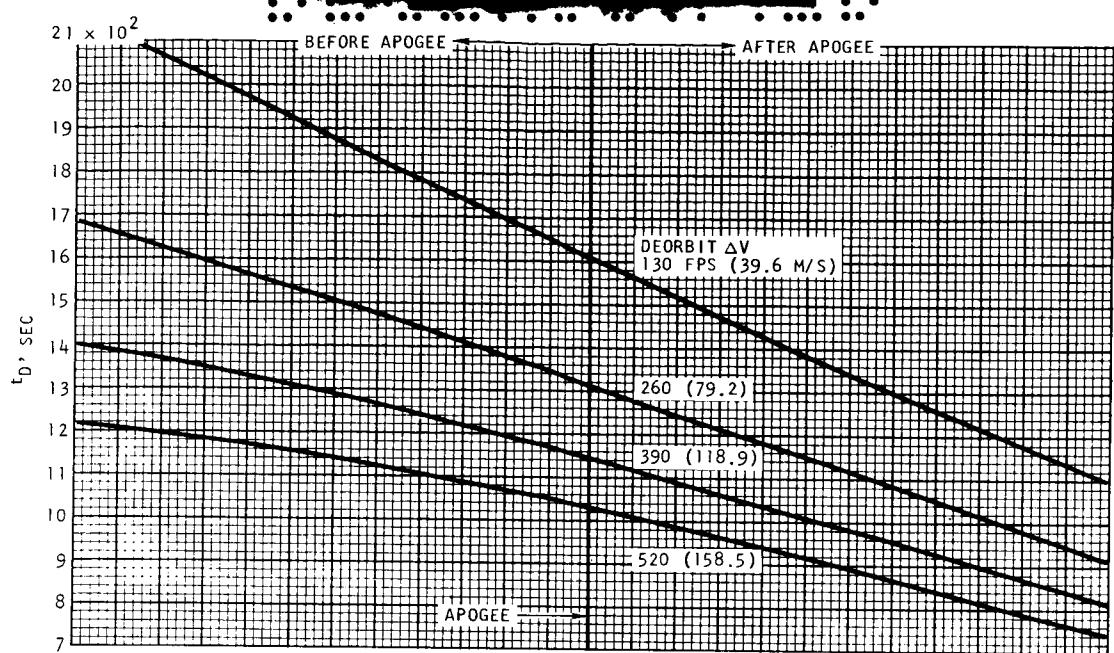
b) $\Delta V_{do} = 520$ FPS (158.5 M/SEC)

FIGURE 27. AVAILABLE ENTRY ANGLES FOR FIXED DEORBIT ΔV

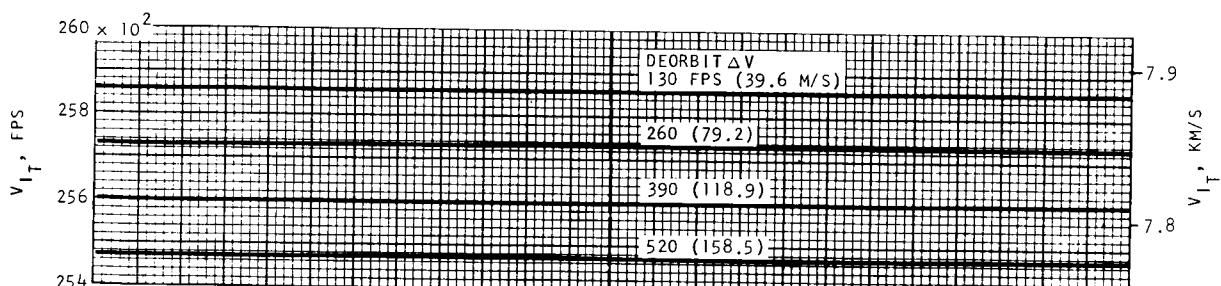


a) INERTIAL GROUND RANGE FROM DEORBIT TO ENTRY ALTITUDE

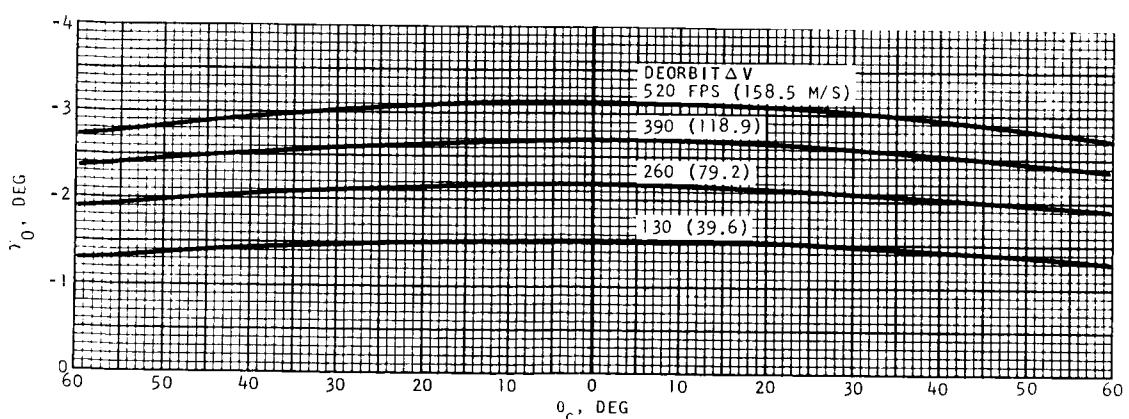
FIGURE 28. DEORBIT NEAR APOGEE OF BASELINE ORBIT



b) TIME FROM DEORBIT TO ENTRY ALTITUDE

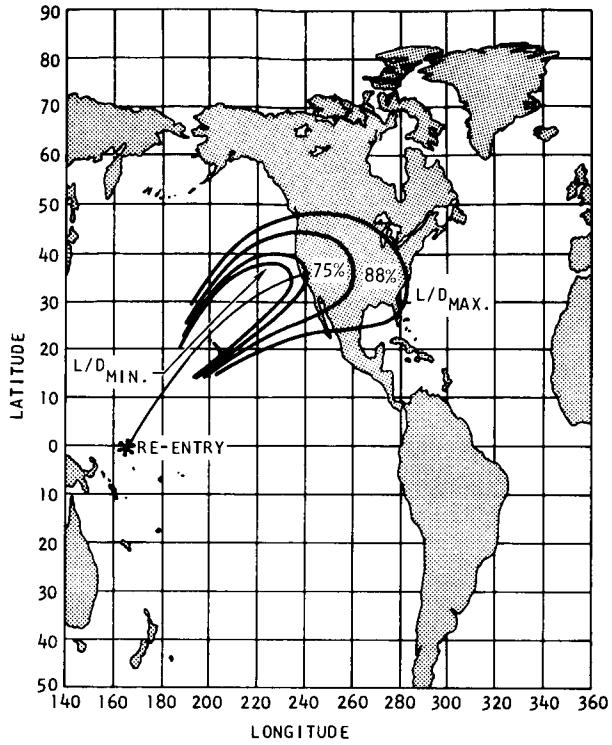


c) TOTAL INERTIAL VELOCITY AT ENTRY ALTITUDE



d) ENTRY ANGLE

FIGURE 28.--CONCLUDED



a) ENTRY FOOTPRINT

b) R_c VERSUS R_d

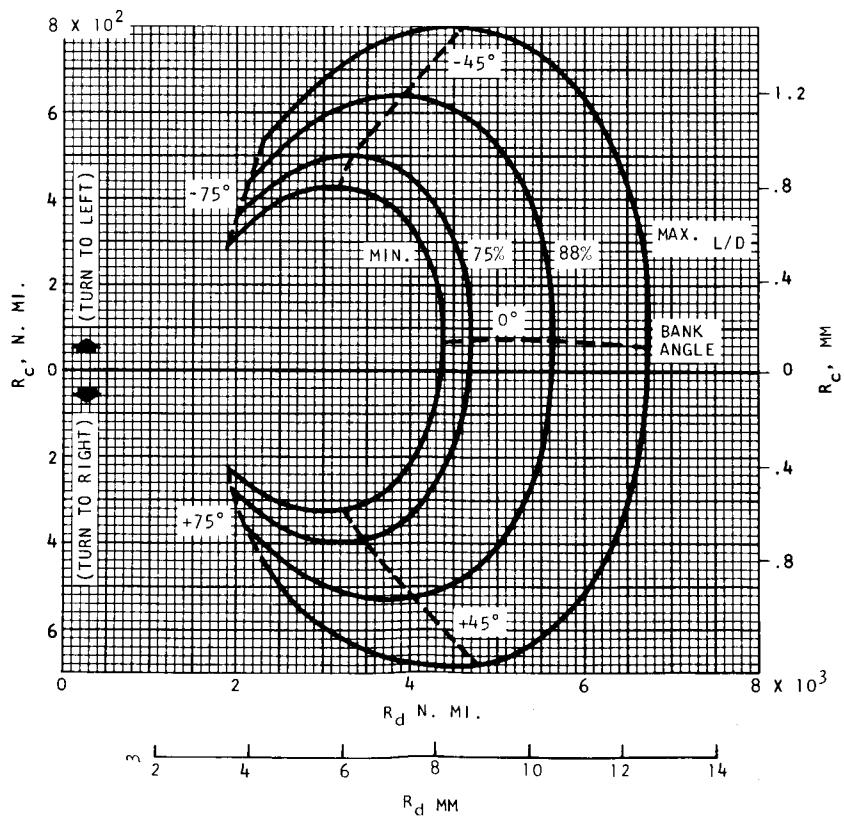
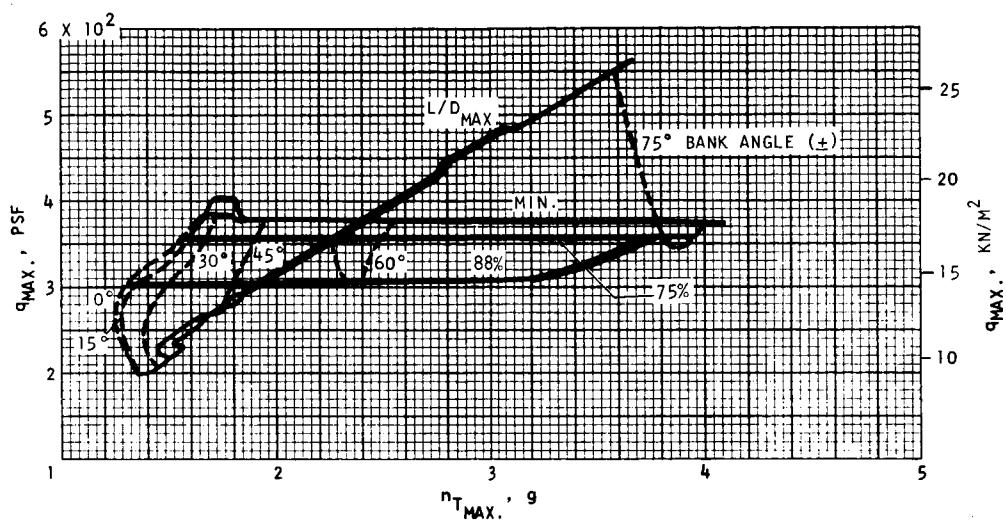


FIGURE 29. ENTRY DATA: $i = 35.7^\circ$, $\gamma = -1.5^\circ$, W/S = 50 PSF (2.39 KN/M^2)



c) $q_{MAX.}$ VERSUS $n_{T_{MAX.}}$

d) Q_{T_S} VERSUS $q_{s_{MAX.}}$

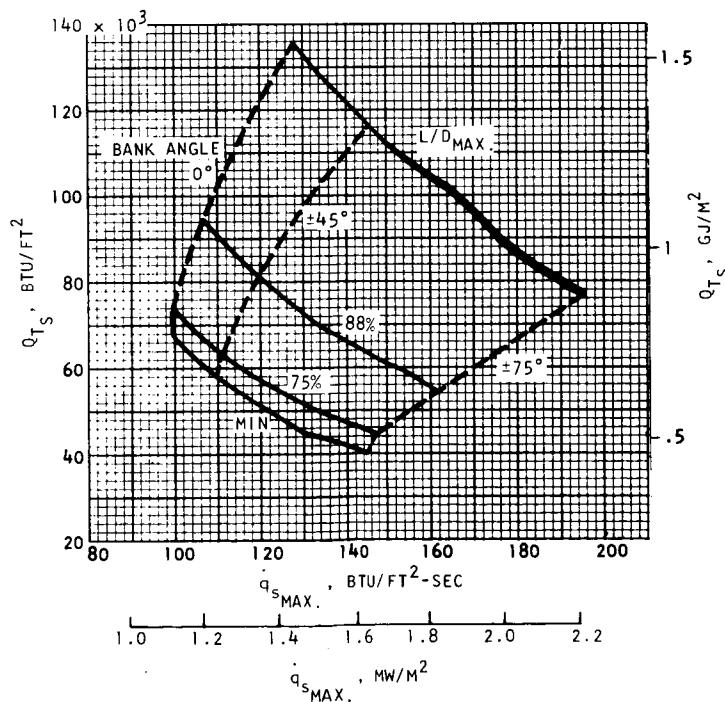
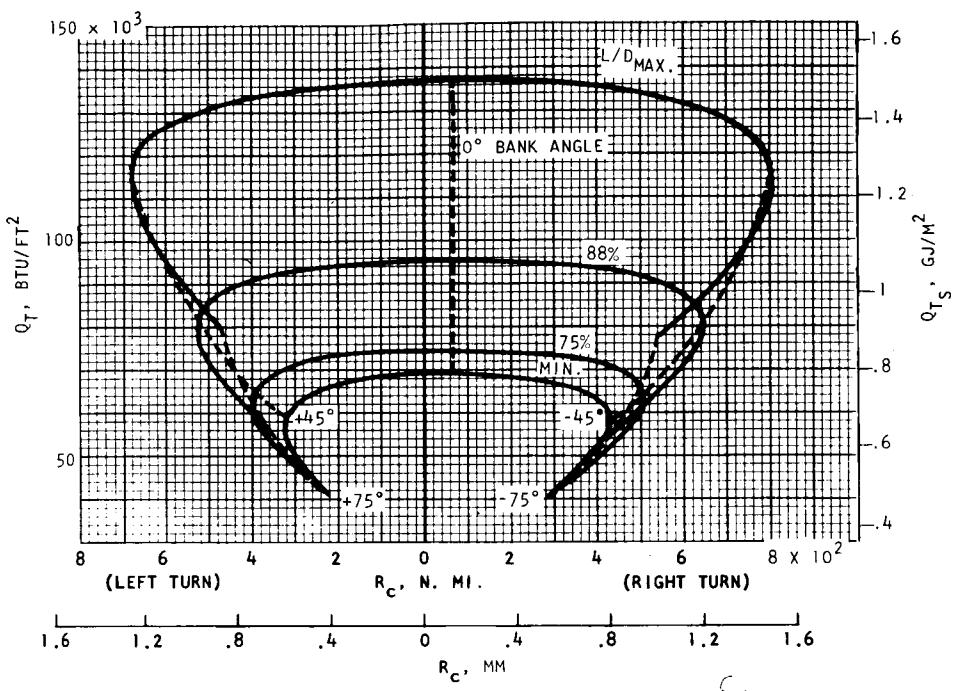


FIGURE 29.--CONTINUED



e) Q_T VERSUS R_c \blacktriangleleft

f) t VERSUS R_c \blacktriangleright

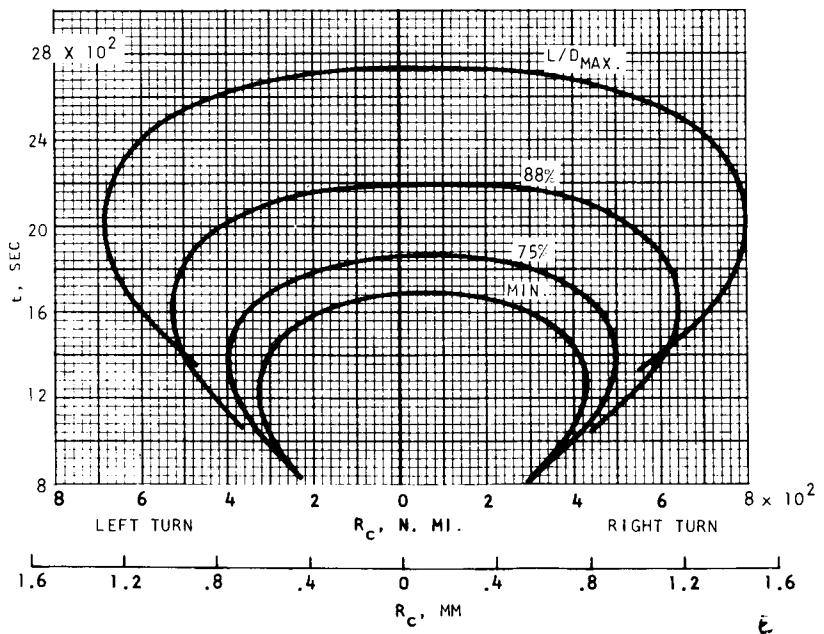
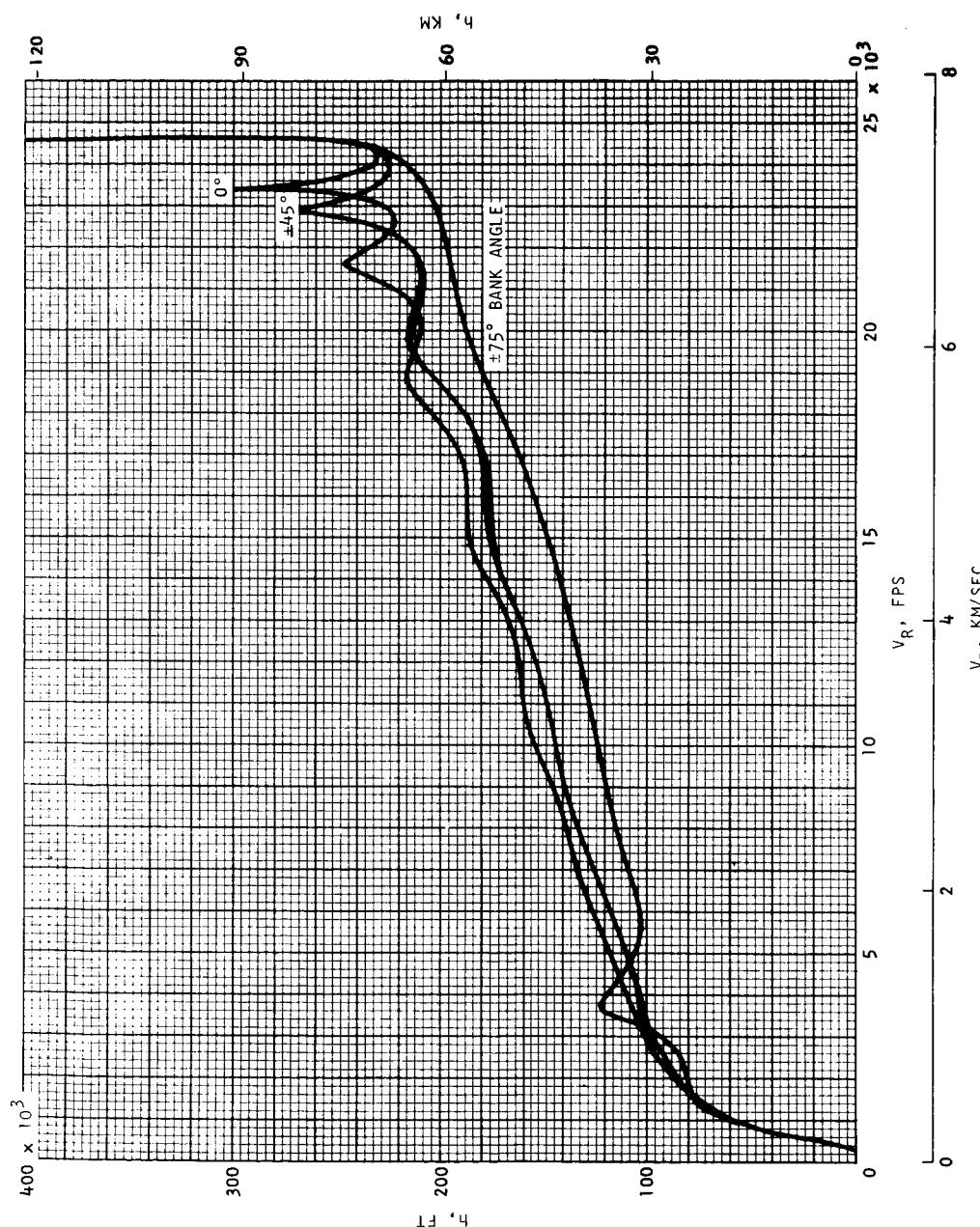
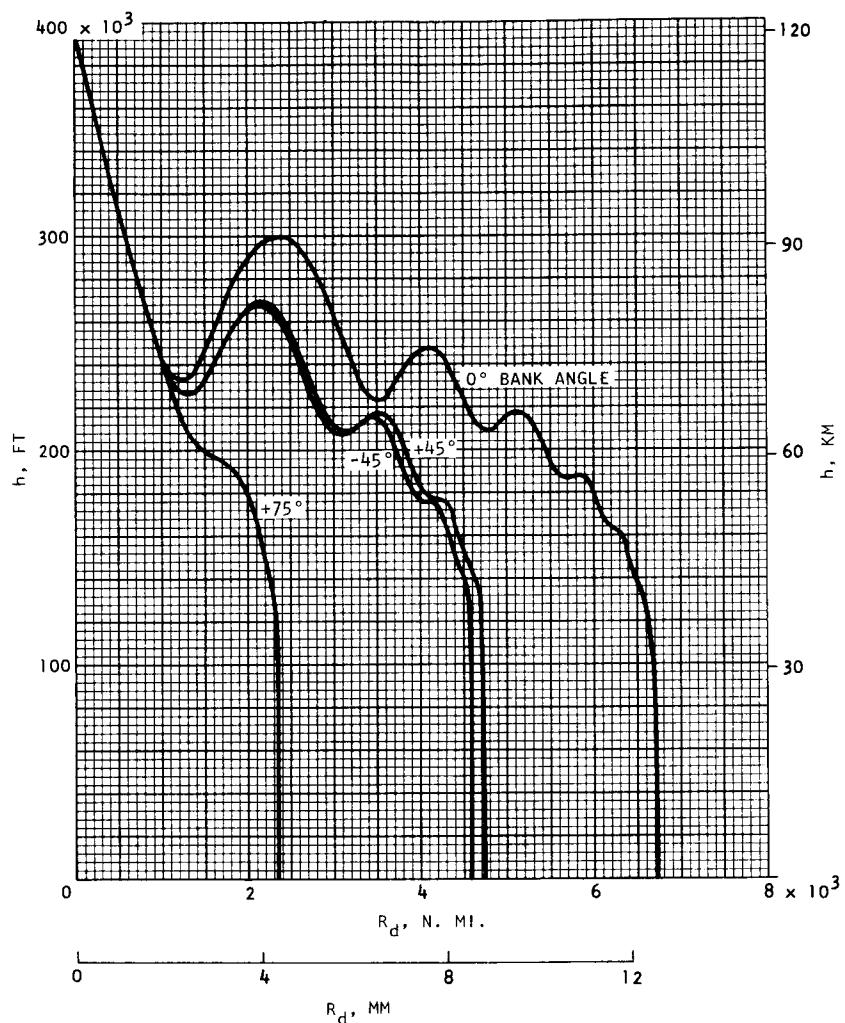


FIGURE 29.--CONTINUED



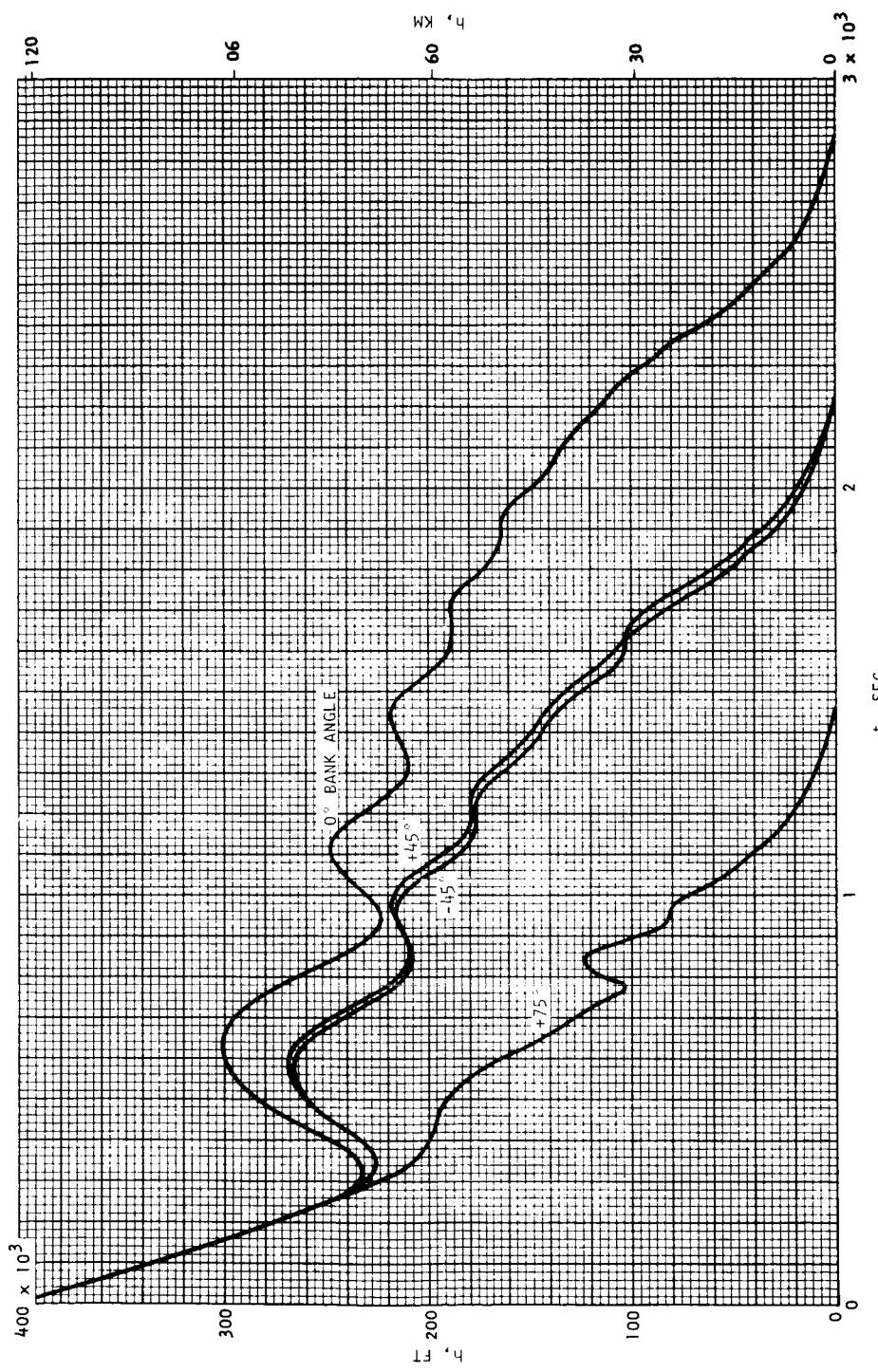
g-1) h VERSUS V_R FOR L/D_{MAX} . ENTRIES

FIGURE 29. --CONTINUED



g-2) h VERSUS R_d FOR L/D_{MAX} . ENTRIES

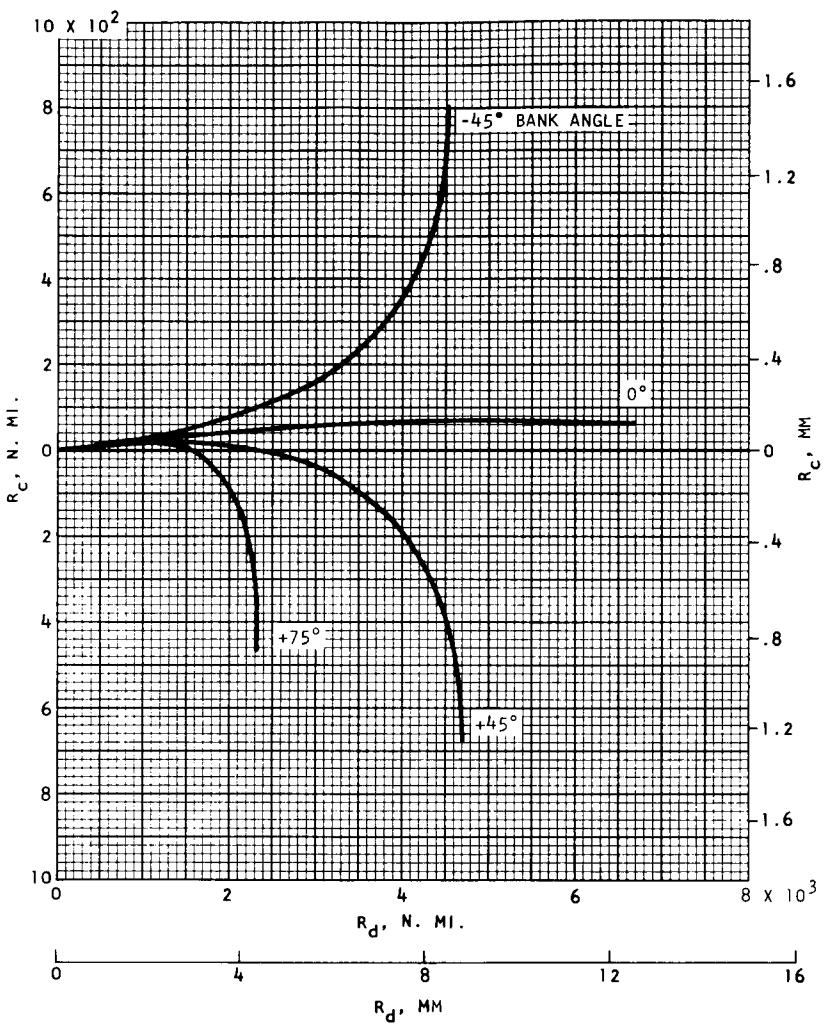
FIGURE 29.--CONTINUED



ER 14471-3

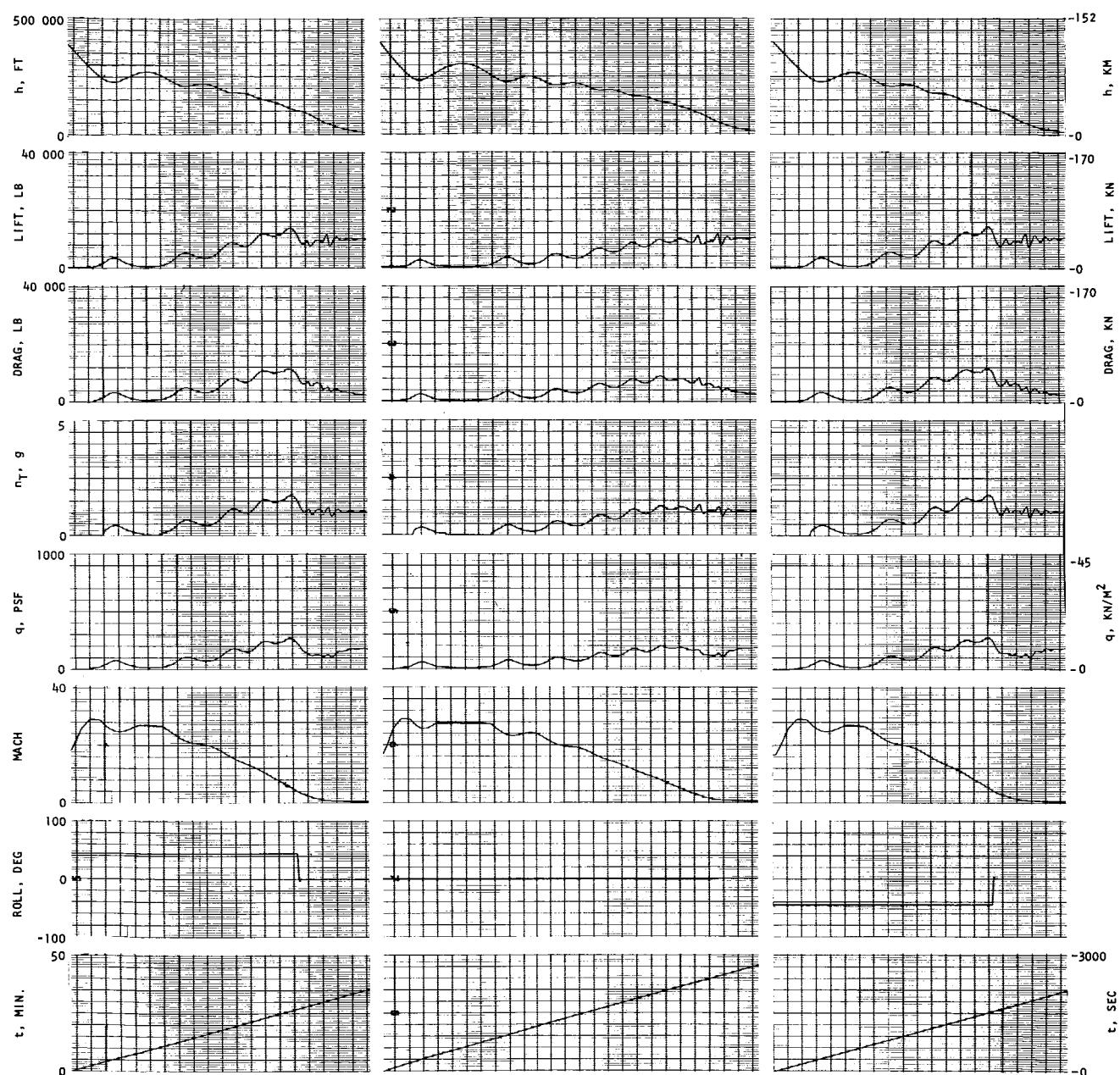
g-3) h VERSUS t FOR L/D_{MAX} . ENTRIES

FIGURE 29.—CONTINUED



g-4) GROUND TRACES FOR L/D_{MAX} . ENTRIES

FIGURE 29.--CONTINUED



g-5) STRIP RECORDER OUTPUT FOR L/D_{MAX}. ENTRIES

FIGURE 29.--CONTINUED

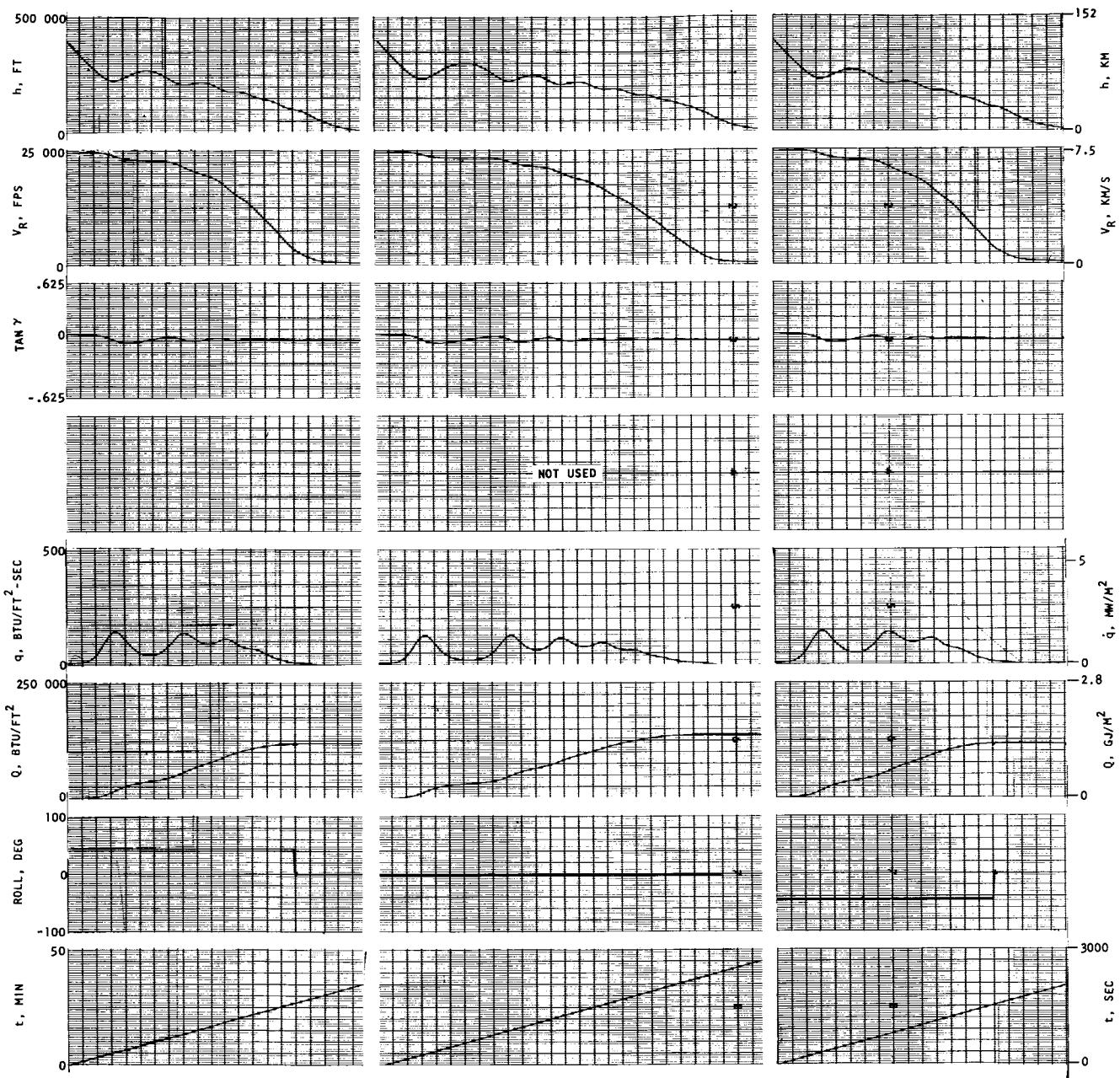
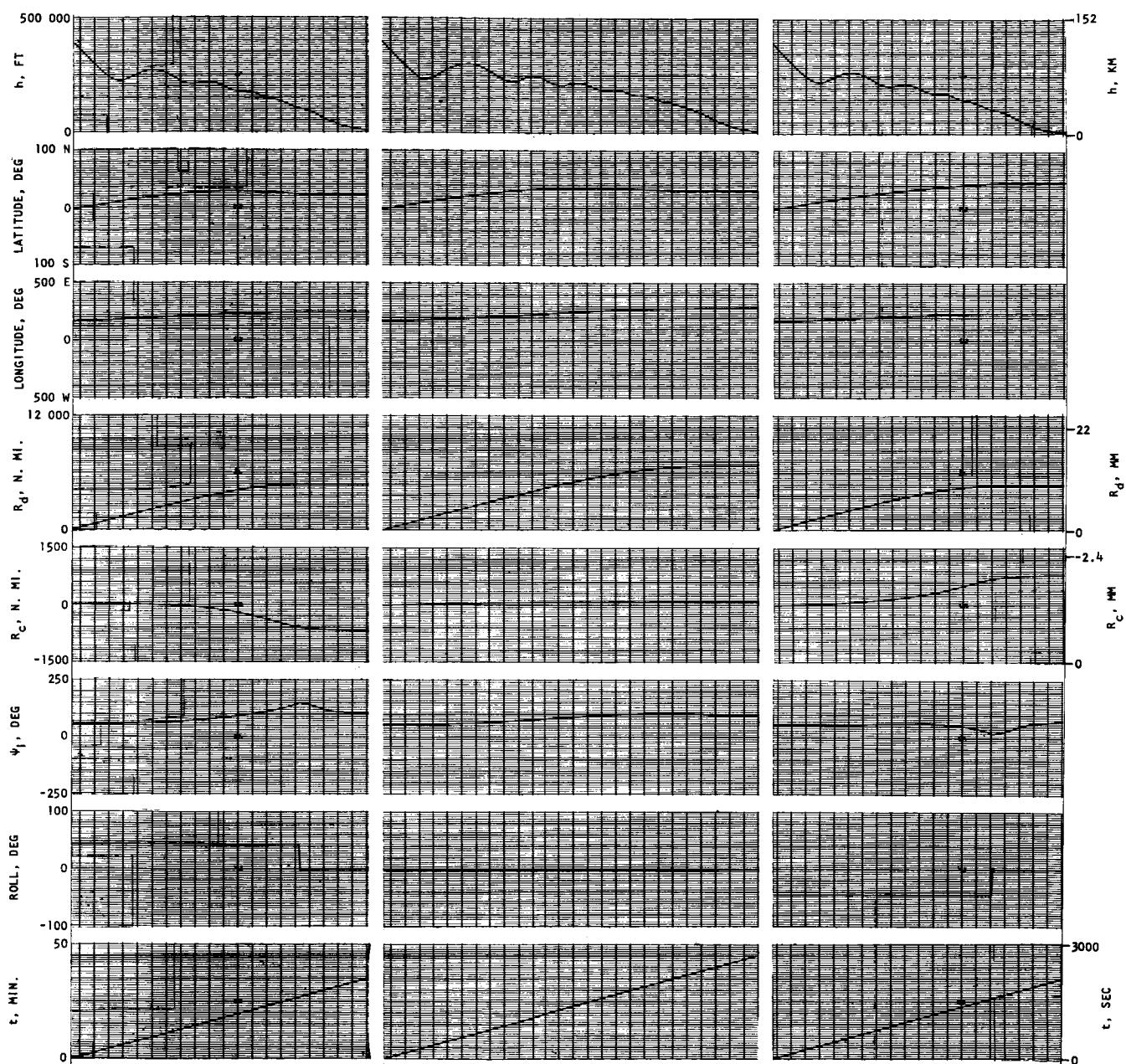
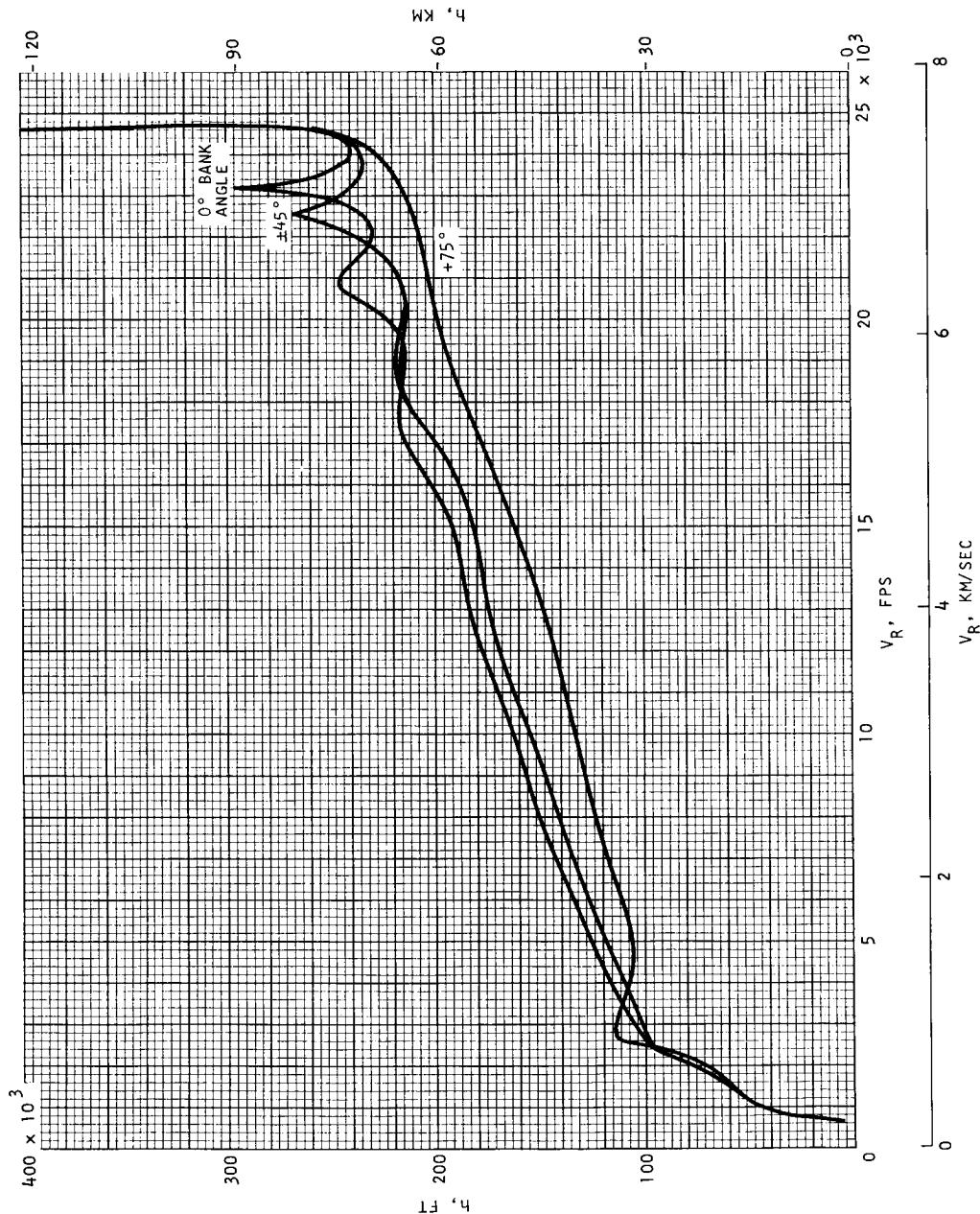


FIGURE 29. --CONTINUED g-5) CONTINUED



g-5) CONCLUDED

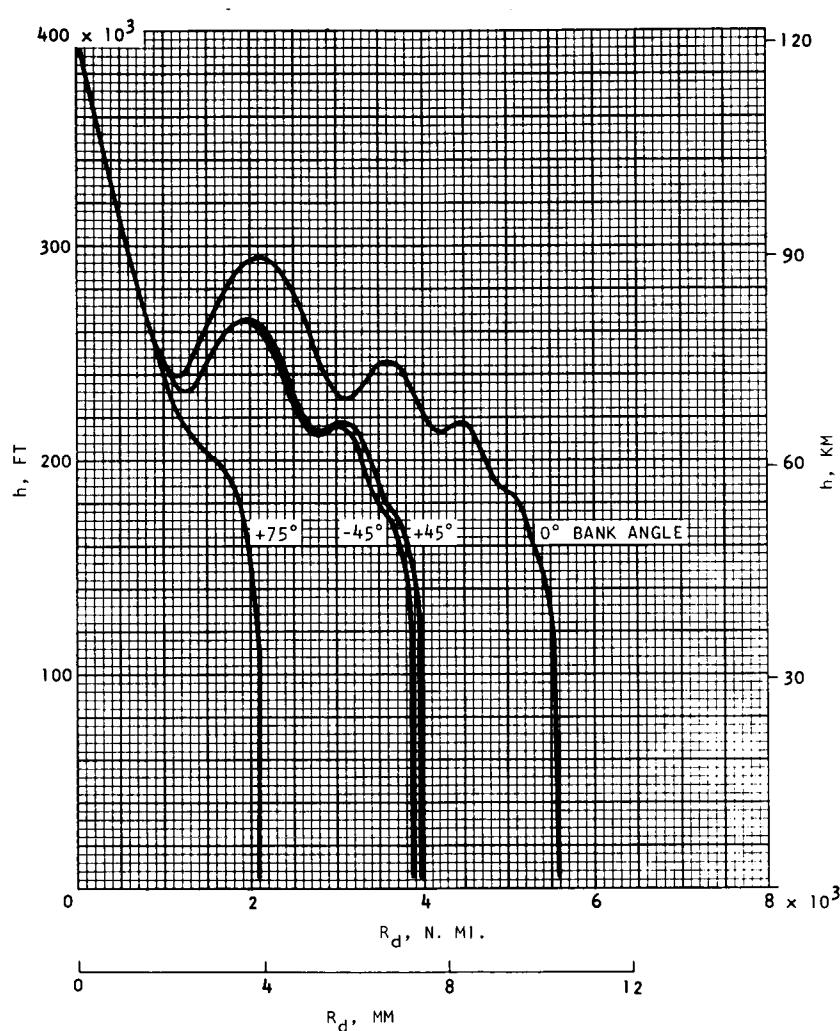
FIGURE 29.--CONTINUED



ER 14471-3

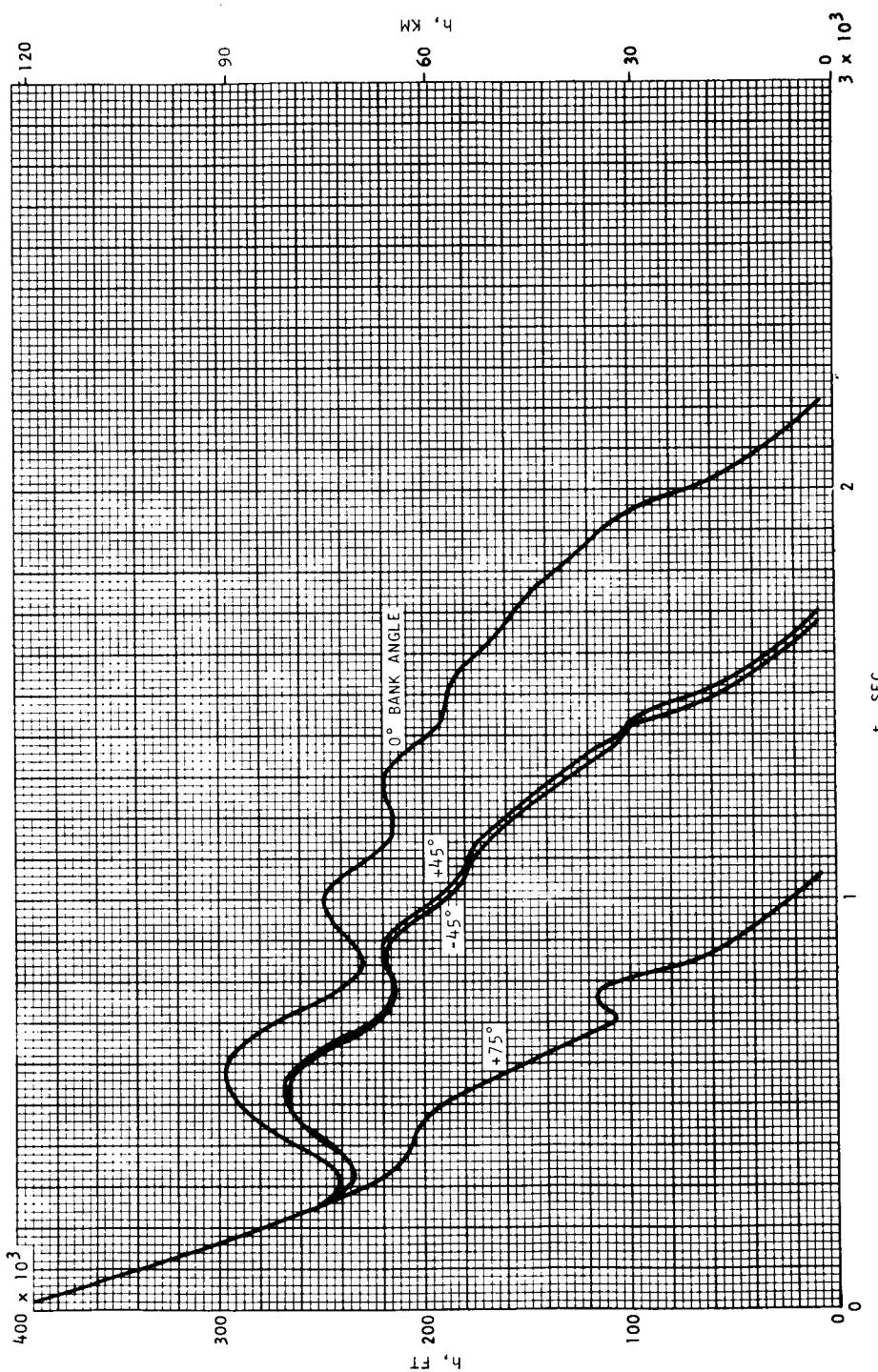
h-1) h VERSUS V_R FOR 88% L/D_{MAX} . ENTRIES

FIGURE 29. --CONTINUED



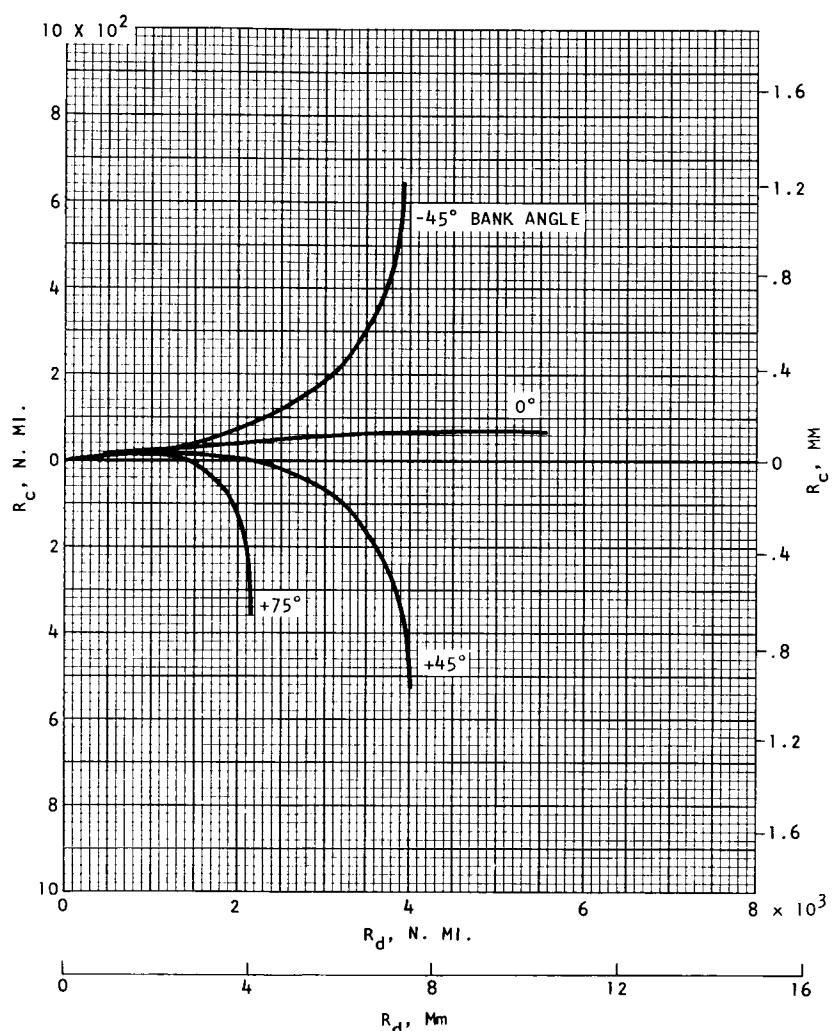
h-2) h VERSUS R_d FOR 88% $L/D_{MAX.}$ ENTRIES

FIGURE 29.--CONTINUED



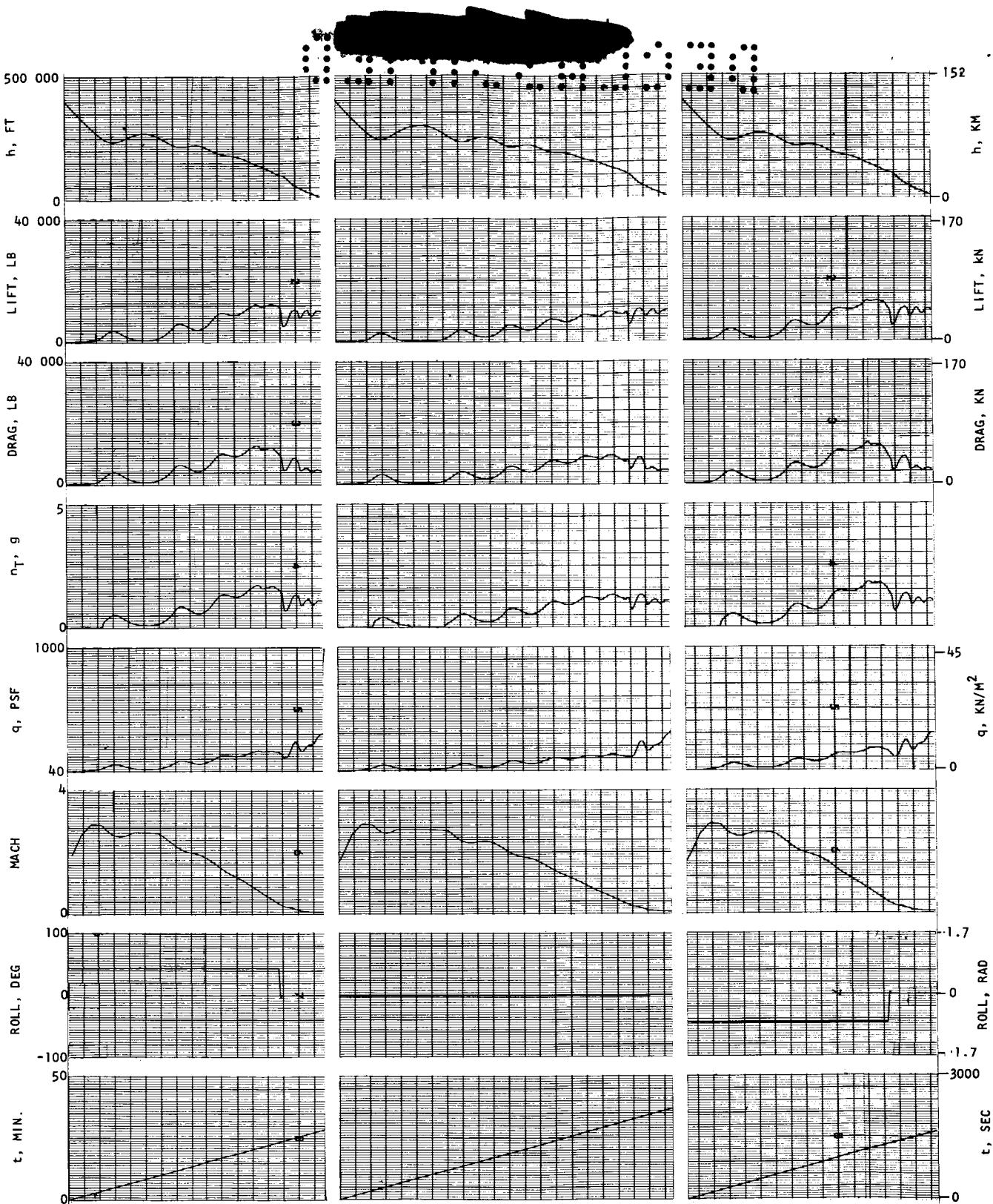
h-3) h VERSUS t FOR 88% L/D_{MAX}. ENTRIES

FIGURE 29. --CONTINUED



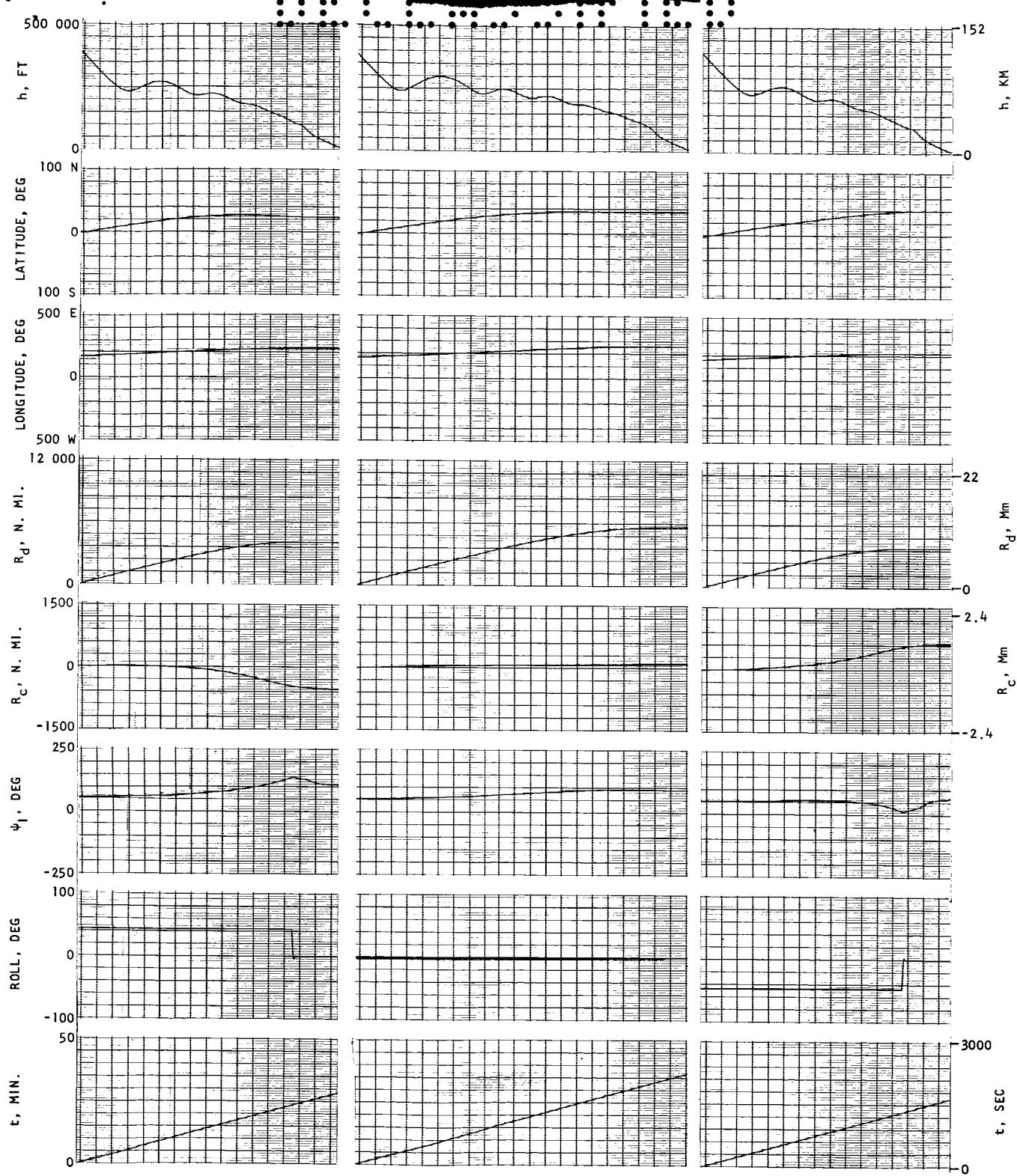
h-4) GROUND TRACES FOR 88% L/D_{MAX.} ENTRIES

FIGURE 29.--CONTINUED



h-5) STRIP RECORDER OUTPUT FOR 88% L/D_{MAX} . ENTRIES

FIGURE 29.--CONTINUED



h-5) CONTINUED

FIGURE 29.--CONTINUED

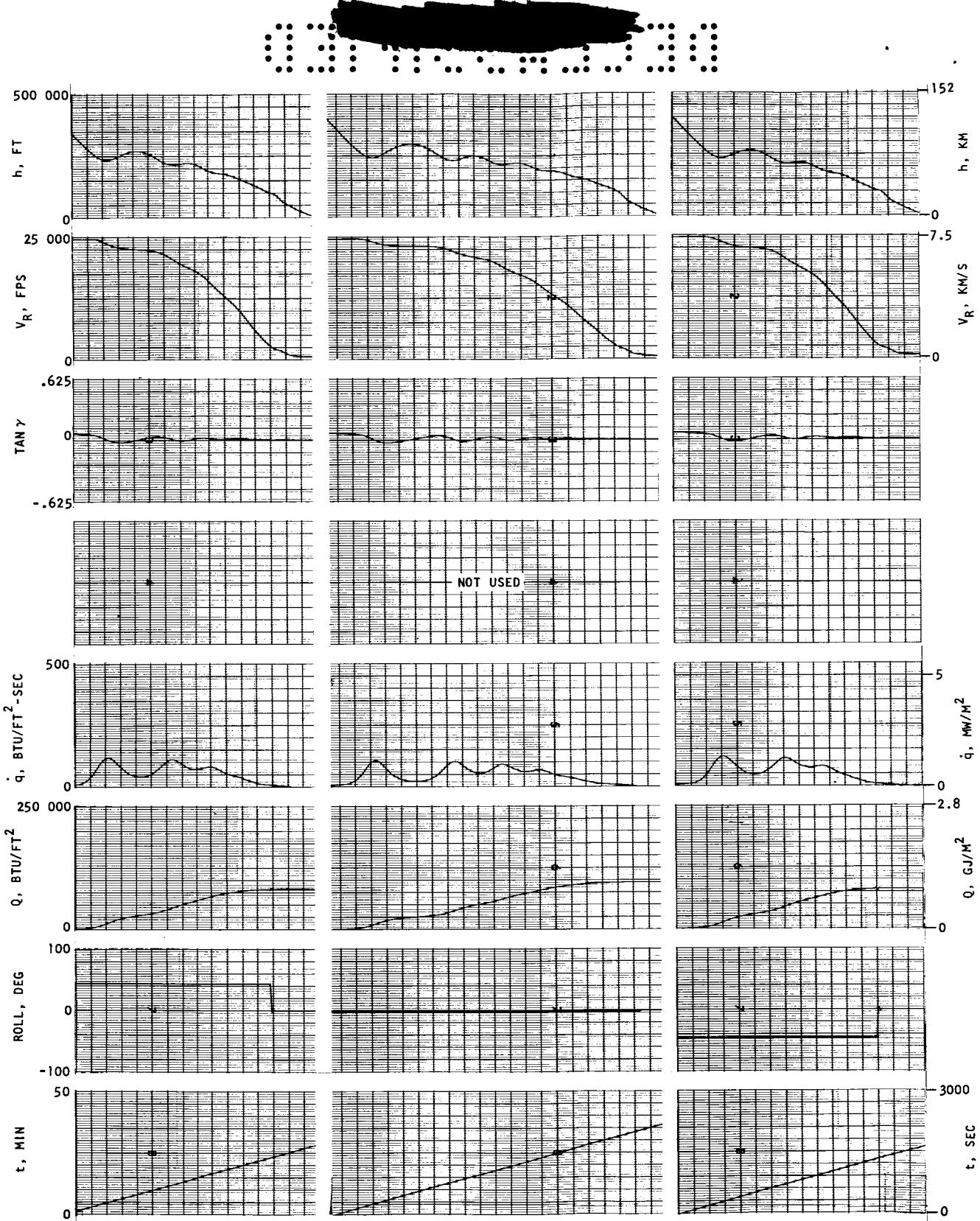
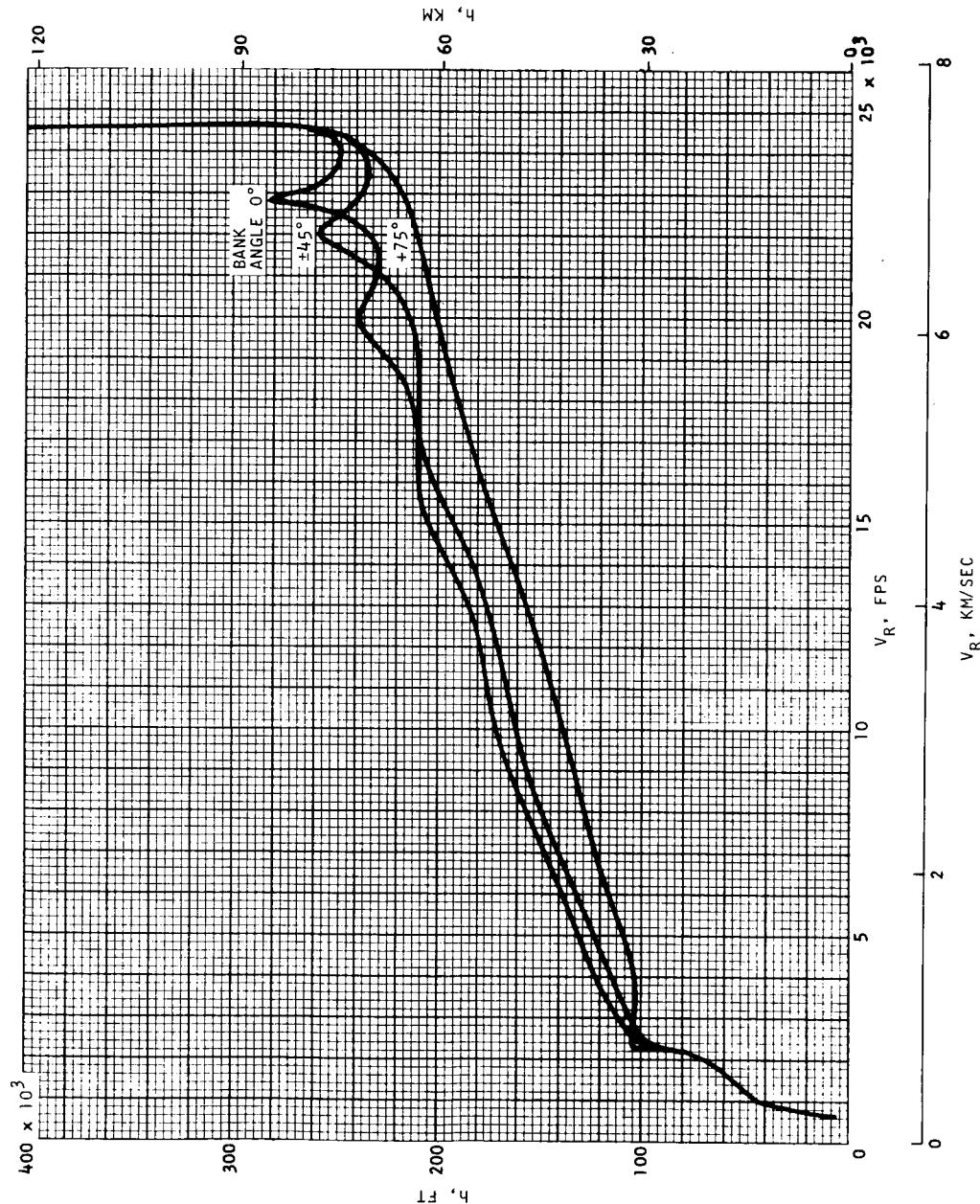
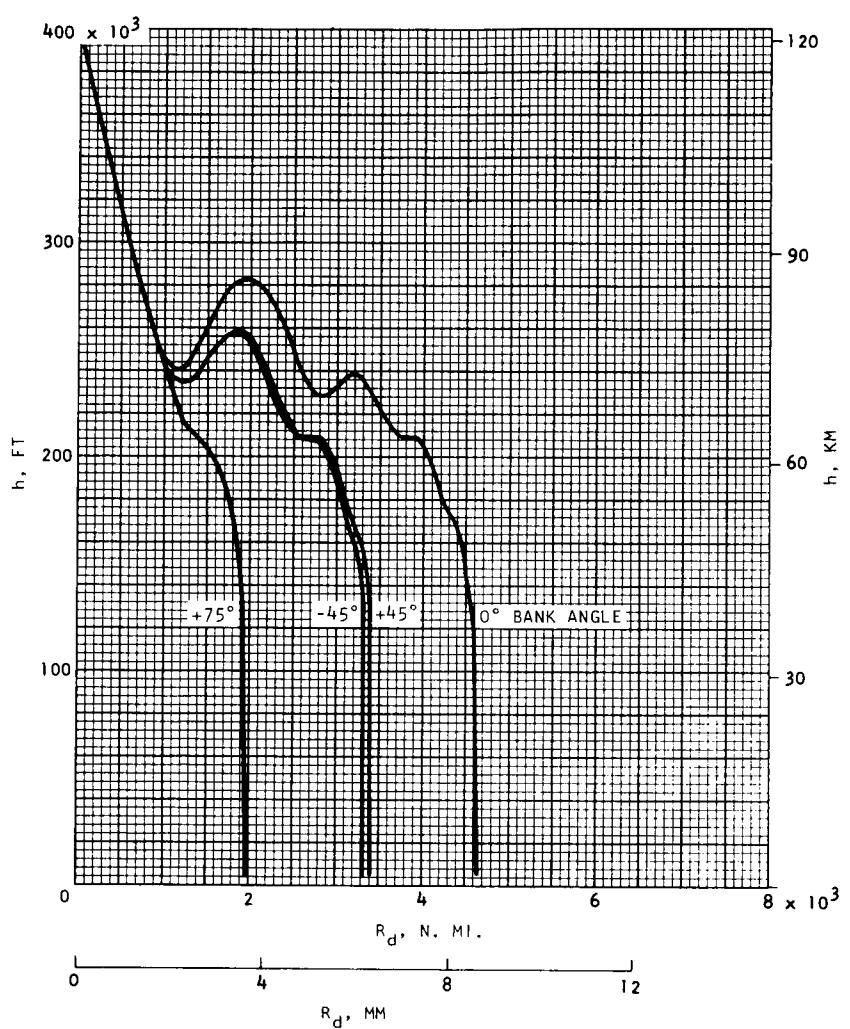


FIGURE 29. --CONTINUED h-5) CONCLUDED



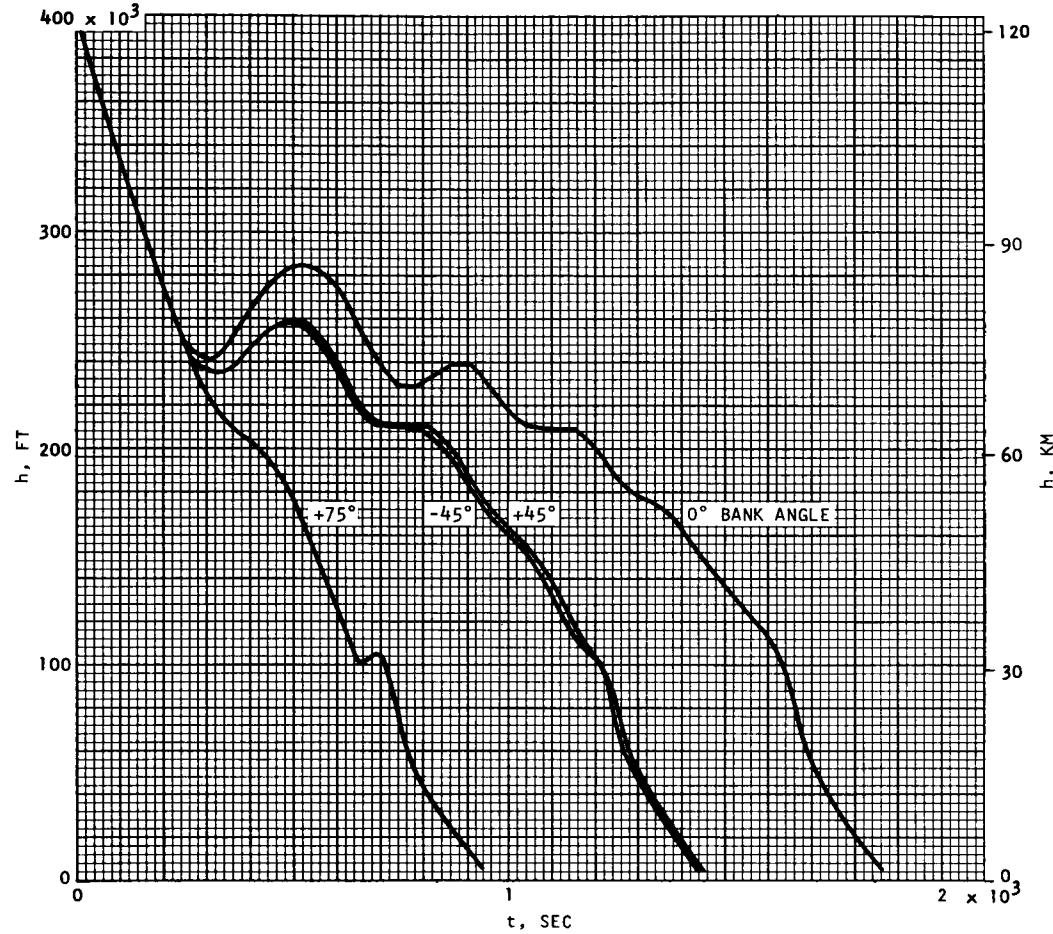
i-1) h VERSUS V_R FOR 75% L/D_{MAX} . ENTRIES

FIGURE 29.--C CONTINUED

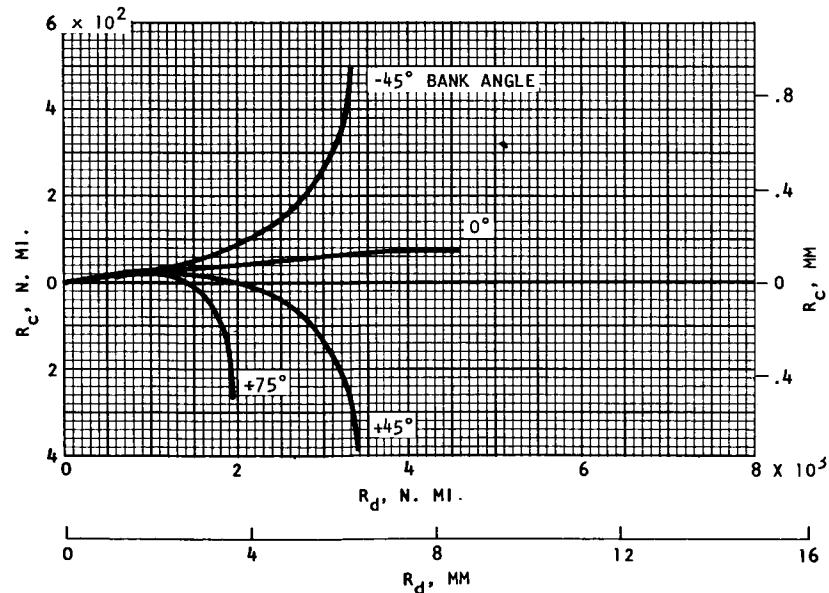


i-2) h VERSUS R_d FOR 75% L/D_{MAX.} ENTRIES

FIGURE 29.--CONTINUED

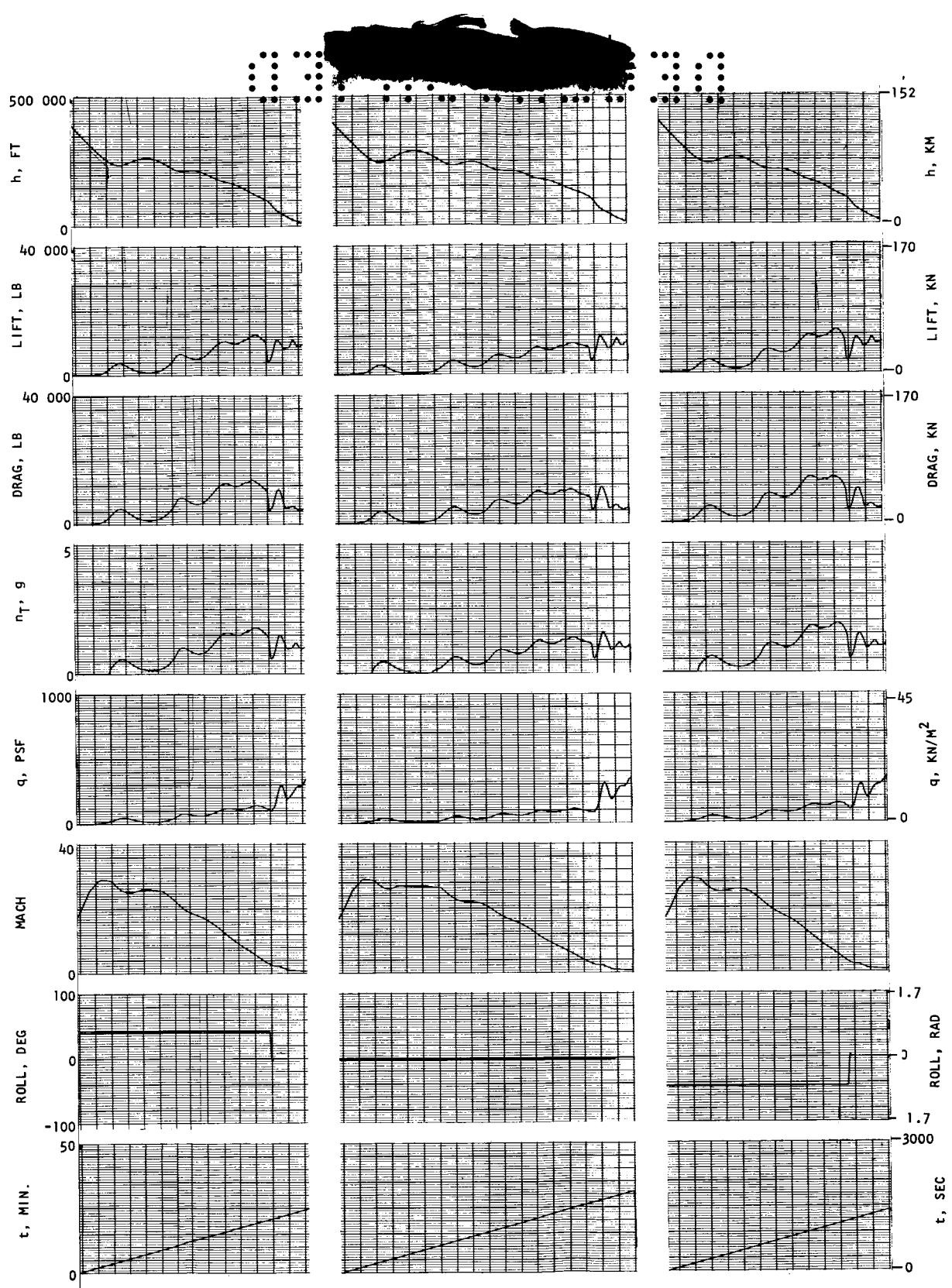


i-3) h VERSUS t FOR 75% L/D_{MAX} . ENTRIES



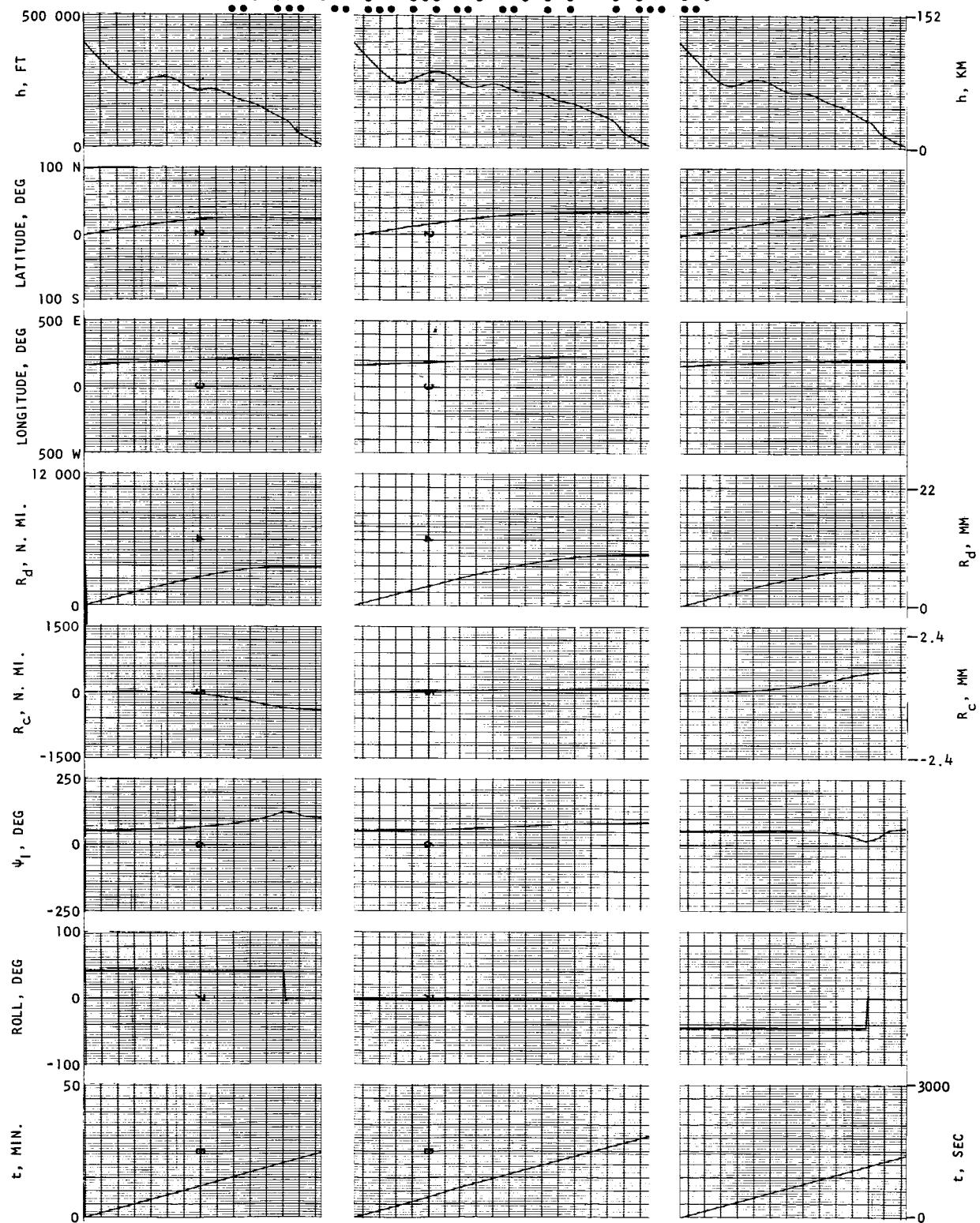
i-4) GROUND TRACES FOR 75% L/D_{MAX} . ENTRIES

FIGURE 29--CONTINUED



i-5) STRIP RECORDER OUTPUT FOR 75% L/D_{MAX} . ENTRIES

FIGURE 29.--CONTINUED



i-5) CONTINUED

FIGURE 29.--CONTINUED

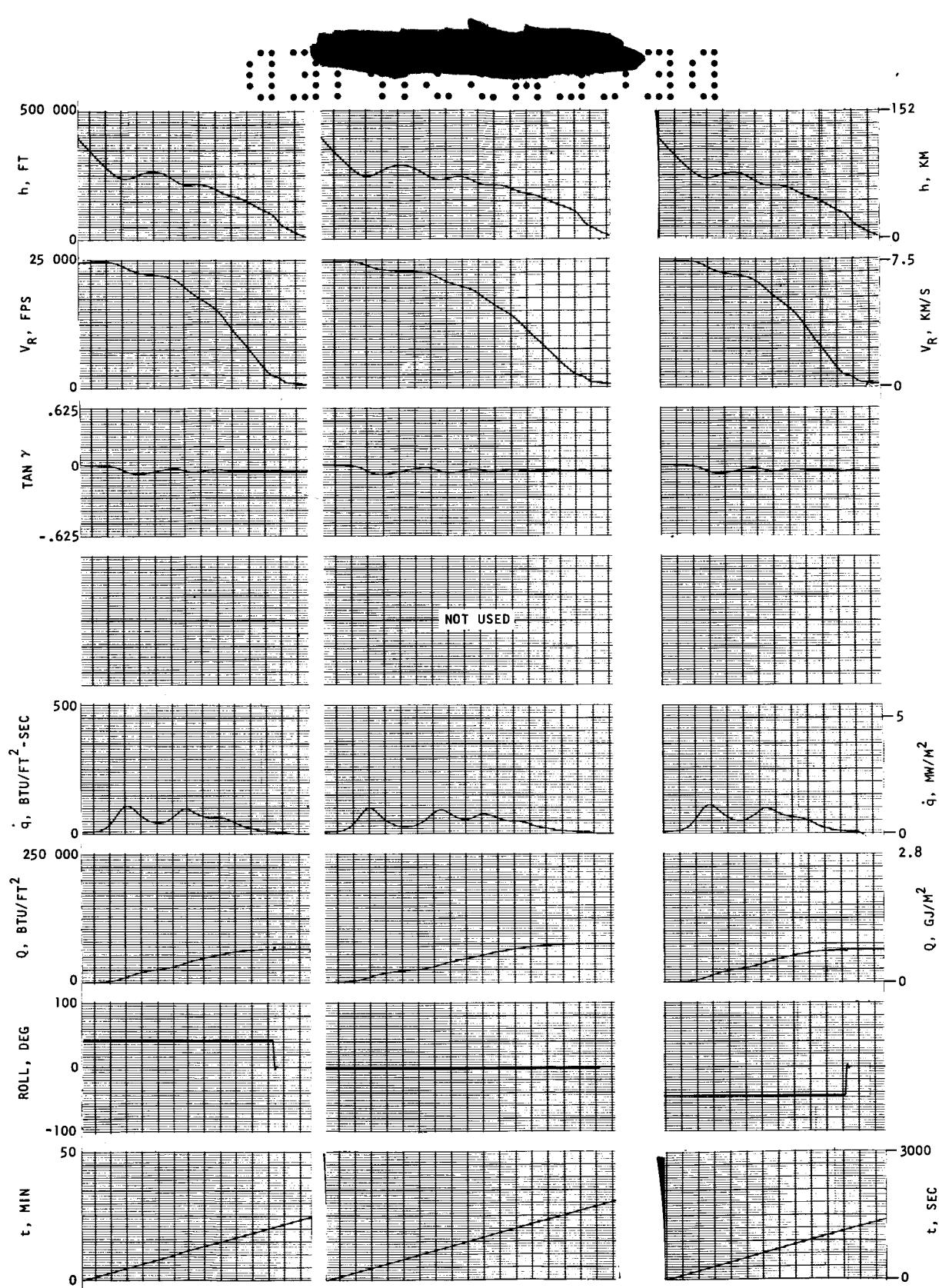
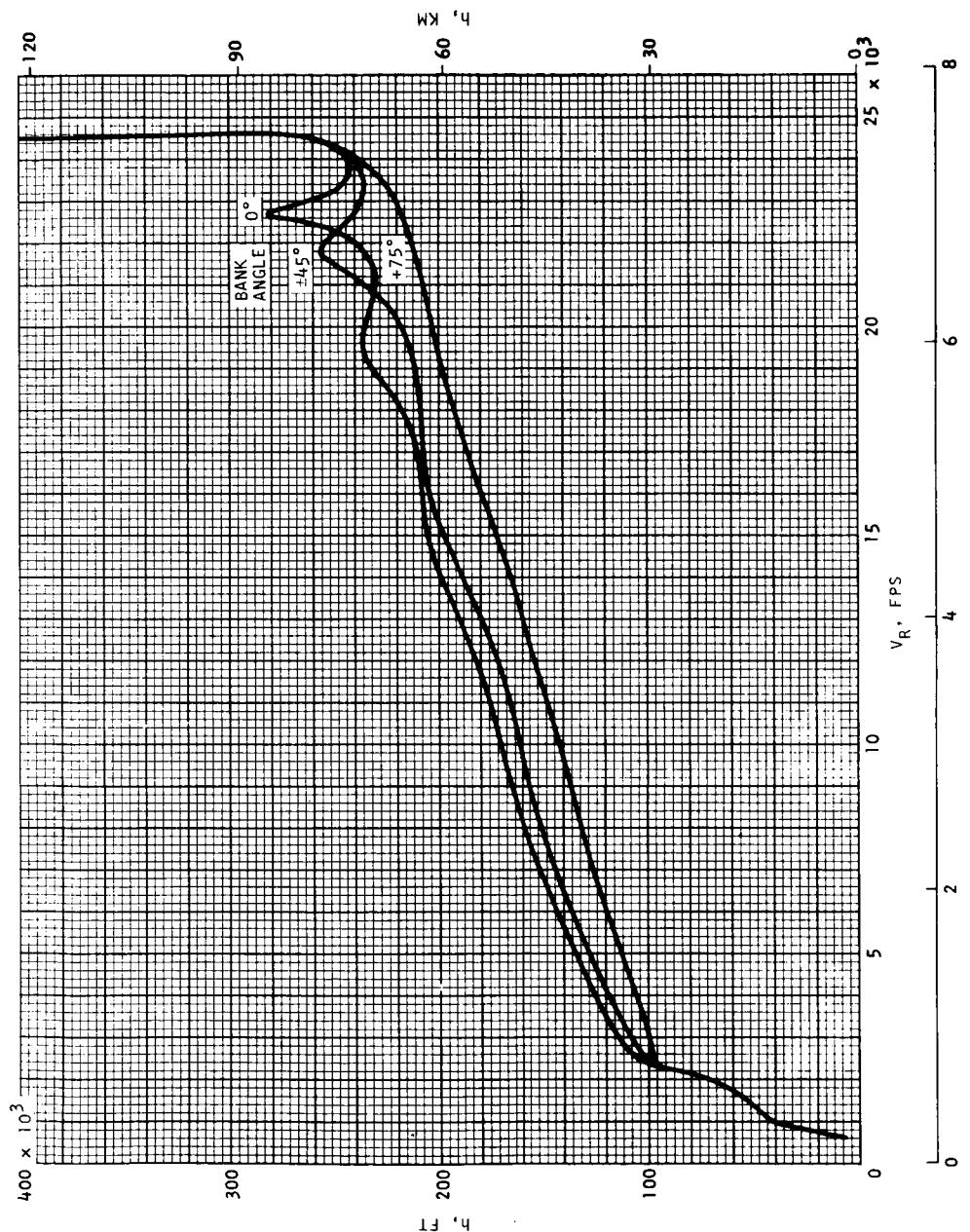


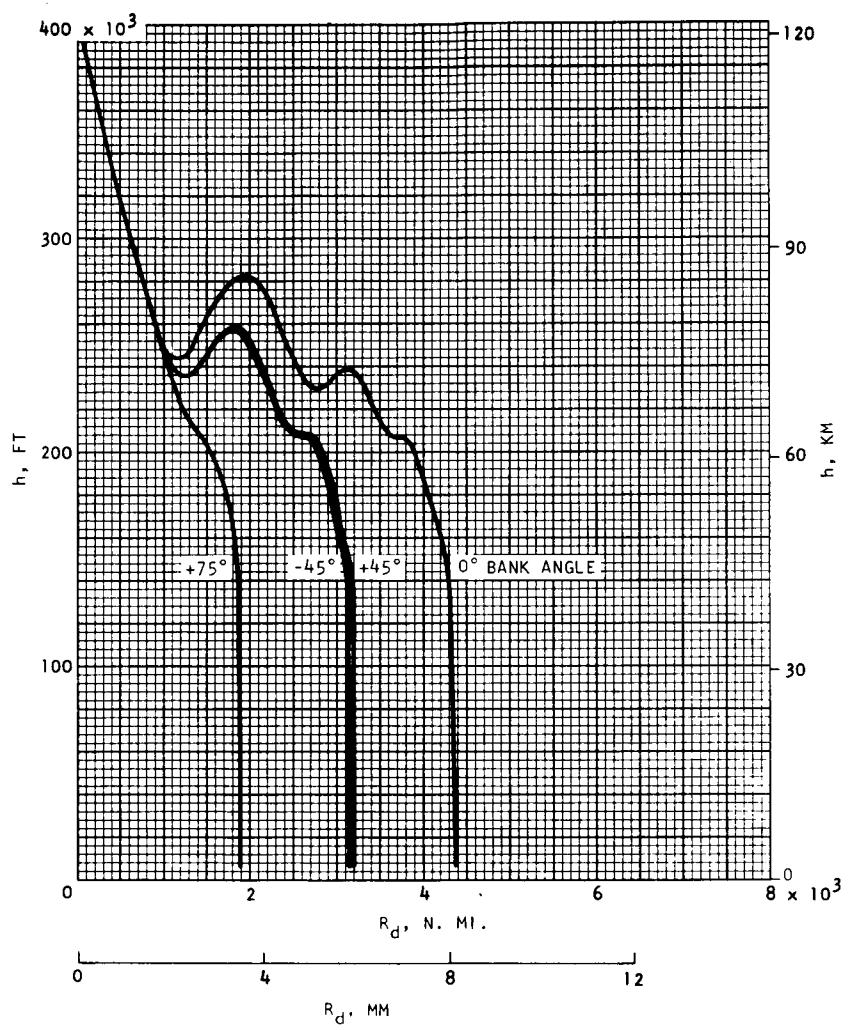
FIGURE 29. --CONTINUED

i-5) CONCLUDED



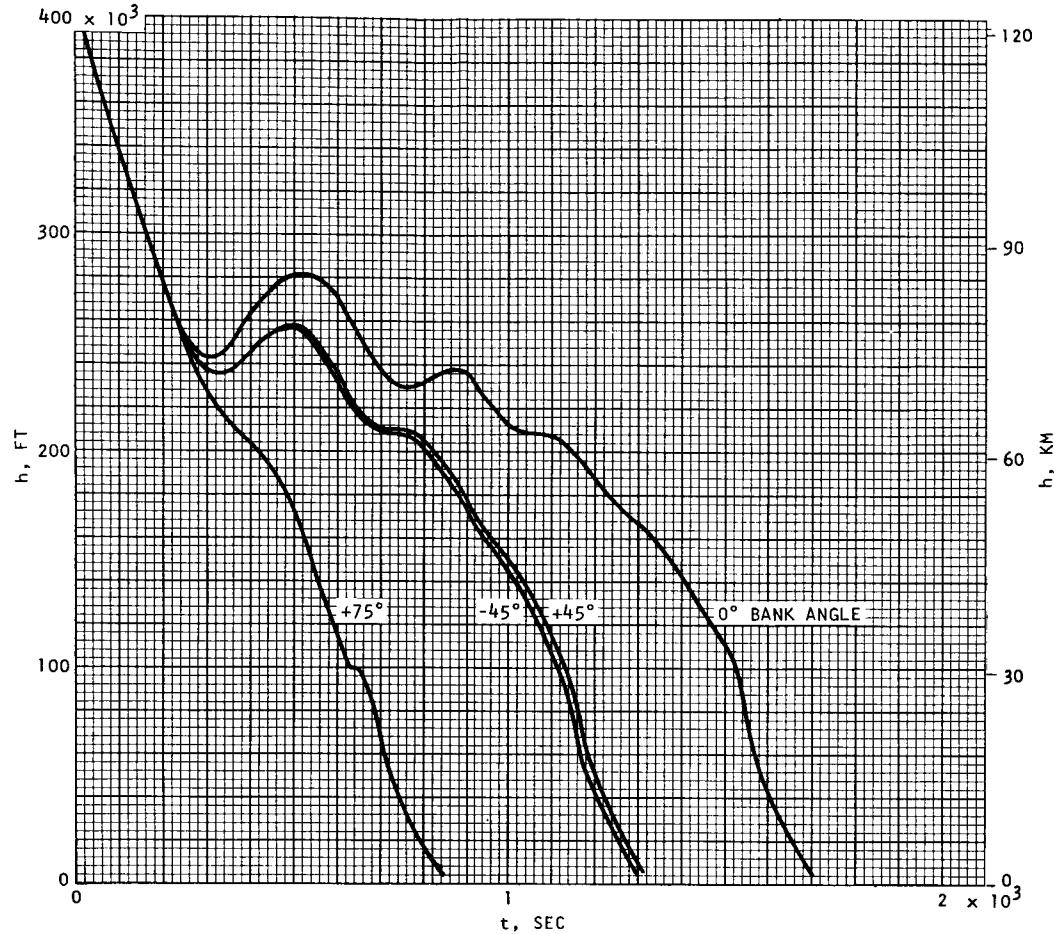
j-1) h VERSUS V_R FOR L/D_{MIN} . ENTRIES

FIGURE 29--CONTINUED

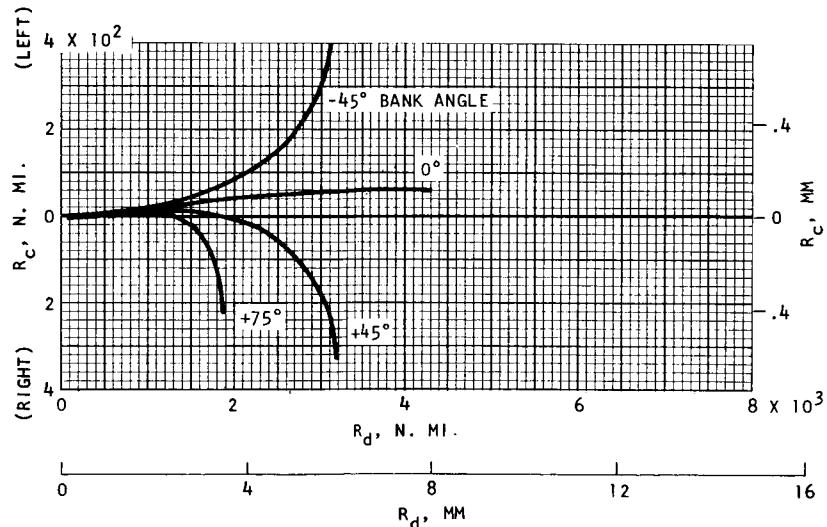


j-2) h VERSUS R_d FOR L/D_{MIN} . ENTRIES

FIGURE 29--CONTINUED

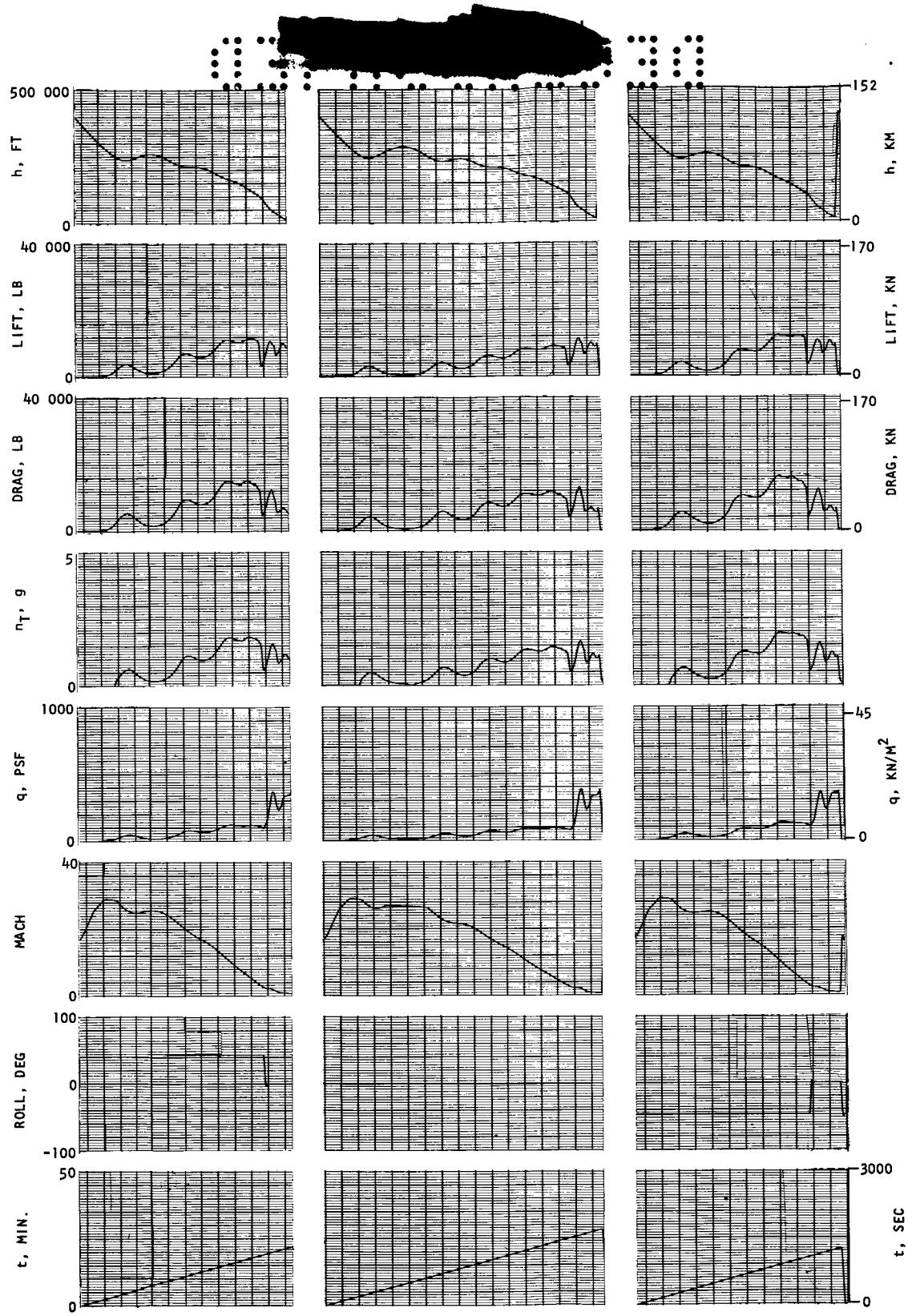


j-3) h VERSUS t FOR $L/D_{MIN.}$ ENTRIES



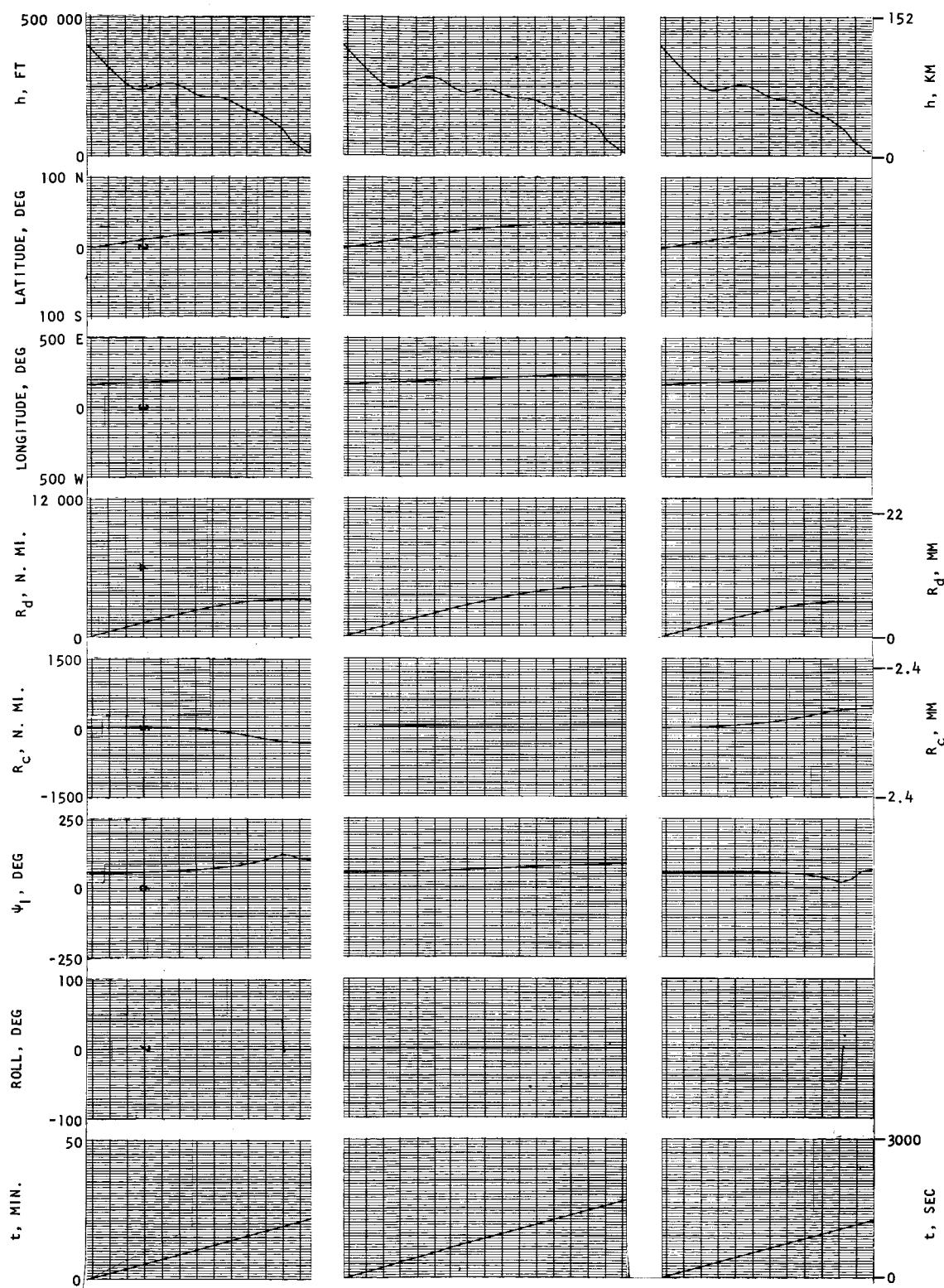
j-4) GROUND TRACES FOR $L/D_{MIN.}$ ENTRIES

FIGURE 29--CONTINUED



j-5) STRIP RECORDER OUTPUT FOR L/D_{MIN.} ENTRIES

FIGURE 29--CONTINUED



j-5) CONTINUED

FIGURE 29--CONTINUED

ER 14471-3

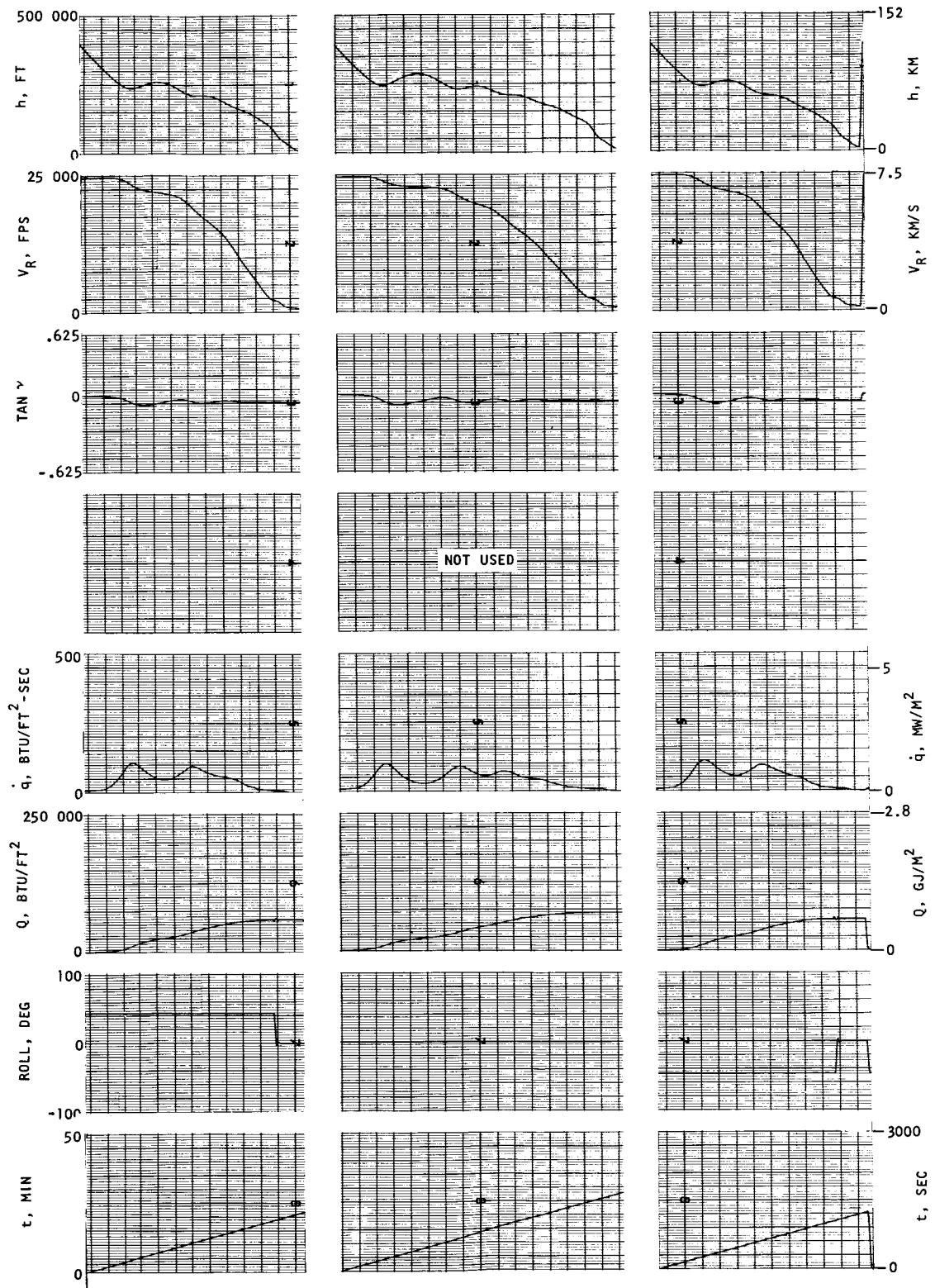
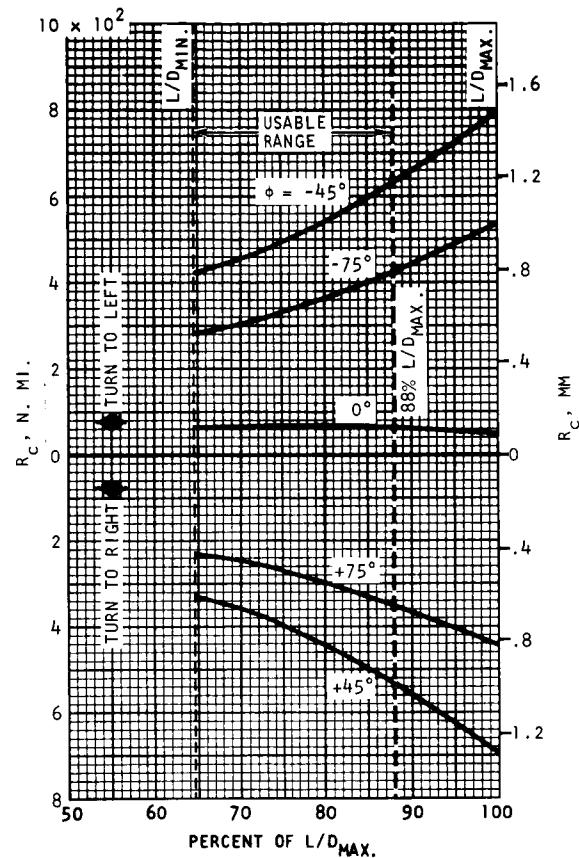
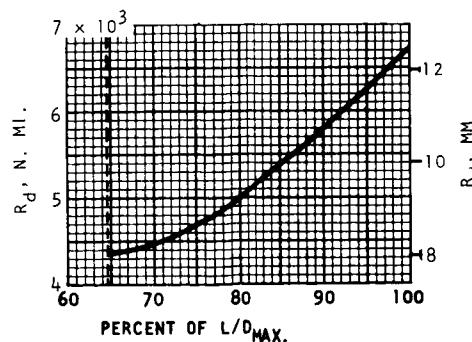


FIGURE 29. --CONTINUED

j-5) CONCLUDED

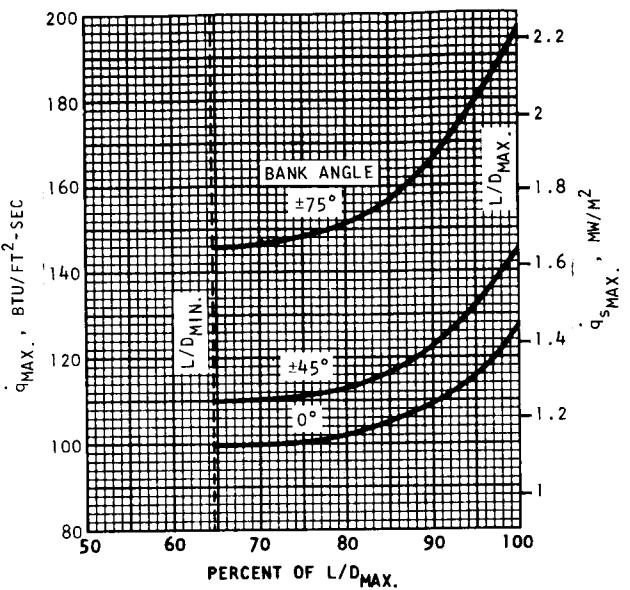


k-1) VARIATION OF R_c WITH L/D

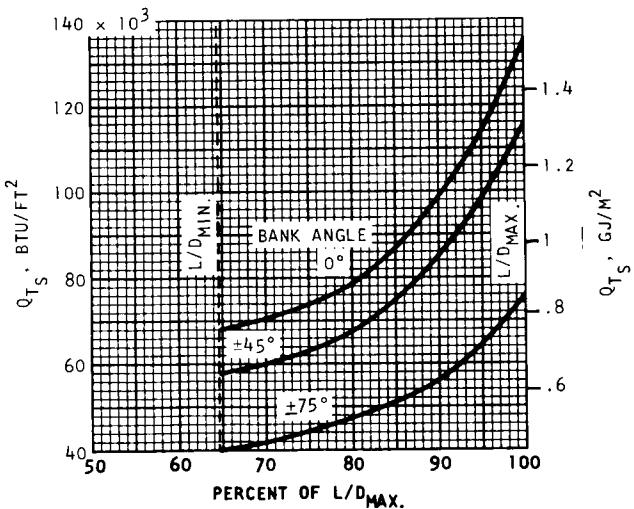


k-2) VARIATION OF R_d WITH L/D

FIGURE 29--CONTINUED

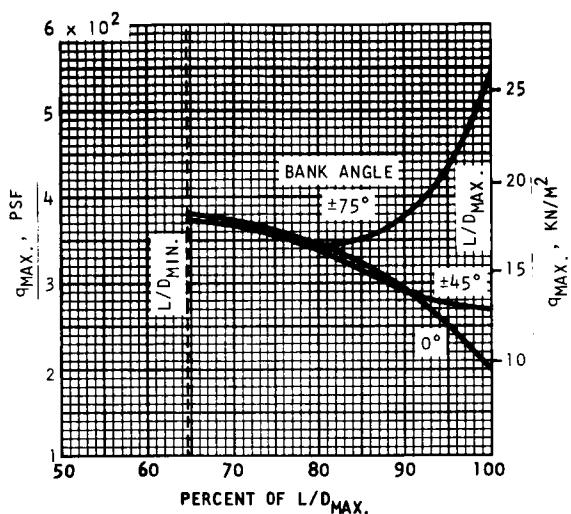


k-3) VARIATION OF $q_s MAX.$ WITH L/D

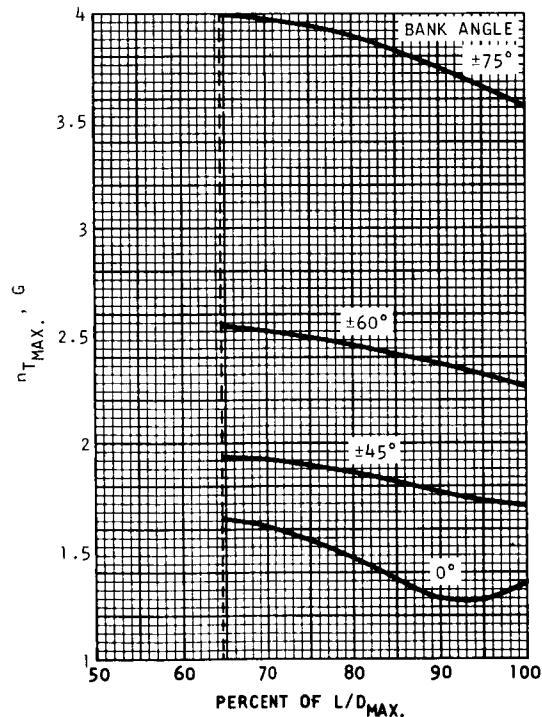


k-4) VARIATION OF $Q_T s$ WITH L/D

FIGURE 29--CONTINUED

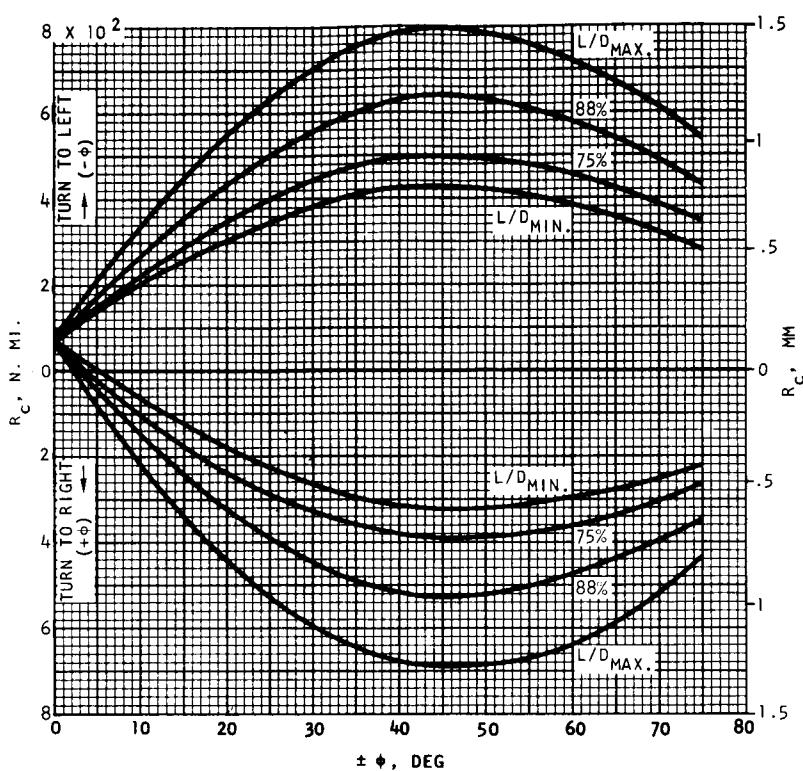


k-5) VARIATION OF q_{MAX} WITH L/D

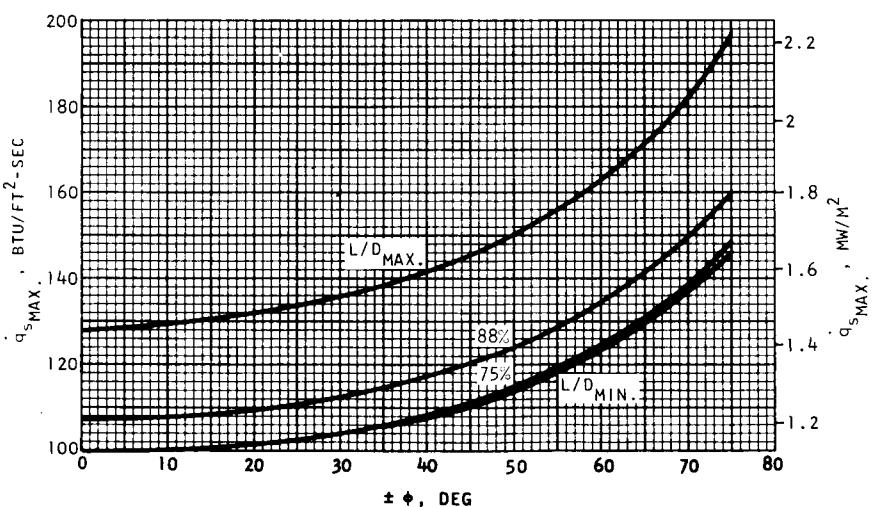


k-6) VARIATION OF $n_{T_{MAX}}$ WITH L/D

FIGURE 29--CONTINUED



I-1) VARIATION OF R_c WITH BANK ANGLE



I-2) VARIATION OF q_s _{MAX.} WITH BANK ANGLE

FIGURE 29--CONTINUED

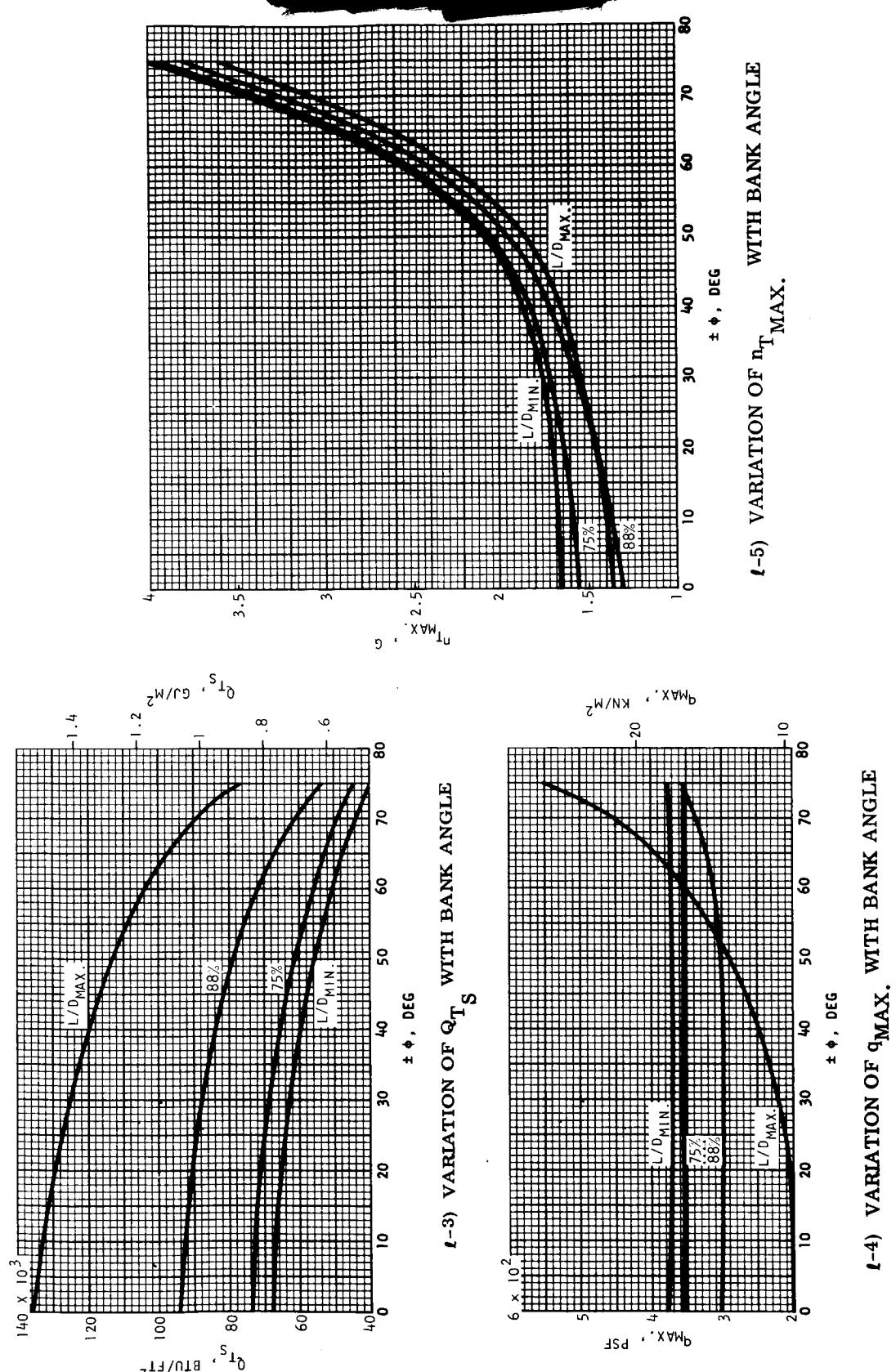
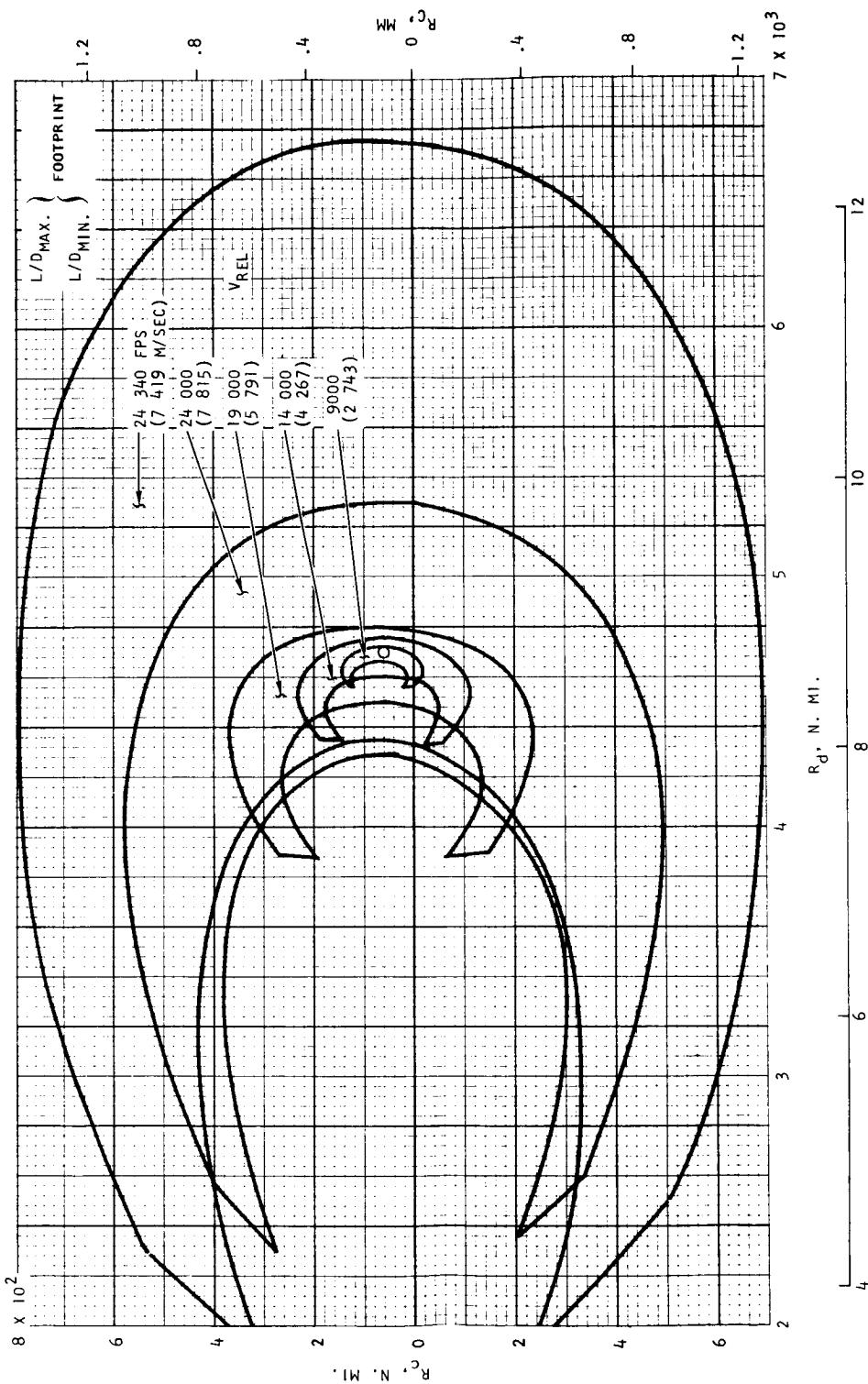
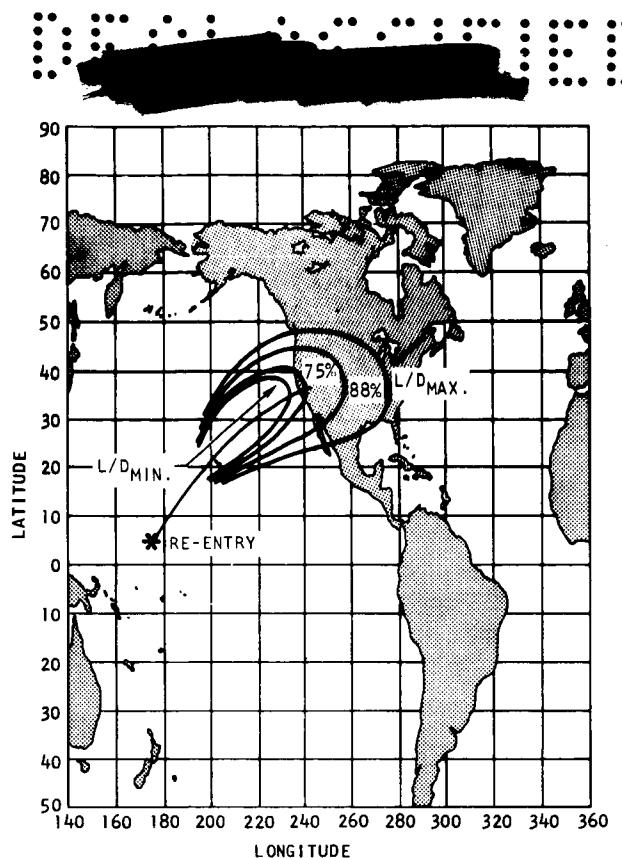


FIGURE 29--CONTINUED



m) FOOTPRINT VARIATION DURING ENTRY

FIGURE 29--CONCLUDED



a) ENTRY FOOTPRINT

b) R_c VERSUS R_d

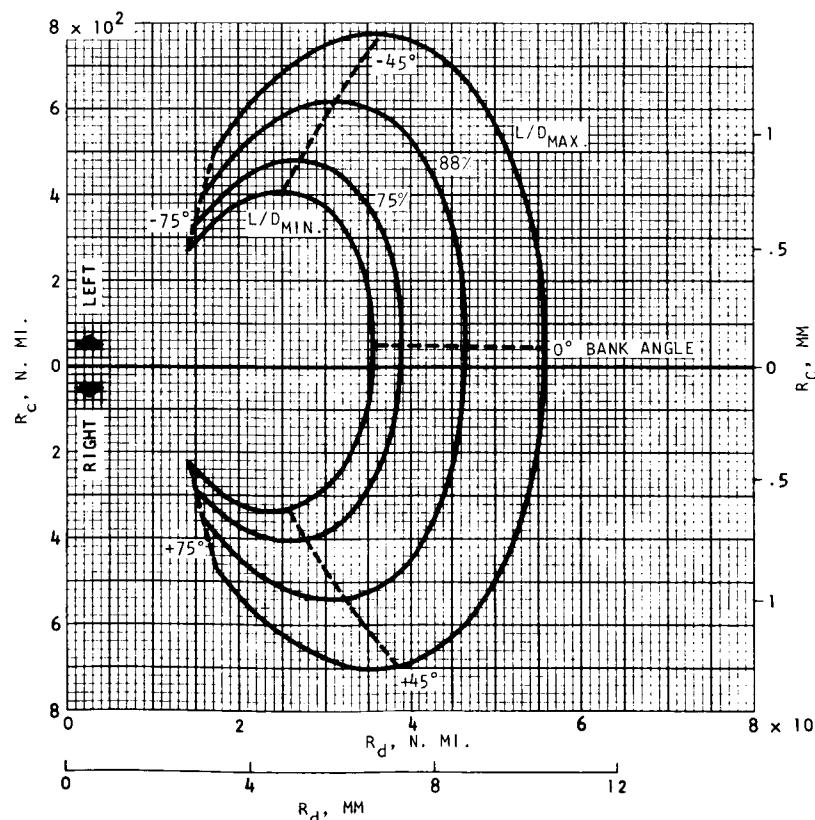
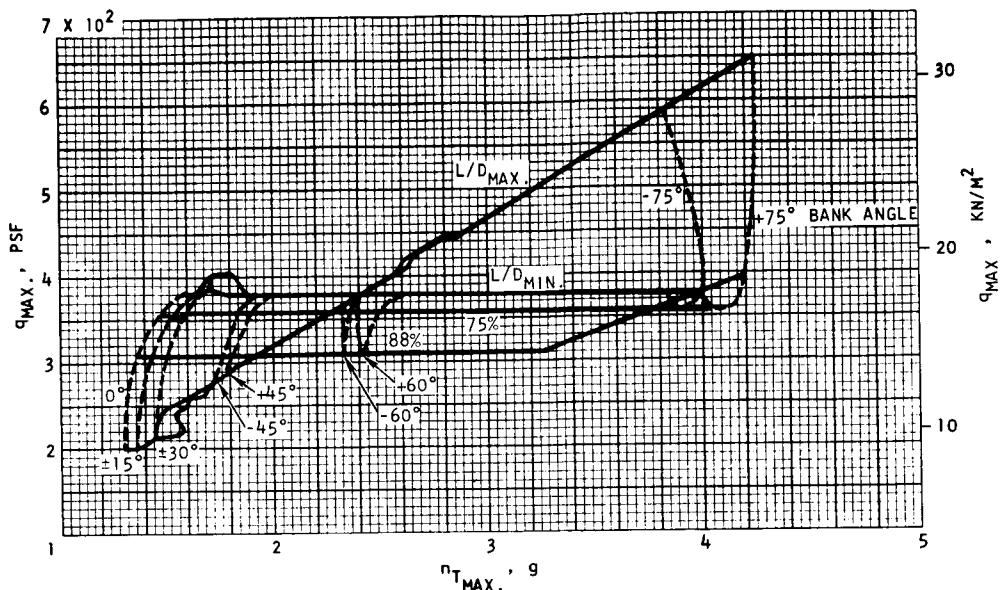
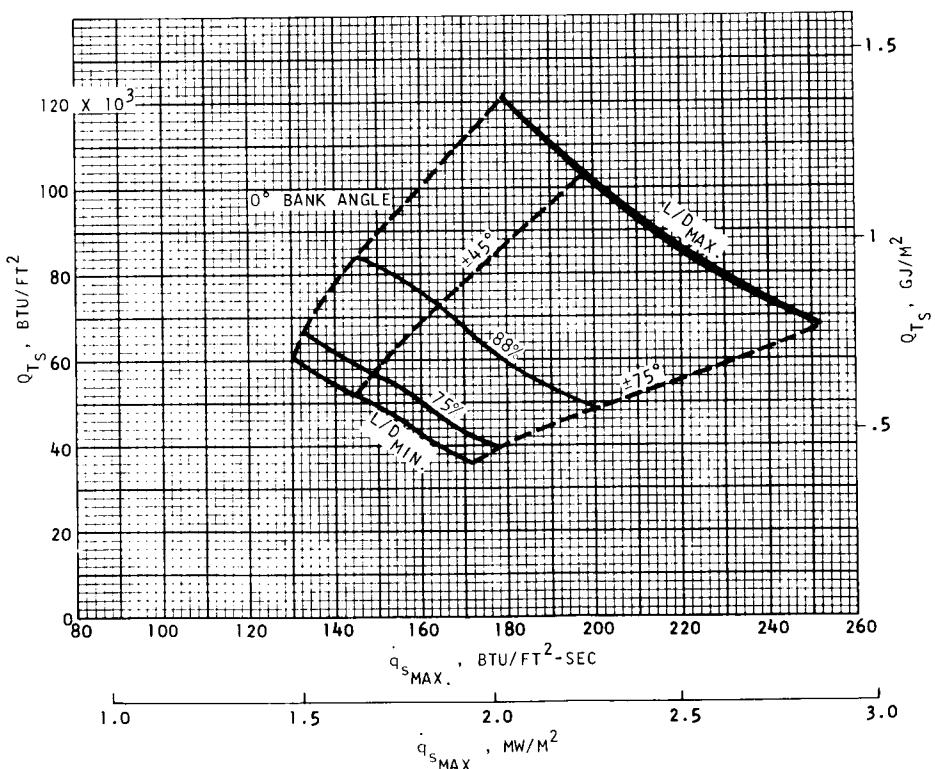


FIGURE 30. ENTRY DATA: $i = 35.7^\circ$, $\gamma = -2.0^\circ$, W/S = 50 PSF (2.39 KN/M^2)

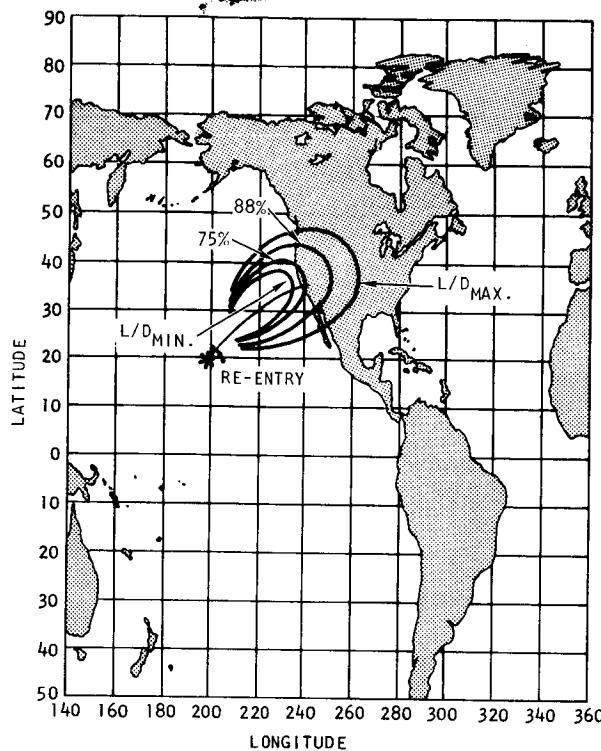


c) $q_{\text{MAX.}}$ VERSUS $n_{T_{\text{MAX.}}}$.



d) Q_{T_s} VERSUS $q_{s_{\text{MAX.}}}$.

FIGURE 30--CONCLUDED



a) ENTRY FOOTPRINT \blacktriangleleft b) R_c VERSUS R_d \blacktriangleright

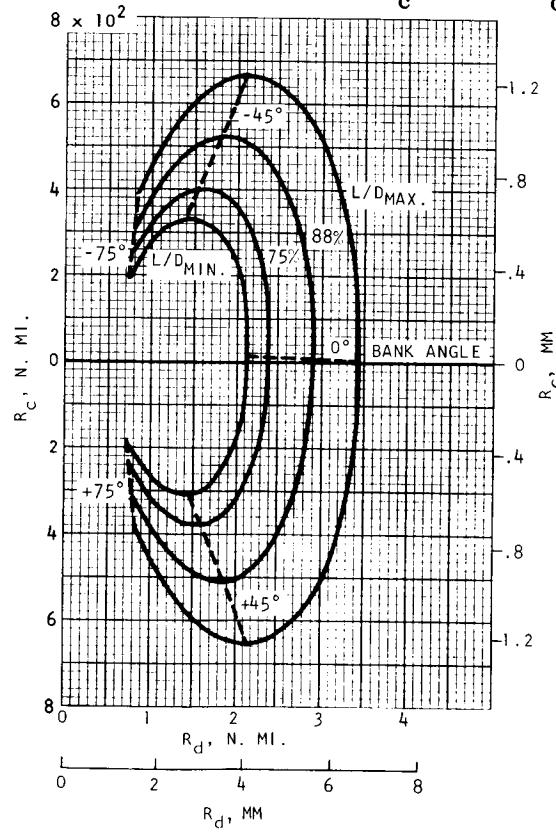
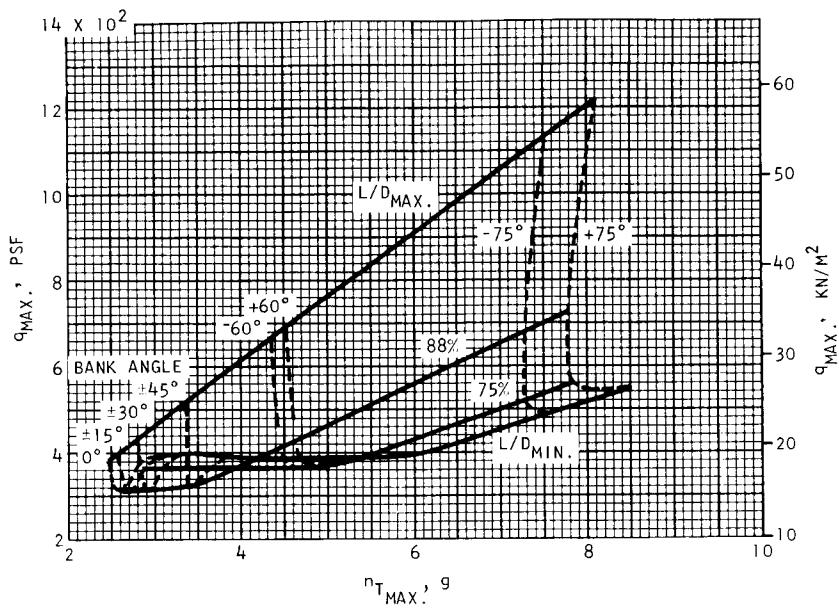
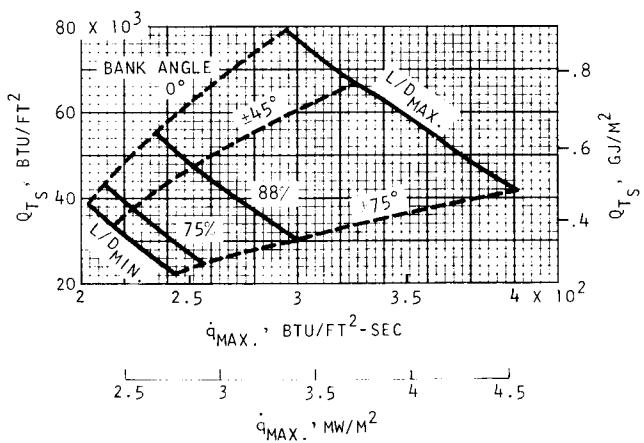


FIGURE 31--ENTRY DATA: $i = 35.7^\circ$, $\gamma = -4.0^\circ$, W/S = 50 PSF (2.39 KN/M^2)



c) $q_{MAX.}$ VERSUS $n_{T_{MAX.}}$.



d) Q_{T_s} VERSUS $q_{s_{MAX.}}$.

FIGURE 31--CONCLUDED

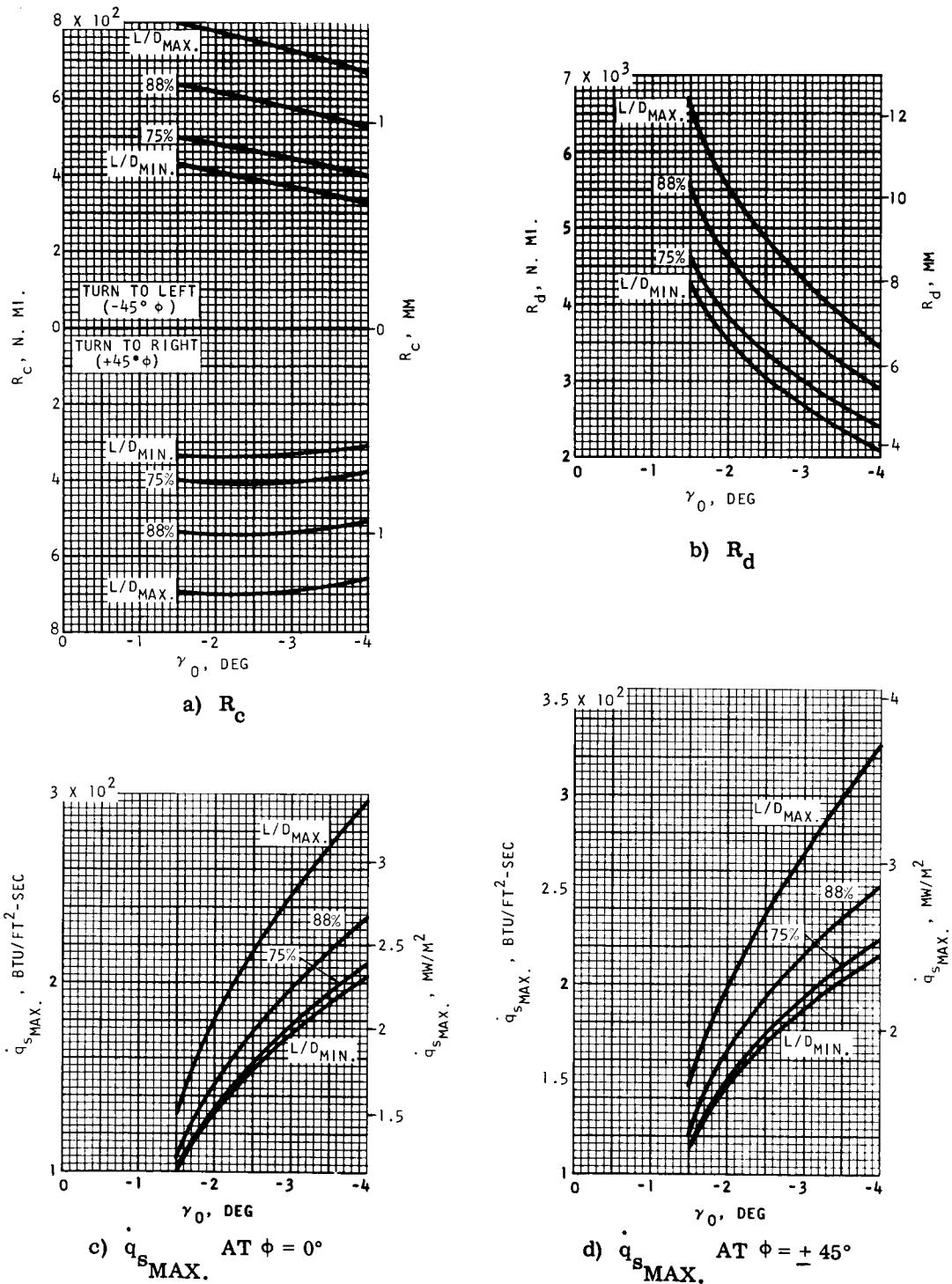
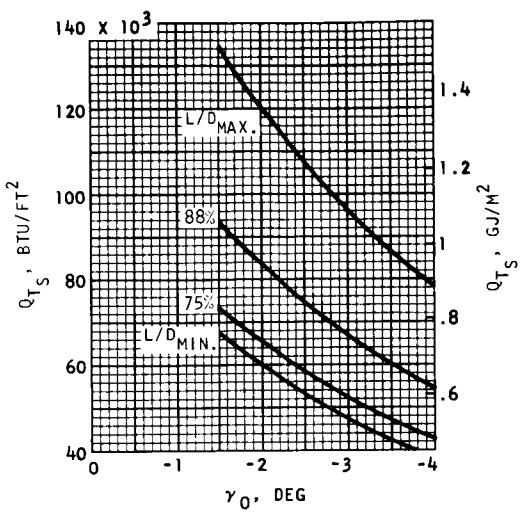
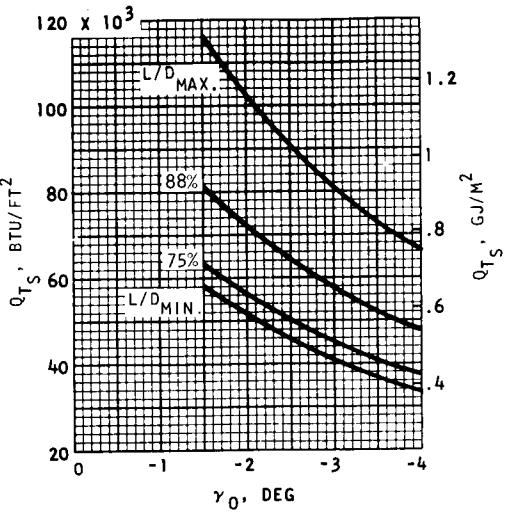


FIGURE 32. VARIATIONS OF TRAJECTORY PARAMETERS WITH ENTRY ANGLE--

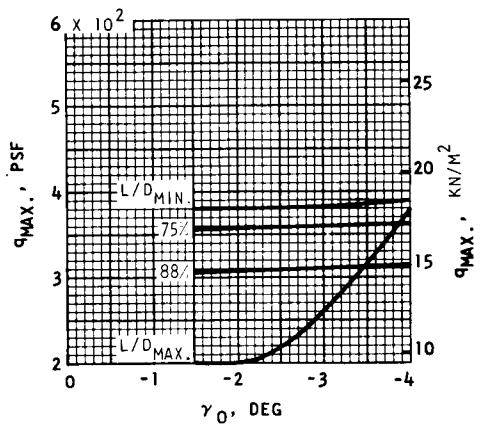
$$i = 35.7^\circ, W/S = 50 \text{ PSF (2.39 KN/M}^2)$$



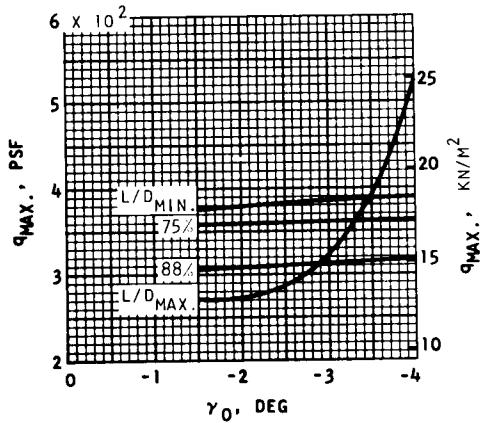
e) Q_{TS} AT $\phi = 0^\circ$



f) Q_{TS} AT $\phi = \pm 45^\circ$



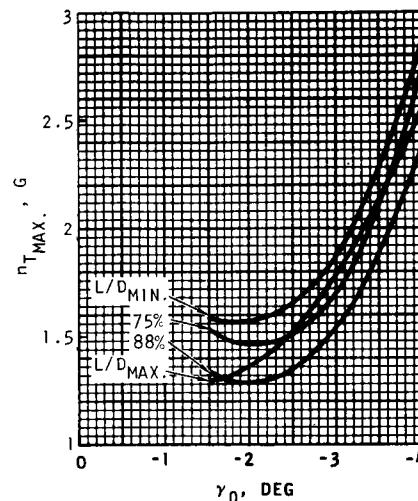
g) q_{MAX} AT $\phi = 0^\circ$



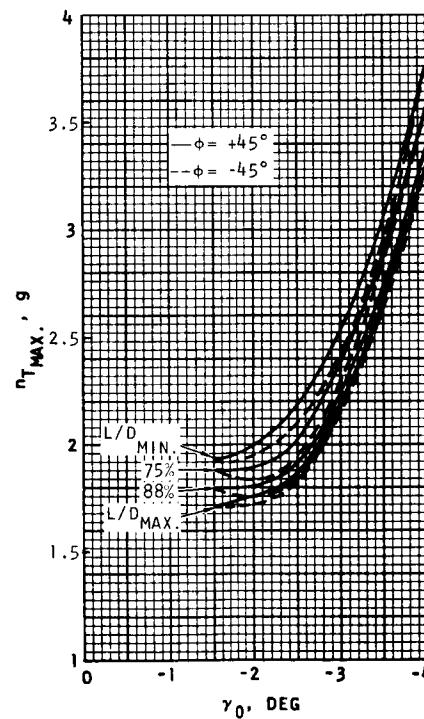
h) q_{MAX} AT $\phi = \pm 45^\circ$

FIGURE 32.--CONTINUED

DECODING CONCLUDED

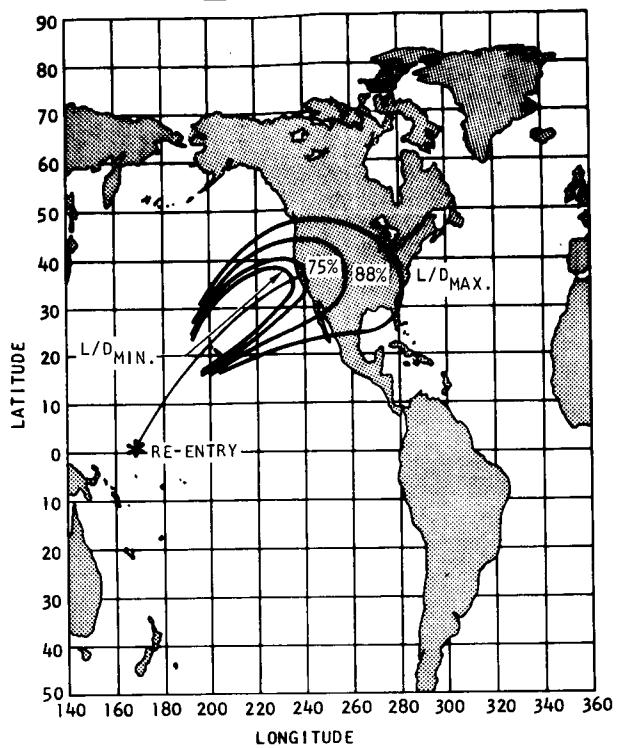


i) $n_T \text{ MAX.}$ AT $\phi = 0^\circ$



j) $n_T \text{ MAX.}$ AT $\phi = \pm 45^\circ$

FIGURE 32. --CONCLUDED



a) ENTRY FOOTPRINT

b) R_c VERSUS R_d

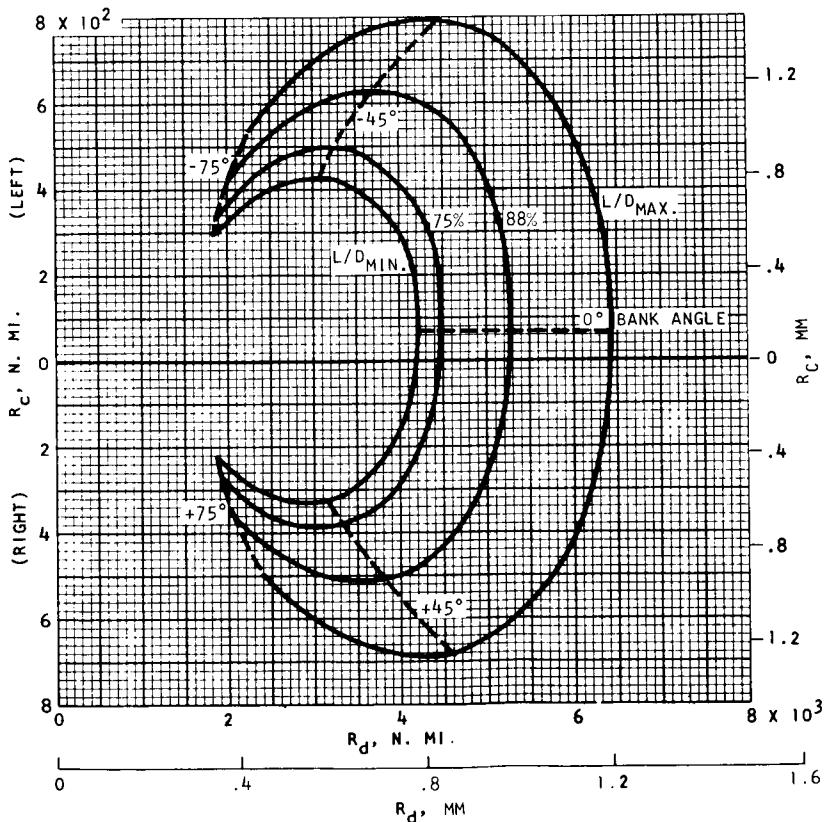
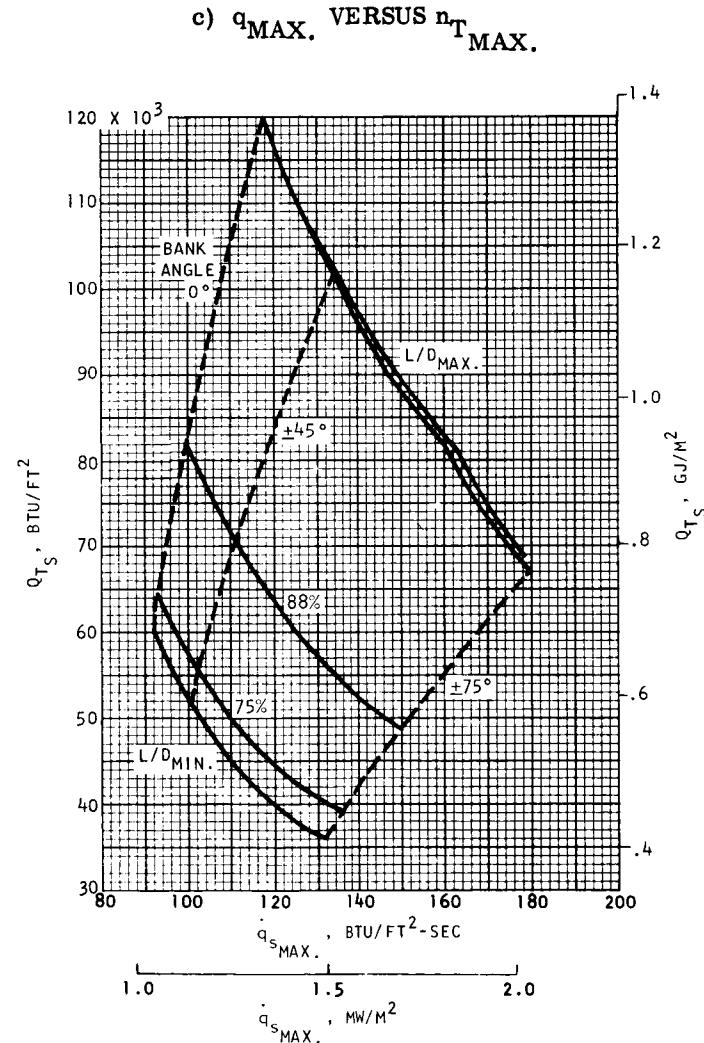
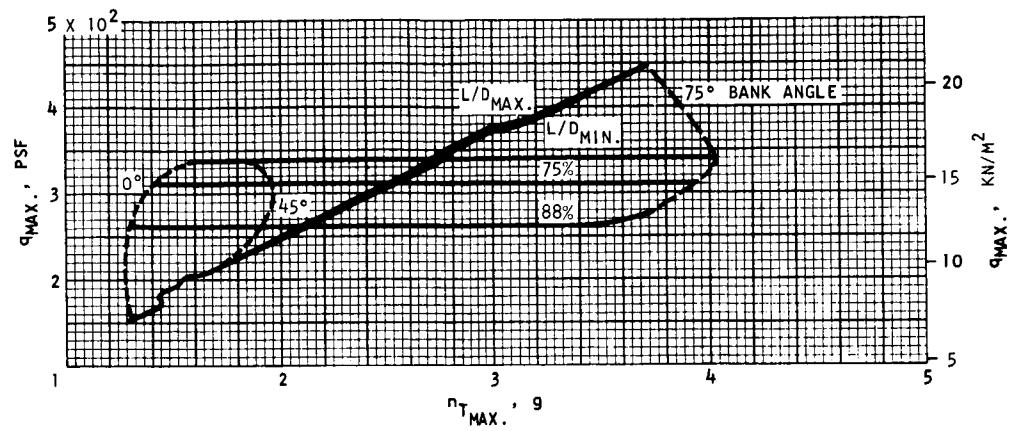
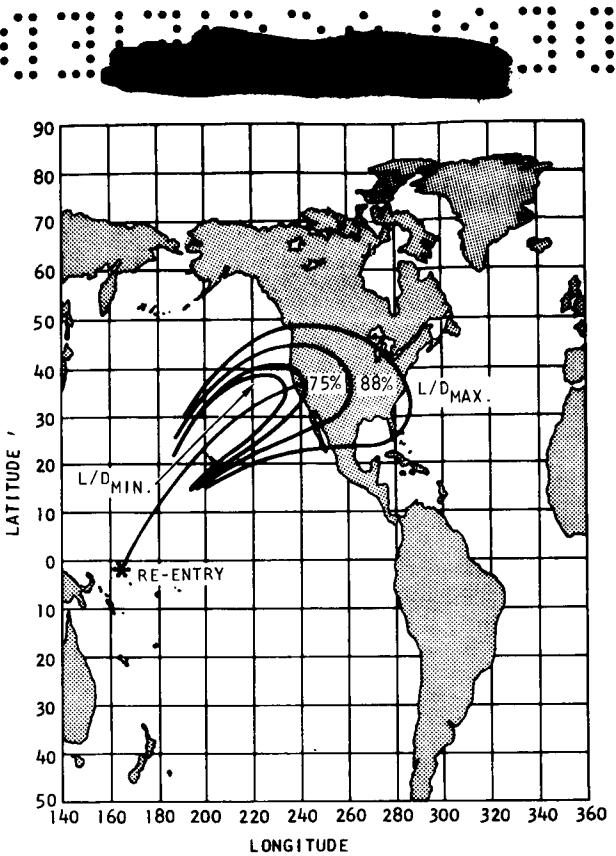


FIGURE 33. ENTRY DATA: $i = 35.7^\circ$, $\gamma = -1.5^\circ$, W/S = 40 PSF (1.92 KN/M²)



d) Q_{T_s} VERSUS $q_{s_{\text{MAX.}}}$.

FIGURE 33. --CONCLUDED



a) ENTRY FOOTPRINT

b) R_c VERSUS R_d

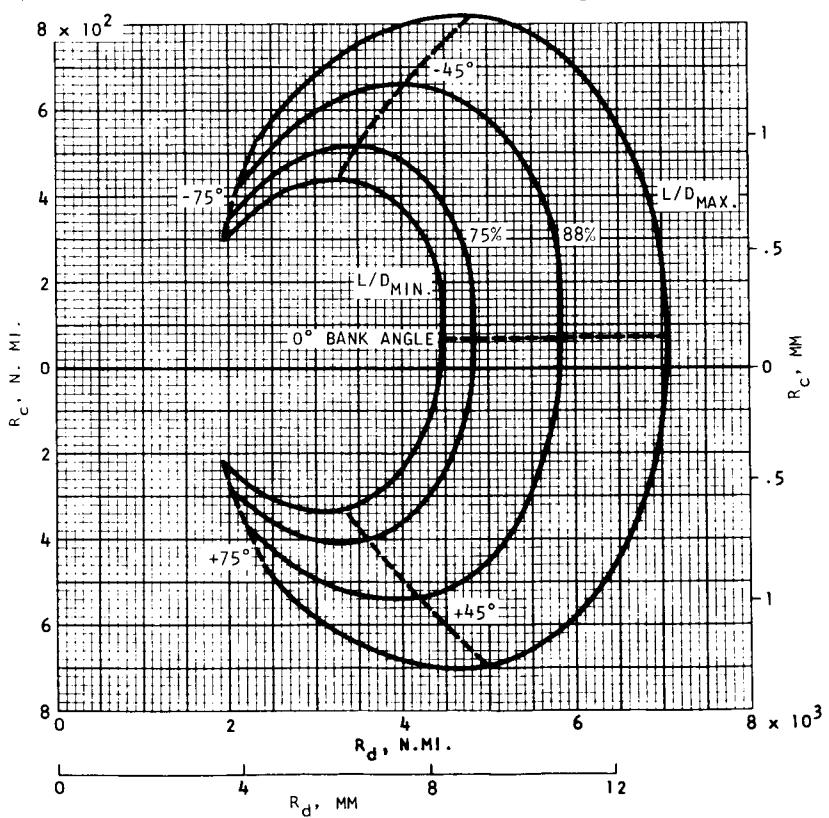
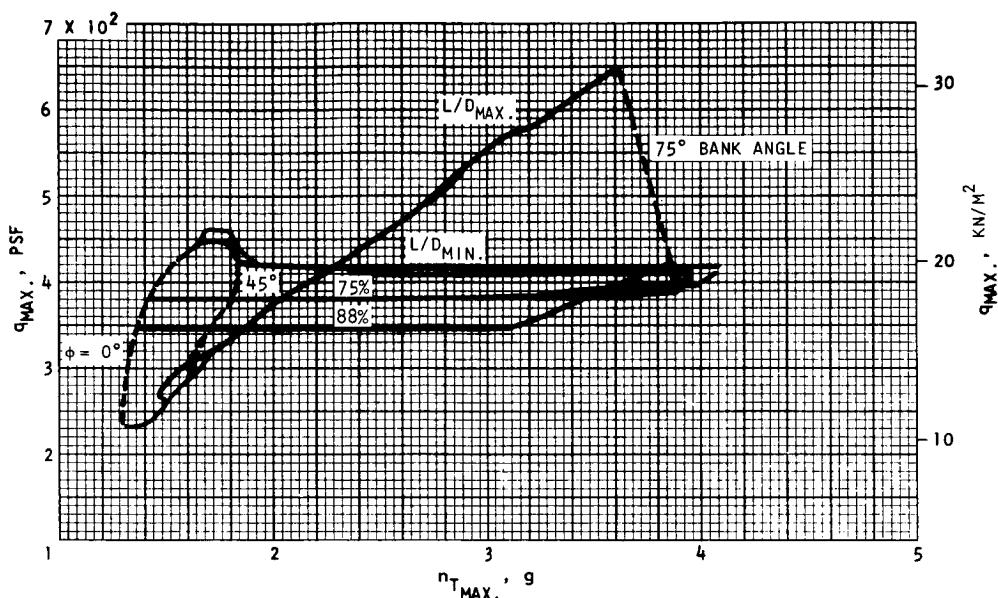
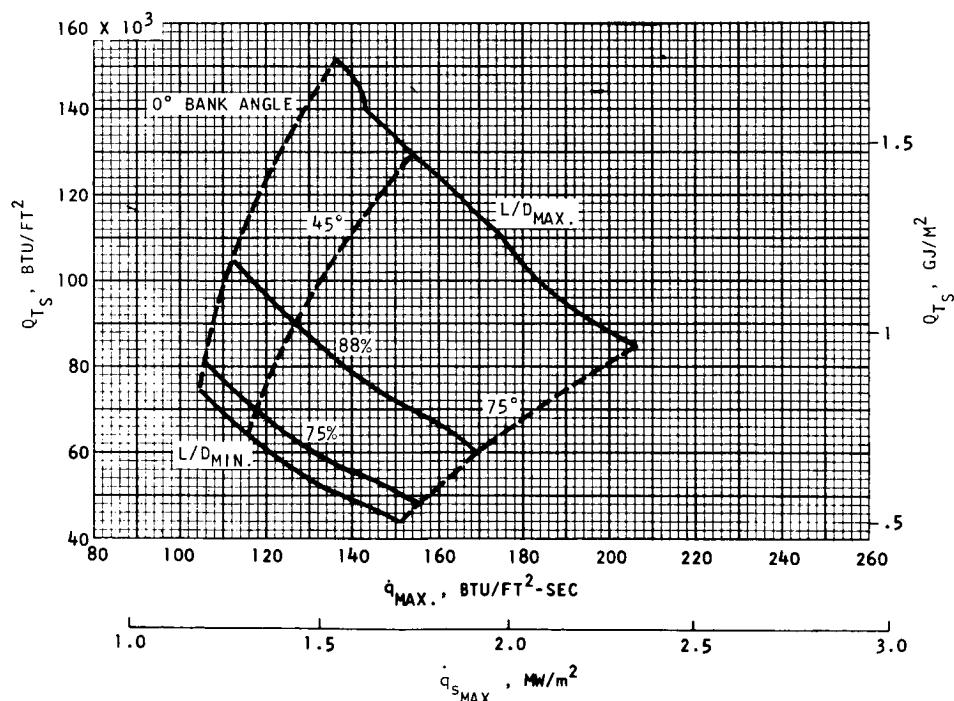


FIGURE 34. ENTRY DATA: $i = 35.7^\circ$, $\gamma = -1.5^\circ$, W/S = 60 PSF (2.87 KN/M^2)

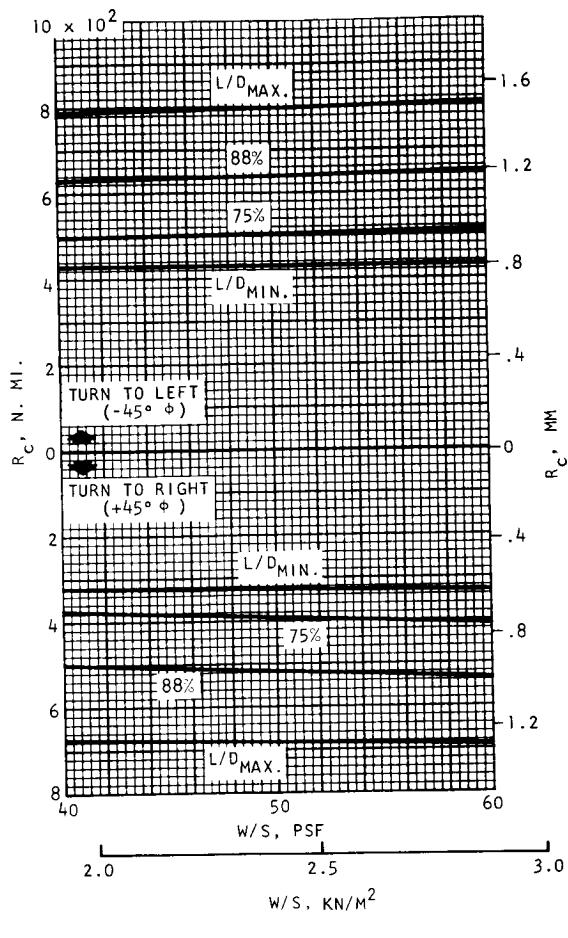


c) $q_{MAX.}$ VERSUS $n_{T_{MAX.}}$

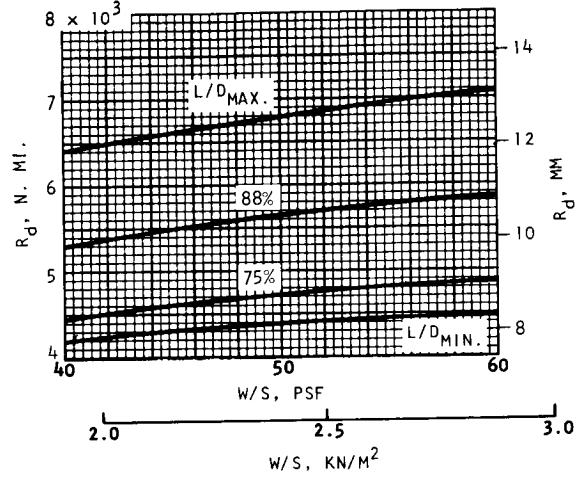


d) Q_{T_S} VERSUS $q_{s_{MAX.}}$

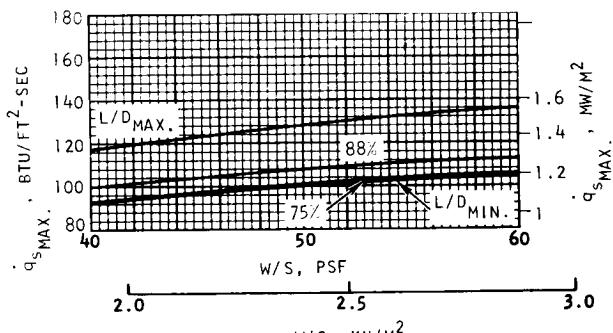
FIGURE 34.--CONCLUDED



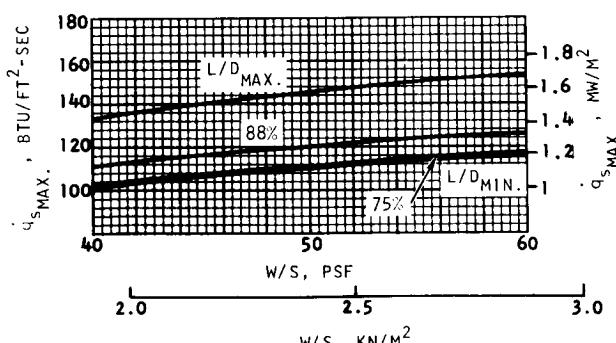
a) R_c



b) R_d



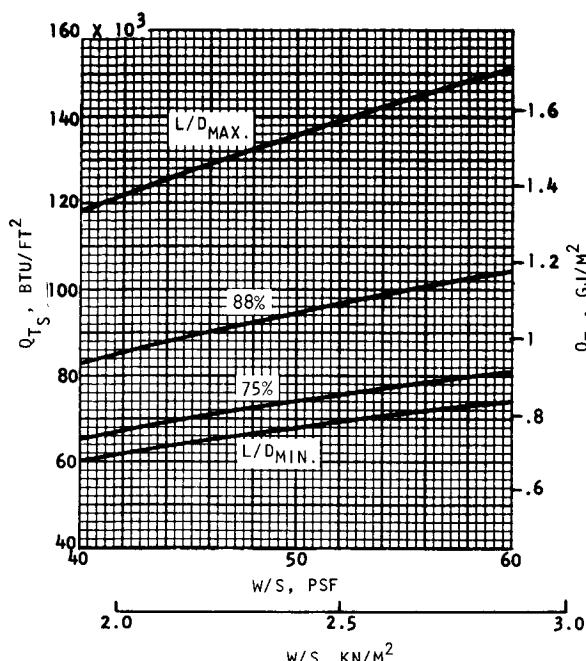
c) $q_s MAX.$ AT $\phi = 0^\circ$



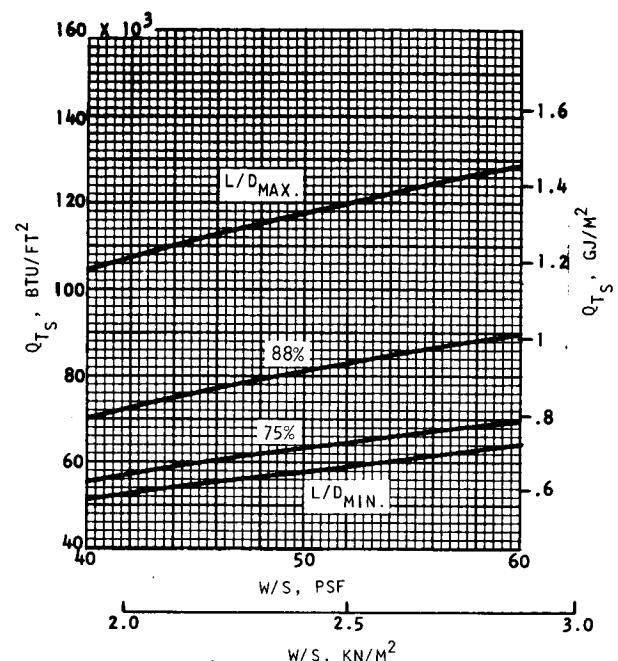
d) $q_s MAX.$ AT $\phi = \pm 45^\circ$

FIGURE 35. VARIATIONS OF TRAJECTORY PARAMETERS WITH WING LOADING--

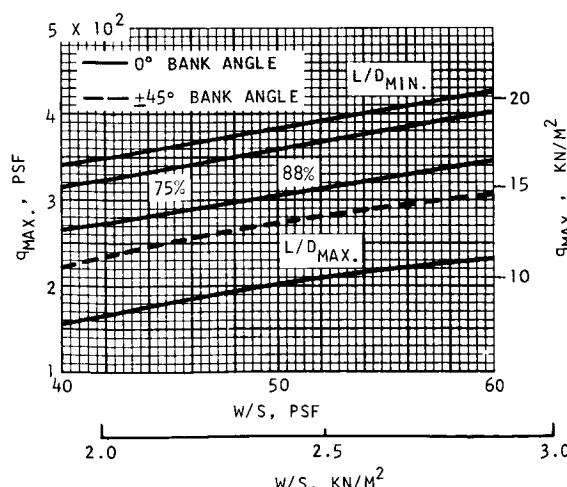
$$i = 35.7^\circ, \gamma = -1.5^\circ$$



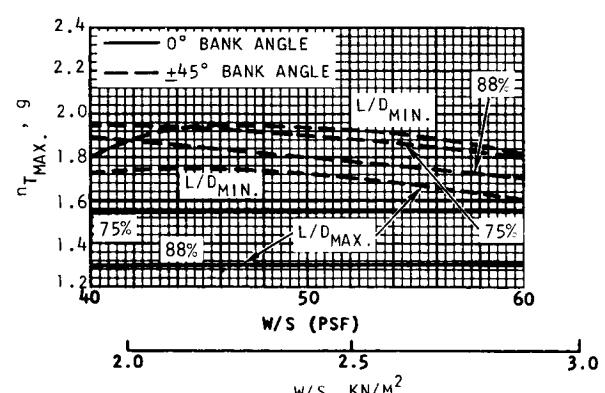
e) Q_{TS} AT $\phi = 0$



f) Q_{TS} AT $\phi = \pm 45^\circ$

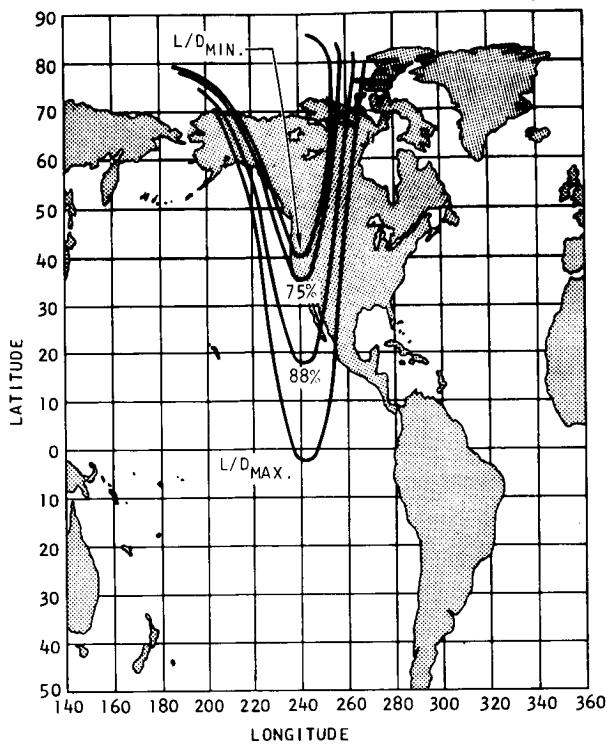


g) $q_{MAX.}$



h) $n_{T MAX.}$

FIGURE 35.--CONCLUDED



a) ENTRY FOOTPRINT

b) R_c VERSUS R_d

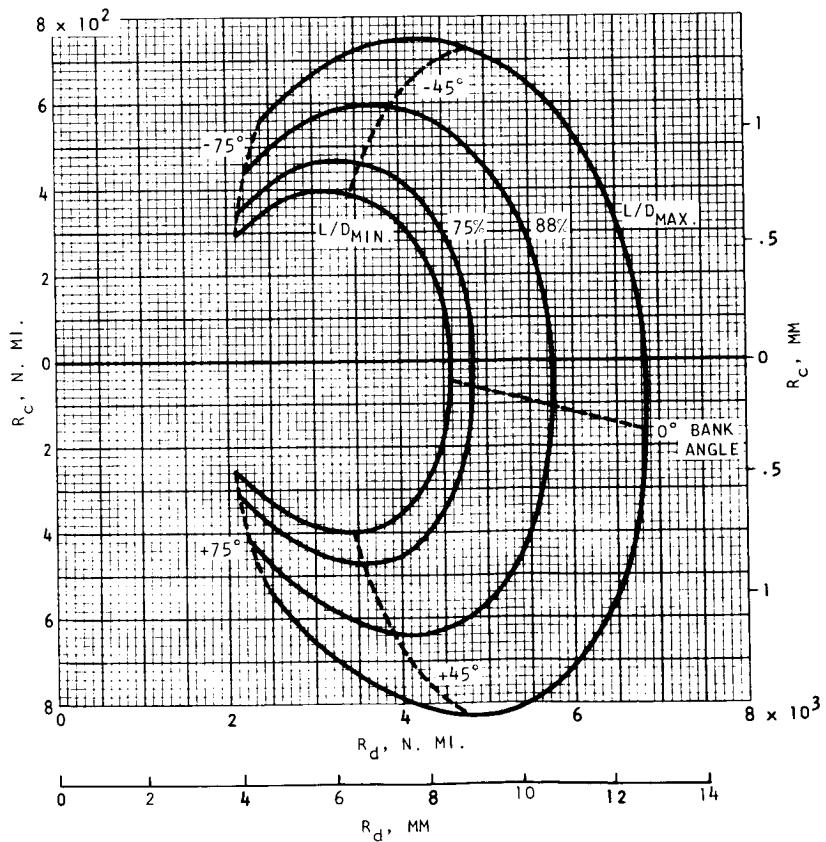
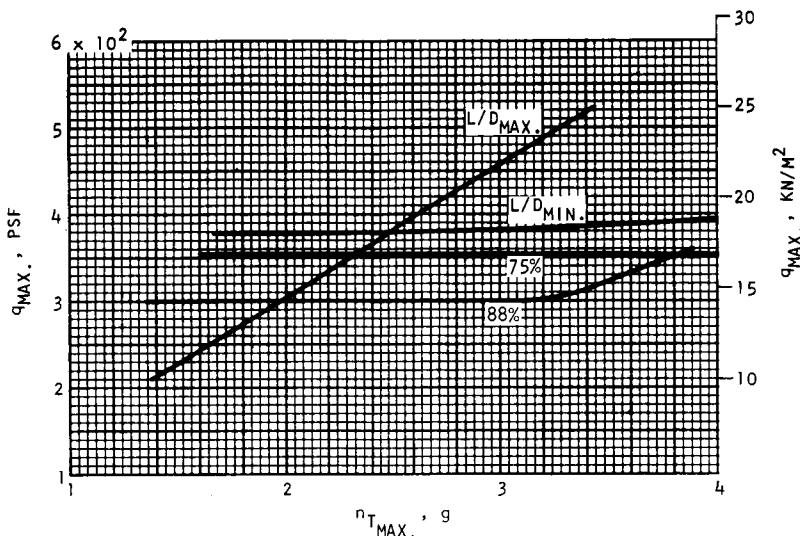
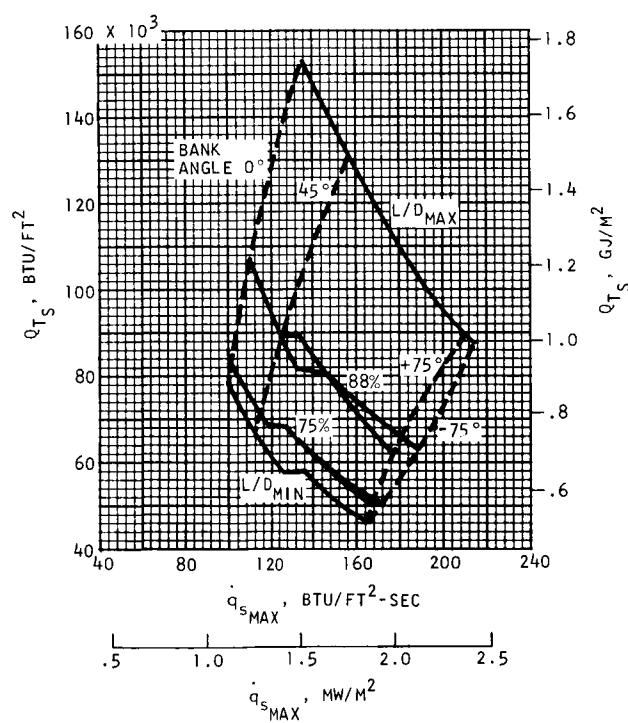


FIGURE 36. ENTRY DATA: $i = 85^\circ$, $\gamma = -1.5^\circ$, W/S = 50 PSF (2.39 KN/M^2)



c) $q_{MAX.}$ VERSUS $n_{T_{MAX.}}$.



d) Q_{T_S} VERSUS $\dot{q}_{s_{MAX.}}$.

FIGURE 36.--CONCLUDED.

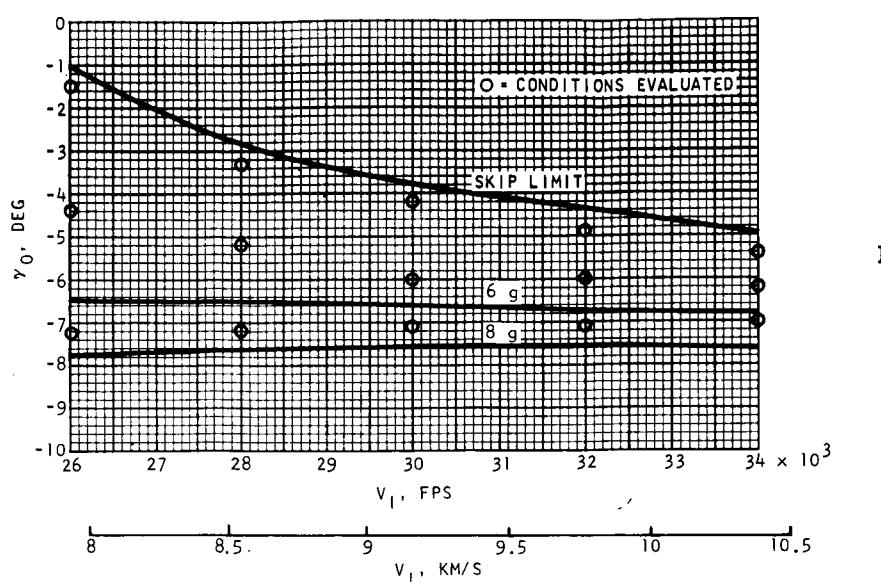
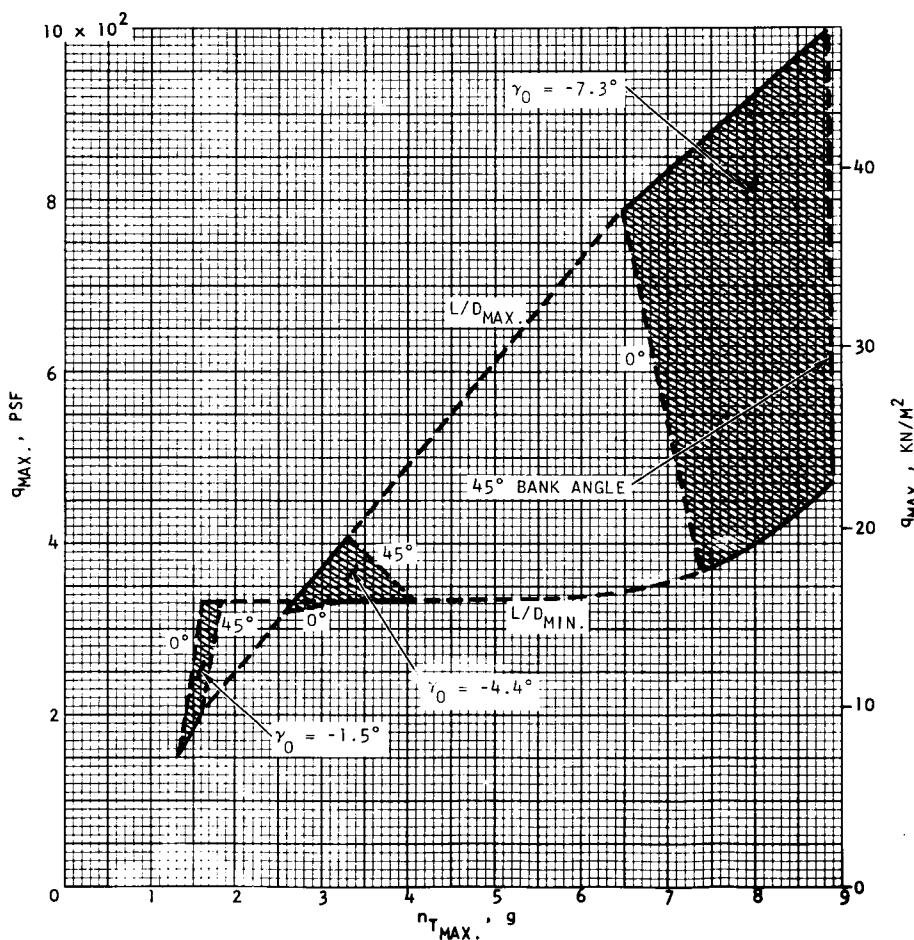
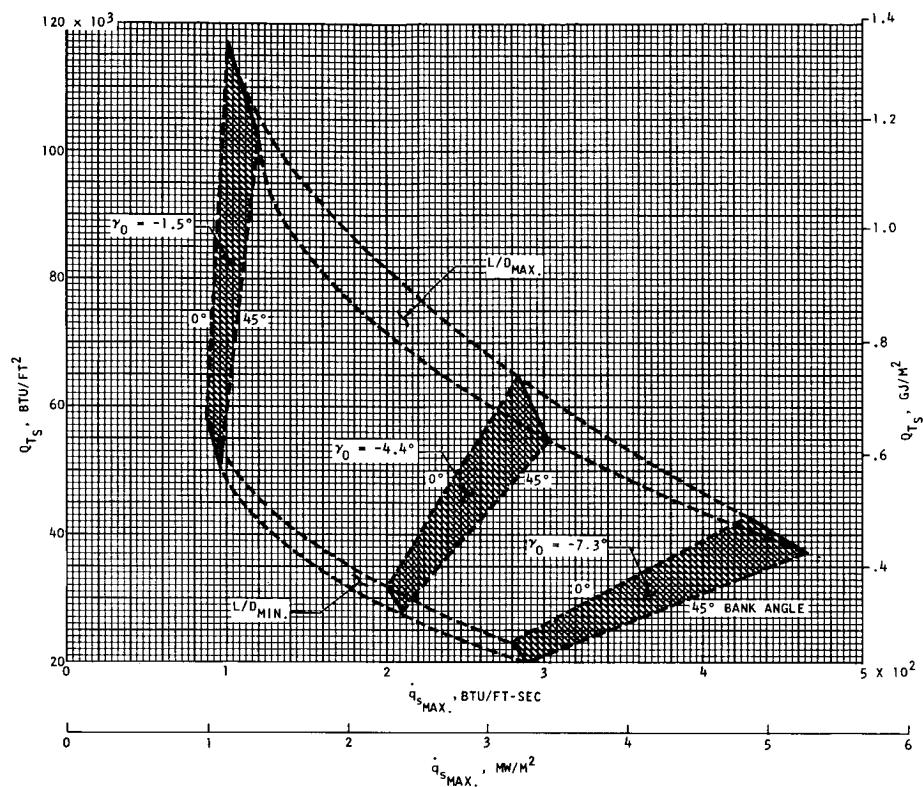


FIGURE 37.
ENTRY CORRIDOR
AT $L/D_{\text{MIN.}}$,
 0° BANK ANGLE

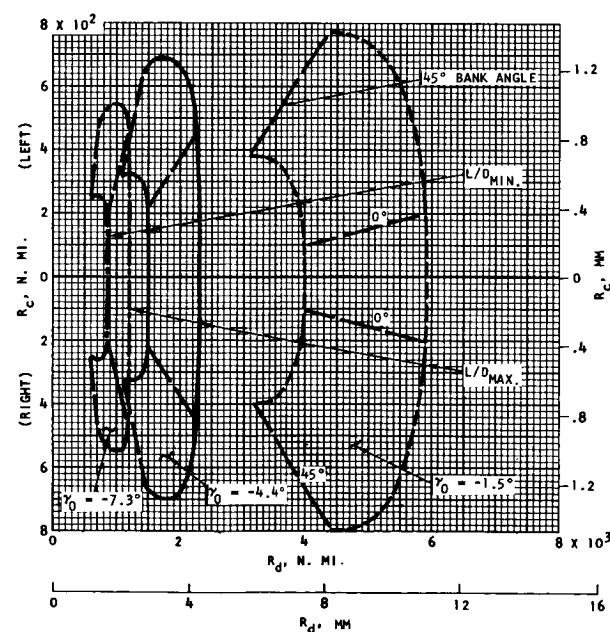


a) $q_{\text{MAX.}}$ VERSUS $n_{T_{\text{MAX.}}}$.

FIGURE 38. ENTRY DATA: $V_I = 26000$ FPS (7.93 KM/SEC)



b) Q_{TS} VERSUS $q_s \text{MAX.}$



c) R_c VERSUS R_d

FIGURE 38. --CONTINUED

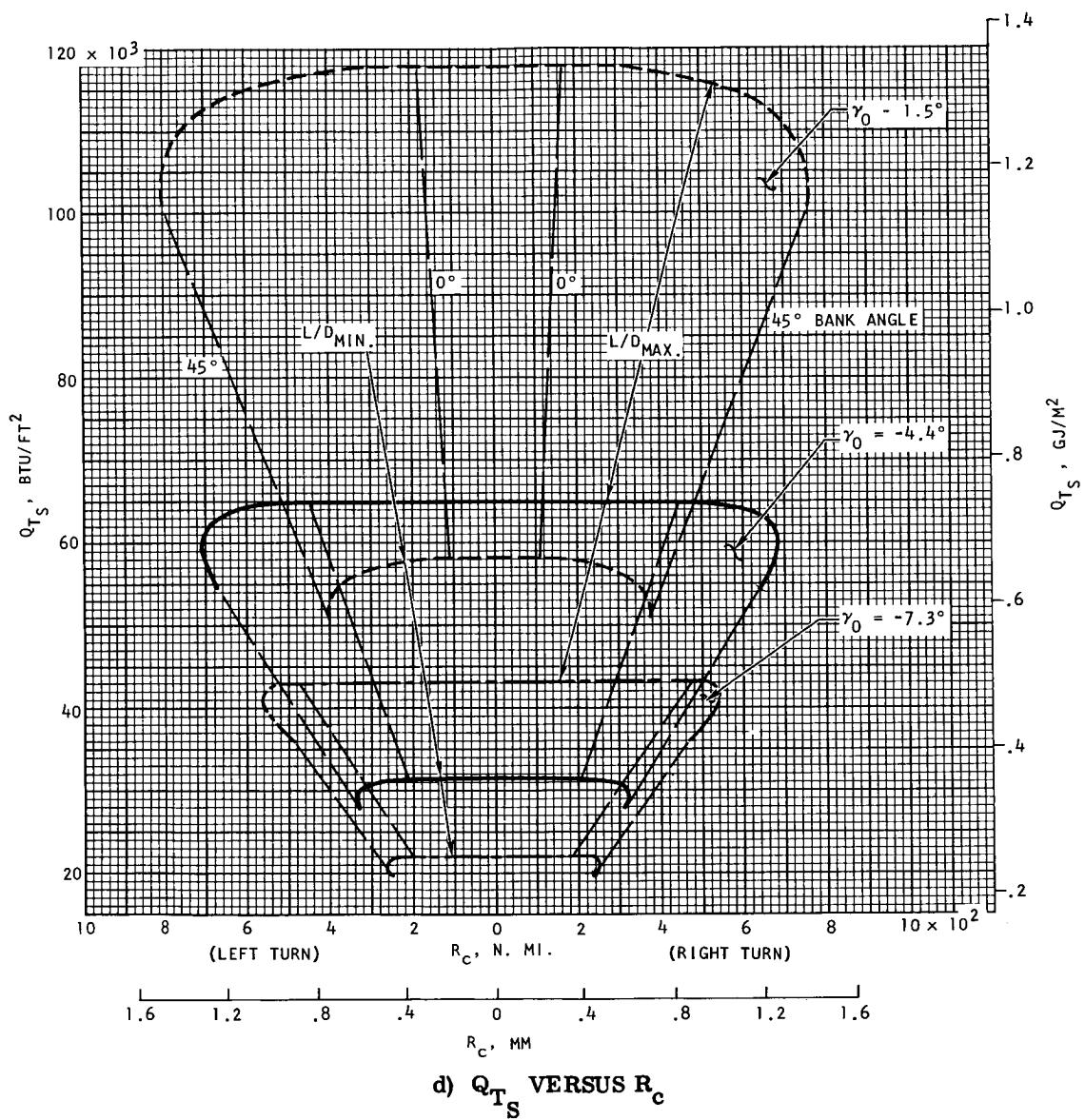
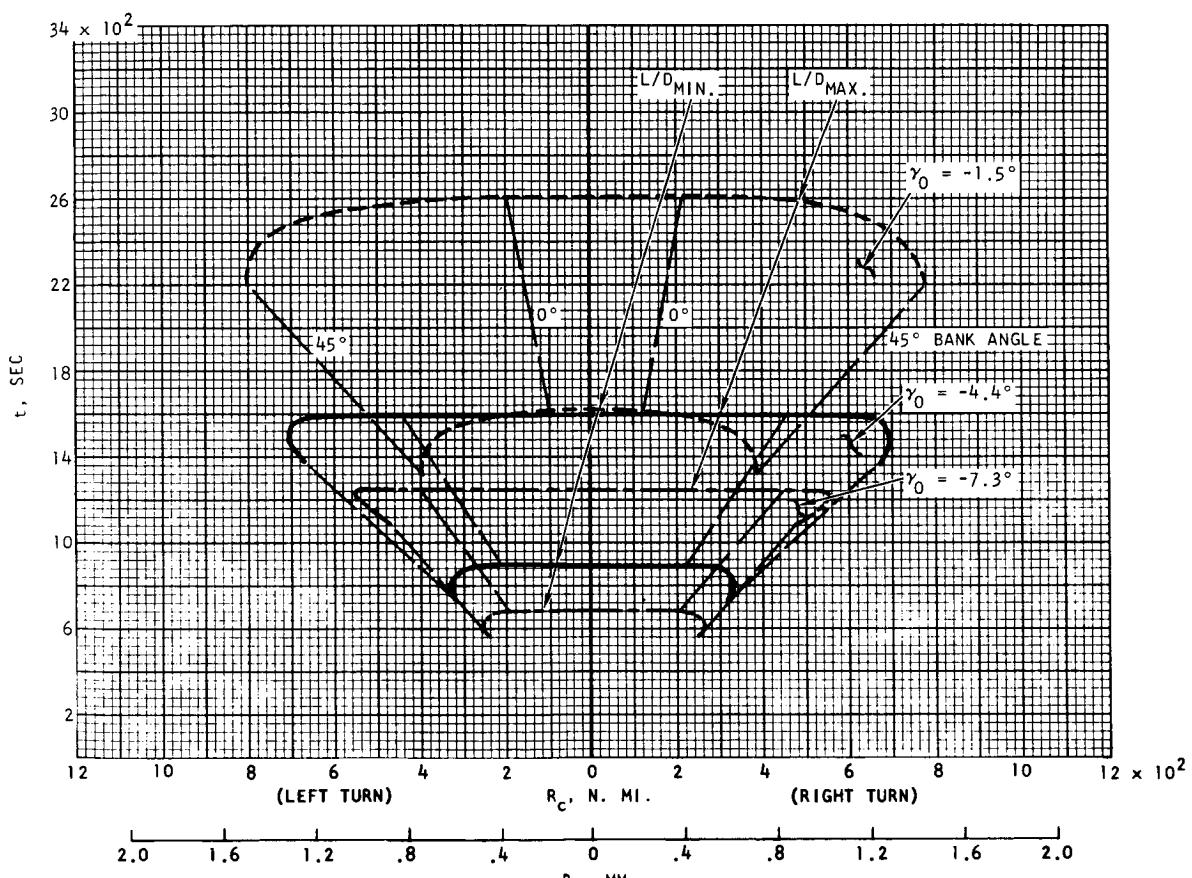
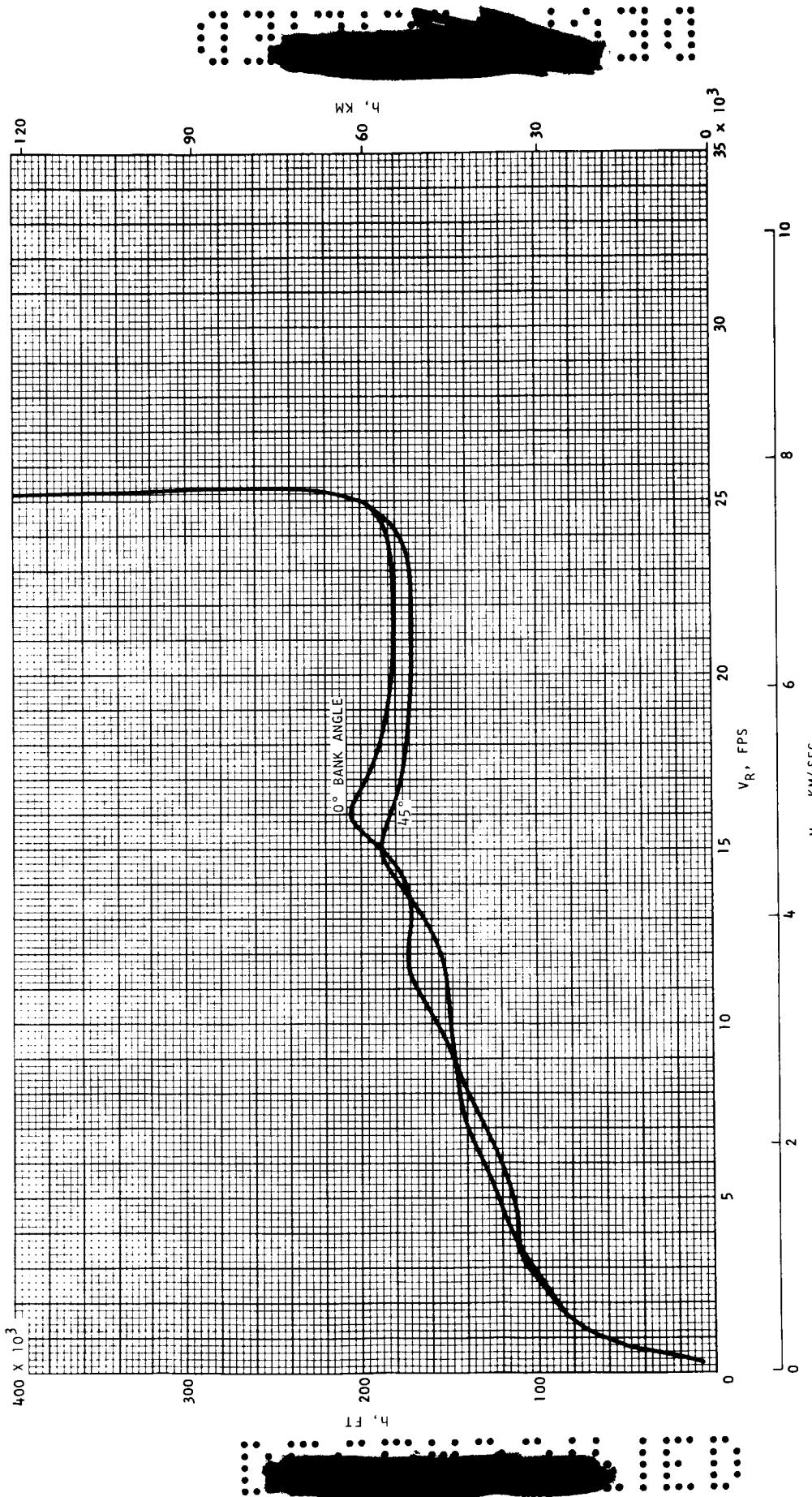


FIGURE 38.--CONTINUED



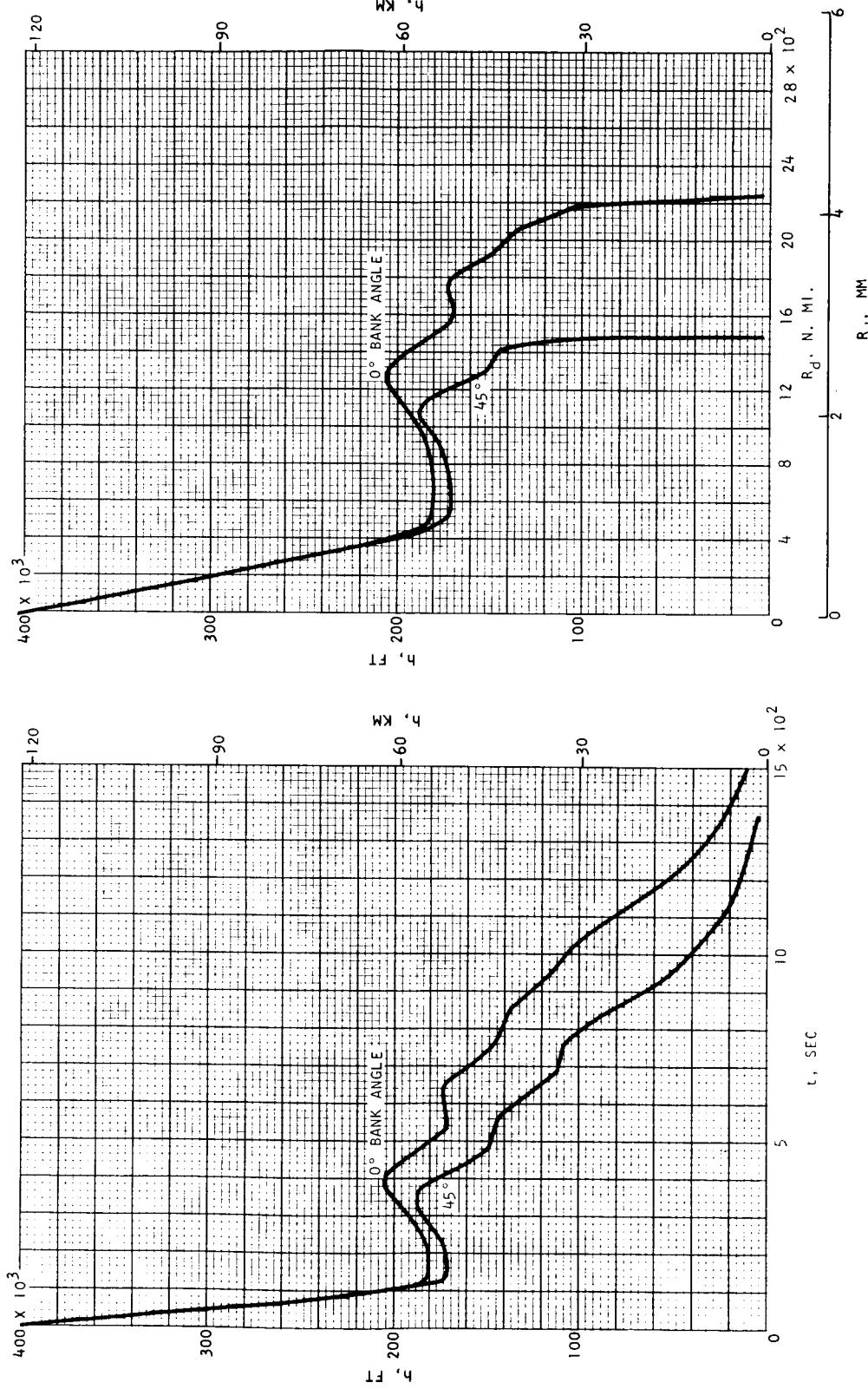
e) t VERSUS R_c

FIGURE 38.--CONTINUED



f-1) h VERSUS V_R FOR $\gamma = -4.4^\circ$ AND L/D_{MAX} .

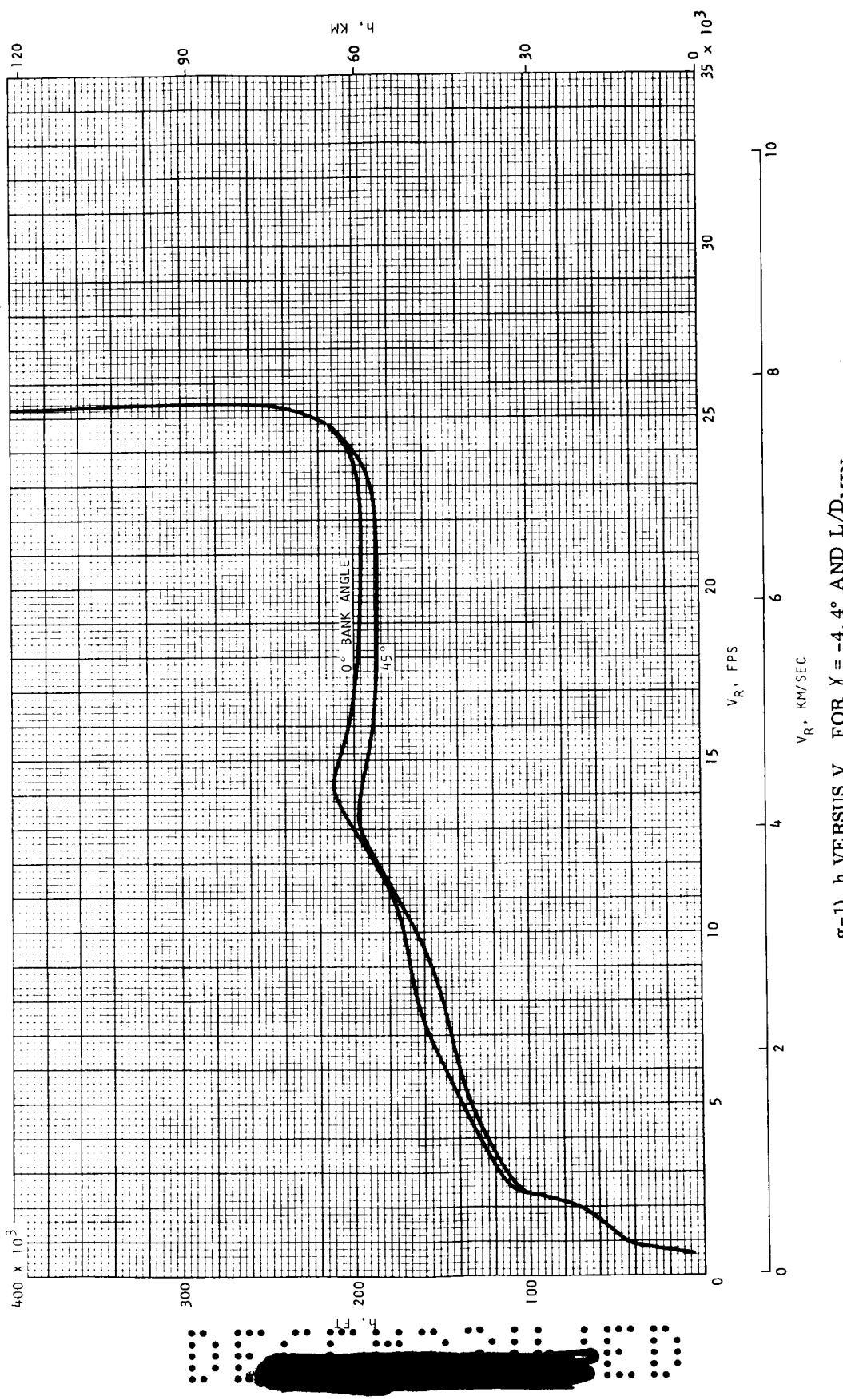
FIGURE 38. --CONTINUED



ER 14471-3

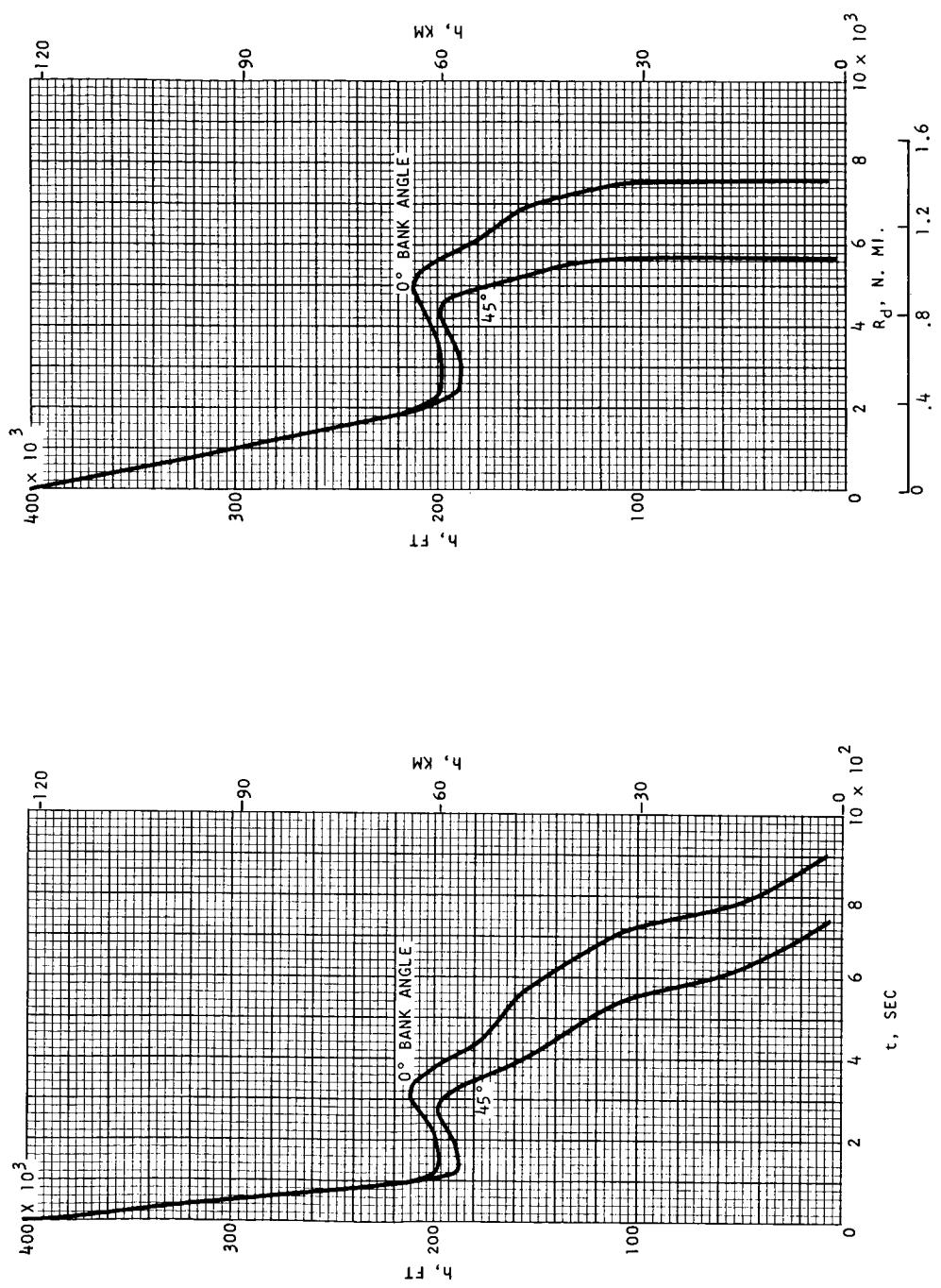
f-2) h VERSUS t FOR $\gamma = -4, 4^\circ$ AND L/D_{MAX} .

FIGURE 38.--CONTINUED



g-1) h VERSUS V_R FOR $\gamma = -4.4^\circ$ AND L/D_{MIN} .

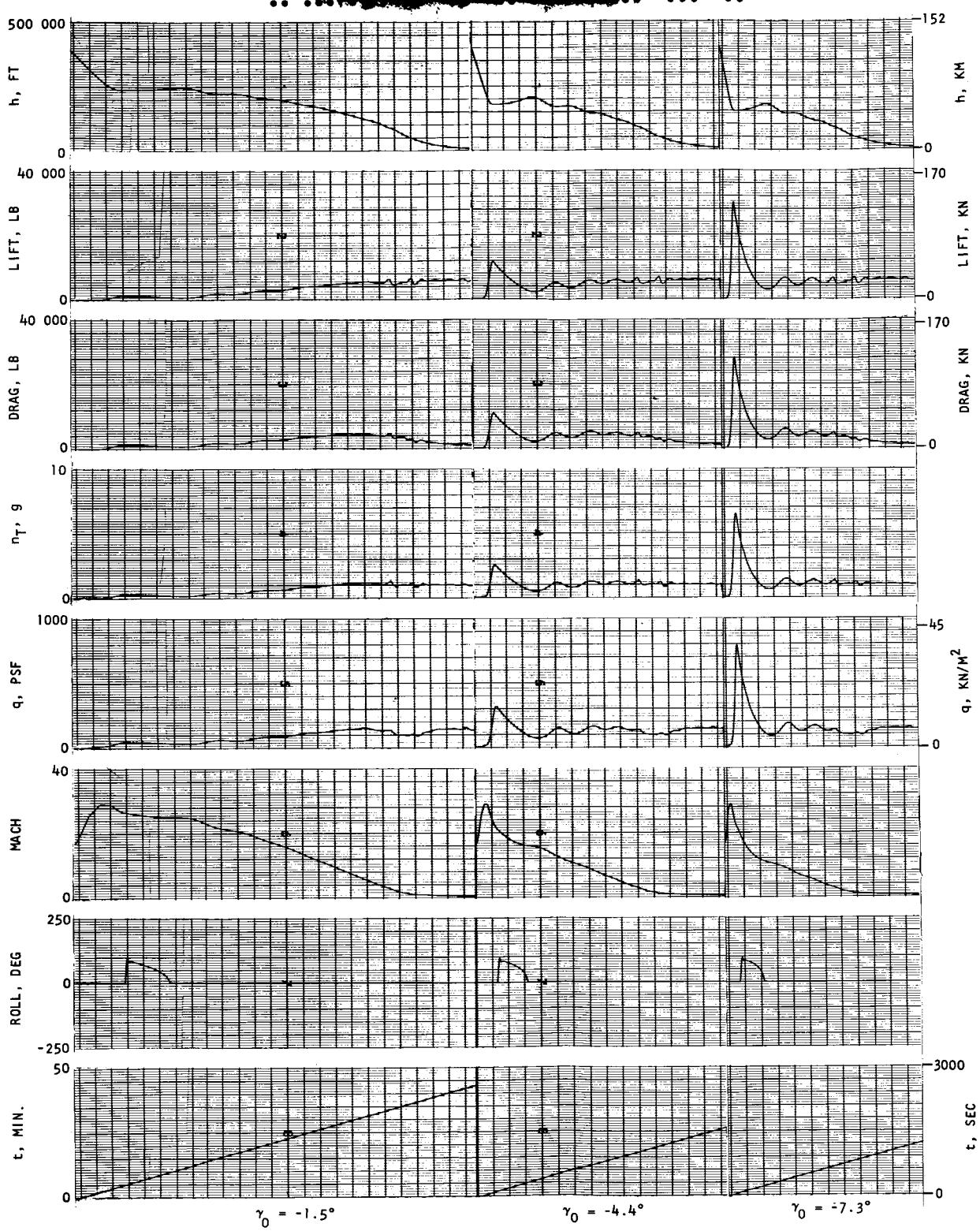
FIGURE 38. --CONTINUED



g-2) h VERSUS t FOR $\gamma = -4.4^\circ$ AND L/D_{MIN} .

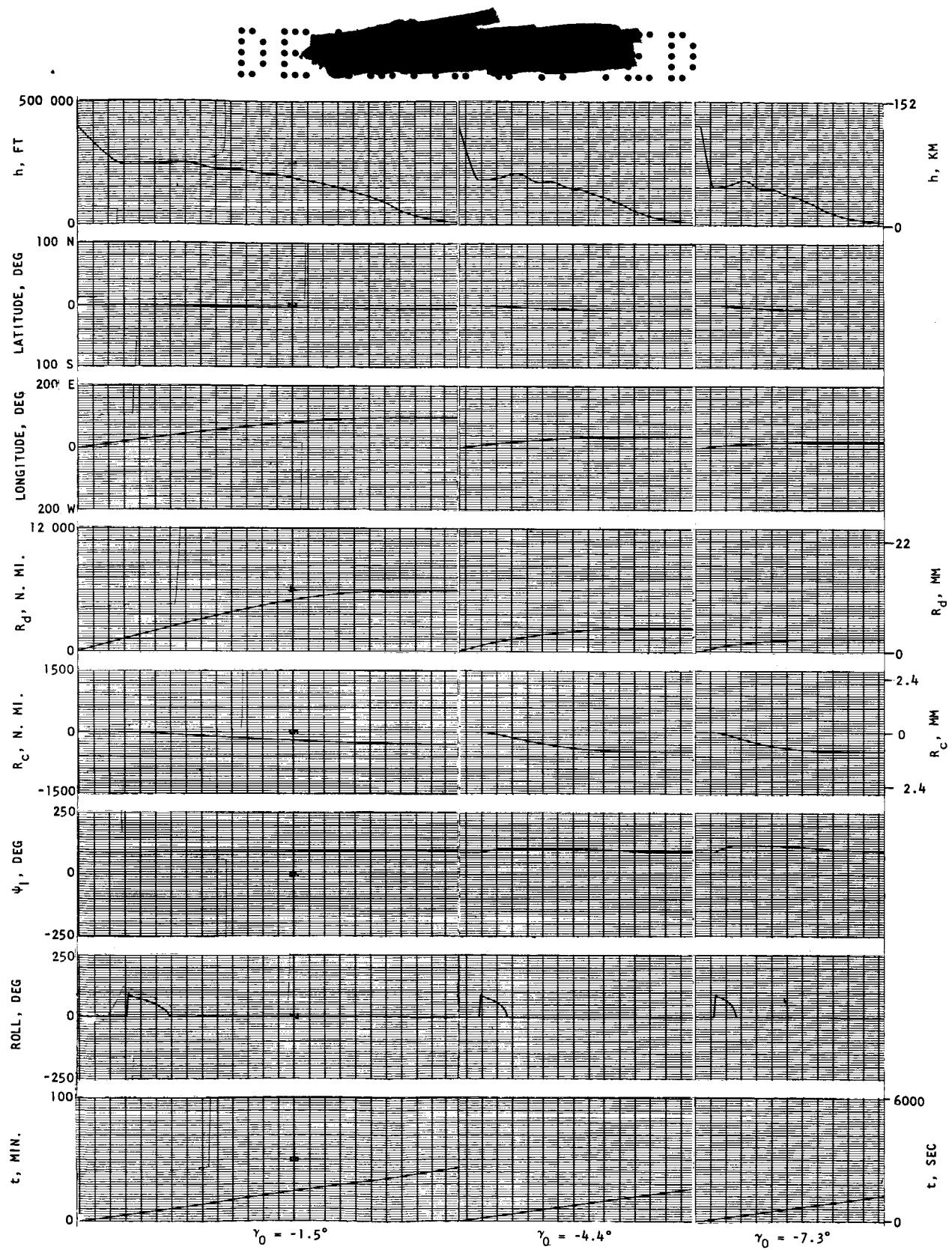
g-3) h VERSUS R_d FOR $\gamma = -4.4^\circ$ AND L/D_{MIN} .

FIGURE 38. --CONTINUED



h) STRIP RECORDER DATA--L/D_{MAX.}, $\phi = 0^\circ$

FIGURE 38.--CONTINUED



h) CONTINUED

FIGURE 38.--CONTINUED

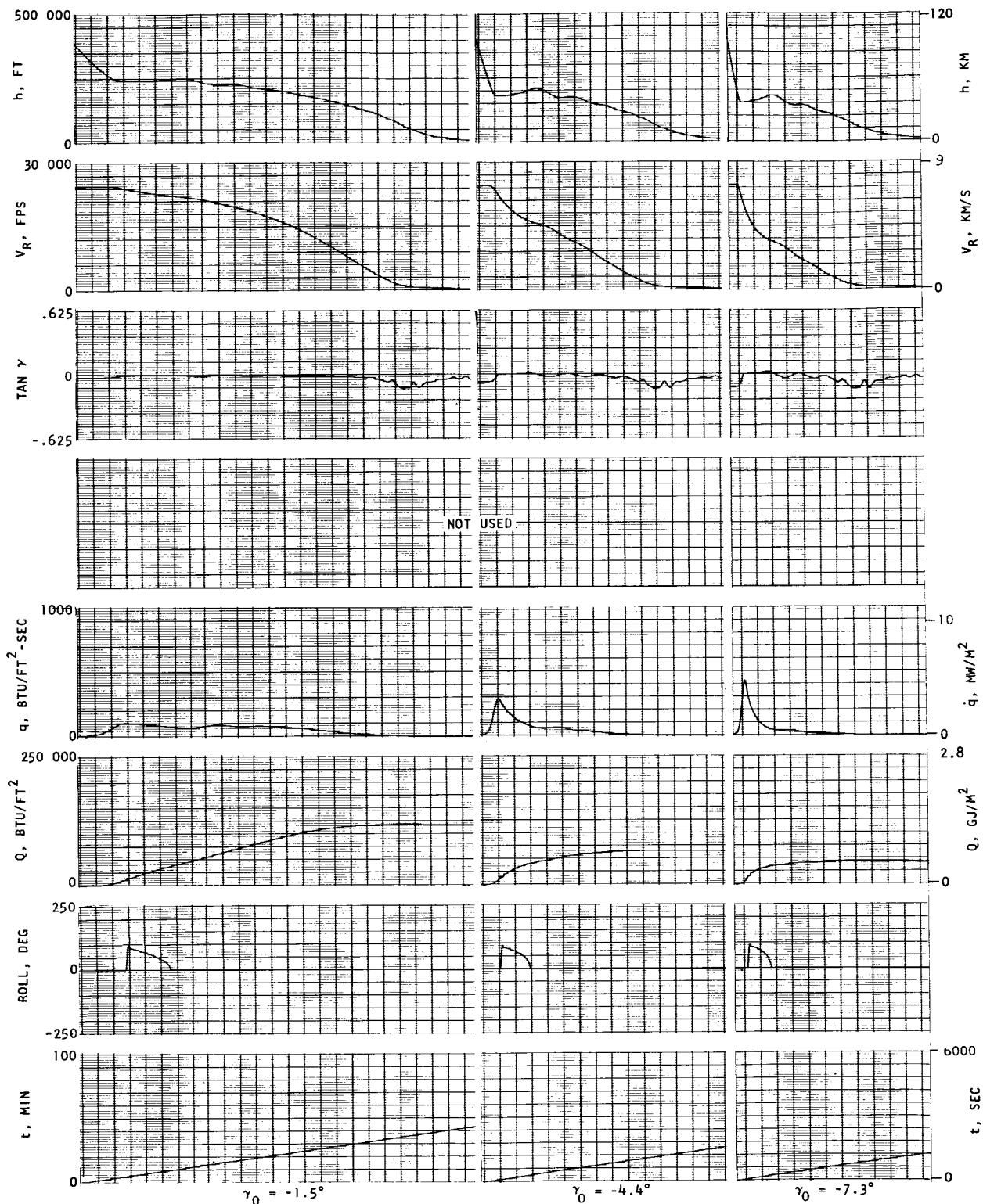
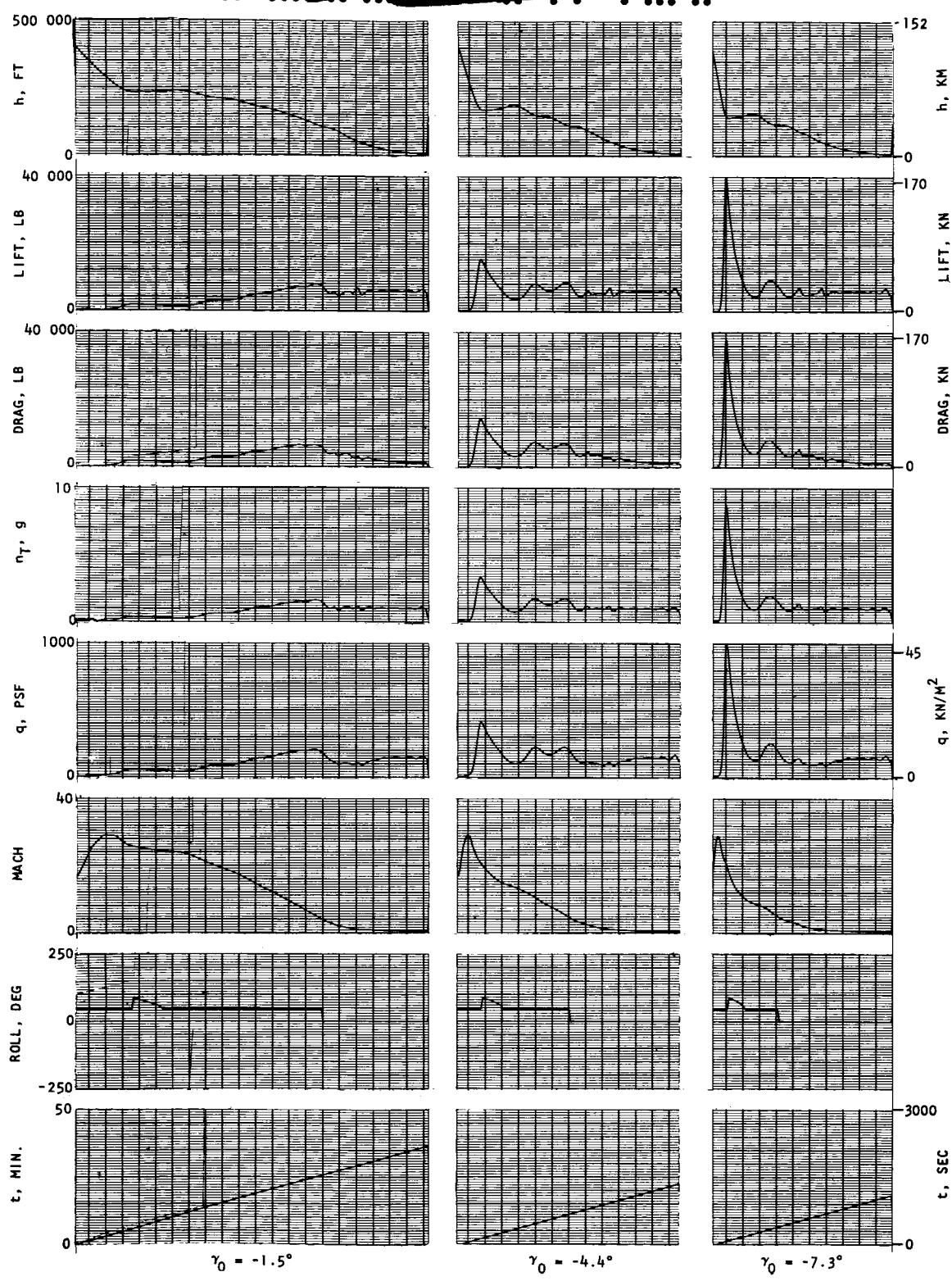


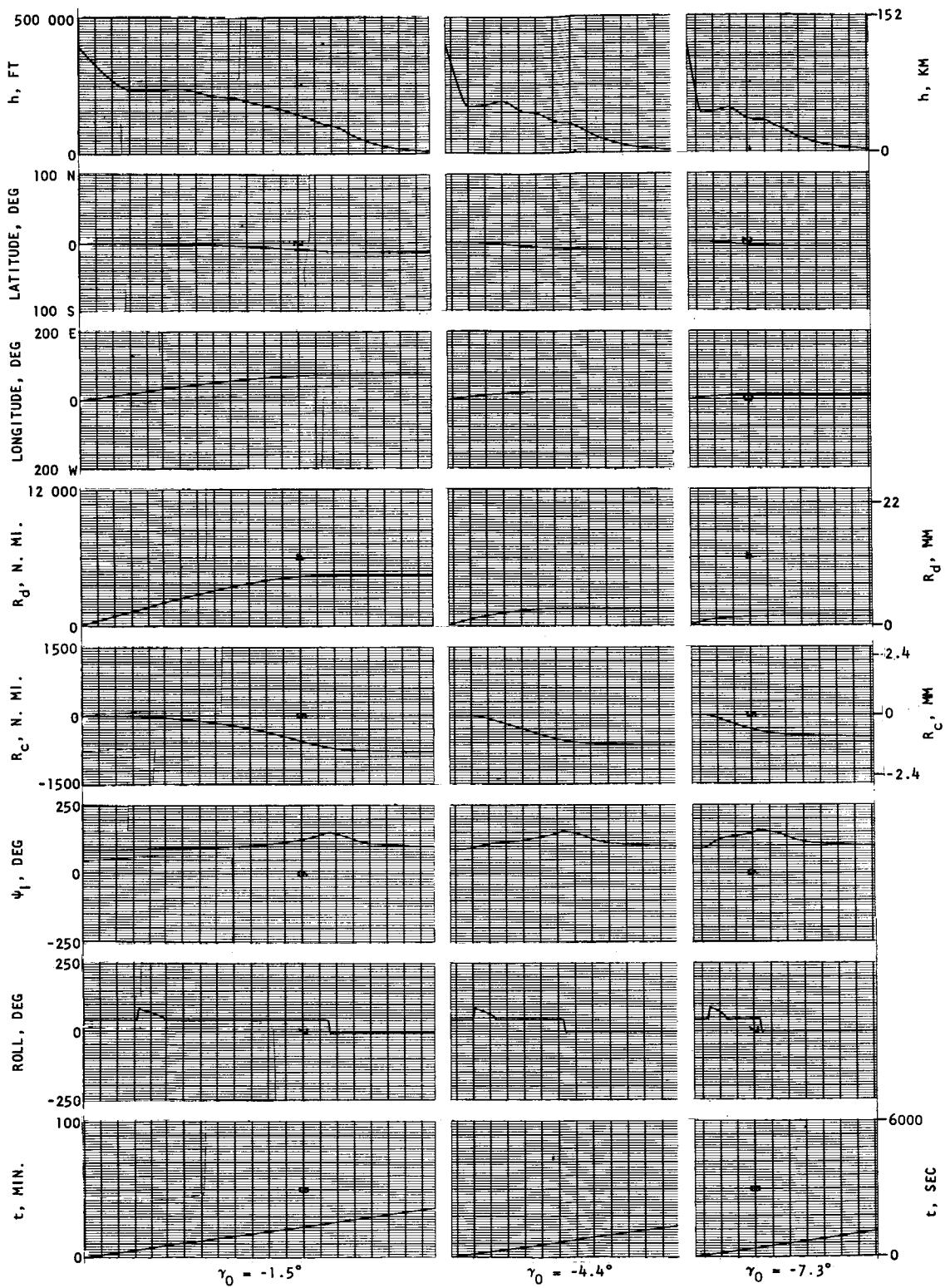
FIGURE 38. --CONTINUED

h) CONCLUDED



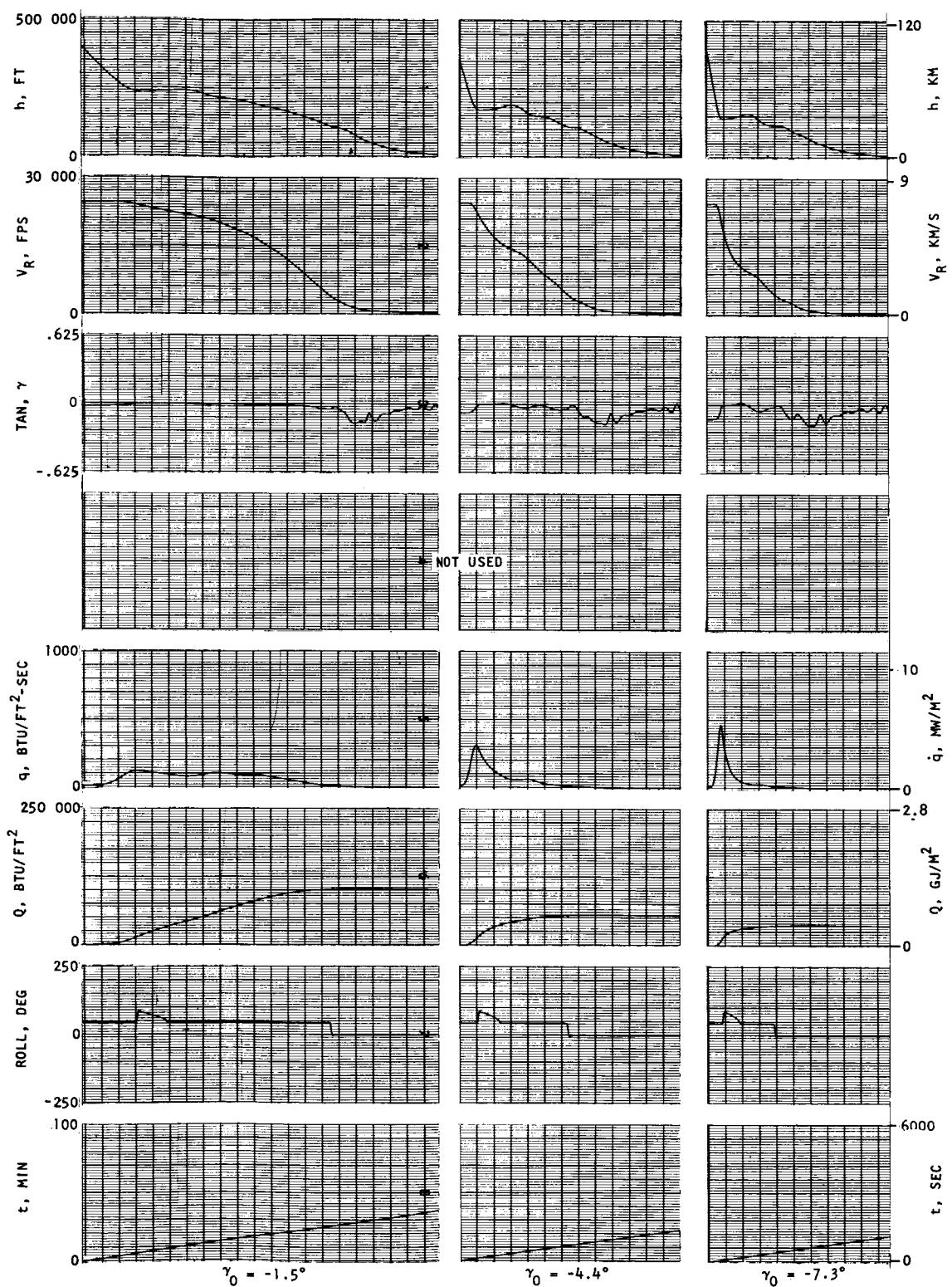
i) STRIP RECORDER DATA--L/D_{MAX}, $\phi = 45^\circ$

FIGURE 38.--CONTINUED



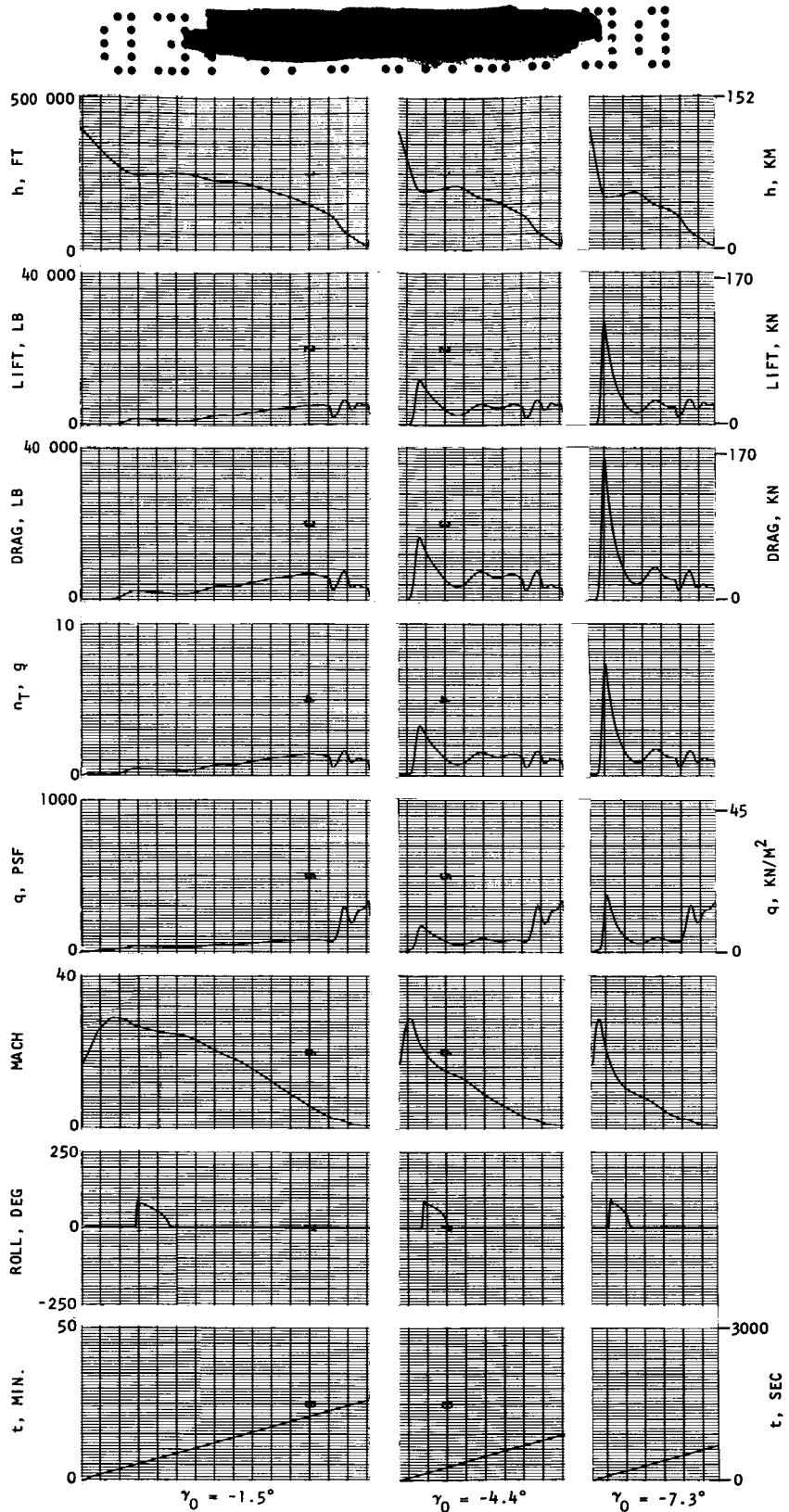
i) CONTINUED

FIGURE 38.--CONTINUED



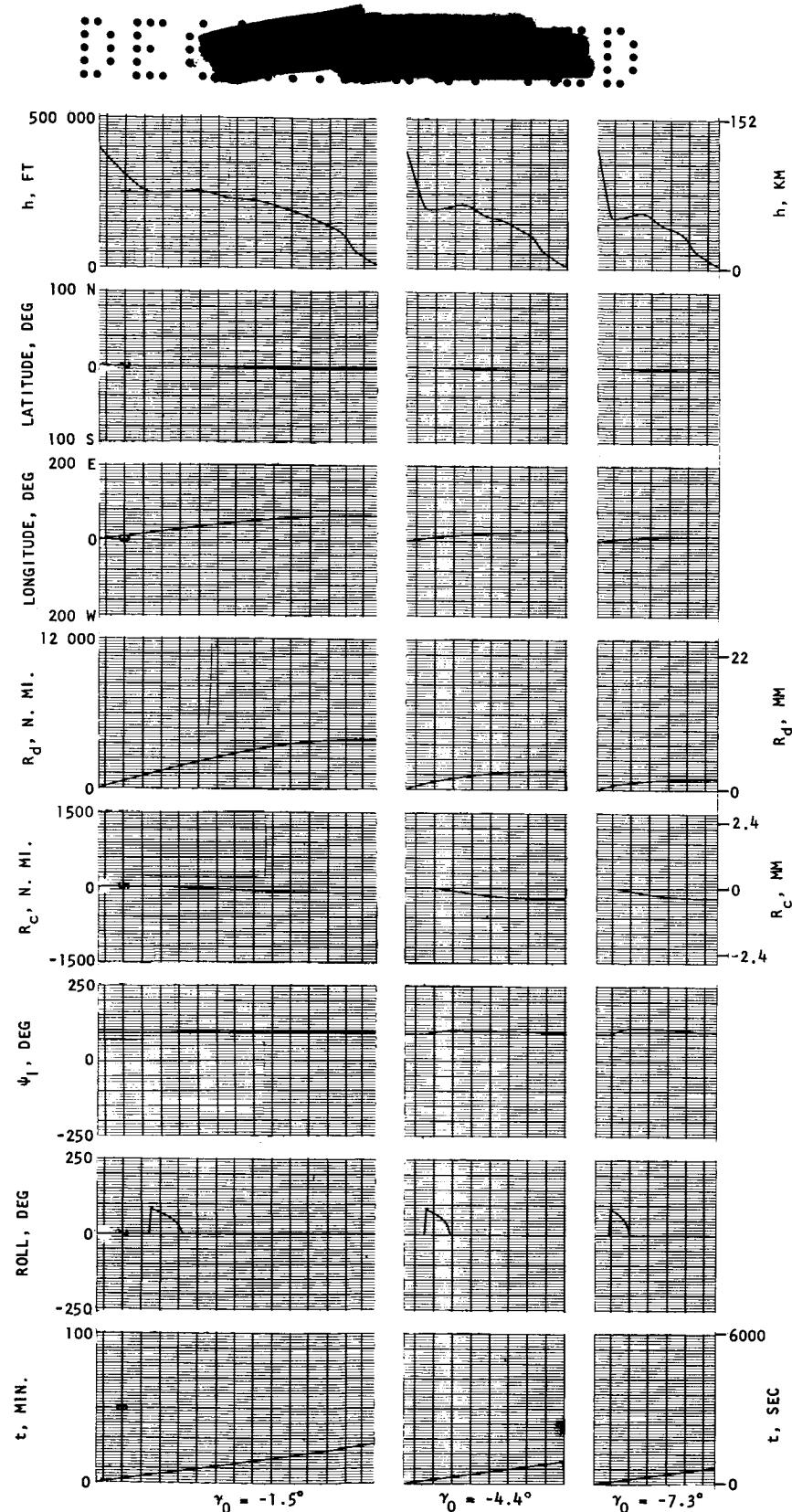
i) CONCLUDED

FIGURE 38.--CONTINUED



j) STRIP RECORDER DATA--L/D_{MIN}, $\phi = 0^\circ$

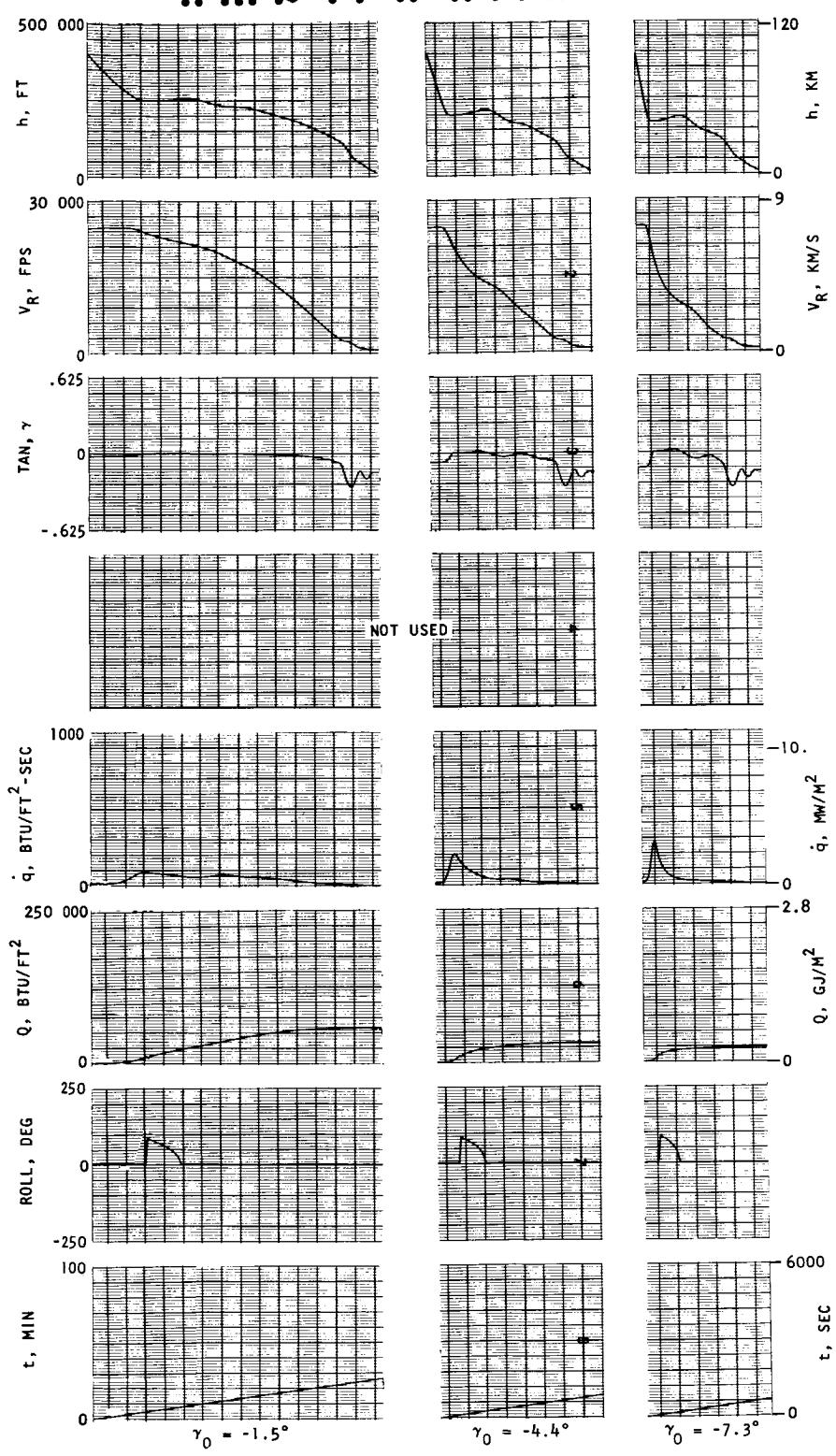
FIGURE 38.--CONTINUED



j) CONTINUED

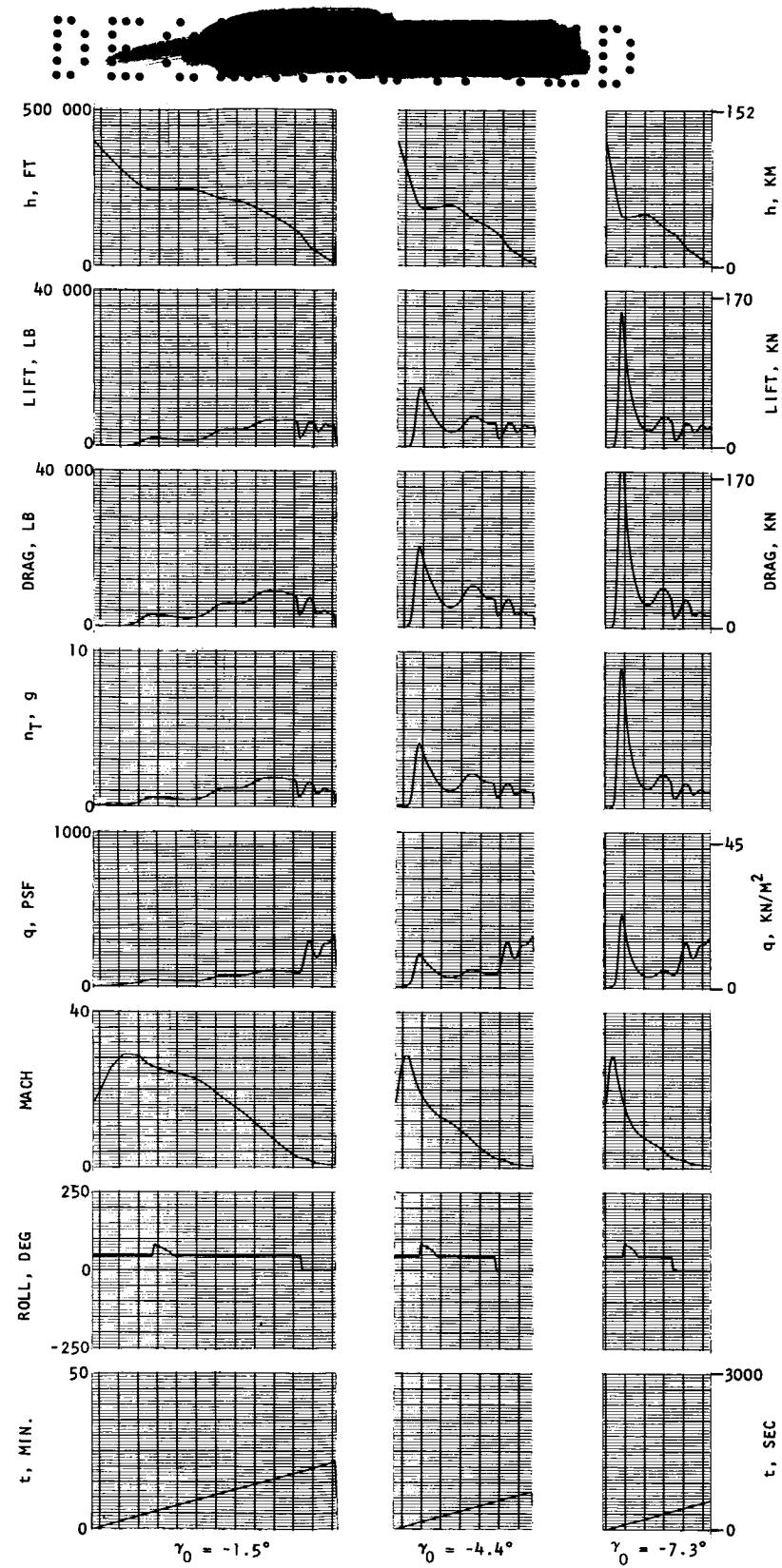
FIGURE 38.--CONTINUED

ER 14471-3



j) CONCLUDED

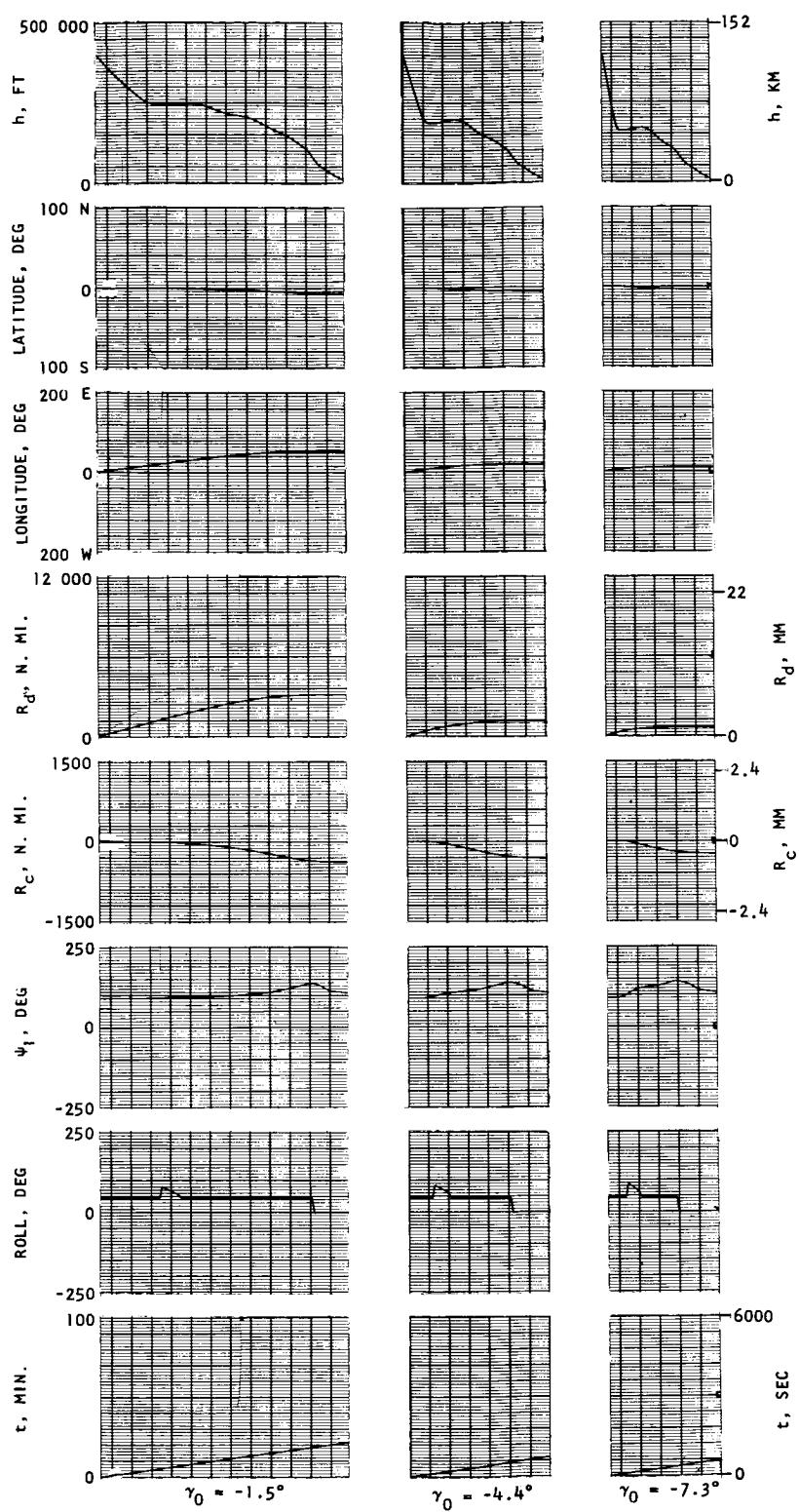
FIGURE 38.--CONTINUED



k) STRIP RECORDER DATA--L/D_{MIN.}, $\phi = 45^\circ$

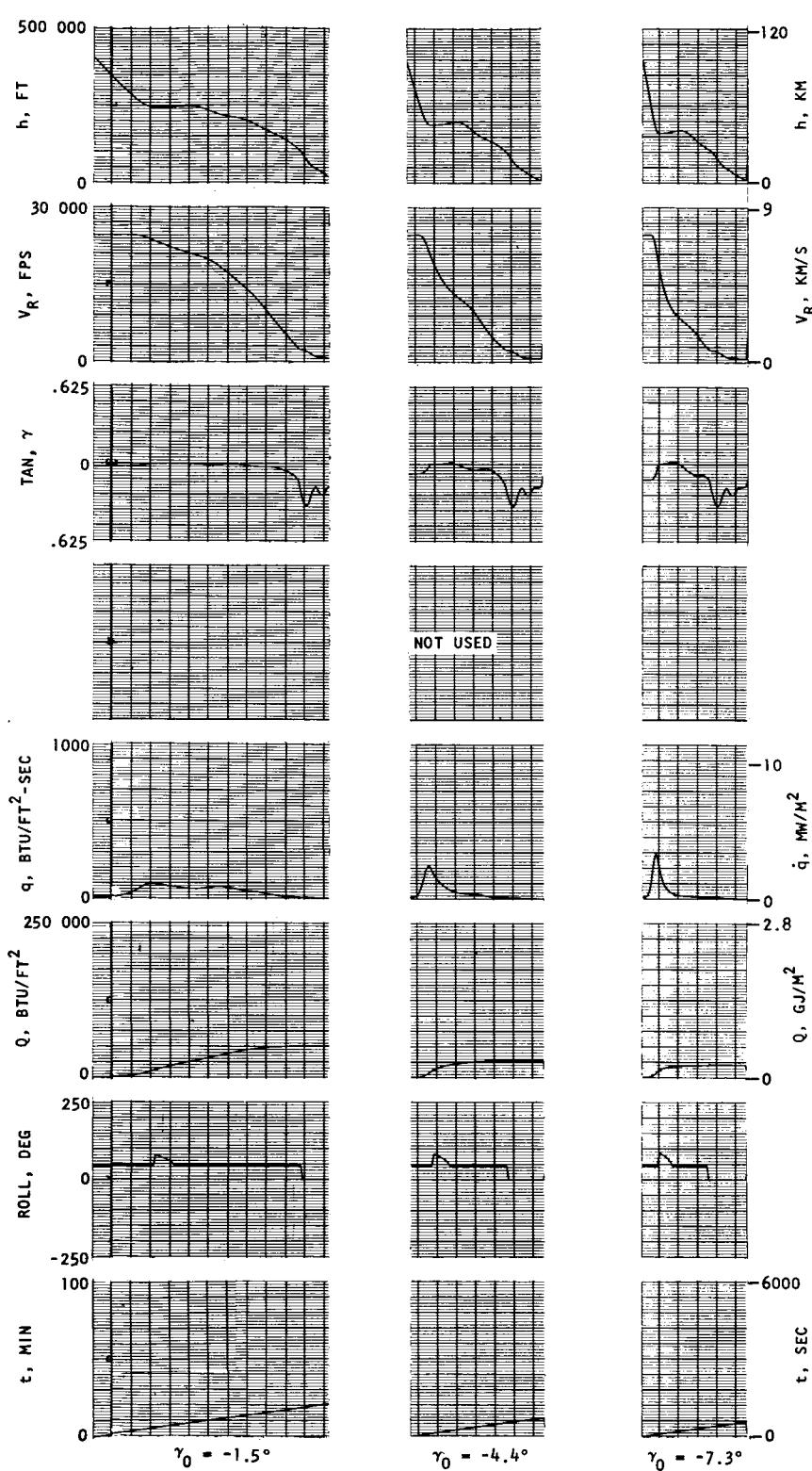
FIGURE 38.--CONTINUED

ER 14471-3



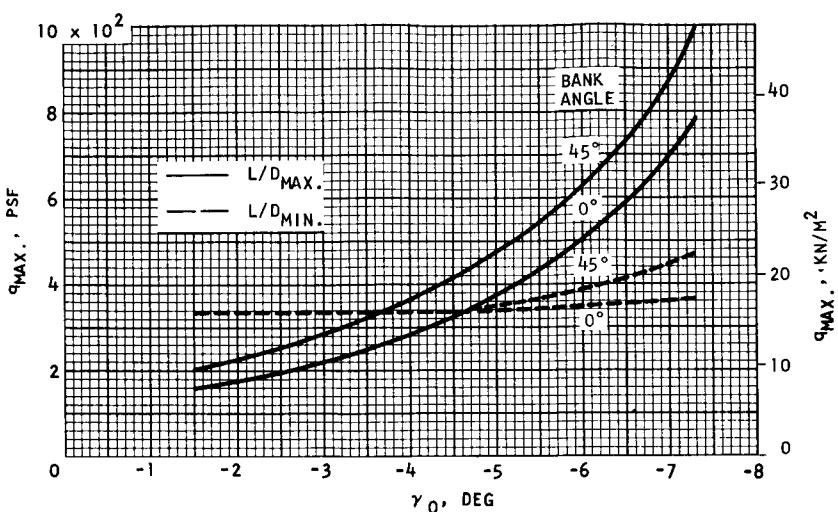
k) CONTINUED

FIGURE 38.--CONTINUED

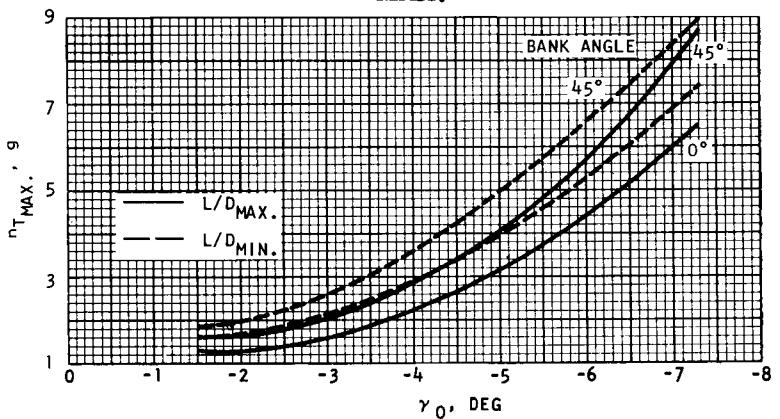


k) CONCLUDED

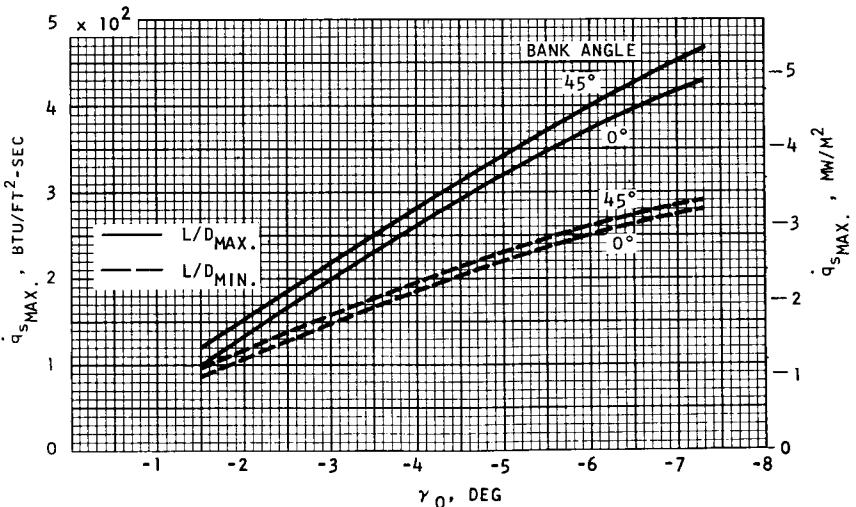
FIGURE 38.--CONTINUED



I-1) VARIATION OF $q_{\text{MAX.}}$ WITH ENTRY ANGLE

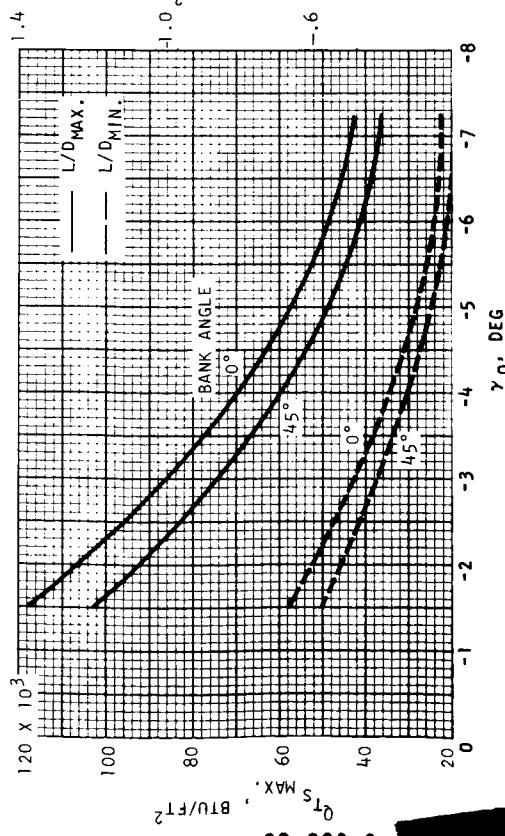


I-2) VARIATION OF $N_{T\text{MAX.}}$ WITH ENTRY ANGLE

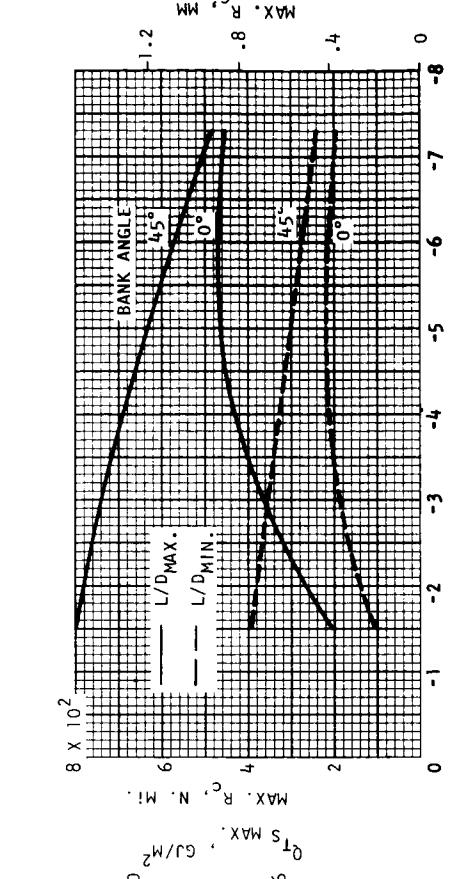


I-3) VARIATION OF $q_{s\text{MAX.}}$ WITH ENTRY ANGLE

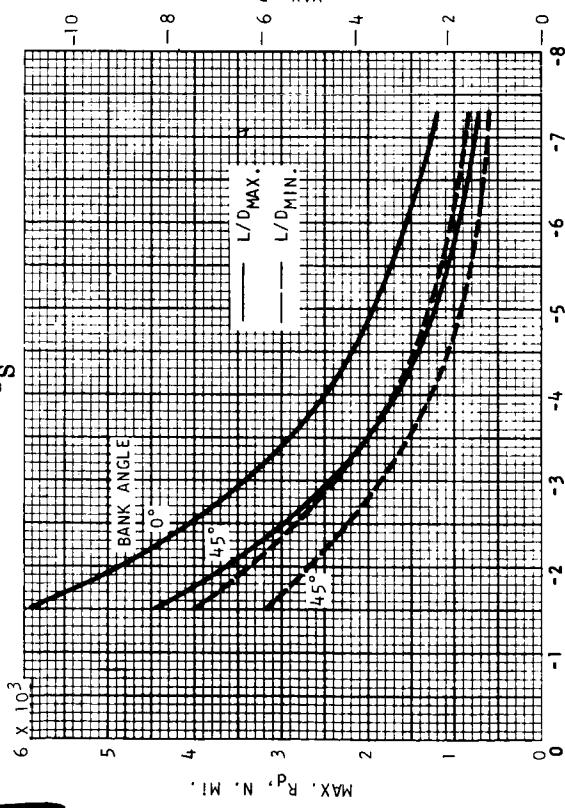
FIGURE 38.--CONTINUED



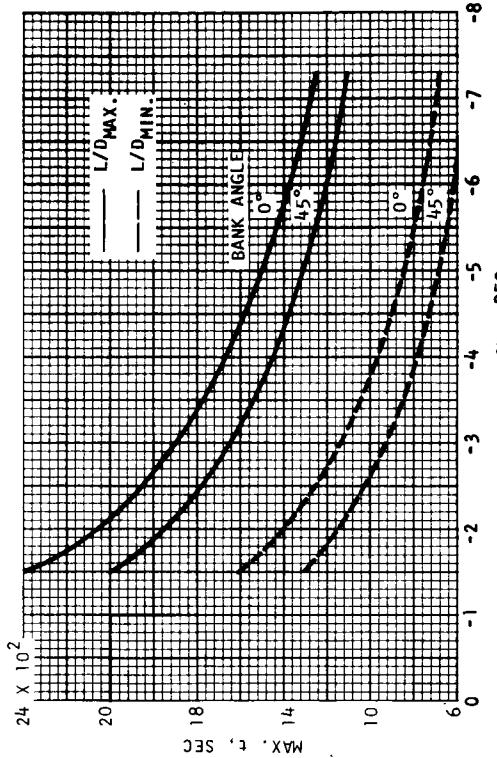
I-4) VARIATION OF $Q_T S$ WITH ENTRY ANGLE.



I-5) VARIATION OF $R_c MAX.$ WITH ENTRY ANGLE.

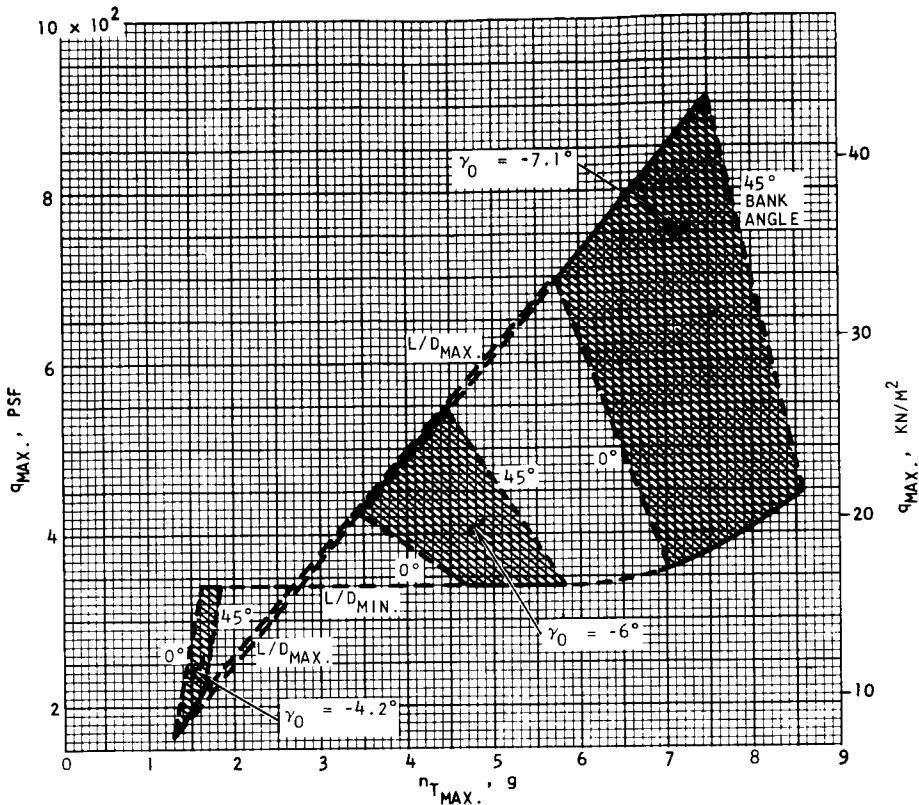


I-6) VARIATION OF $R_d MAX.$ WITH ENTRY ANGLE.



I-7) VARIATION OF $t MAX.$ WITH ENTRY ANGLE.

FIGURE 38. -- CONCLUDED



a) $q_{\text{MAX.}}$ VERSUS $n_{t_{\text{MAX.}}}$.

b) Q_{T_S} VERSUS $q_{s_{\text{MAX.}}}$.

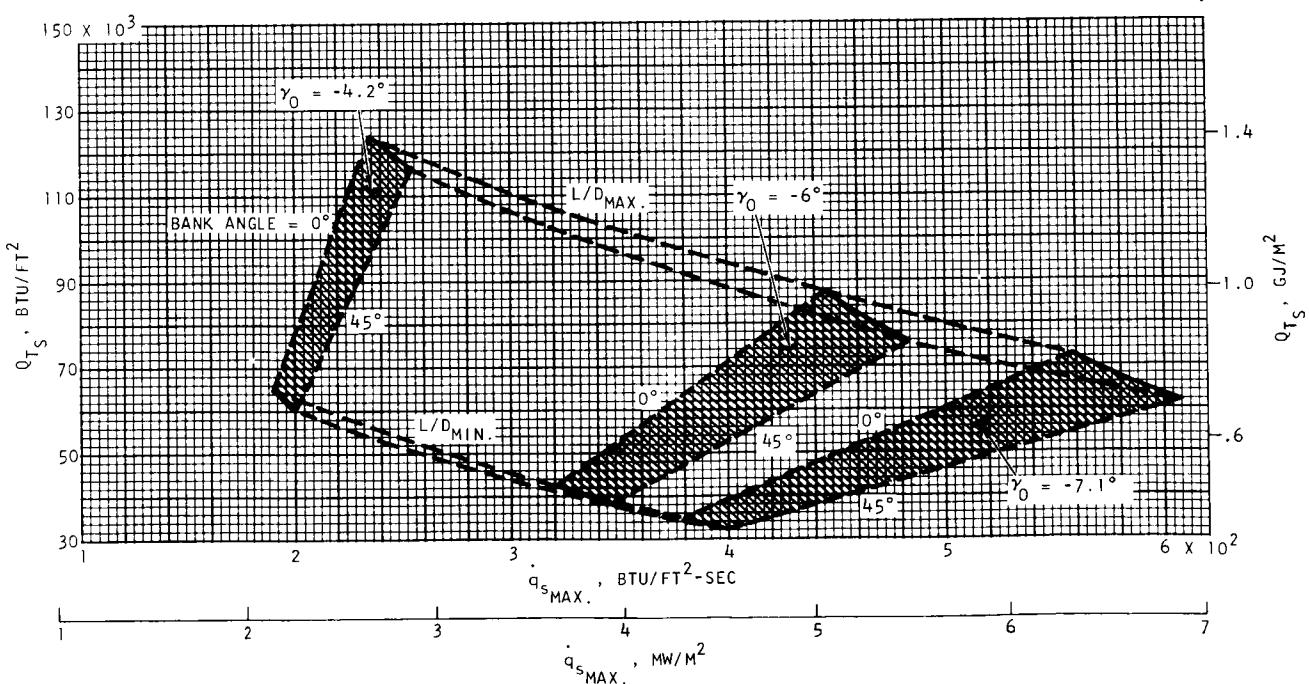
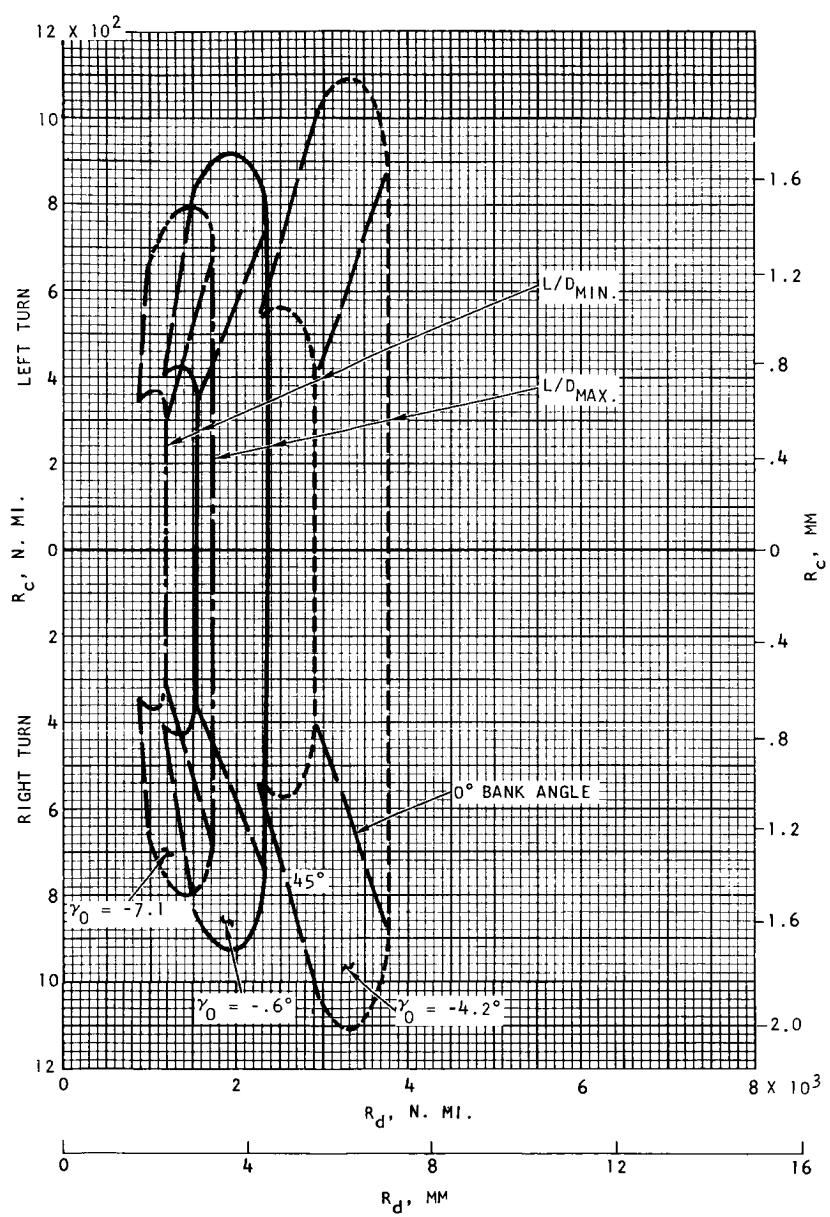


FIGURE 39. ENTRY DATA: $V_I = 30\,000 \text{ FPS (10.4 KM/SEC)}$



c) R_c VERSUS R_d

FIGURE 39.--CONTINUED

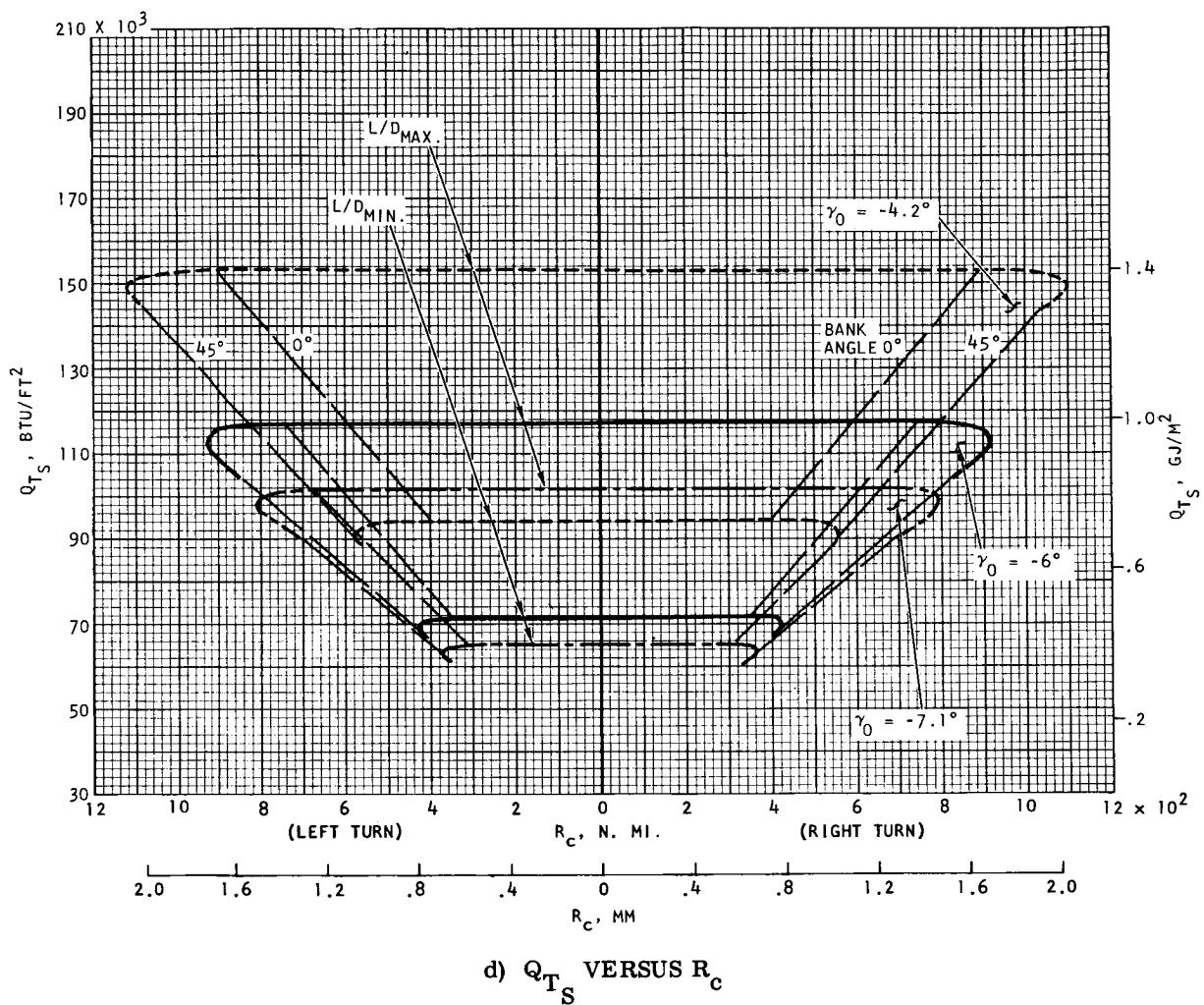


FIGURE 39.--CONTINUED

DEC 1966

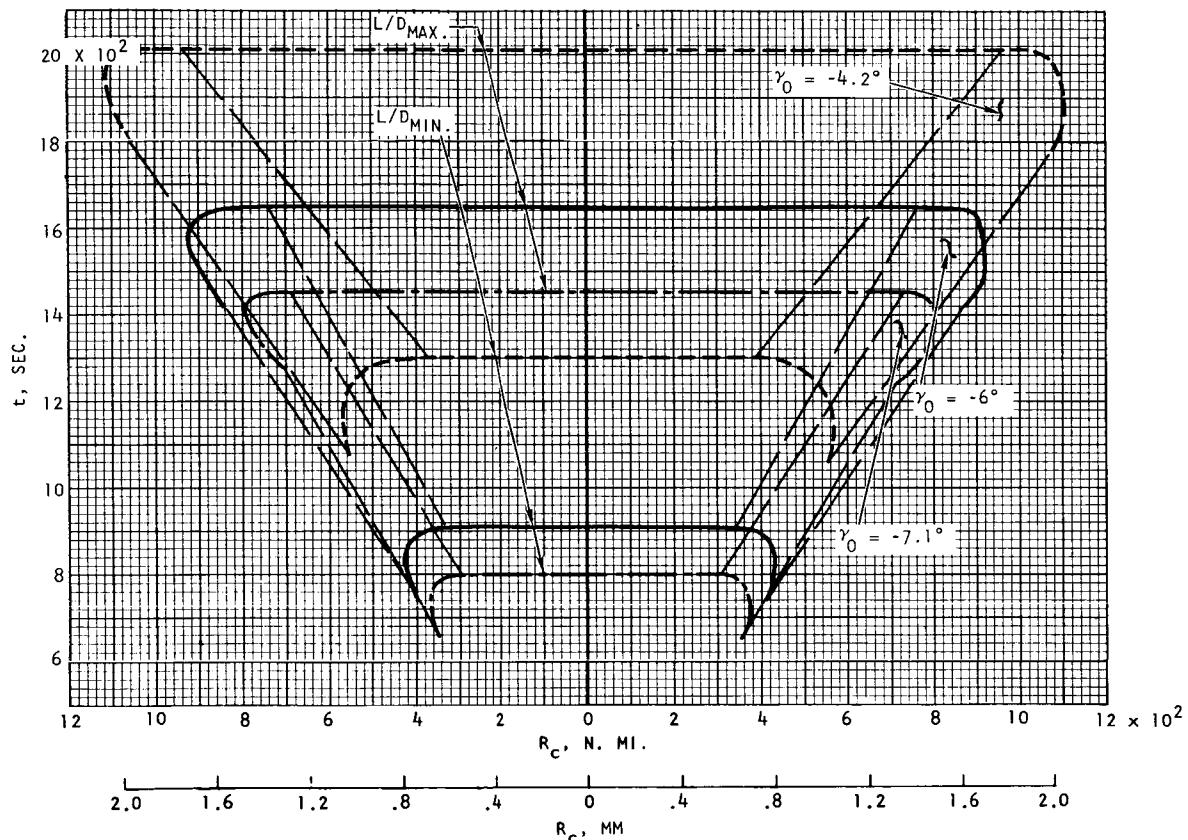
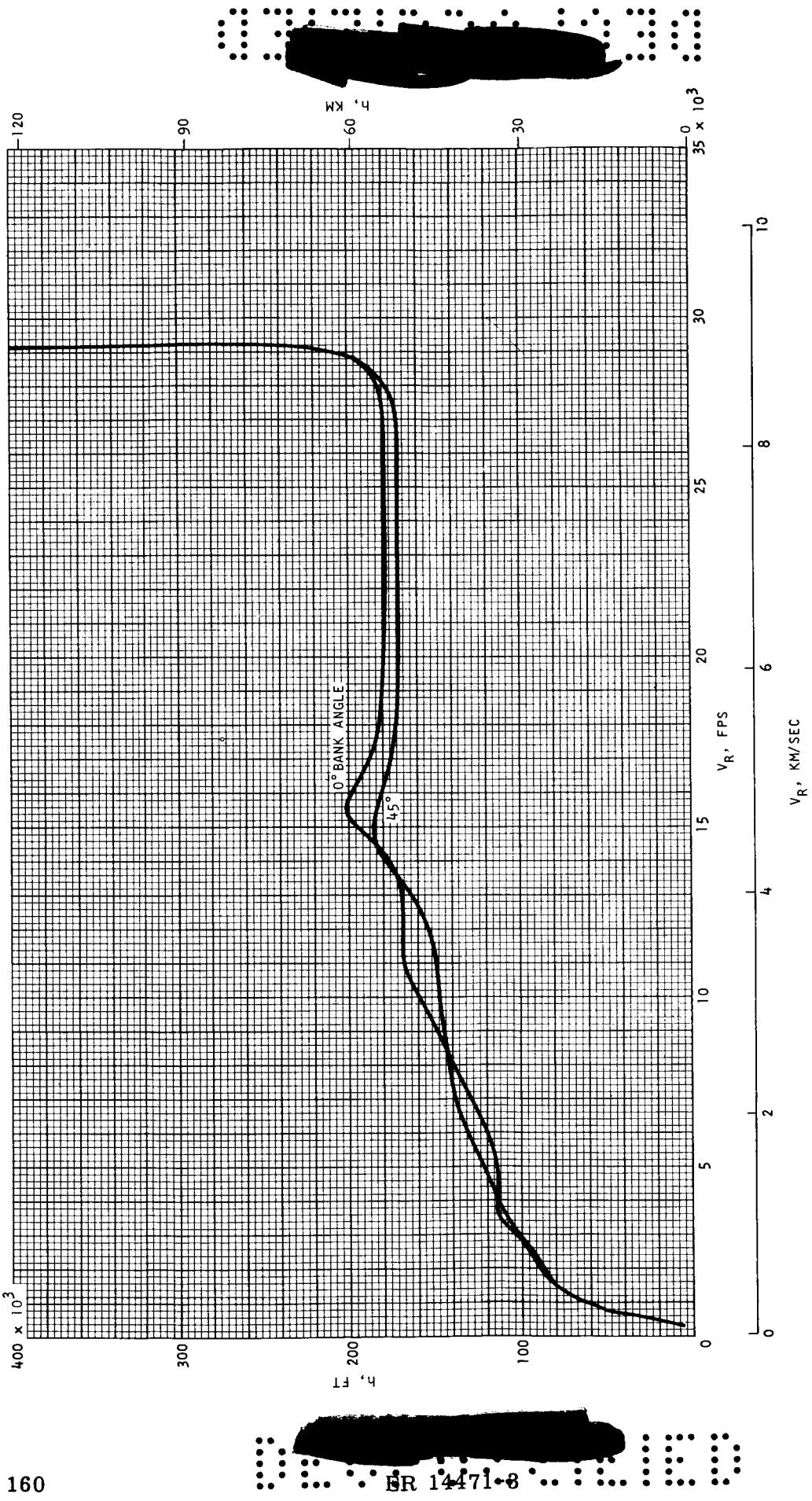
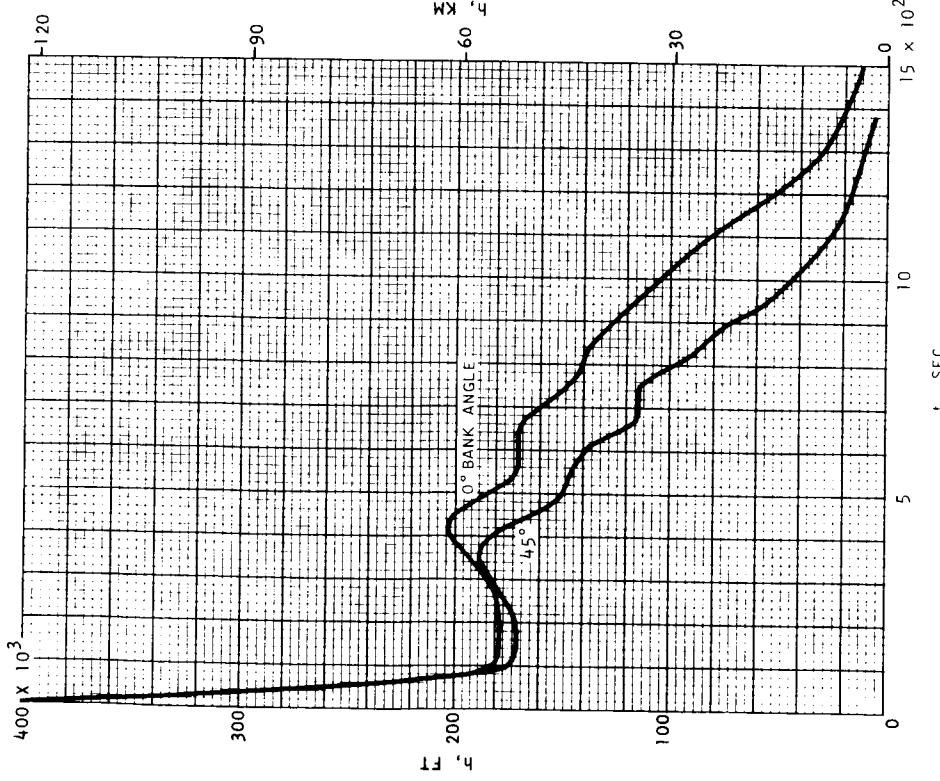


FIGURE 39.--CONTINUED

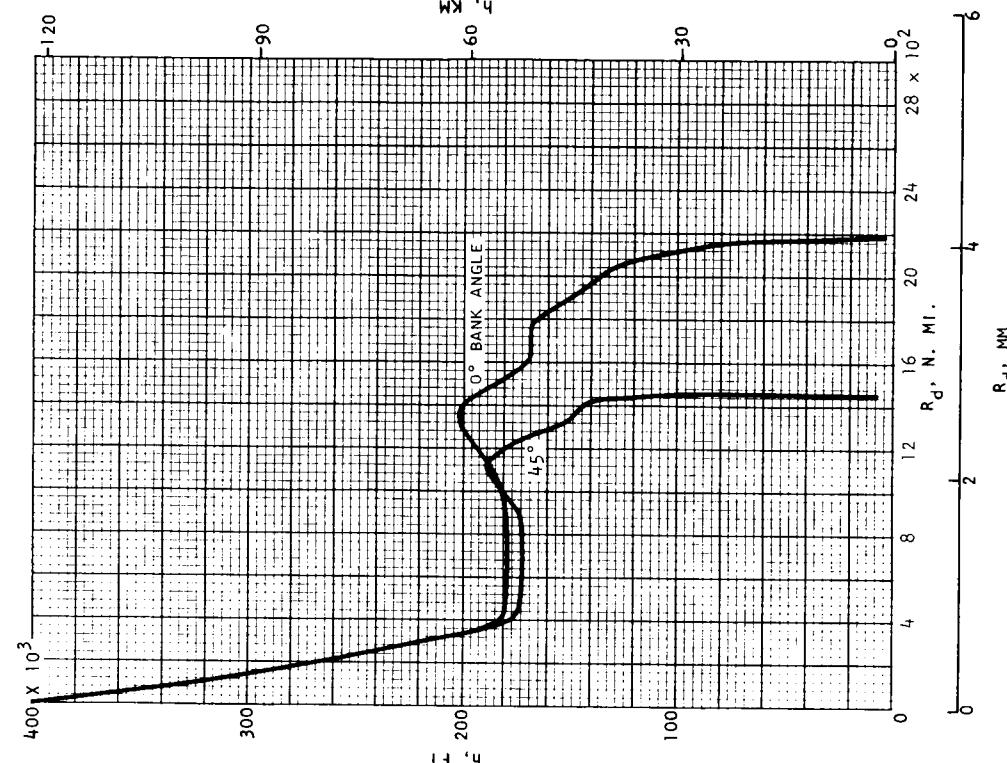


f-1) h VERSUS V_R FOR $\gamma = -6^\circ$ AND L/D_{MAX} .

FIGURE 39. --CONTINUED

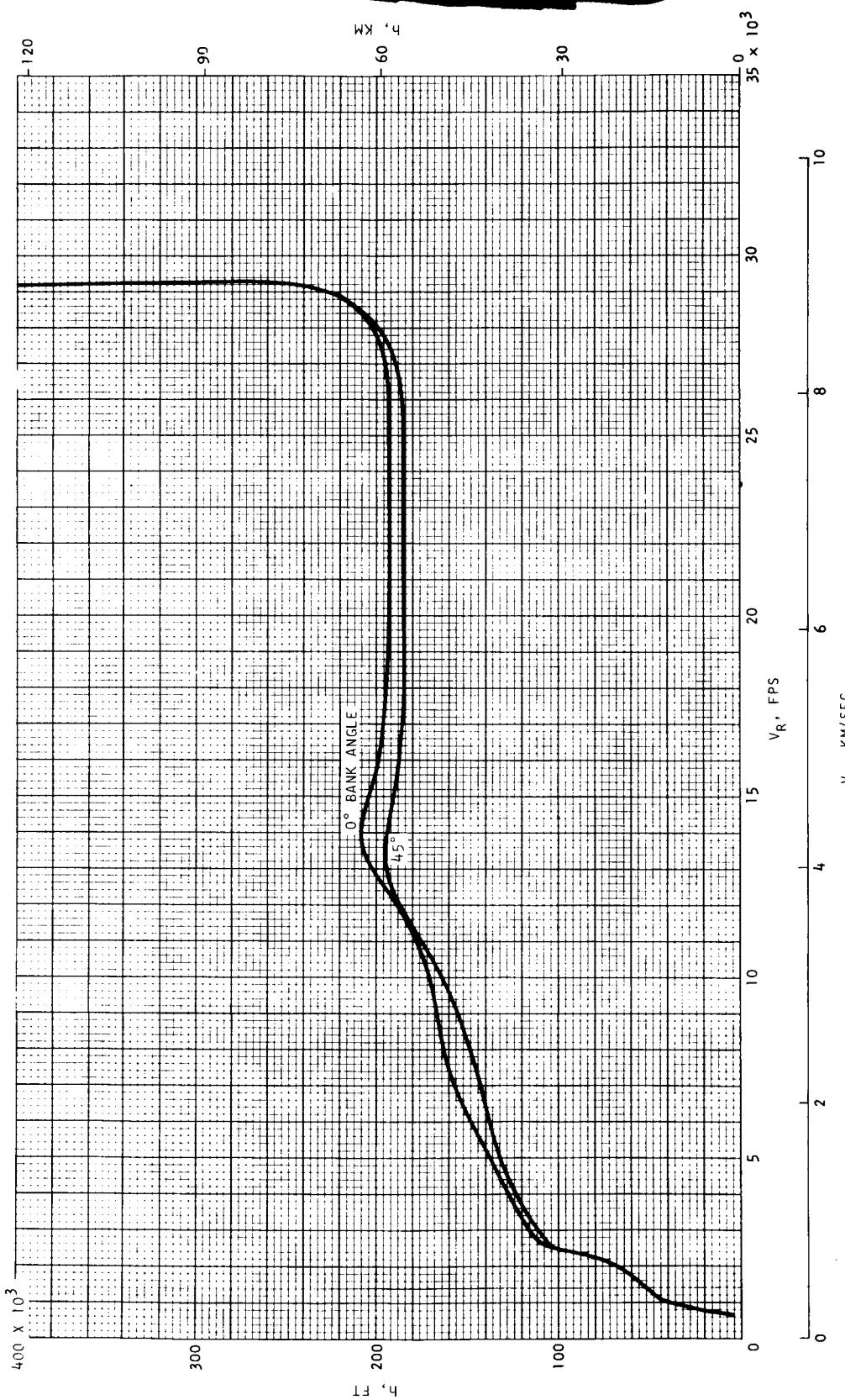


f-2) h VERSUS t FOR $\gamma = -6^\circ$ AND L/D_{MAX} .



f-3) h VERSUS R_d FOR $\gamma = -6^\circ$ AND L/D_{MAX} .

FIGURE 39. --CONTINUED



g-1) h VERSUS V_R FOR $\gamma = -6^\circ$ AND L/D_{MIN} .

FIGURE 39. --CONTINUED

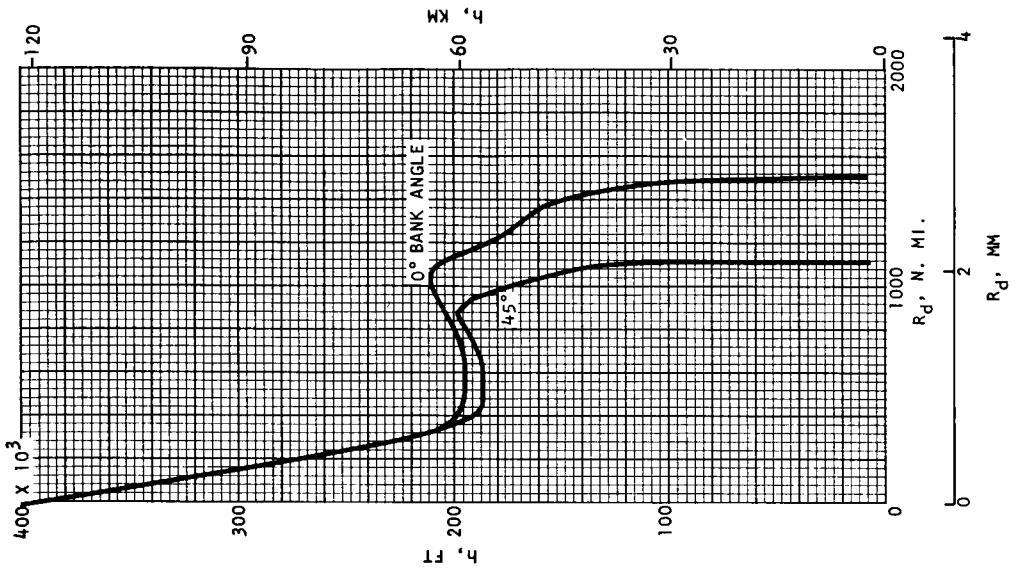
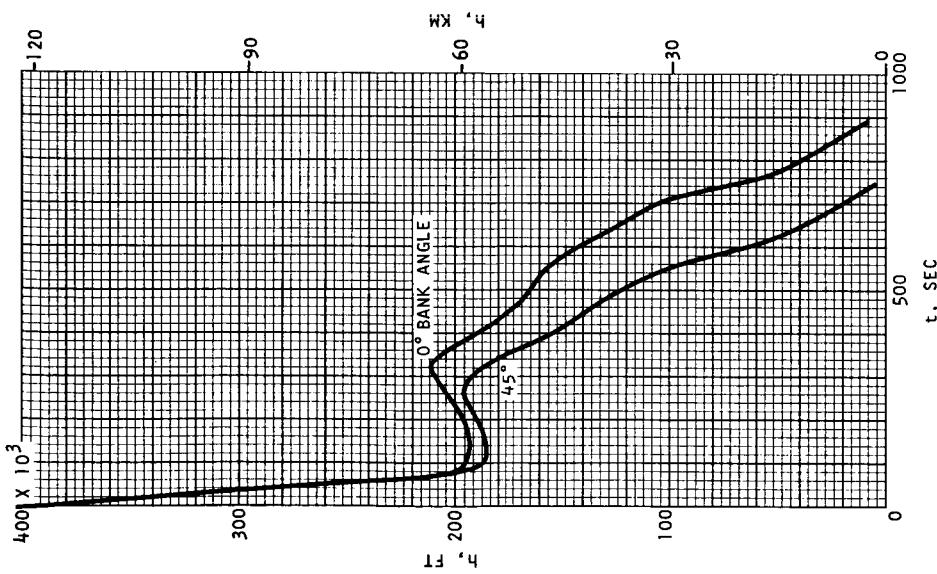
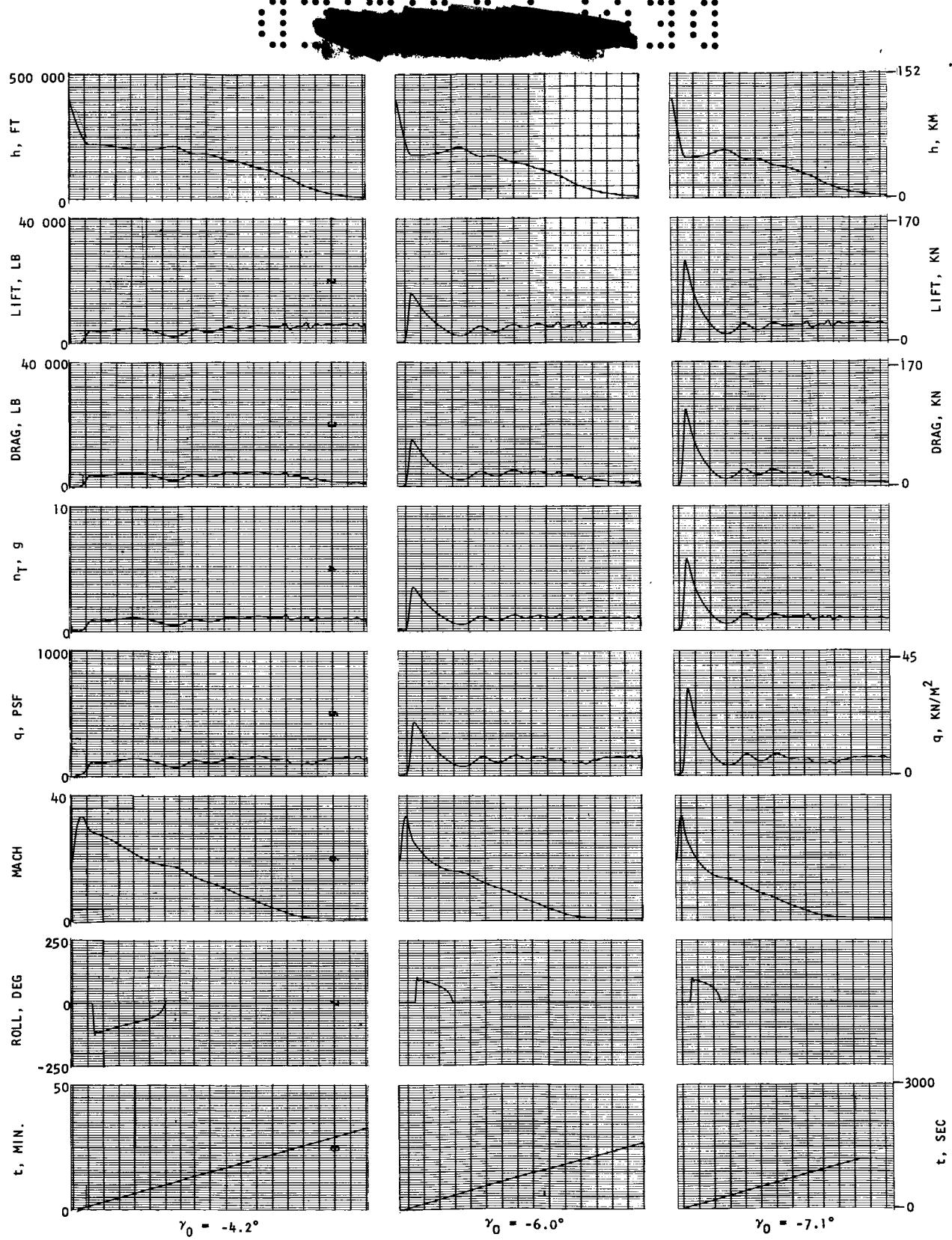
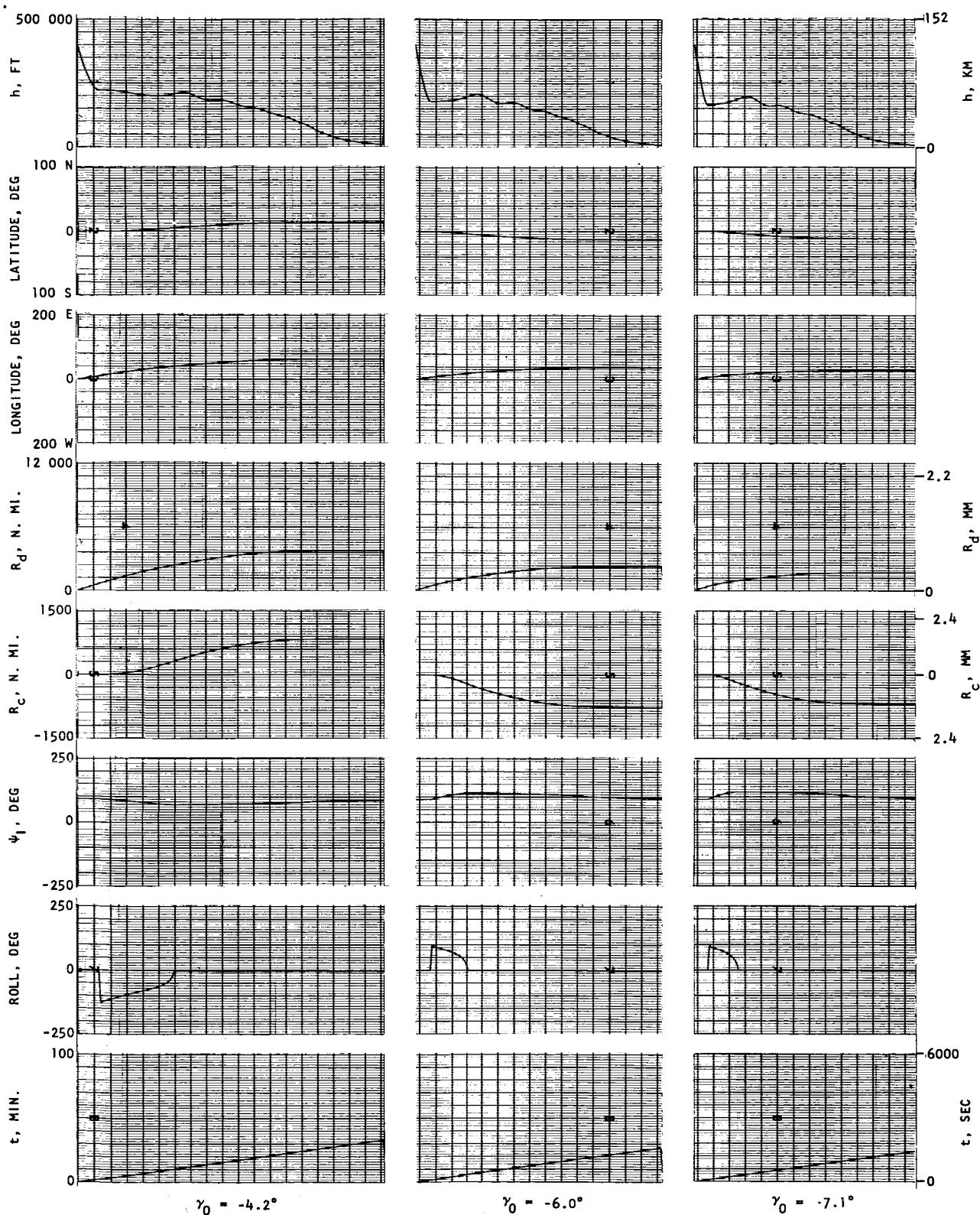


FIGURE 39. --CONTINUED



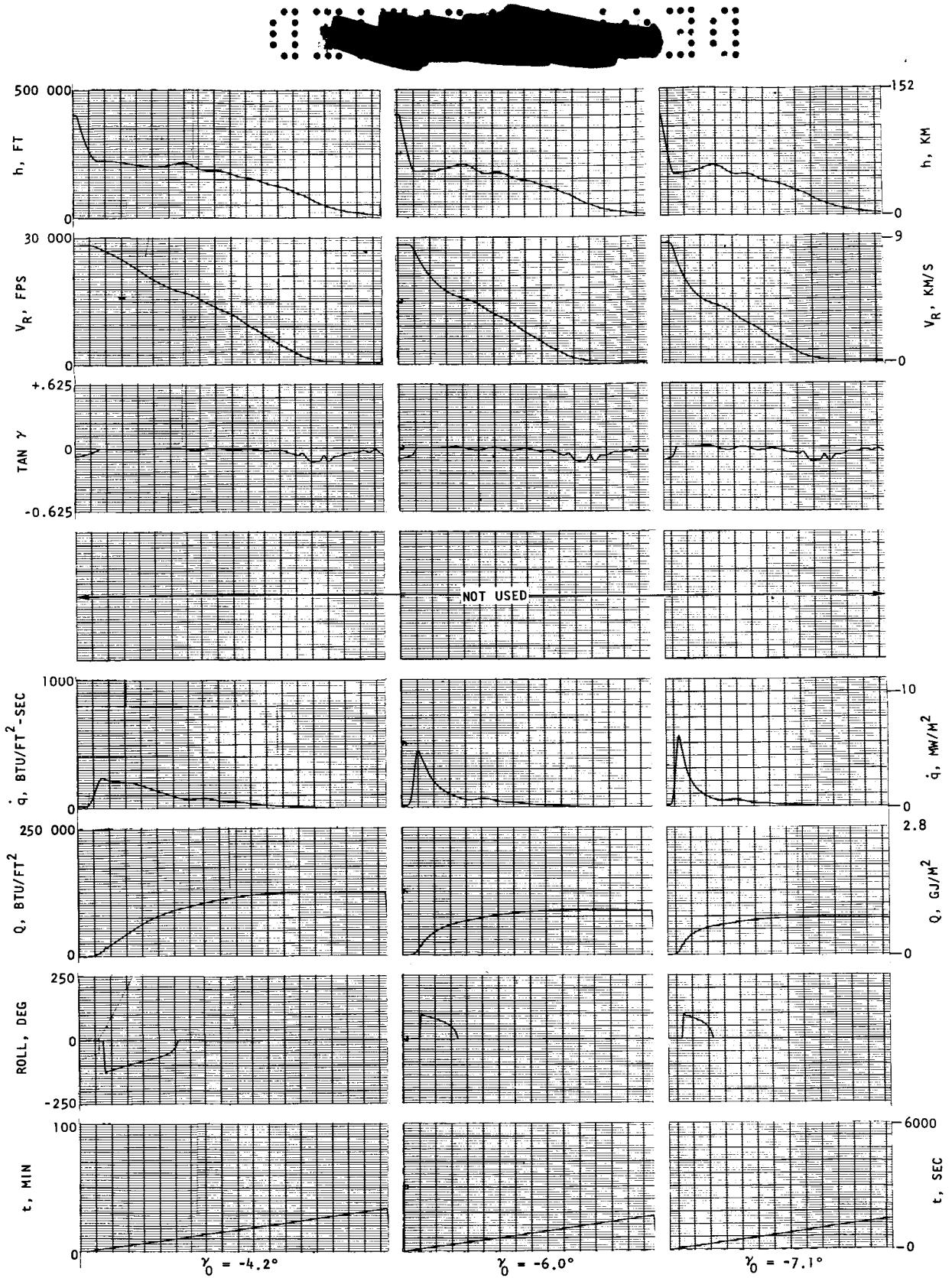
h) STRIP RECORDER DATA--L/D_{MAX}, $\phi = 0^\circ$

FIGURE 39.--CONTINUED



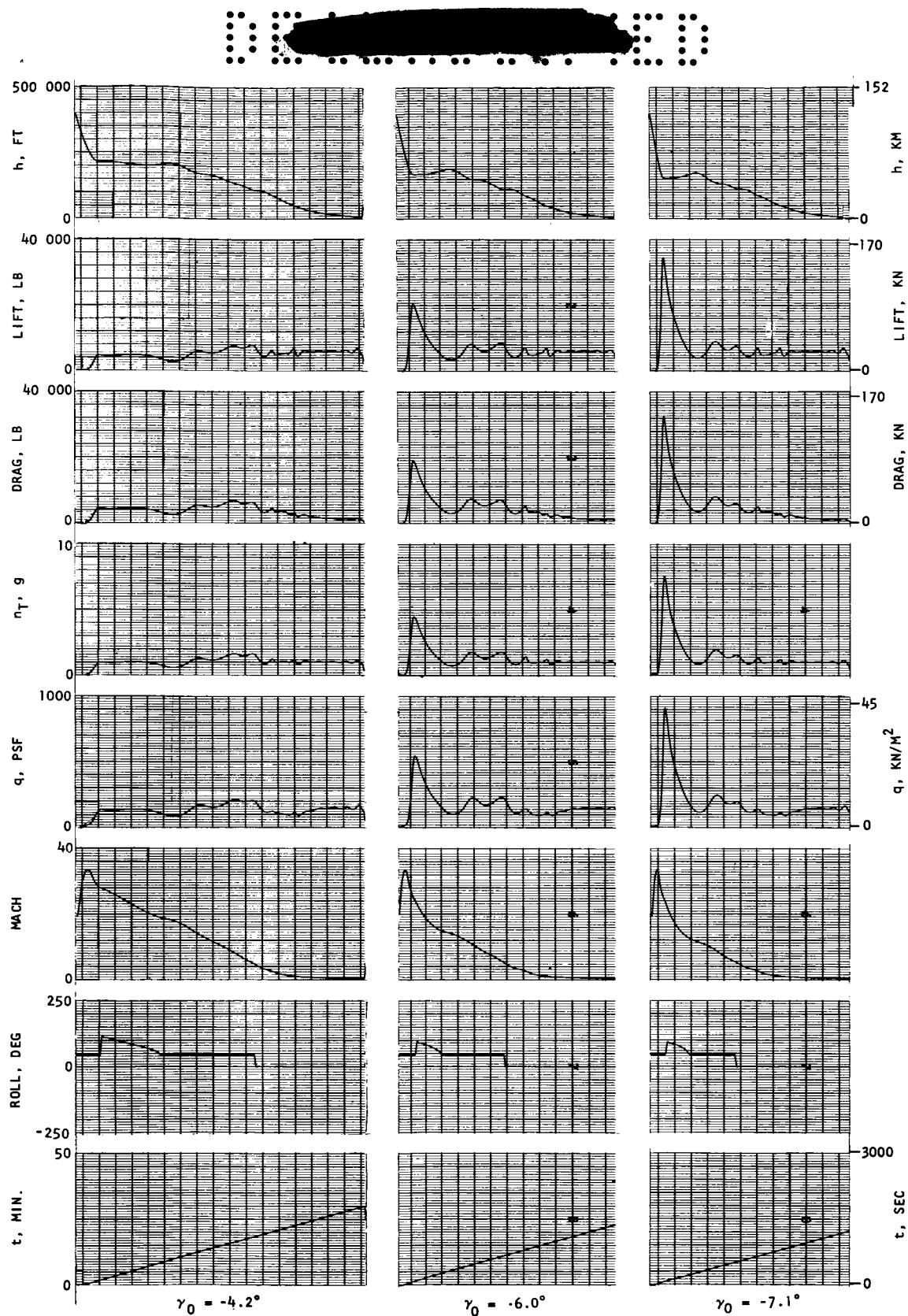
h) CONTINUED

FIGURE 39.--CONTINUED



h) CONCLUDED

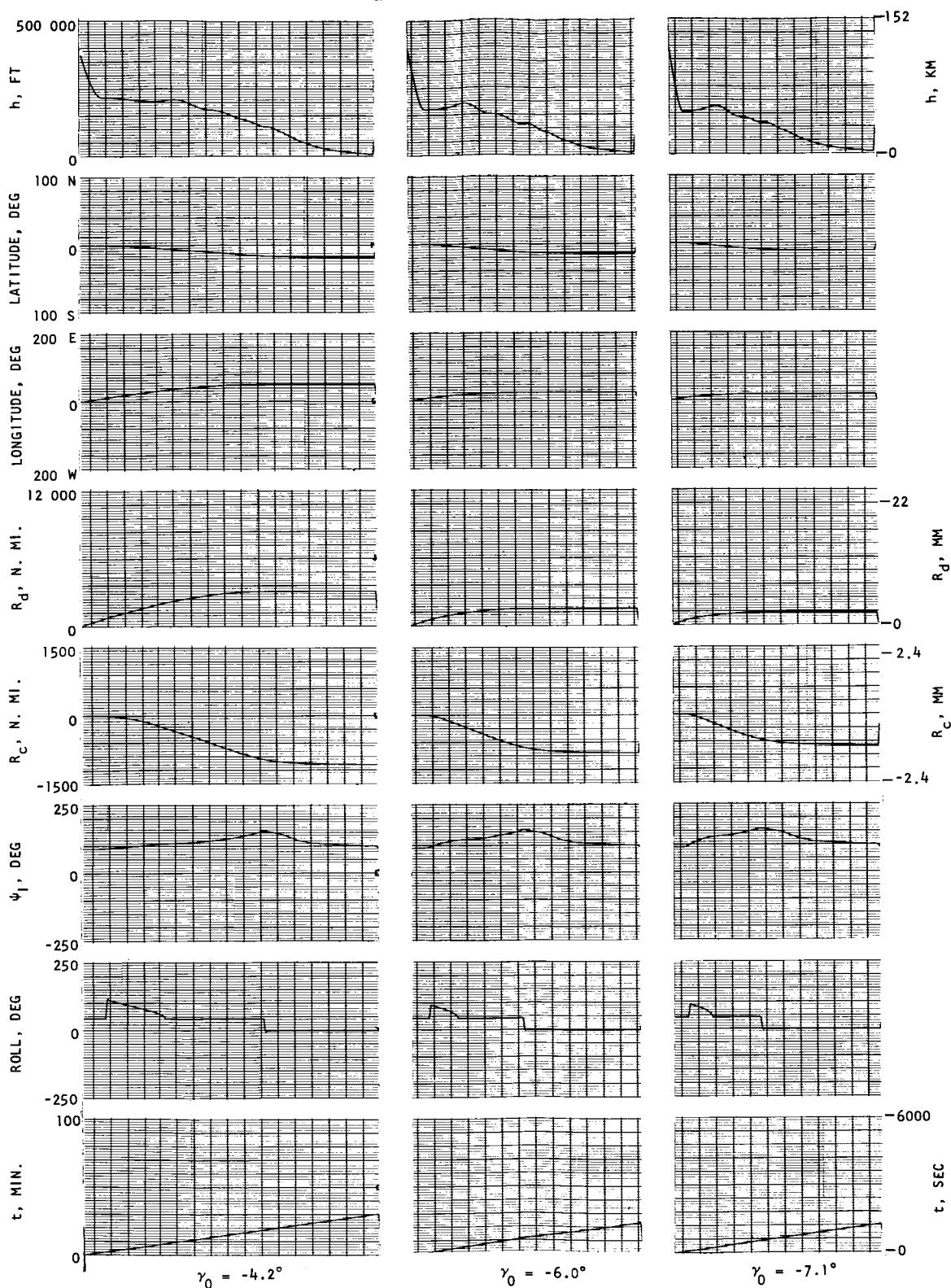
FIGURE 39.--CONTINUED



i) STRIP RECORDER DATA--L/D_{MAX}, $\phi = 45^\circ$

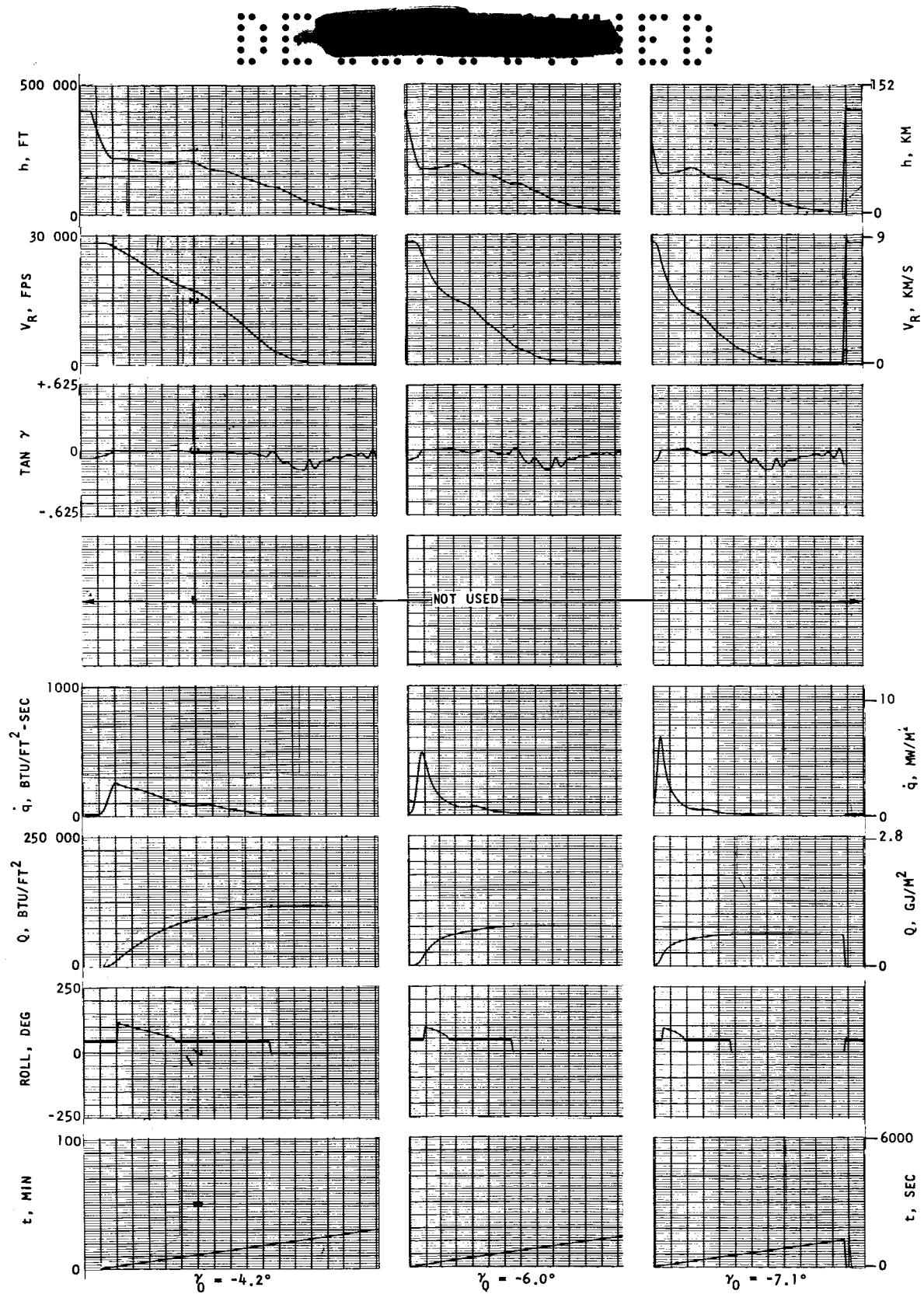
FIGURE 39.--CONTINUED

ER 14471-3



i) CONTINUED

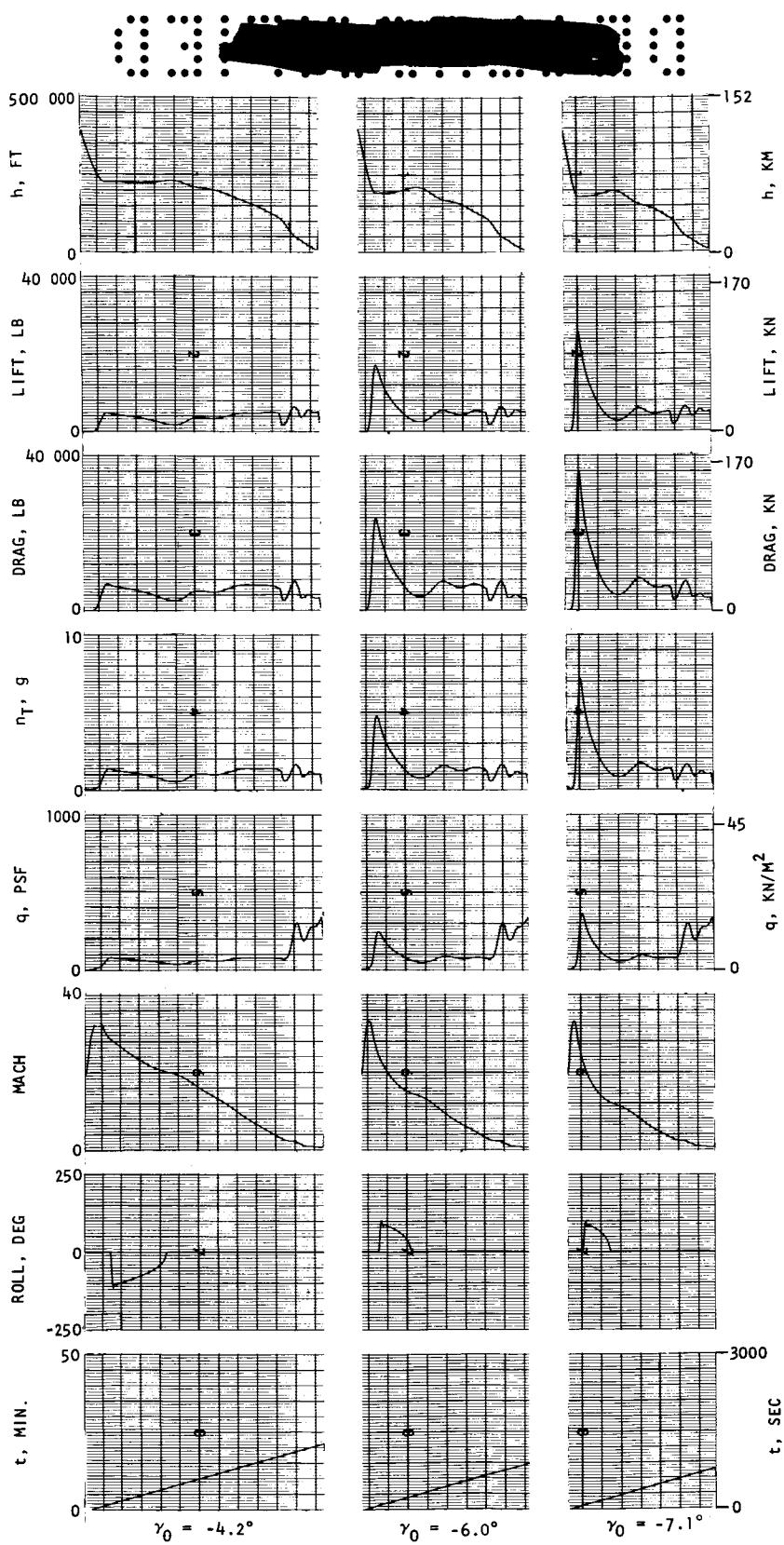
FIGURE 39. --CONTINUED



i) CONCLUDED

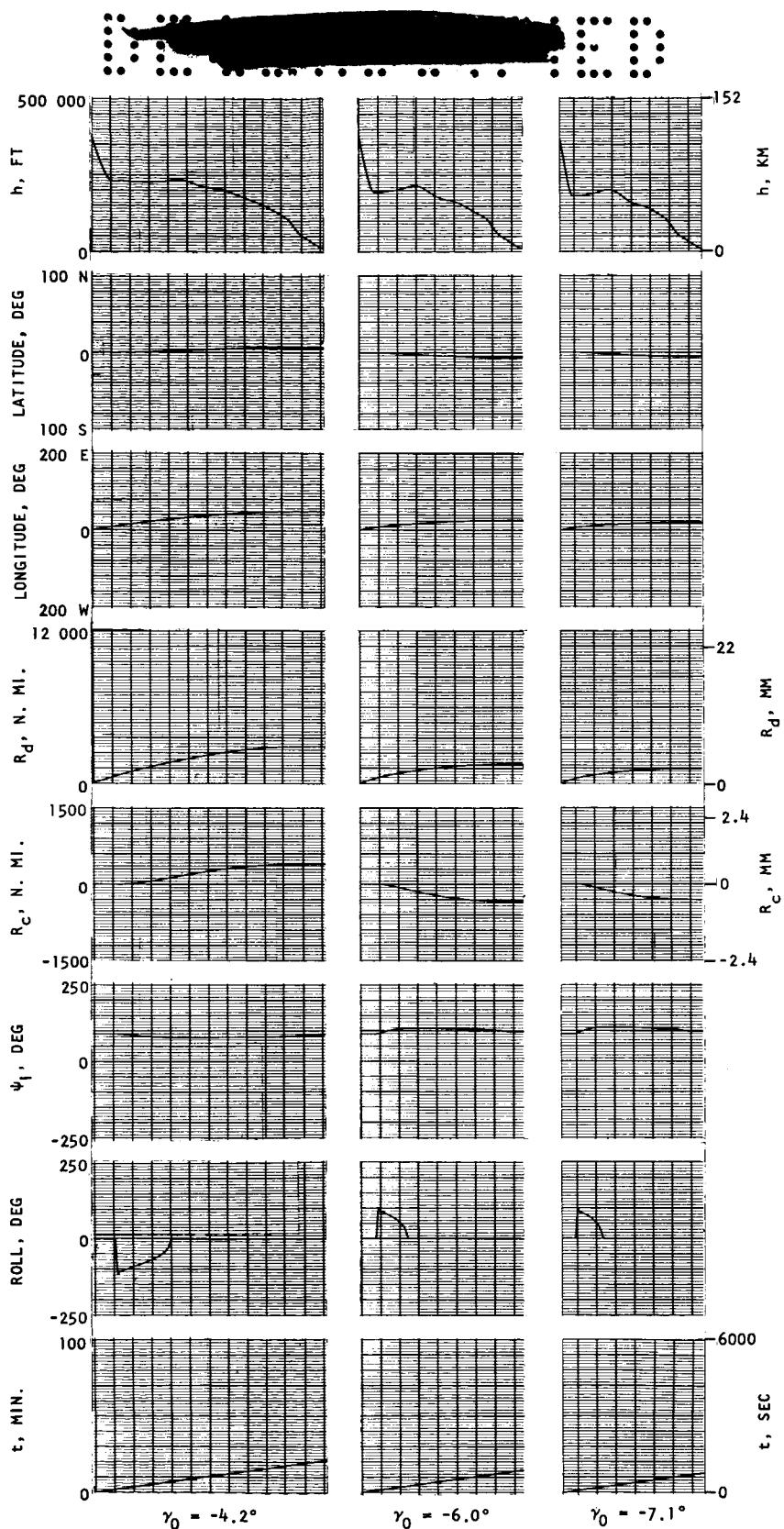
FIGURE 39.--CONTINUED

031811 ER 1447 R-3



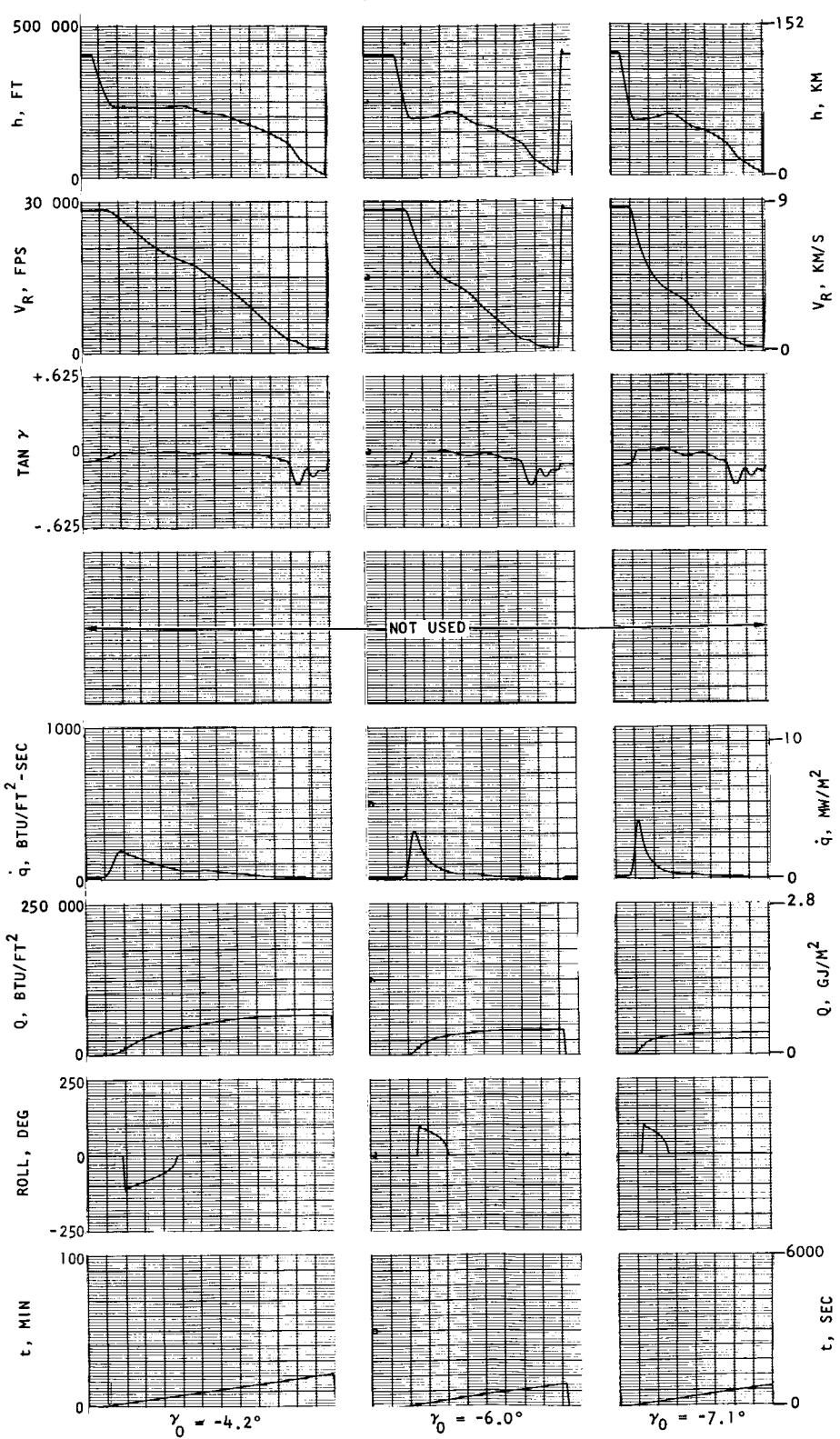
j) STRIP RECORDER DATA--L/D_{MIN.}, $\phi = 0^\circ$

FIGURE 39.--CONTINUED



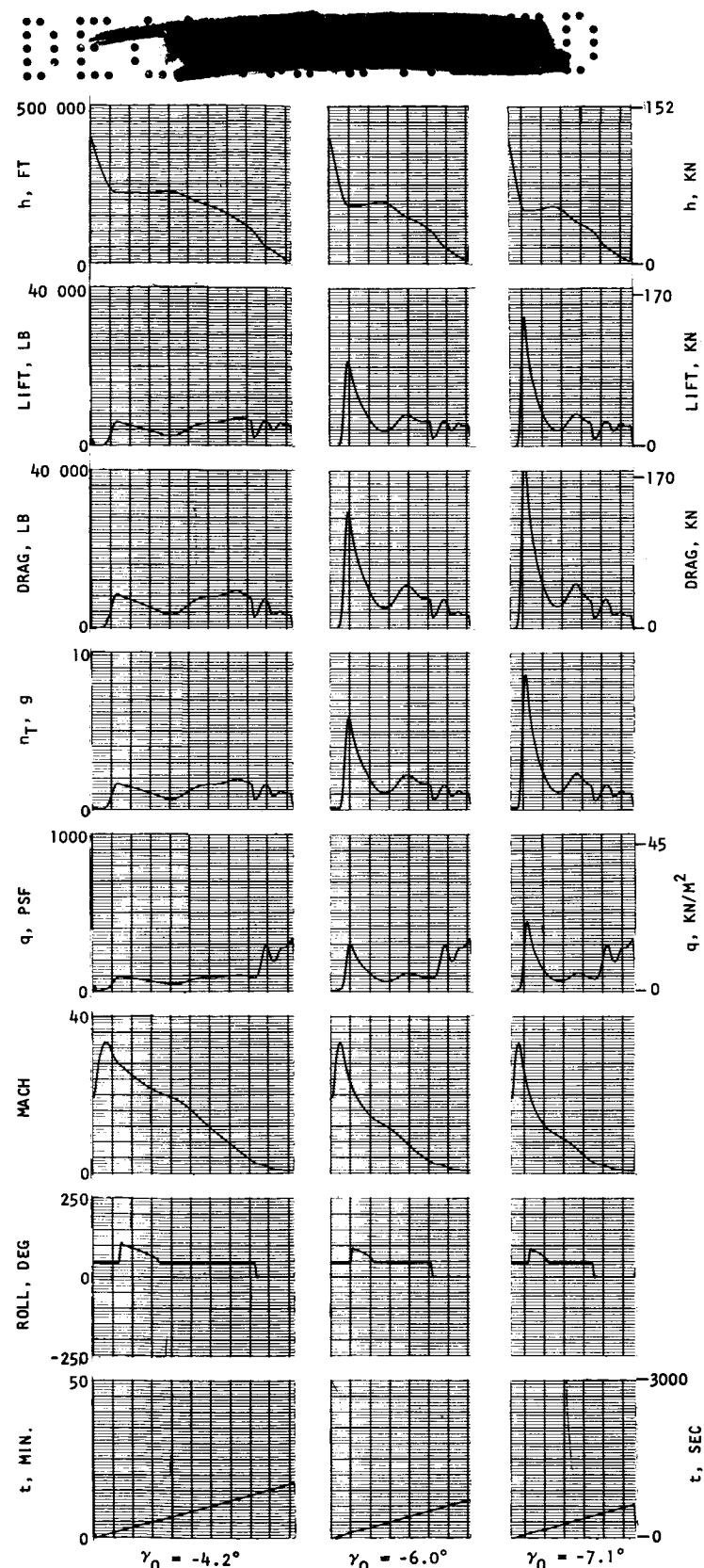
j) CONTINUED

FIGURE 39. --CONTINUED



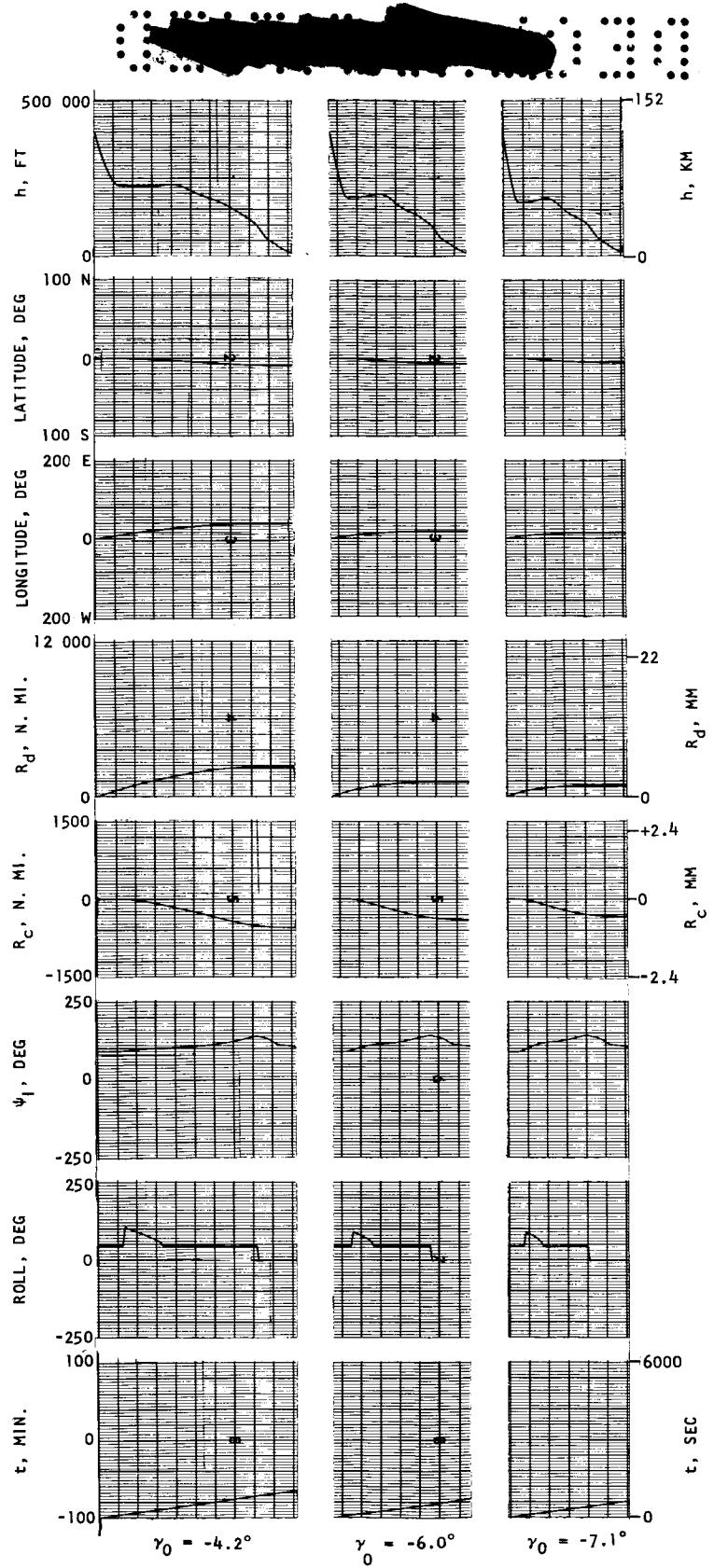
j) CONCLUDED

FIGURE 39. --CONTINUED



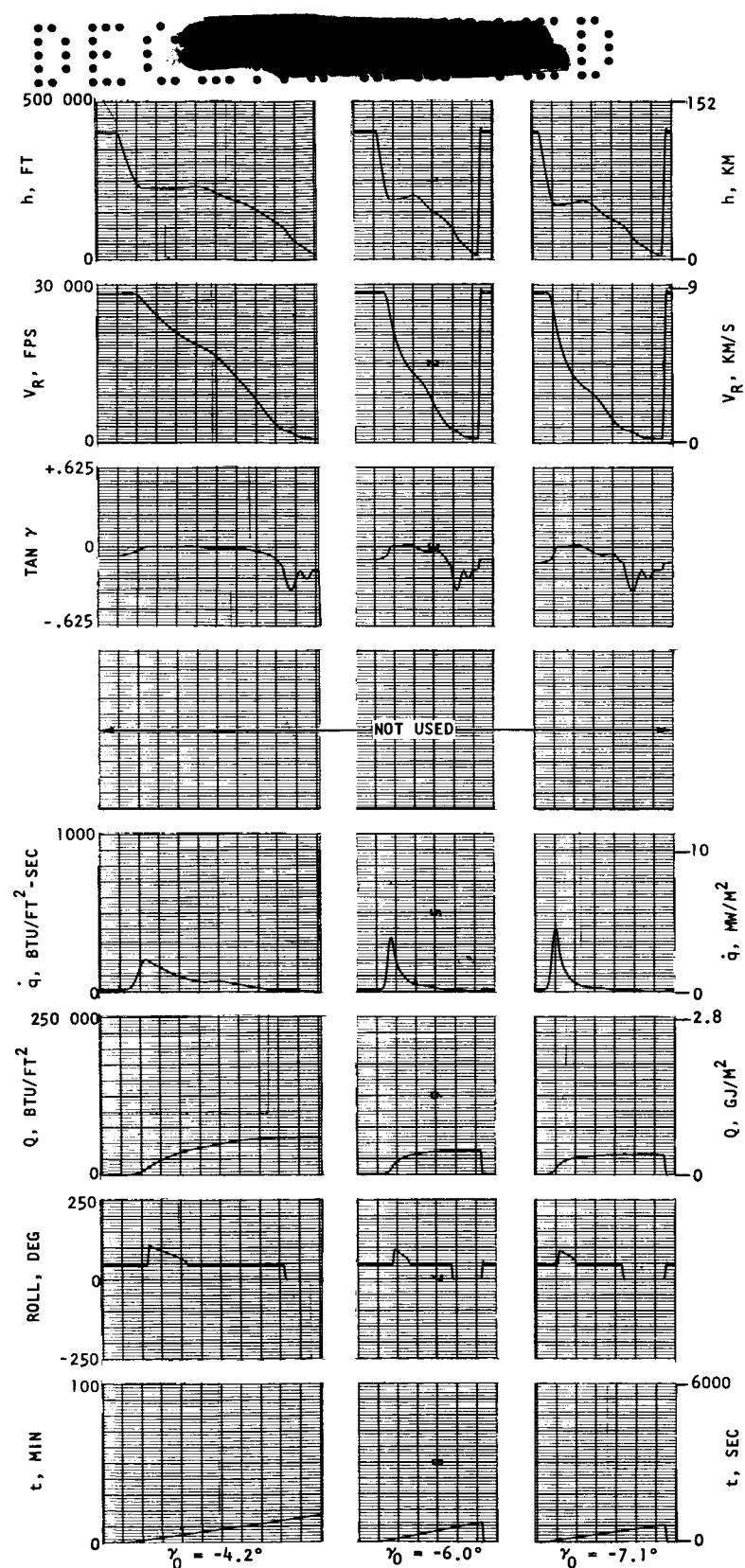
k) STRIP RECORDER DATA--L/D_{MIN.}, $\phi = 45^\circ$

FIGURE 39.--CONTINUED



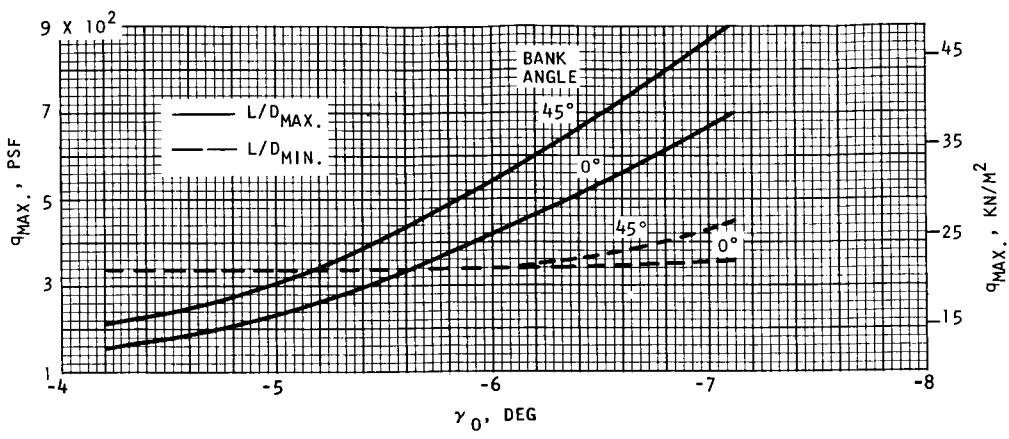
k) CONTINUED

FIGURE 39.--CONTINUED

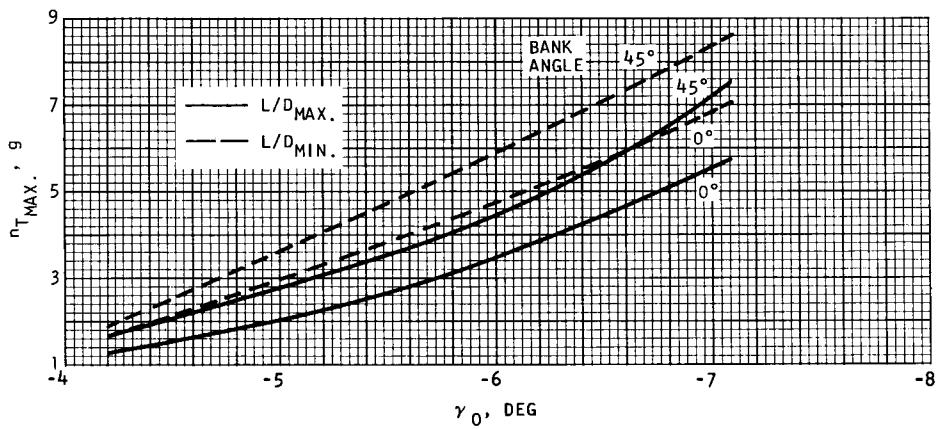


k) CONCLUDED

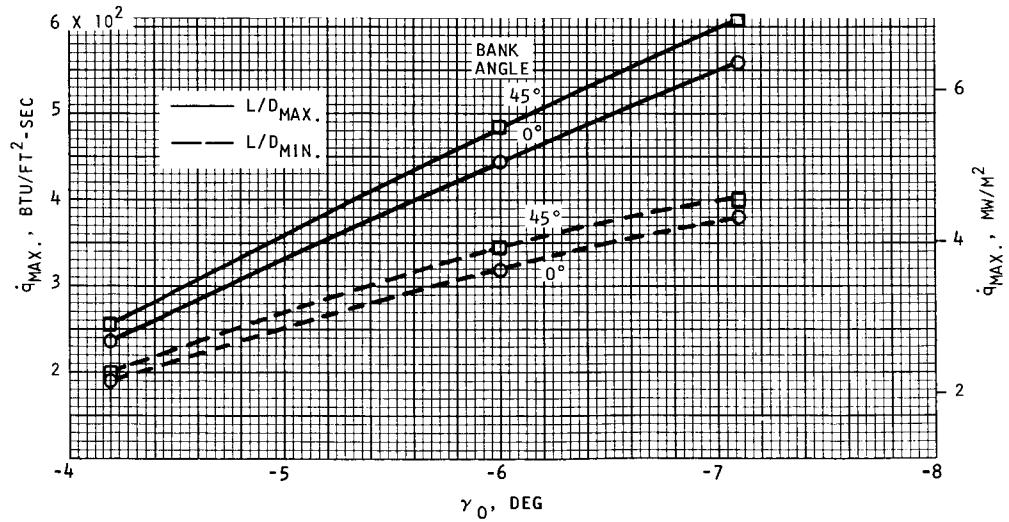
FIGURE 39.--CONTINUED



t-1) VARIATION OF q_{MAX} WITH ENTRY ANGLE

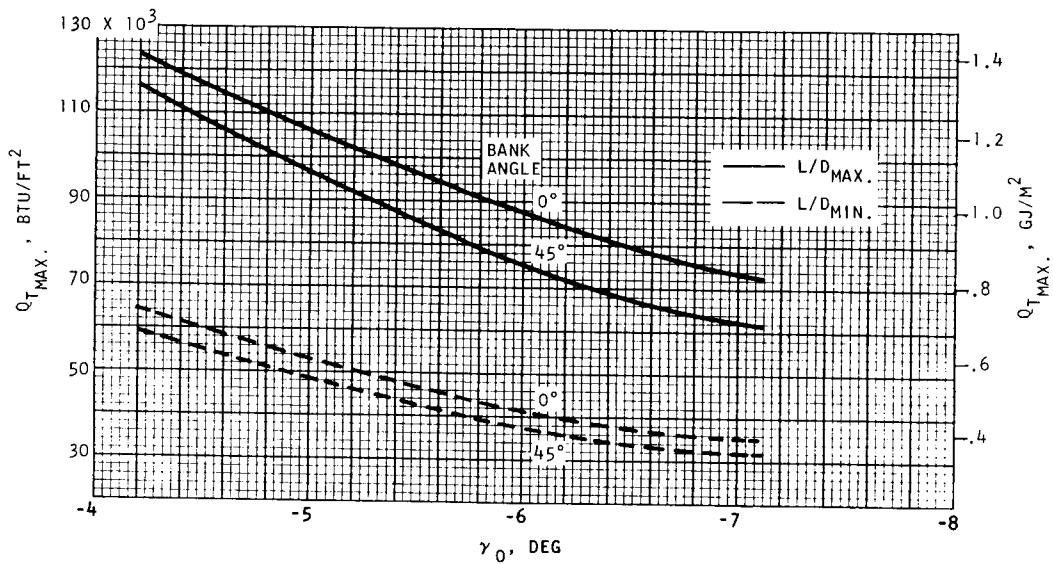


t-2) VARIATION OF $n_{T_{\text{MAX}}}$ WITH ENTRY ANGLE

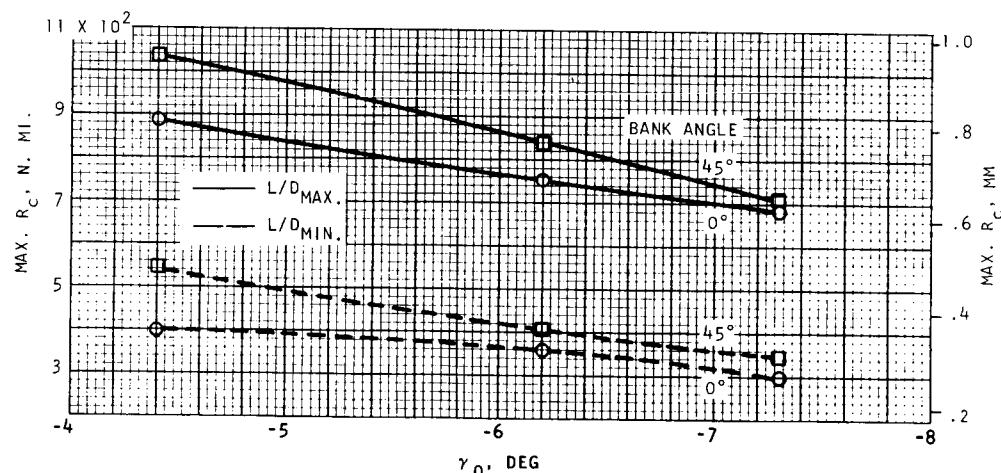


t-3) VARIATION OF $\dot{q}_{s_{\text{MAX}}}$ WITH ENTRY ANGLE

FIGURE 39.--CONTINUED

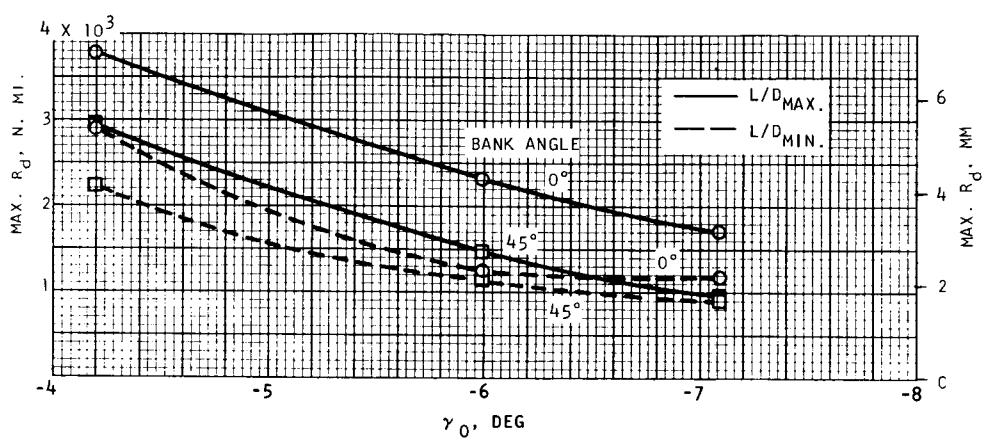


I-4) VARIATION OF $Q_T \text{ MAX}$ WITH ENTRY ANGLE

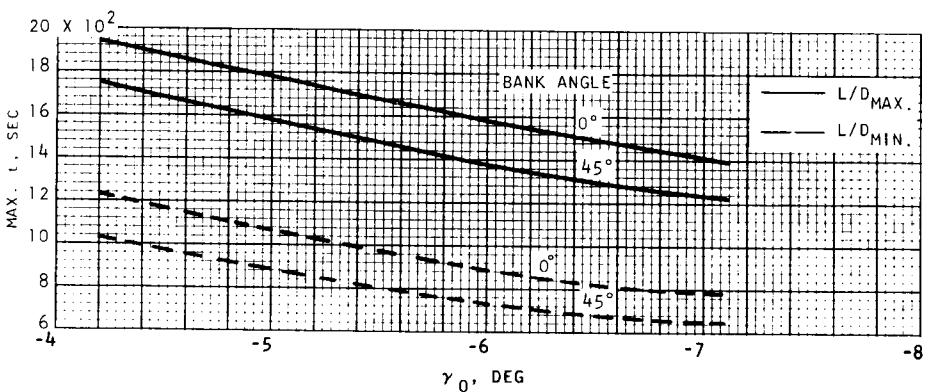


I-5) VARIATION OF $R_C \text{ MAX}$ WITH ENTRY ANGLE

FIGURE 39.--CONTINUED

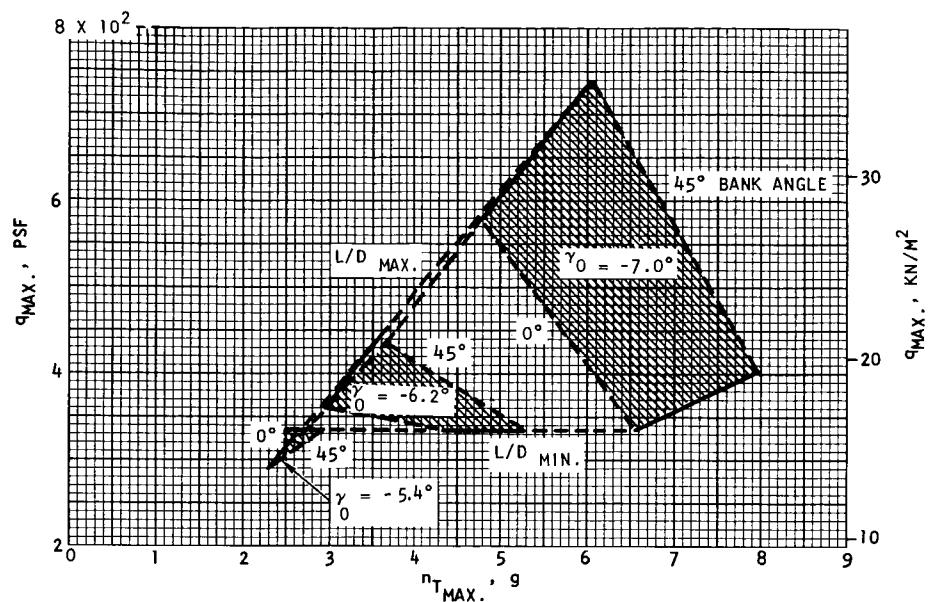


I-6) VARIATION OF R_d WITH ENTRY ANGLE
MAX.

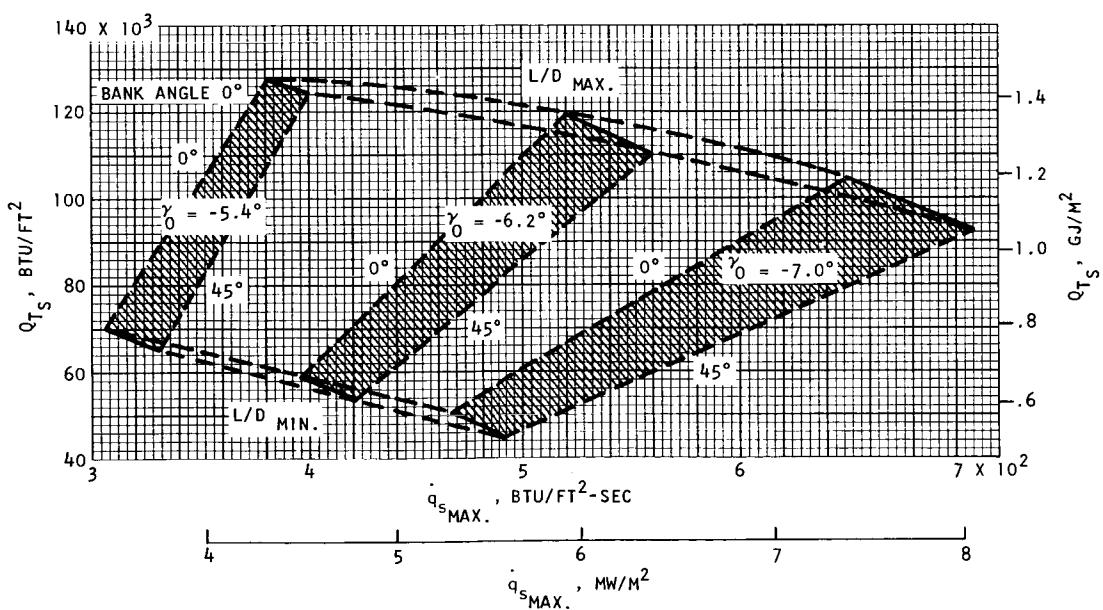


I-7) VARIATION OF $t_{MAX.}$ WITH ENTRY ANGLE

FIGURE 39.--CONCLUDED

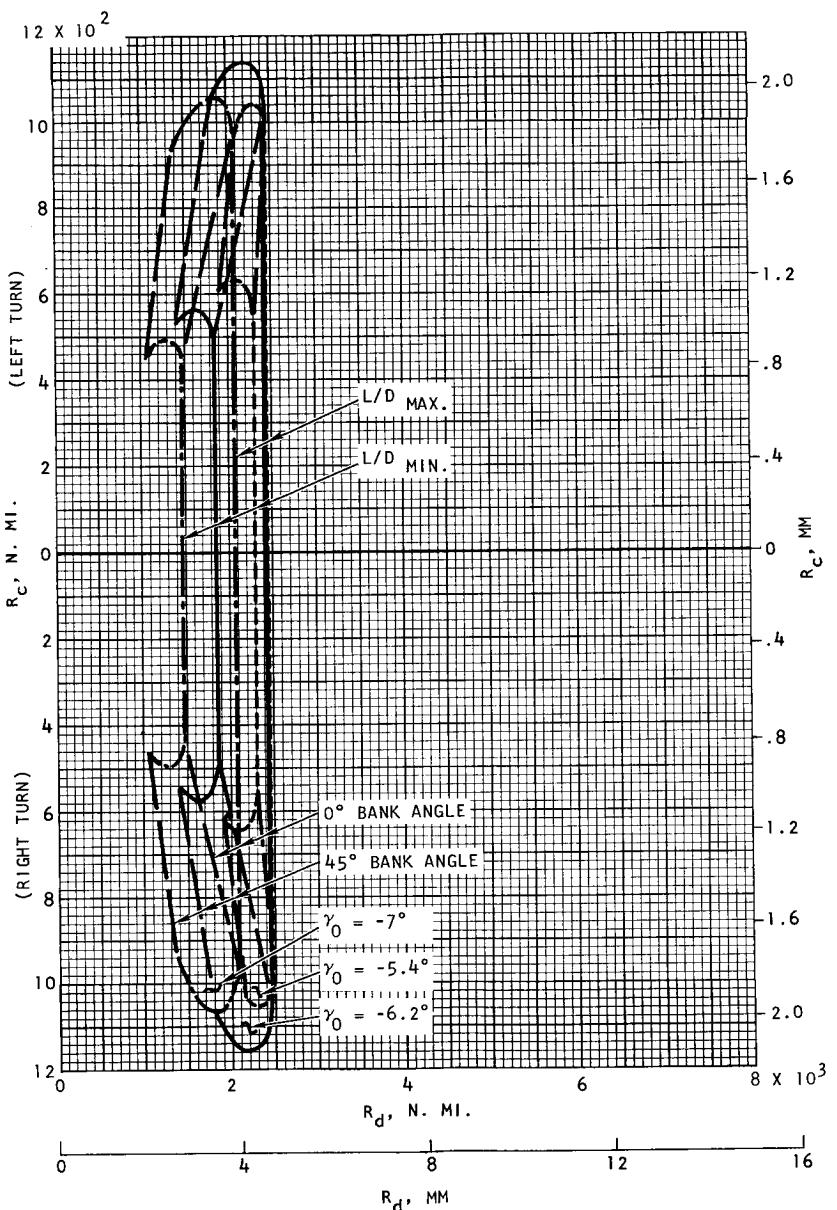


a) $q_{\text{MAX.}}$ VERSUS $n_{\text{T MAX.}}$



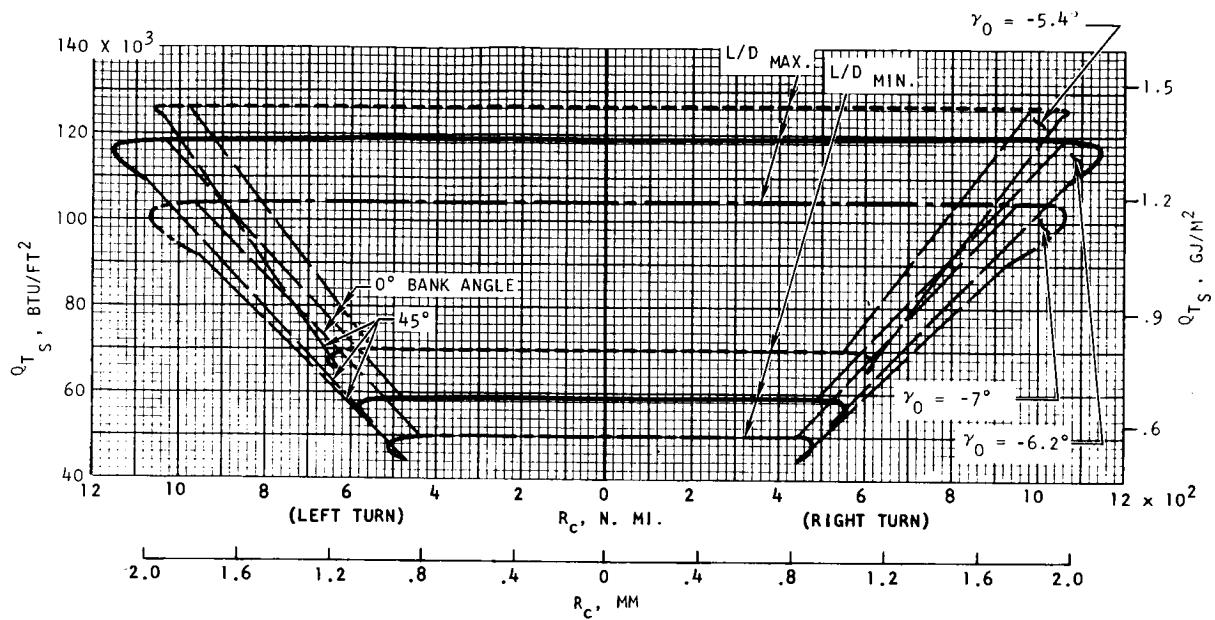
b) Q_{T_S} VERSUS $q_{s \text{ MAX.}}$

FIGURE 40. ENTRY DATA: $V_I = 34\ 000$ FPS (10.4 KM/SEC)

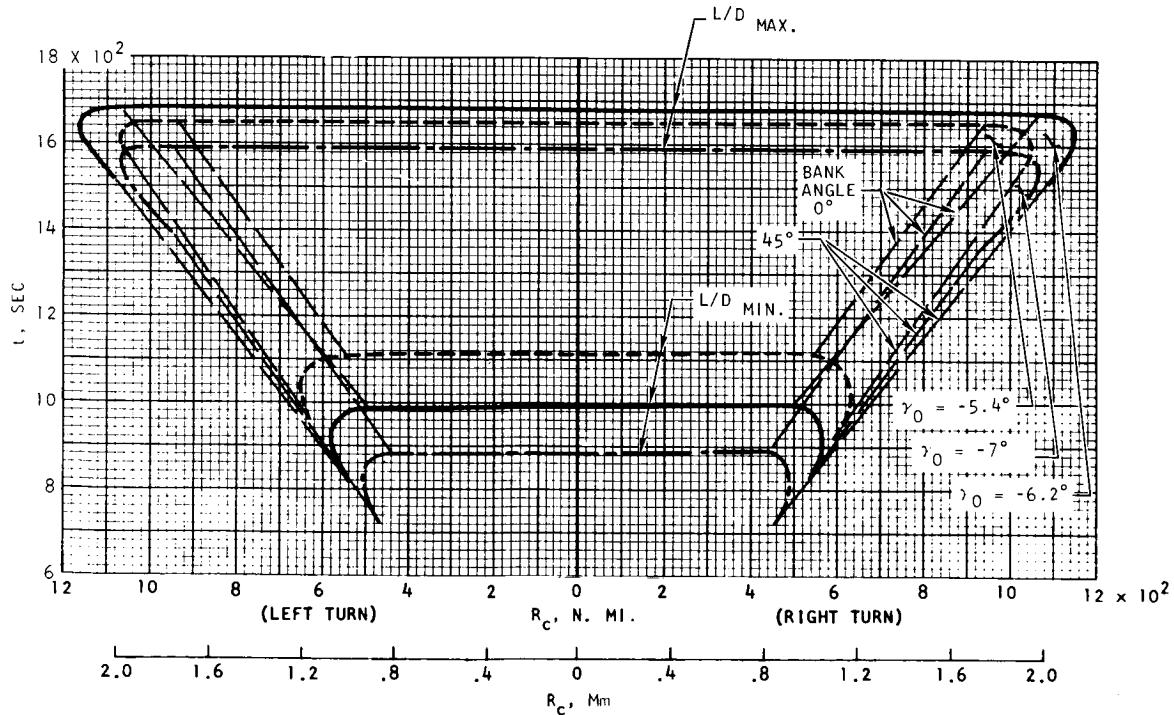


c) R_c VERSUS R_d

FIGURE 40. --CONTINUED

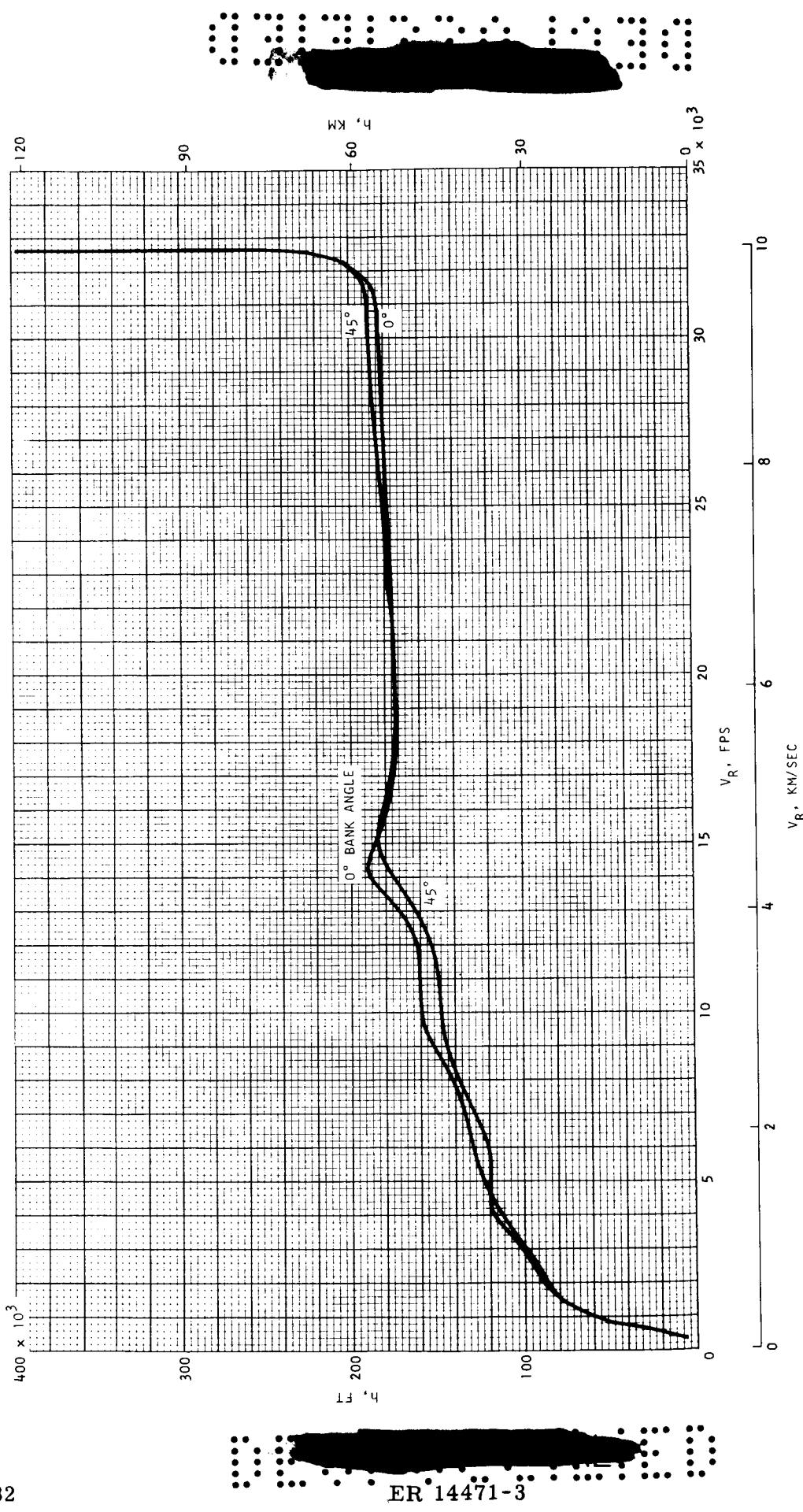


d) Q_{TS} VERSUS R_c



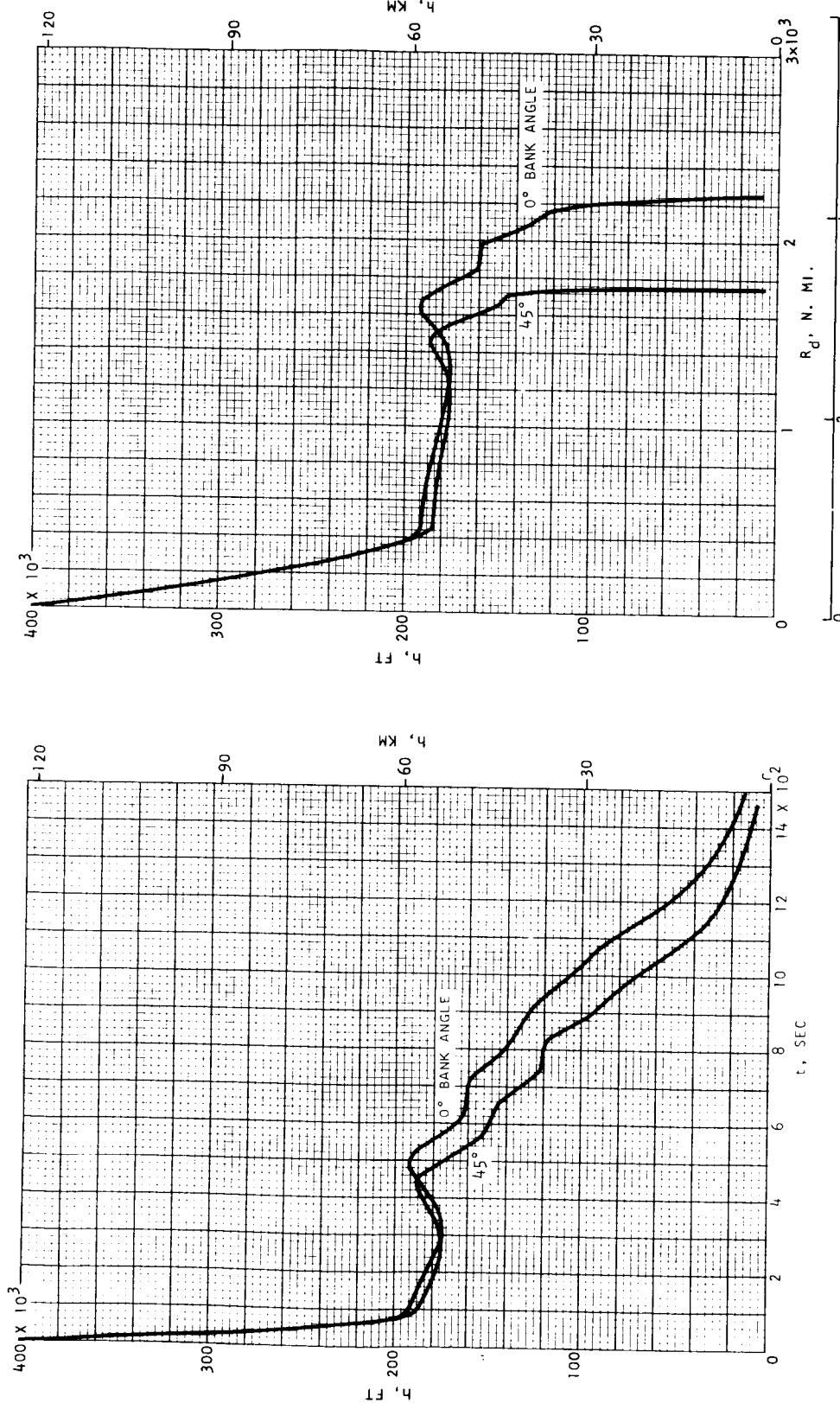
e) t VERSUS R_c

FIGURE 40.--CONTINUED



f-1) h VERSUS V_R FOR $\gamma = -6.2^\circ$ AND L/D_{MAX} .

FIGURE 40. --CONTINUED



f-2) h VERSUS t FOR $\gamma = -6.2^\circ$ AND L/D_{MAX} .

f-3) h VERSUS R_d FOR $\gamma = -6.2^\circ$ AND L/D_{MAX} .

FIGURE 40. --CONTINUED

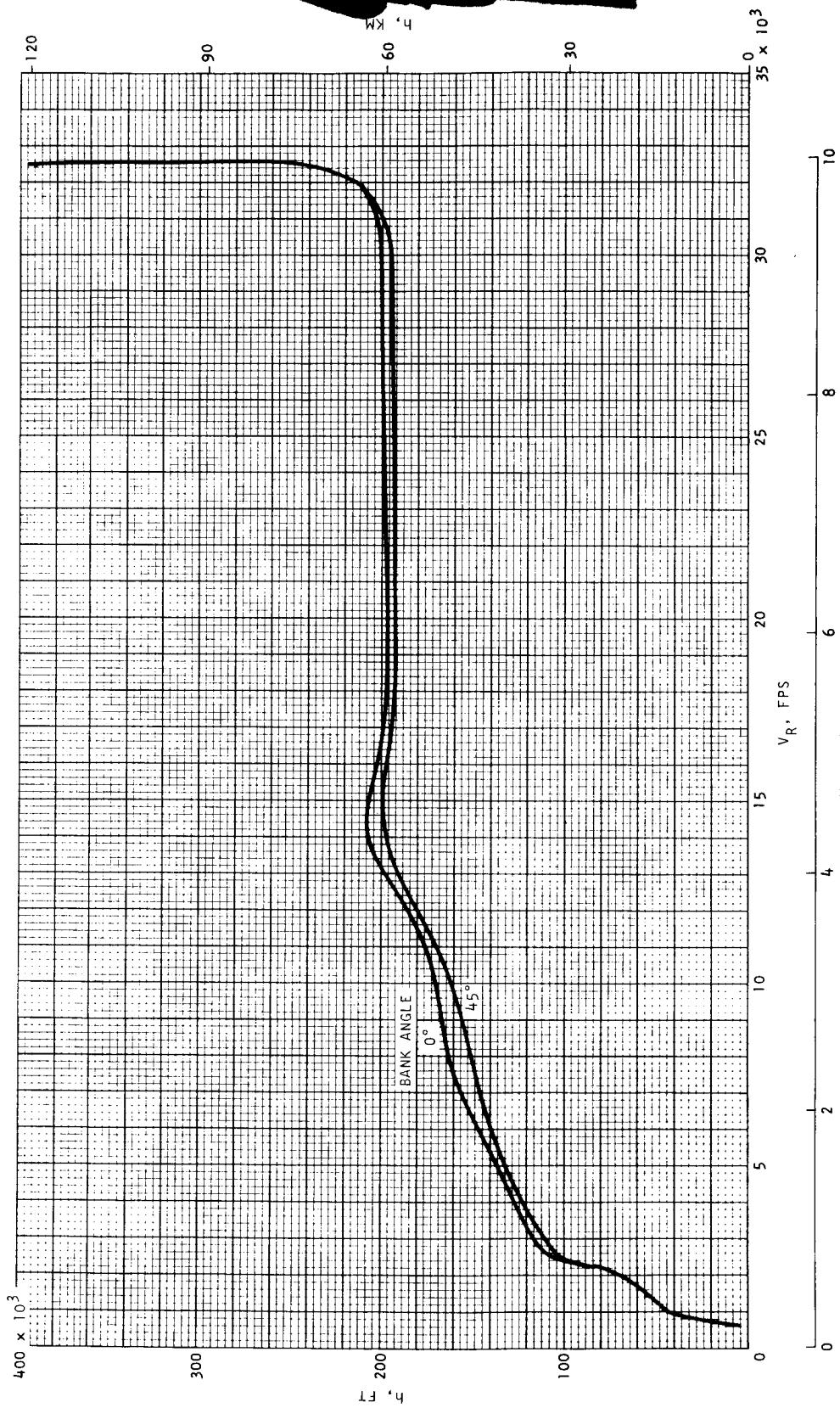
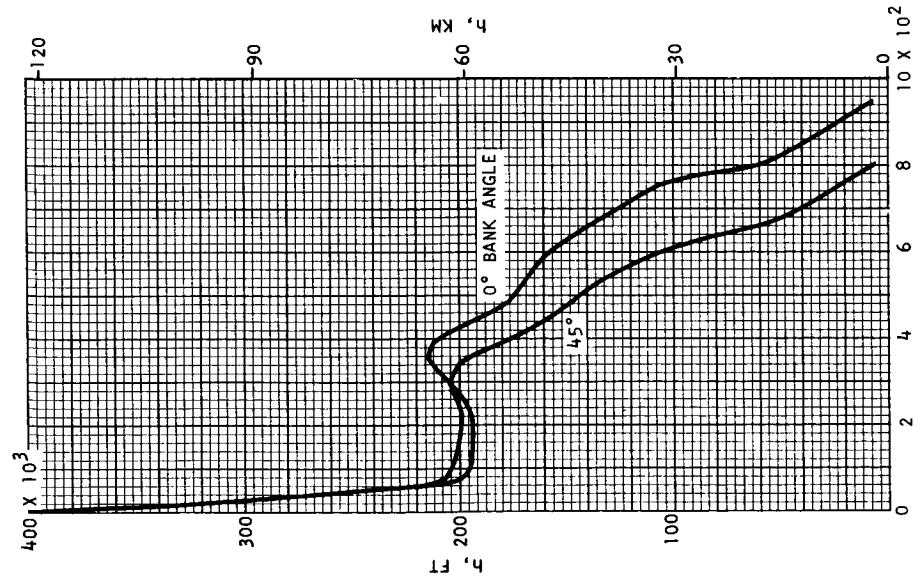
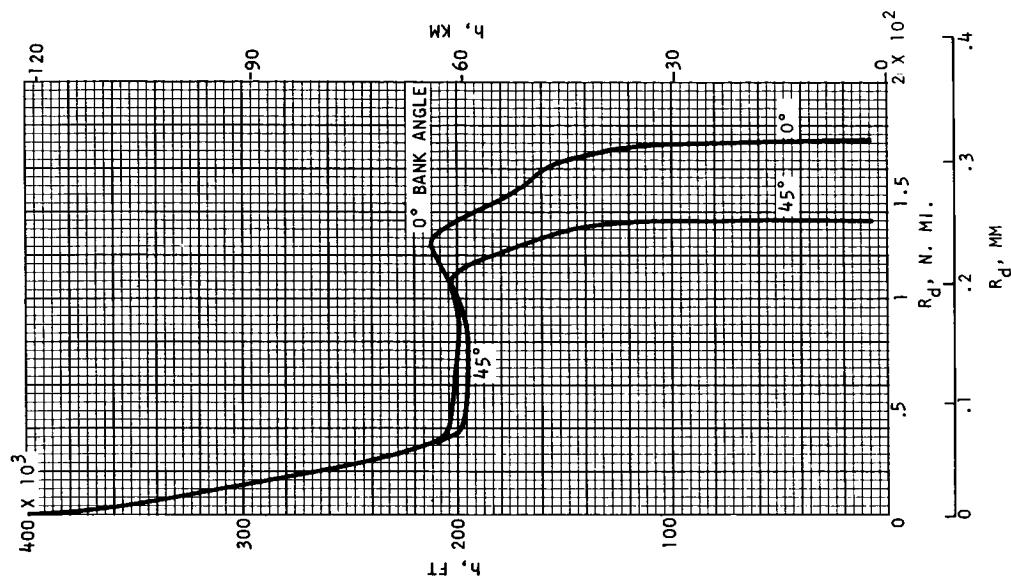


FIGURE 40.--CONTINUED

g-1) h VERSUS V_R FOR $\gamma = -6.2^\circ$ AND L/D_{MIN} .

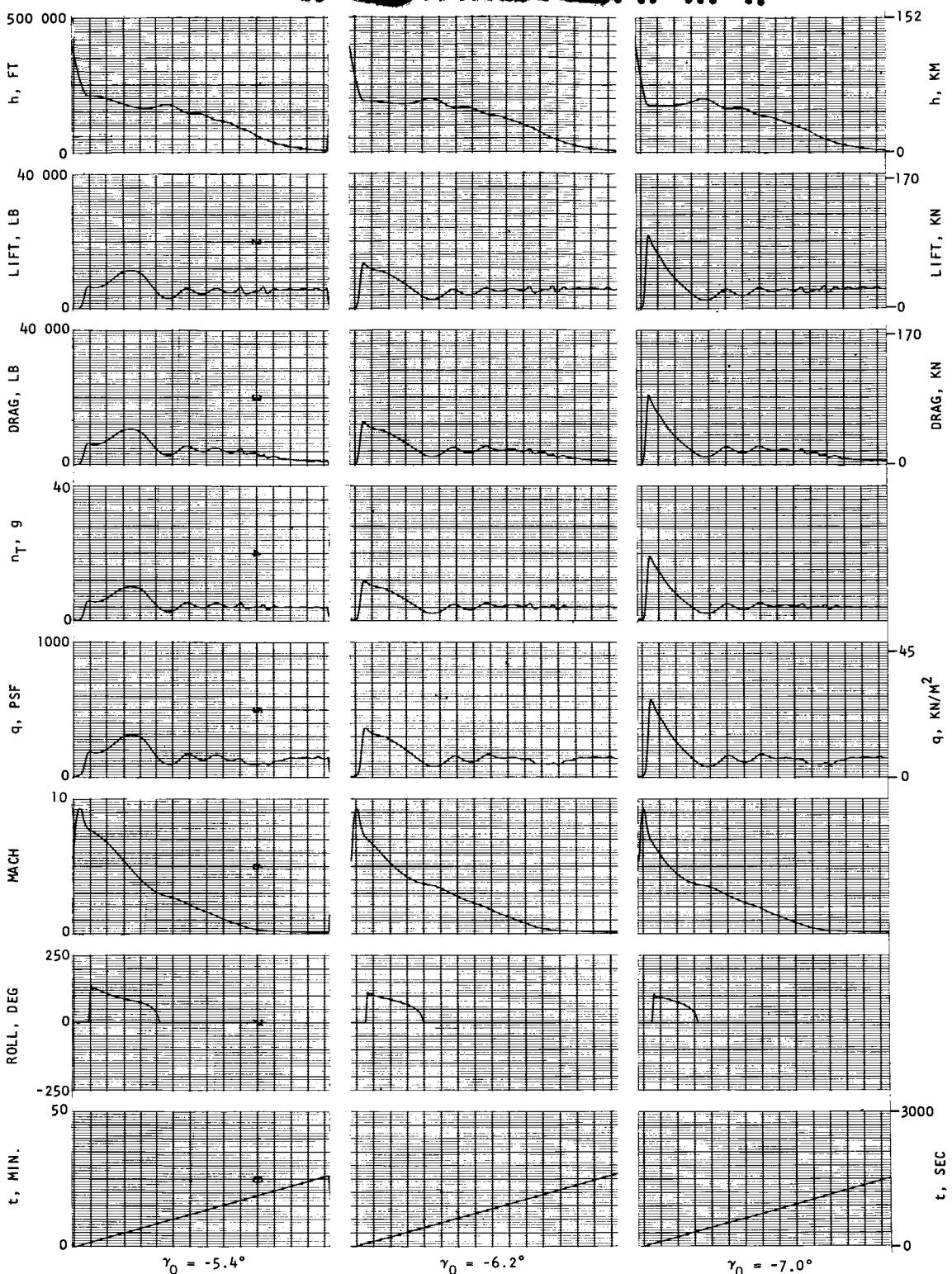


g-2) h VERSUS t FOR $\gamma = -6.2^\circ$ AND L/D_{MIN} .



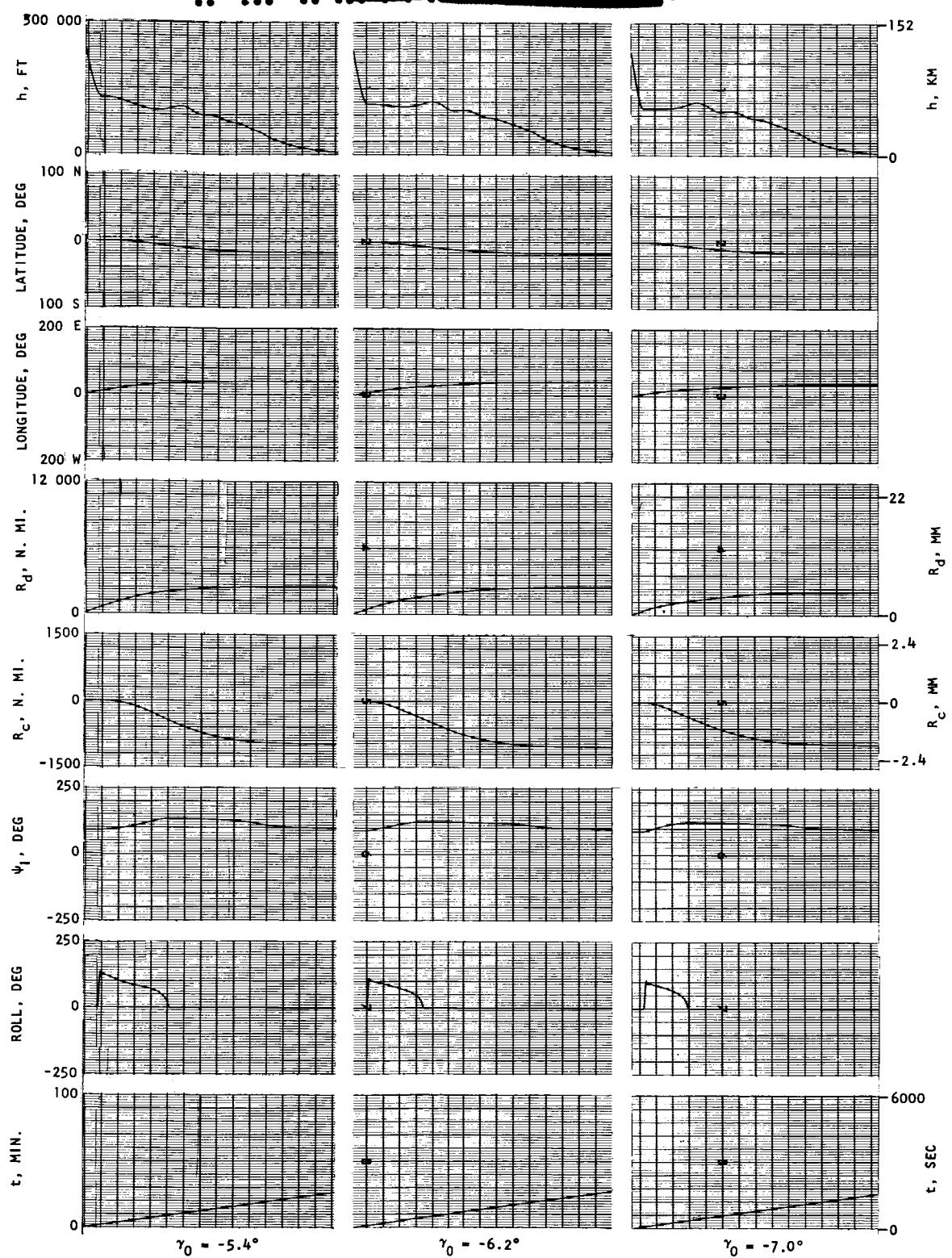
g-3) h VERSUS R_d FOR $\gamma = -6.2^\circ$ AND L/D_{MIN} .

FIGURE 40.--CONTINUED



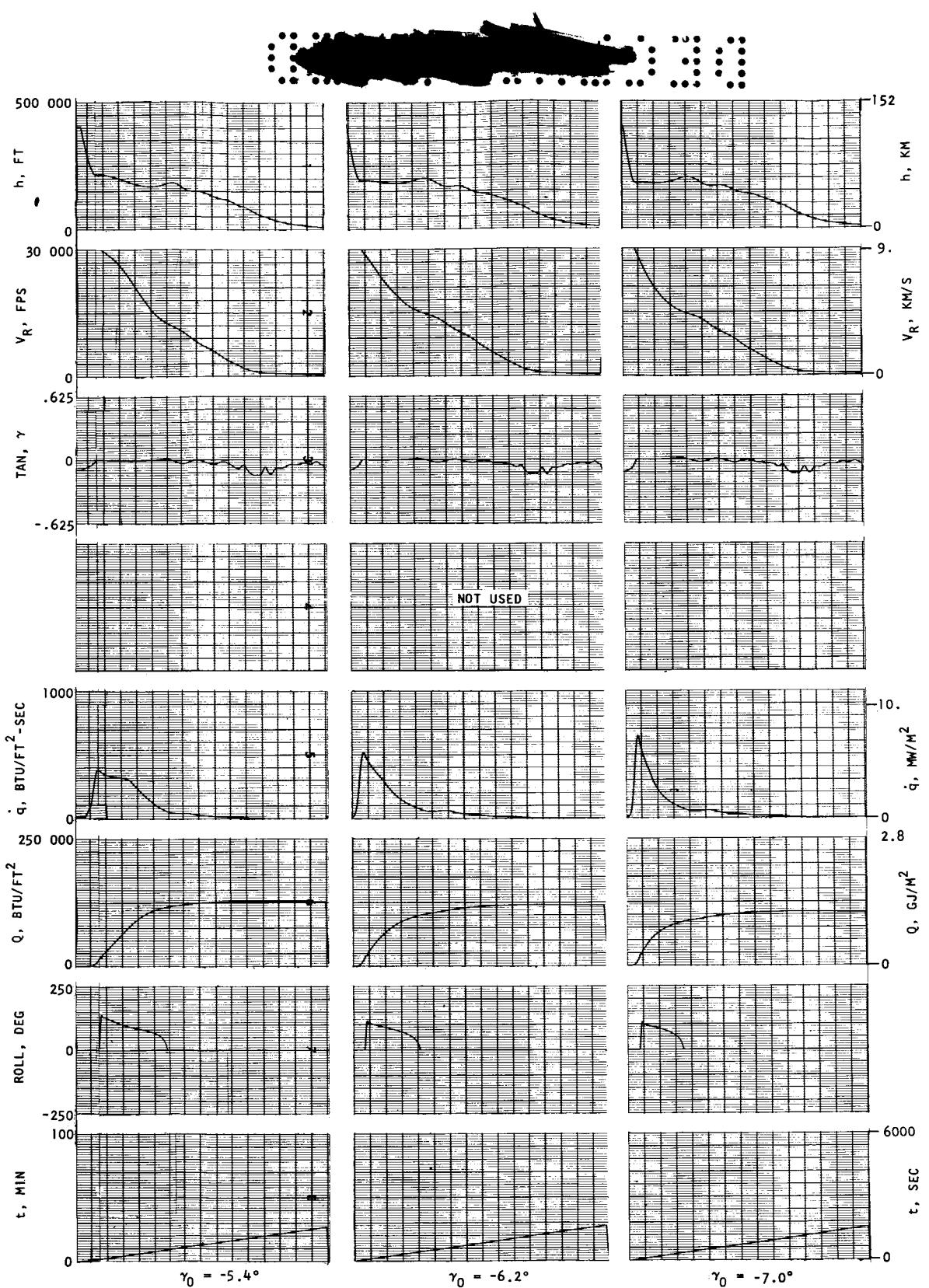
h) STRIP RECORDER DATA--L/D_{MAX.}, $\phi = 0^\circ$

FIGURE 40.--CONTINUED



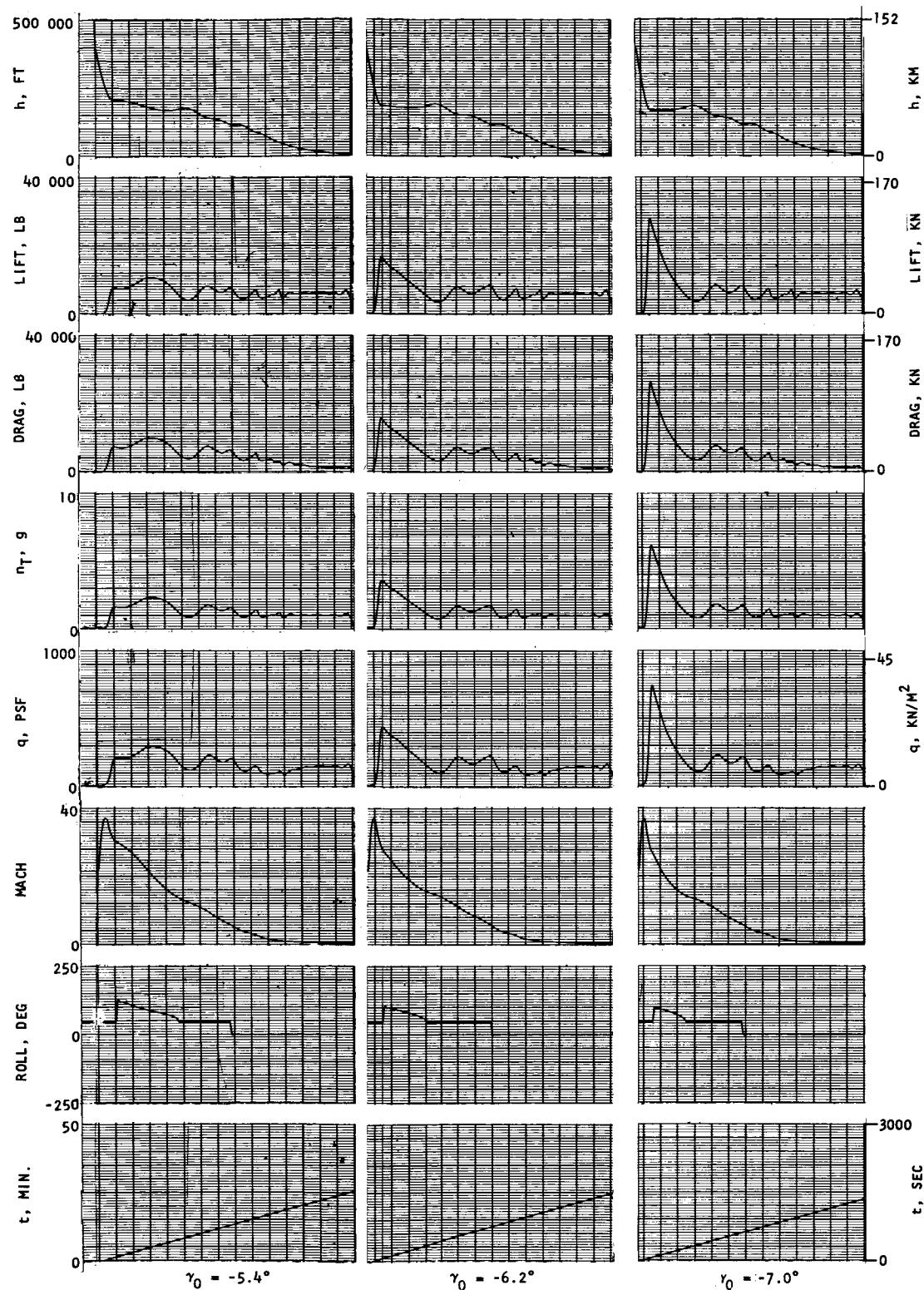
h) CONTINUED

FIGURE 40.--CONTINUED



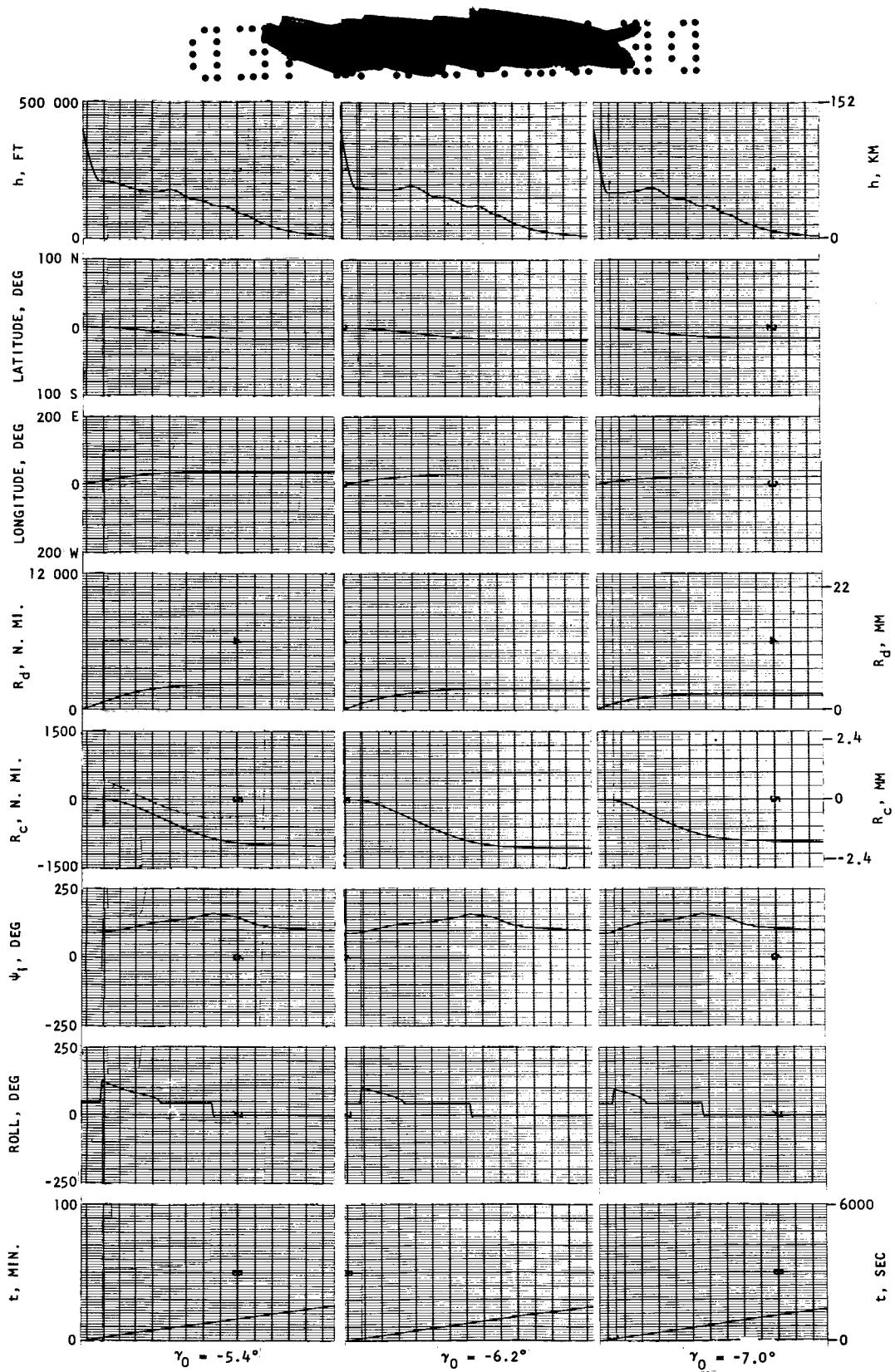
h) CONCLUDED

FIGURE 40.--CONTINUED



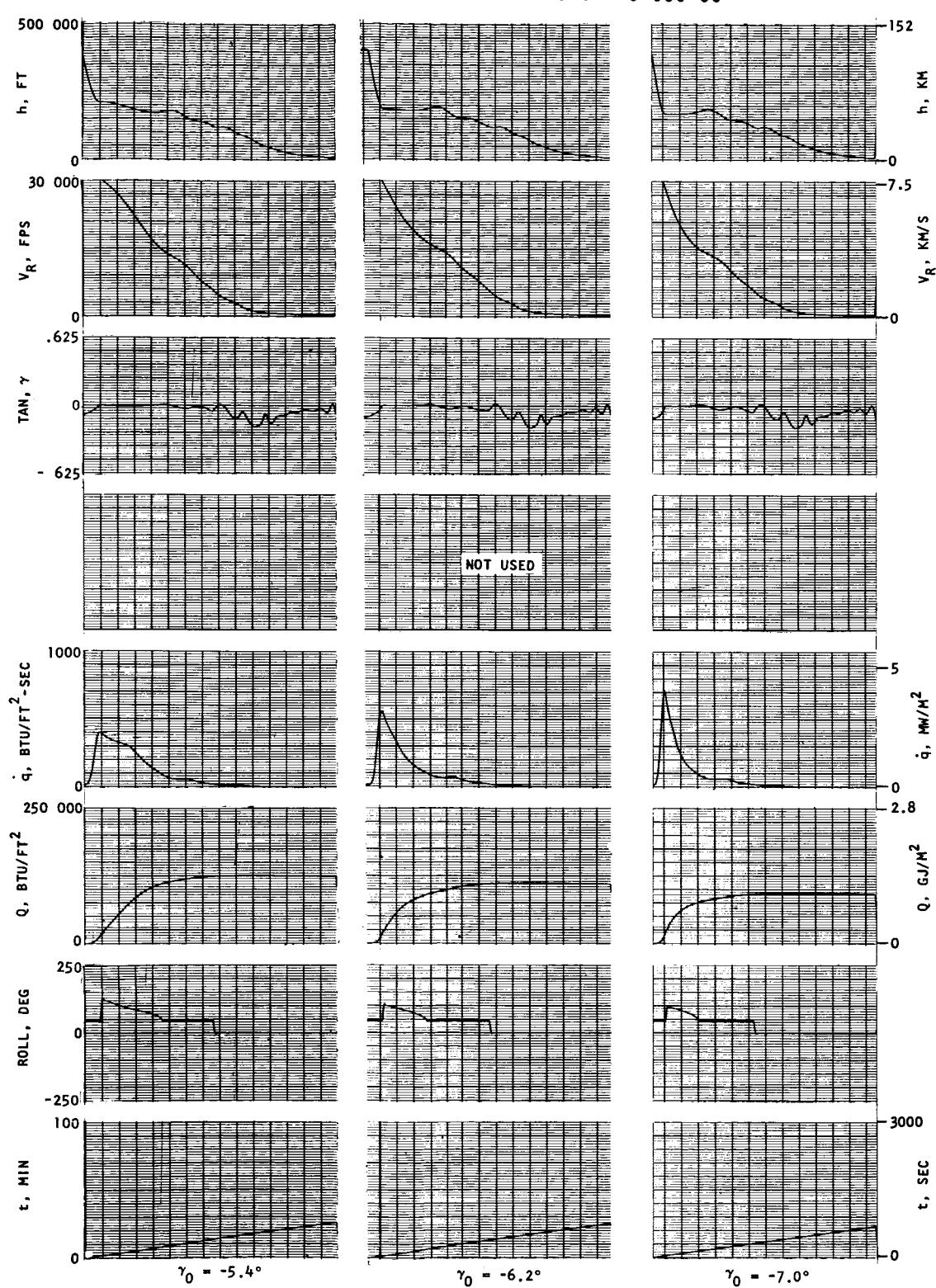
i) STRIP RECORDER DATA--L/D_{MAX.}, $\phi = 45^\circ$

FIGURE 40.--CONTINUED



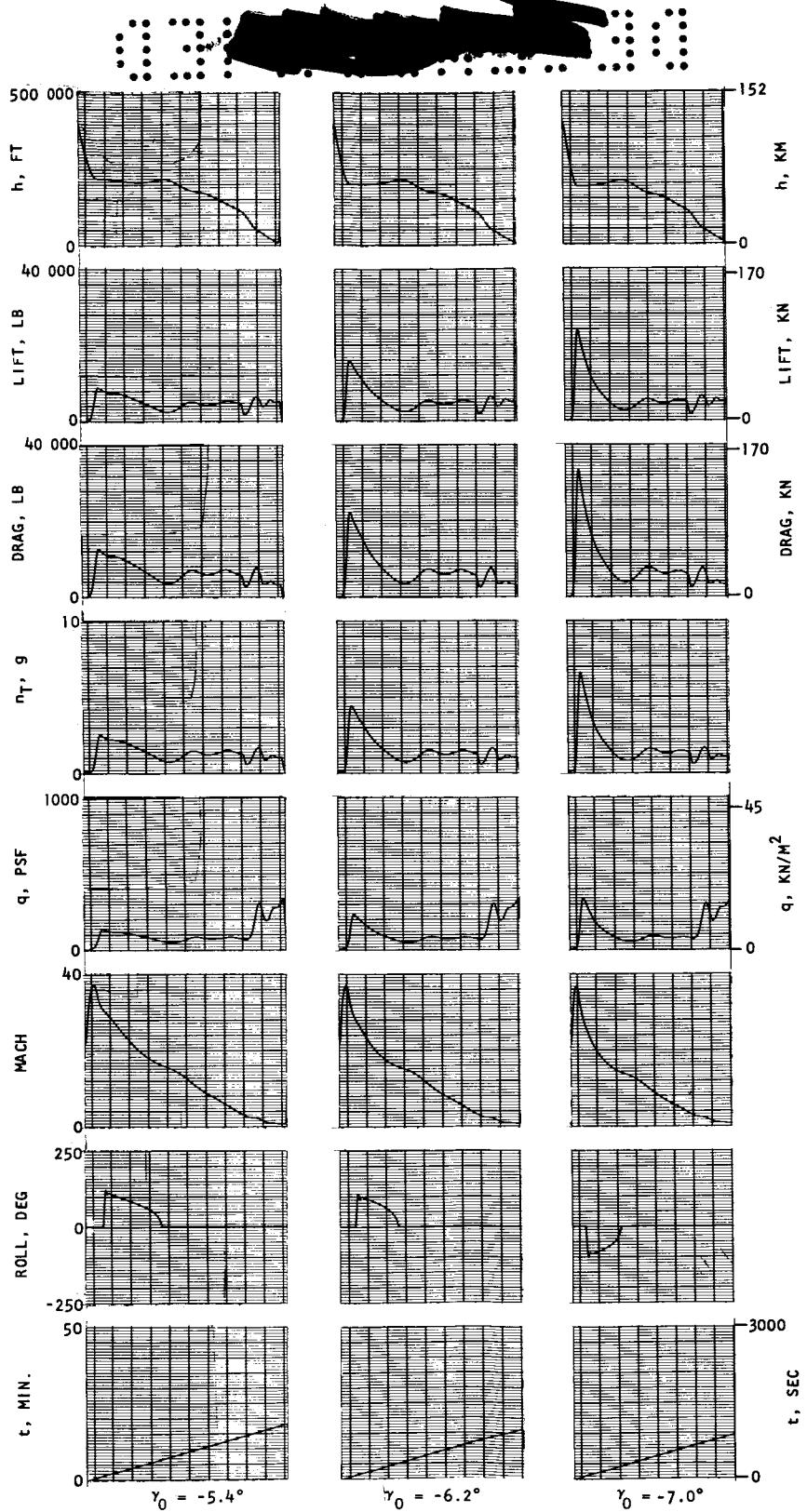
i) CONTINUED

FIGURE 40.--CONTINUED



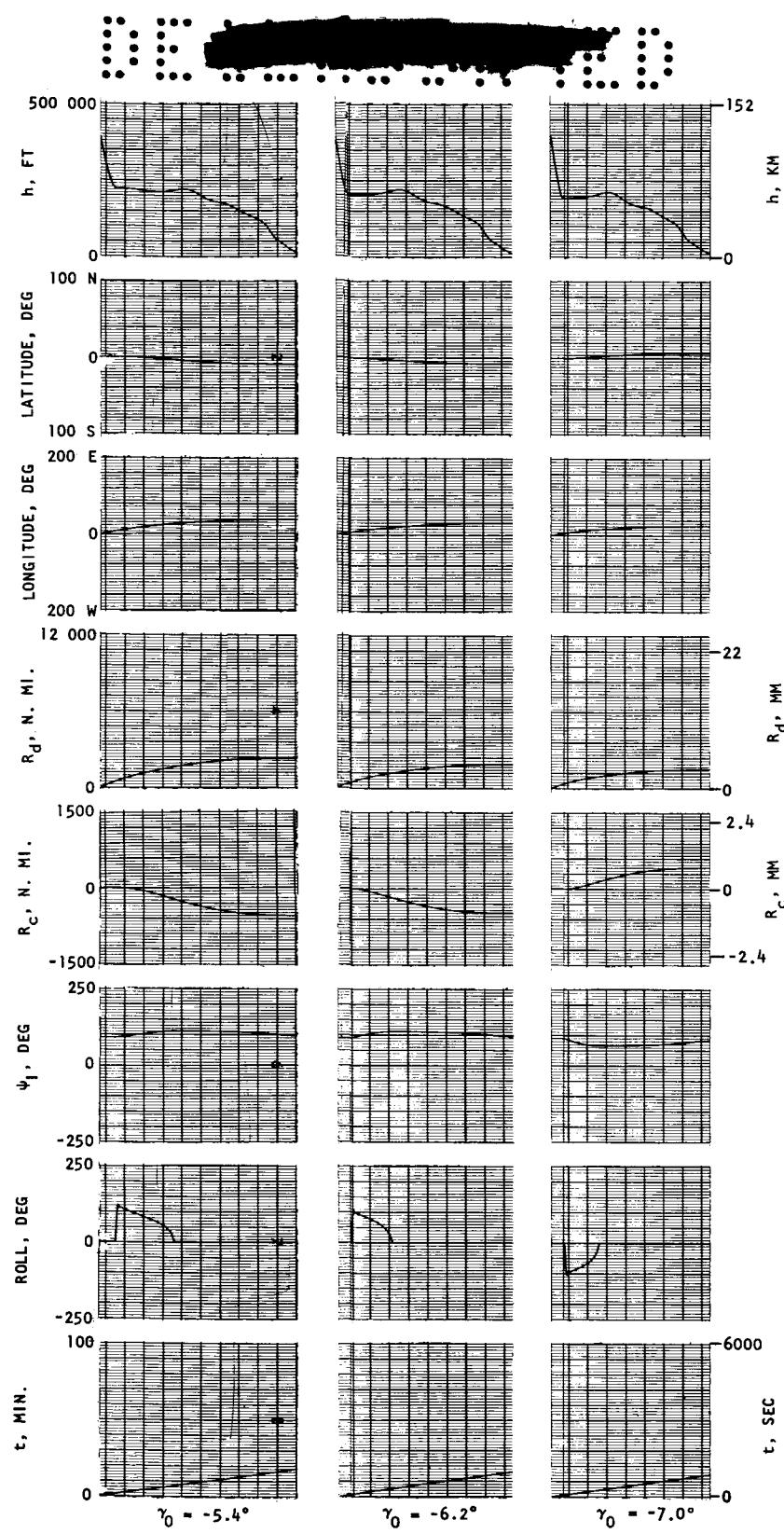
i) CONCLUDED

FIGURE 40.--CONTINUED



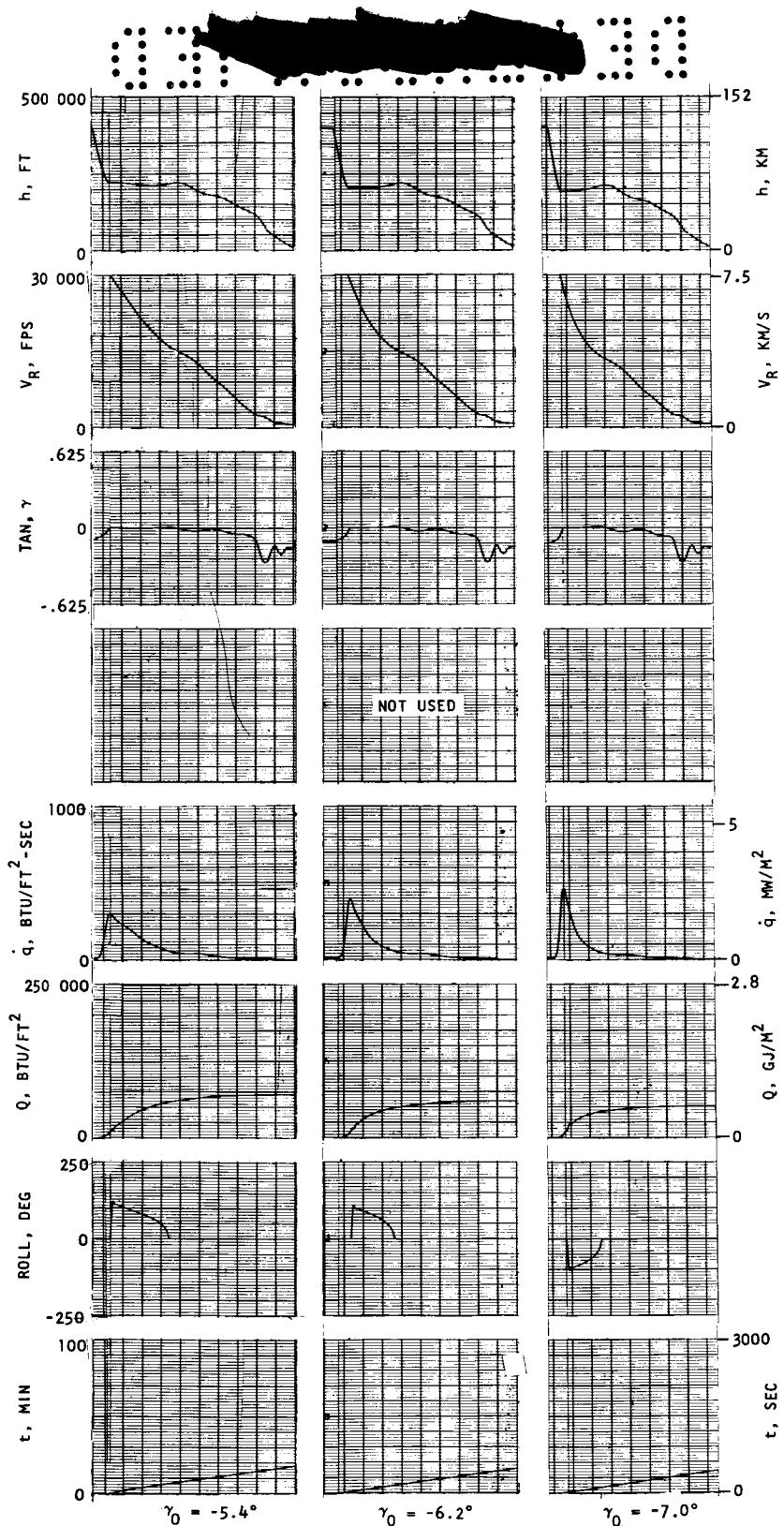
j) STRIP RECORDER DATA--L/D_{MIN.}, $\phi = 0^\circ$

FIGURE 40.--CONTINUED



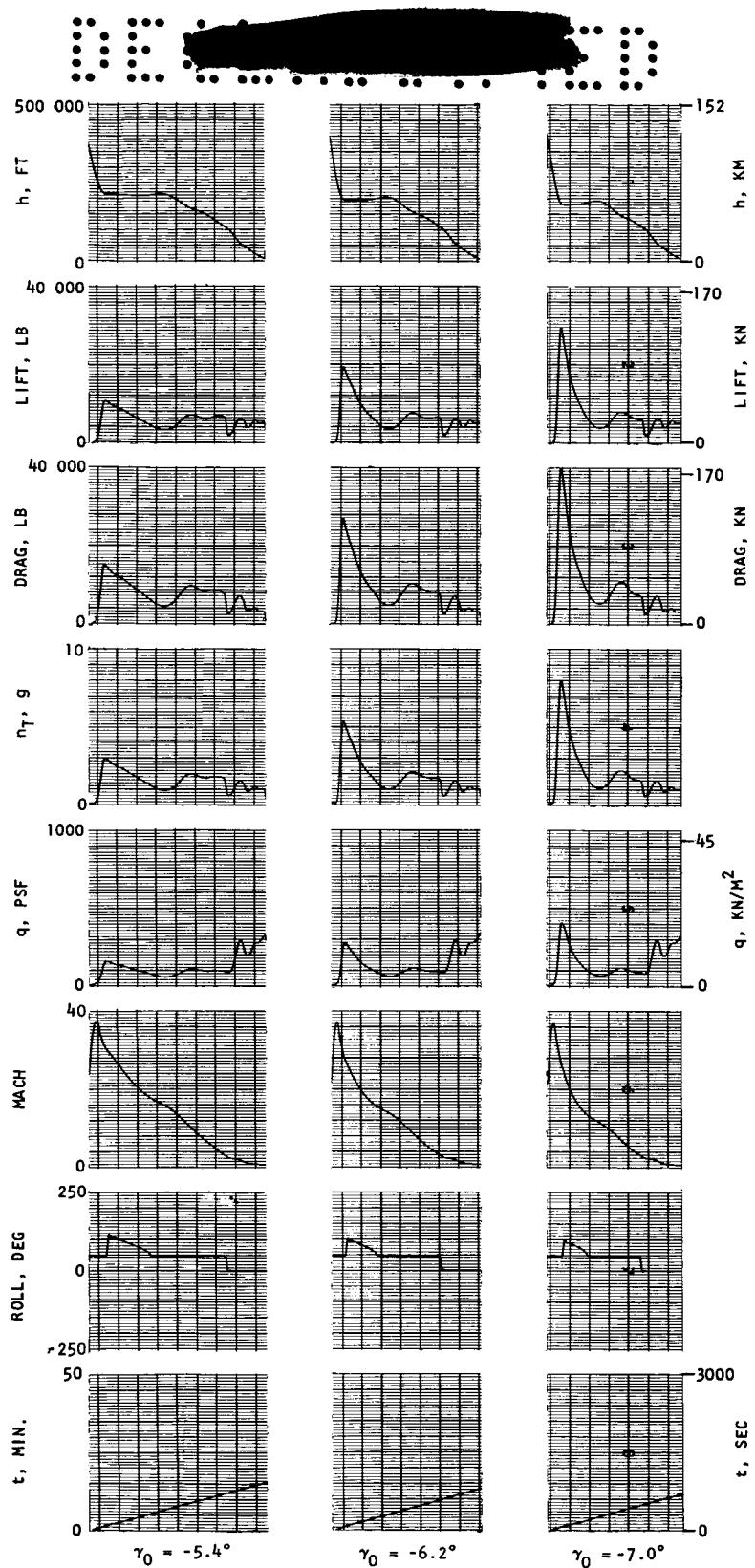
CONTINUED

FIGURE 40.--CONTINUED



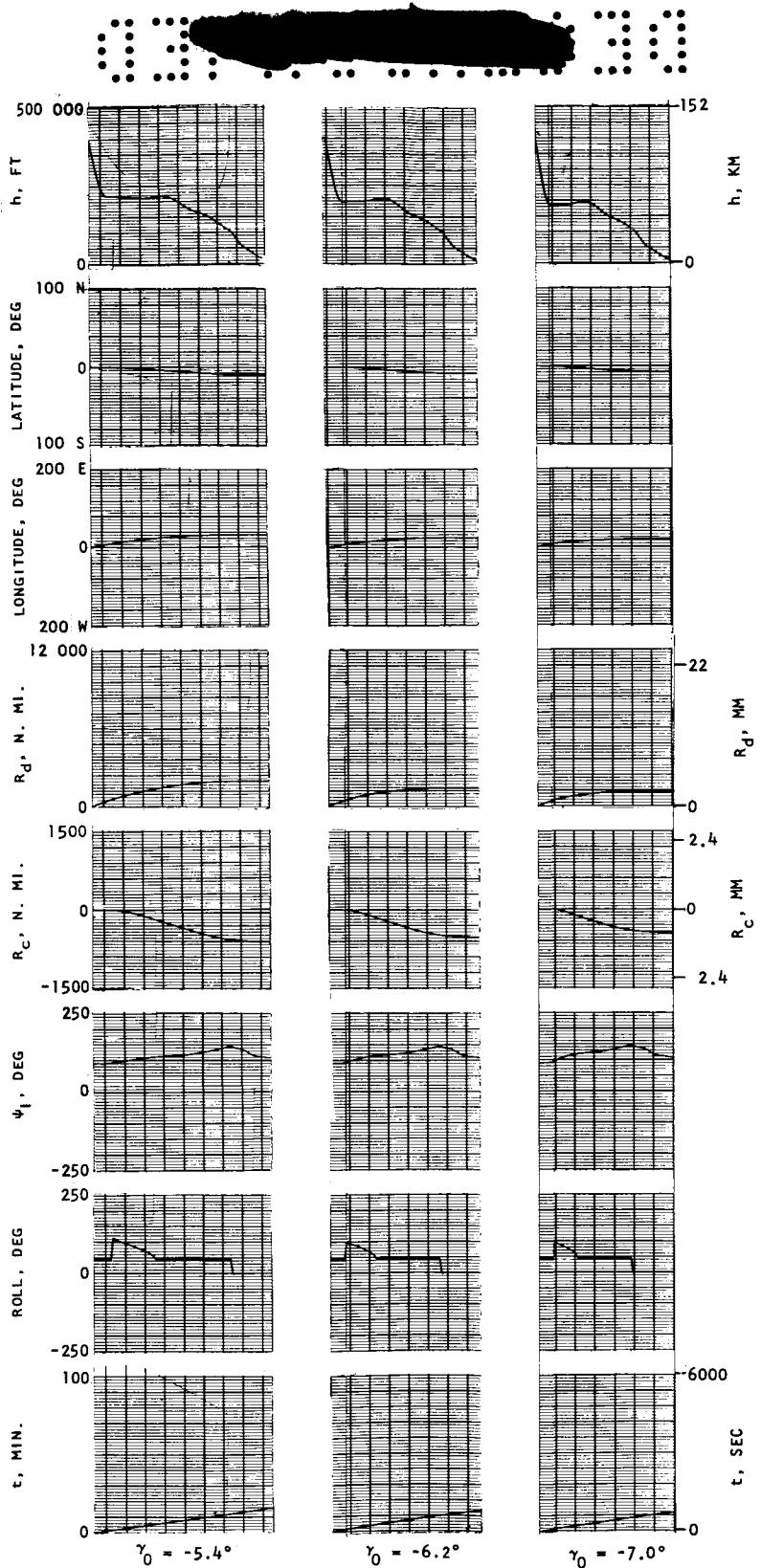
j) CONCLUDED

FIGURE 40.--CONTINUED



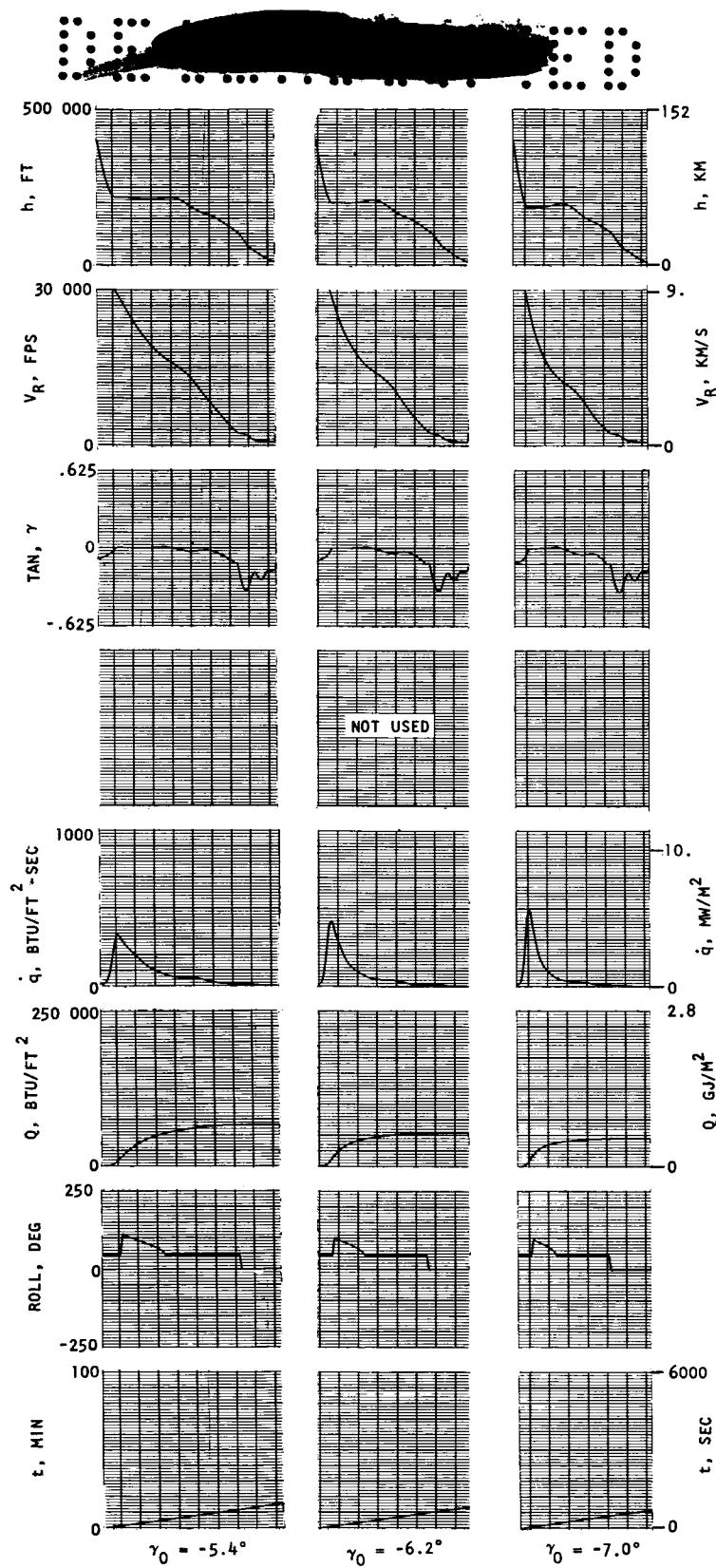
k) STRIP RECORDER DATA--L/D_{MIN.}, $\phi = 45^\circ$

FIGURE 40.--CONTINUED



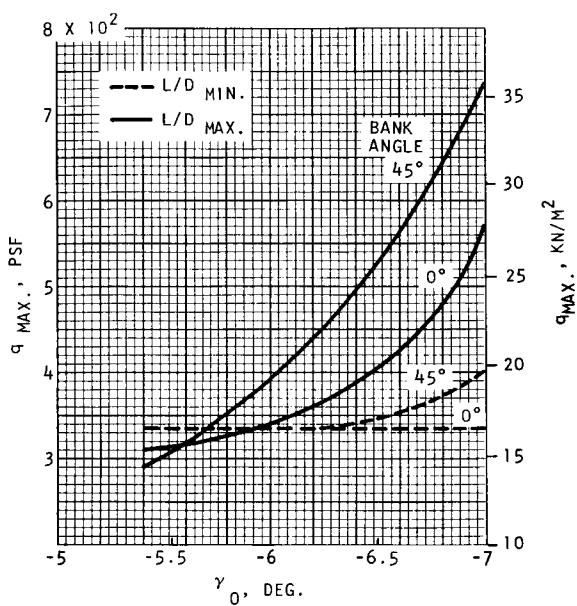
k) CONTINUED

FIGURE 40.--CONTINUED

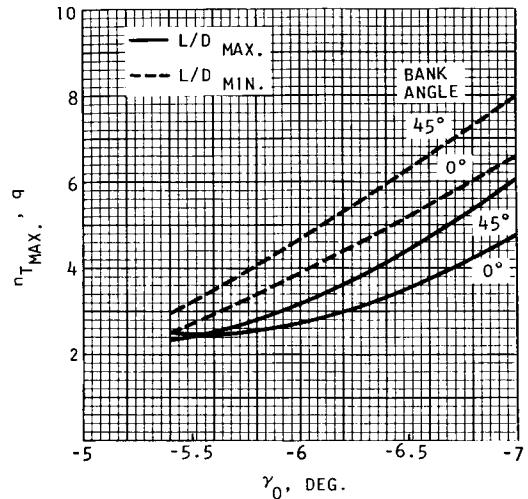


k) CONCLUDED

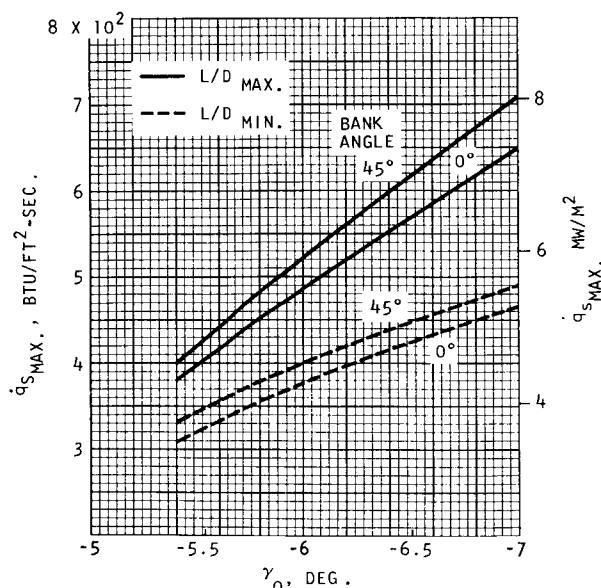
FIGURE 40.--CONTINUED



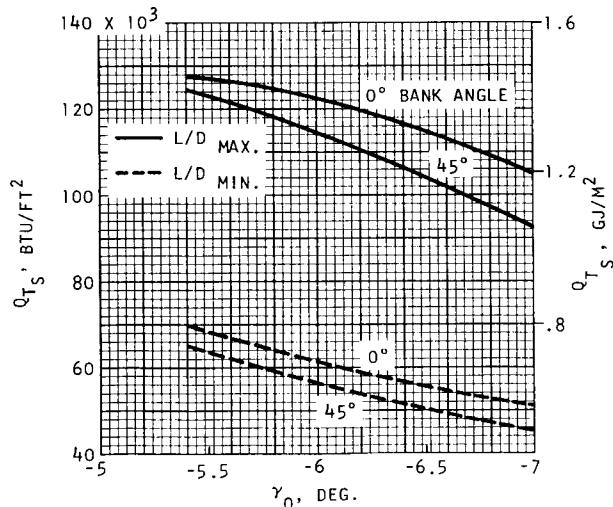
I-1) VARIATION OF $q_{\text{MAX.}}$ WITH ENTRY ANGLE



I-2) VARIATION OF $n_{T_{\text{MAX.}}}$ WITH ENTRY ANGLE

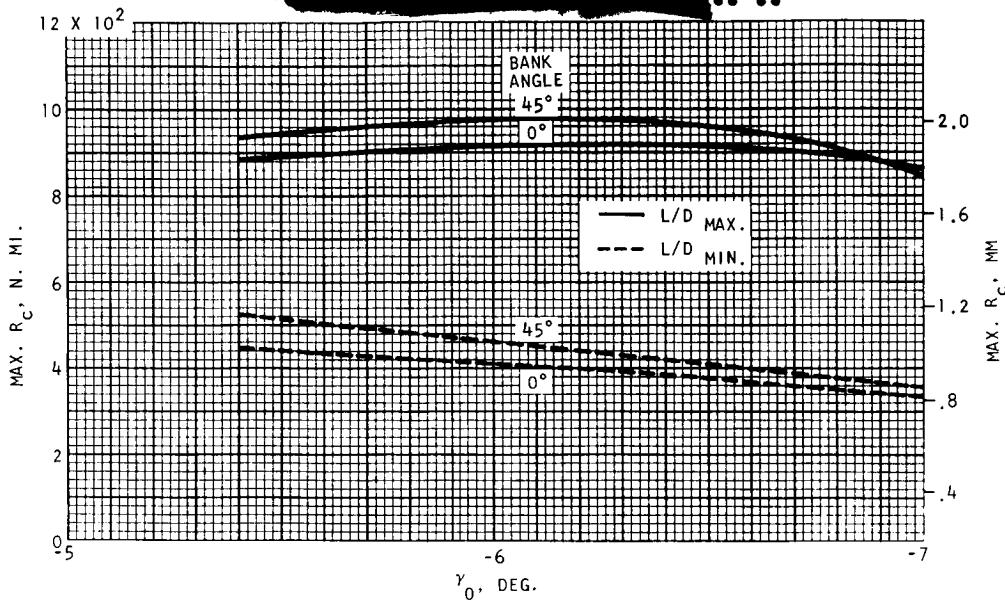


I-3) VARIATION OF $q_{s_{\text{MAX.}}}$ WITH ENTRY ANGLE

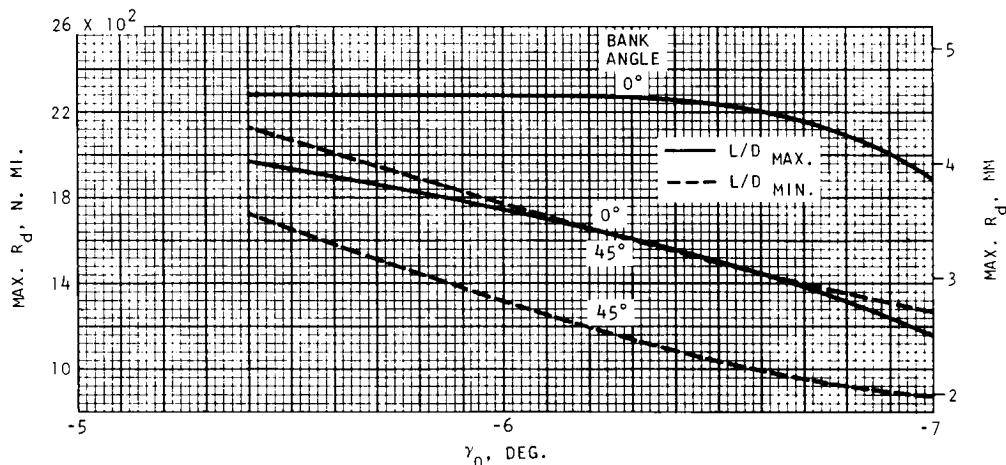


I-4) VARIATION OF Q_{T_s} WITH ENTRY ANGLE

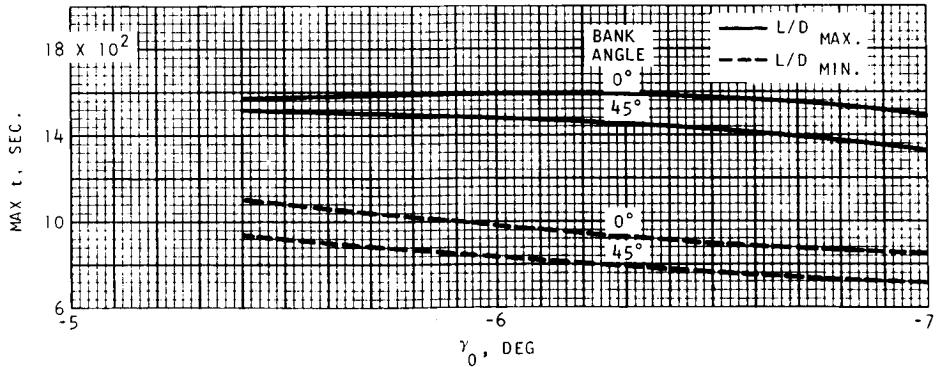
FIGURE 40.--CONTINUED



I-5) VARIATION OF R_c _{MAX.} WITH ENTRY ANGLE

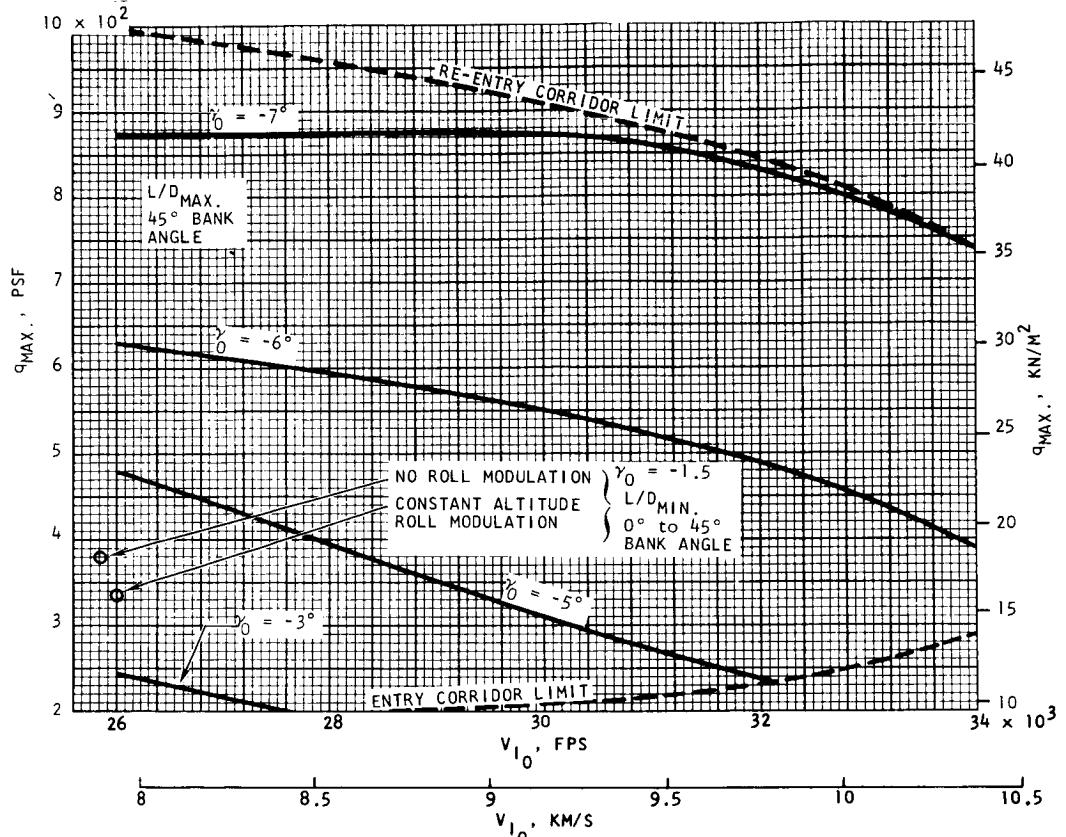


I-6) VARIATION OF R_d _{MAX.} WITH ENTRY ANGLE

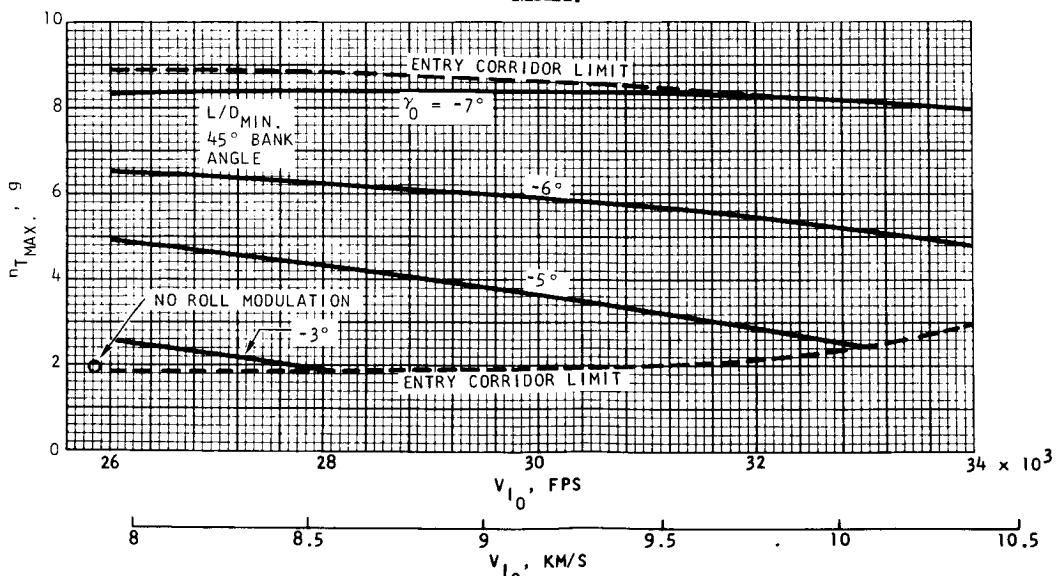


I-7) VARIATION OF t _{MAX.} WITH ENTRY ANGLE

FIGURE 40.--CONCLUDED

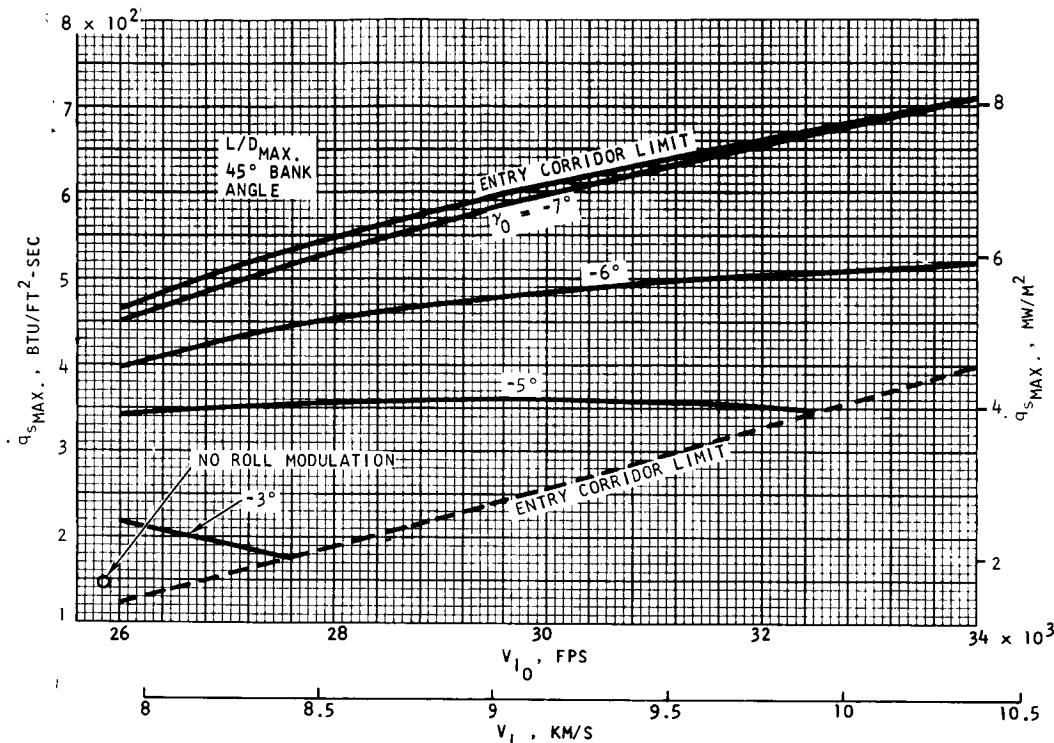


a) q_{MAX} .

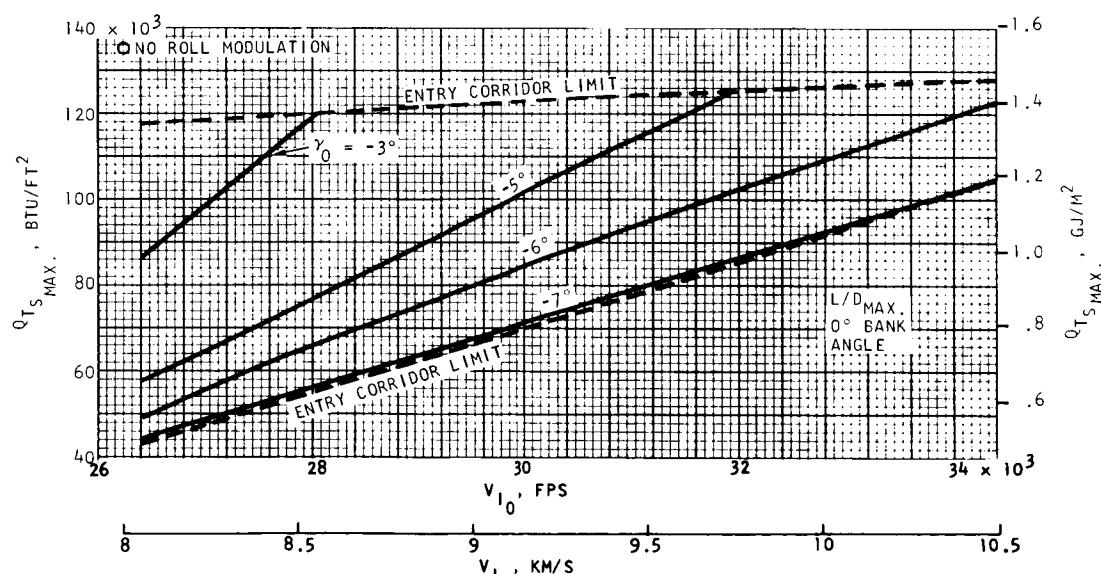


b) $n_{T MAX}$.

FIGURE 41. EFFECTS OF VARYING ENTRY VELOCITY

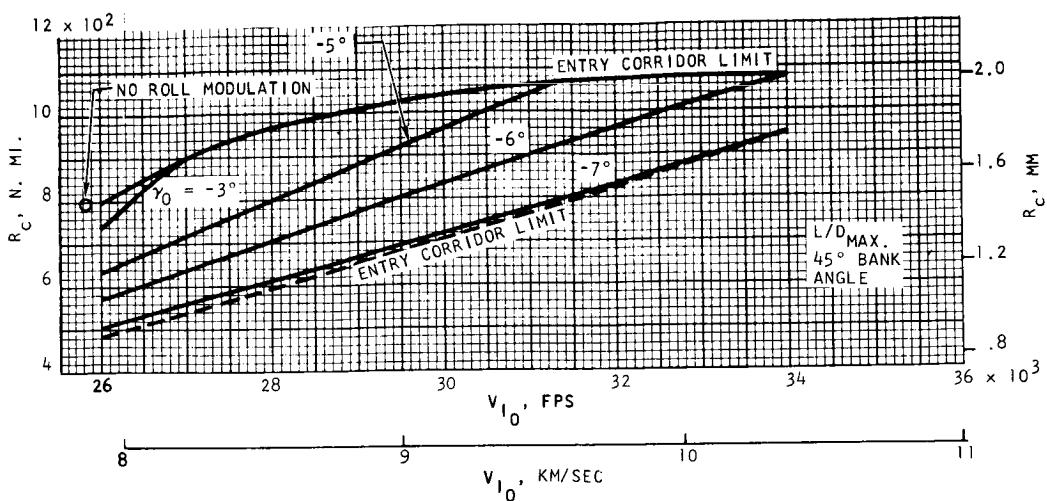


c) $q_s \text{ MAX.}$

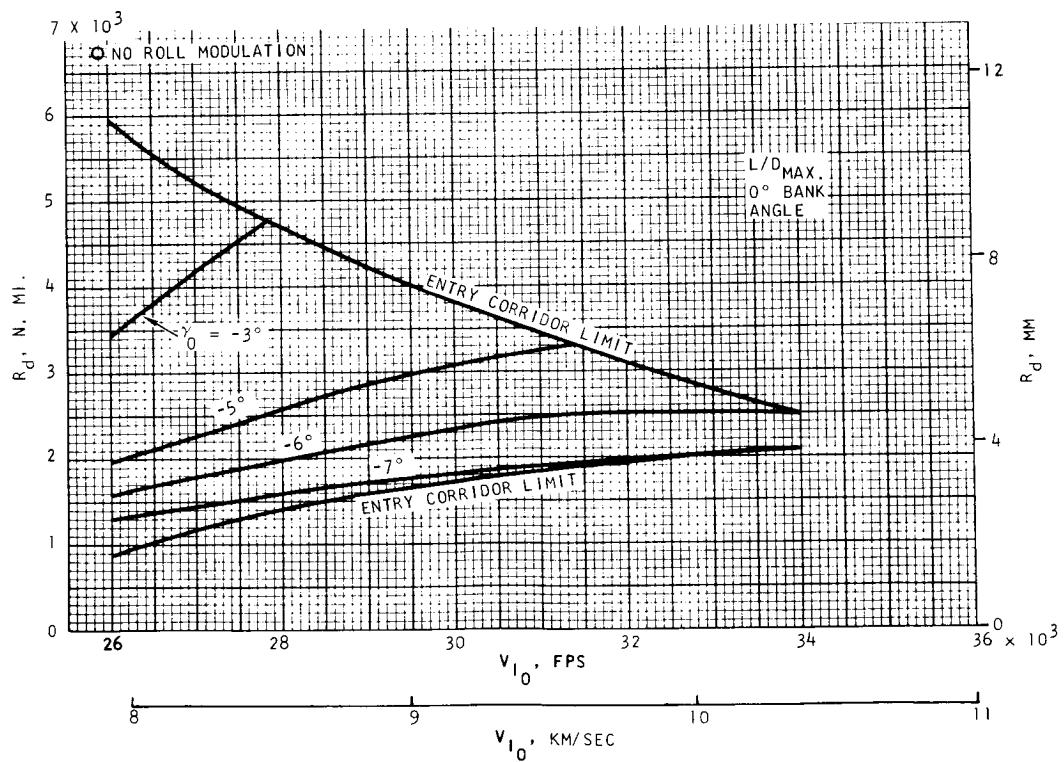


d) $Q_{T_s} \text{ MAX.}$

FIGURE 41.--CONTINUED



e) R_c MAX.



f) R_d MAX.

FIGURE 41.--CONTINUED

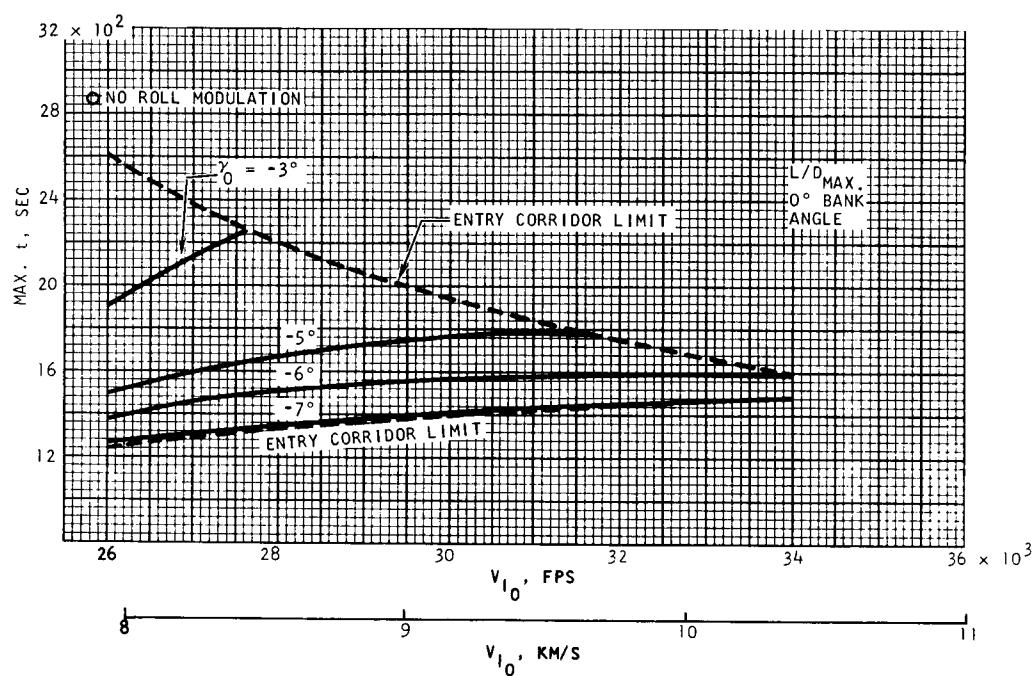


FIGURE 41.--CONCLUDED

DOCUMENT RELEASED

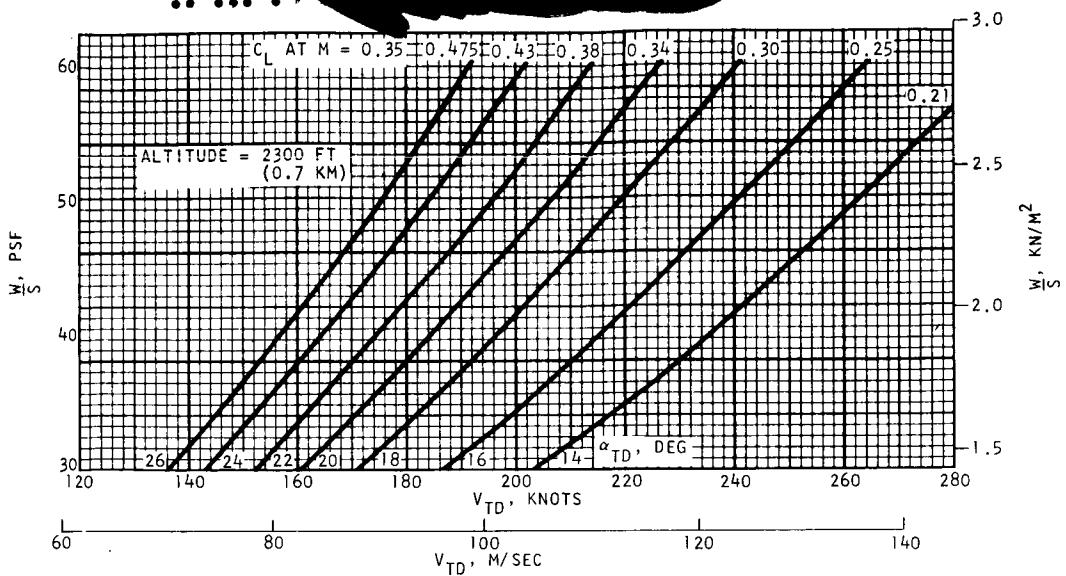


FIGURE 42. TOUCHDOWN SPEEDS AT EDWARDS AFB

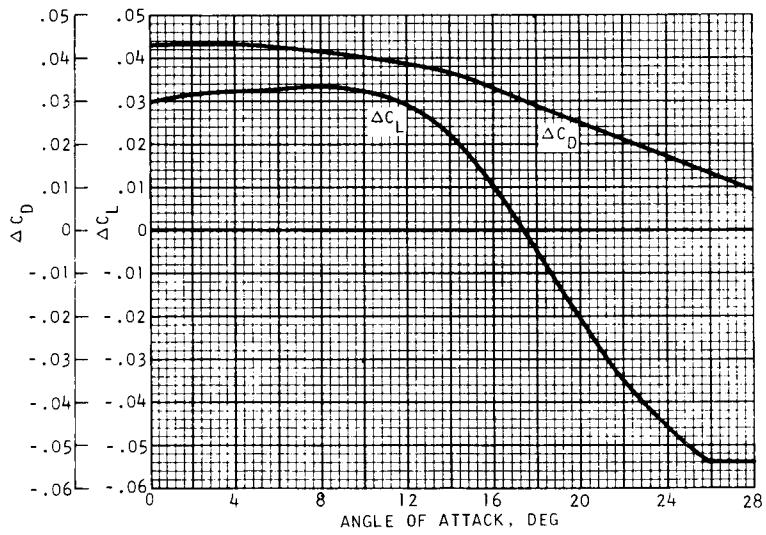


FIGURE 43. LANDING GEAR EFFECTS ON AERODYNAMICS

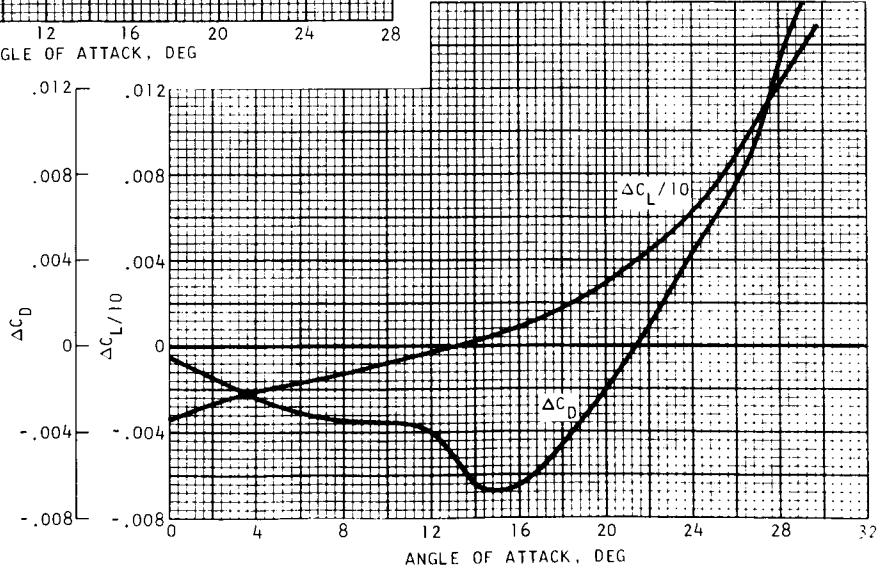
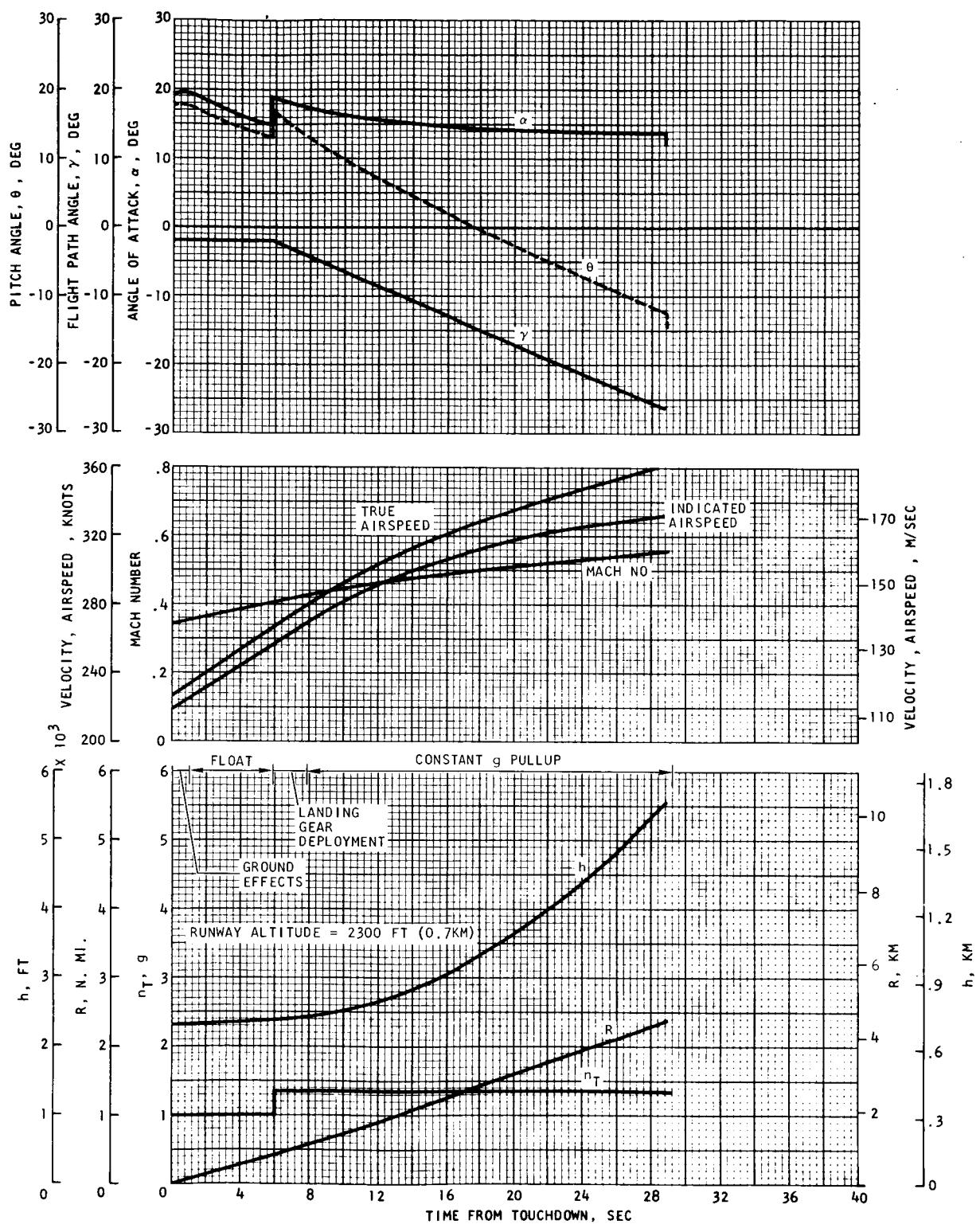
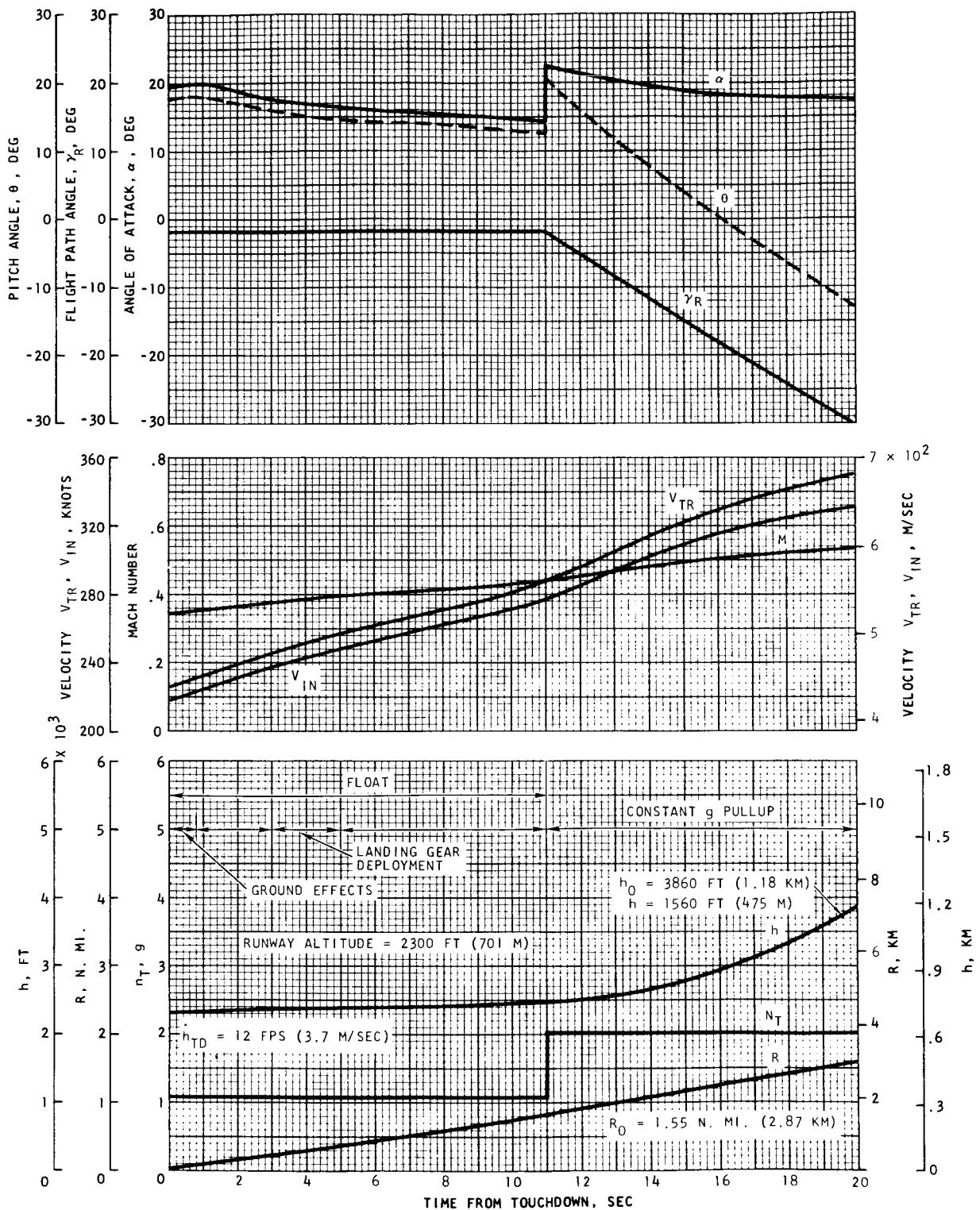


FIGURE 44. GROUND EFFECTS ON AERODYNAMICS



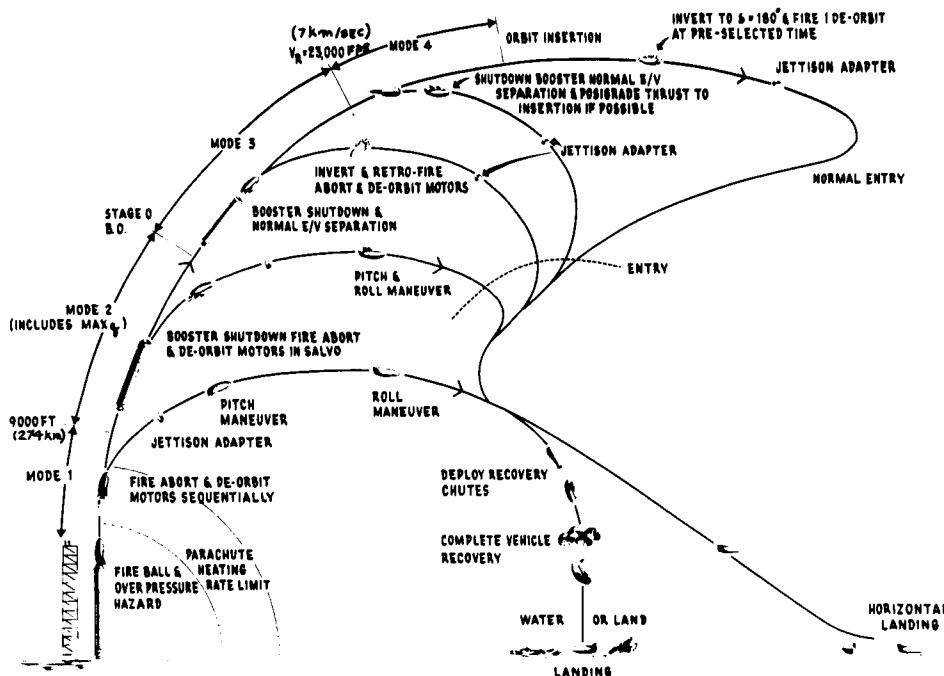
a) 1.35-g PULL-UP

FIGURE 45. LANDING TRAJECTORY



b) 2.0-g PULL-UP

FIGURE 15--CONCLUDED



MODE	RANGE	ABORT PROCEDURE	RECOVERY PROCEDURE
1	PAD ABORT TO 9000 FT (2.74 KM)	FIRE ABORT AND THEN DEORBIT MOTORS SEQUENTIALLY. JETTISON ADAPTER AT MOTOR BURNOUT. PITCH TO ANGLE OF ATTACK FOR C_L MAX (ALSO L/D_{MAX} SUB-SONICALLY). AT APOGEE ROLL 180° TO WINGS LEVEL ATTITUDE AND PROCEED TO PERTINENT RECOVERY PROCEDURE.	INITIATE COMPLETE VEHICLE RECOVERY ANYTIME AFTER APOGEE ALTITUDE AND BEFORE 1500 FT (457 M)
2	9000 FT (2.74 KM) TO STAGE 0 BURNOUT (INCLUDES MAX G)	SHUT DOWN BOOSTER ENGINES AND FIRE THE ABORT AND DEORBIT MOTORS SIMULTANEOUSLY (IN SALVO). JETTISON ADAPTER AT MOTOR BURNOUT. PITCH TO ANGLE OF ATTACK FOR C_L MAX. CONTINUE ENTRY TO RECOVERY.	INITIATE COMPLETE VEHICLE RECOVERY.
3	STAGE 0 BURNOUT TO $V_R = 23,000$ FPS (7.02 KM/SEC)	SHUT DOWN BOOSTER ENGINES. SEPARATE ENTRY VEHICLE AS IN NORMAL ORBIT INSERTION. PITCH TO AN INVERTED ATTITUDE FOR RETRO FIRE AND FIRE ANY COMBINATION OF ABORT AND DEORBIT MOTORS AS NECESSARY TO ROUGHLY CONTROL LANDING POINT. JETTISON ADAPTER AT MOTOR BURNOUT AND PITCH TO ANGLE OF ATTACK FOR C_L MAX. CONTINUE ENTRY TO RECOVERY.	SAME AS MODE 2.
4	$V_R = 23,000$ FPS (7.02 KM/SEC) TO ORBIT INSERTION	SHUT DOWN BOOSTER ENGINES. COAST AS NECESSARY. SEPARATE ENTRY VEHICLE AS IN NORMAL DIRECTION BY FIRING ANY COMBINATION OF THE ABORT AND DEORBIT MOTORS AS REQUIRED TO AVOID AN AFRICA LANDING, OR TO GO INTO ORBIT. IF ORBITAL VELOCITY IS NOT REACHED, PITCH TO ANGLE OF ATTACK, AS REQUIRED, TO ACHIEVE DOWNRANGE DISTANCE TO OVERTHROW AFRICA. JETTISON ADAPTER AND CONTINUE ENTRY TO RECOVERY. IF ORBIT INSERTION IS ATTAINED, SELECT DESIRED DEORBIT POINT AND DEORBIT IN NORMAL MANNER.	SAME AS MODE 2.

FIGURE 46. ASCENT ABORT MODES

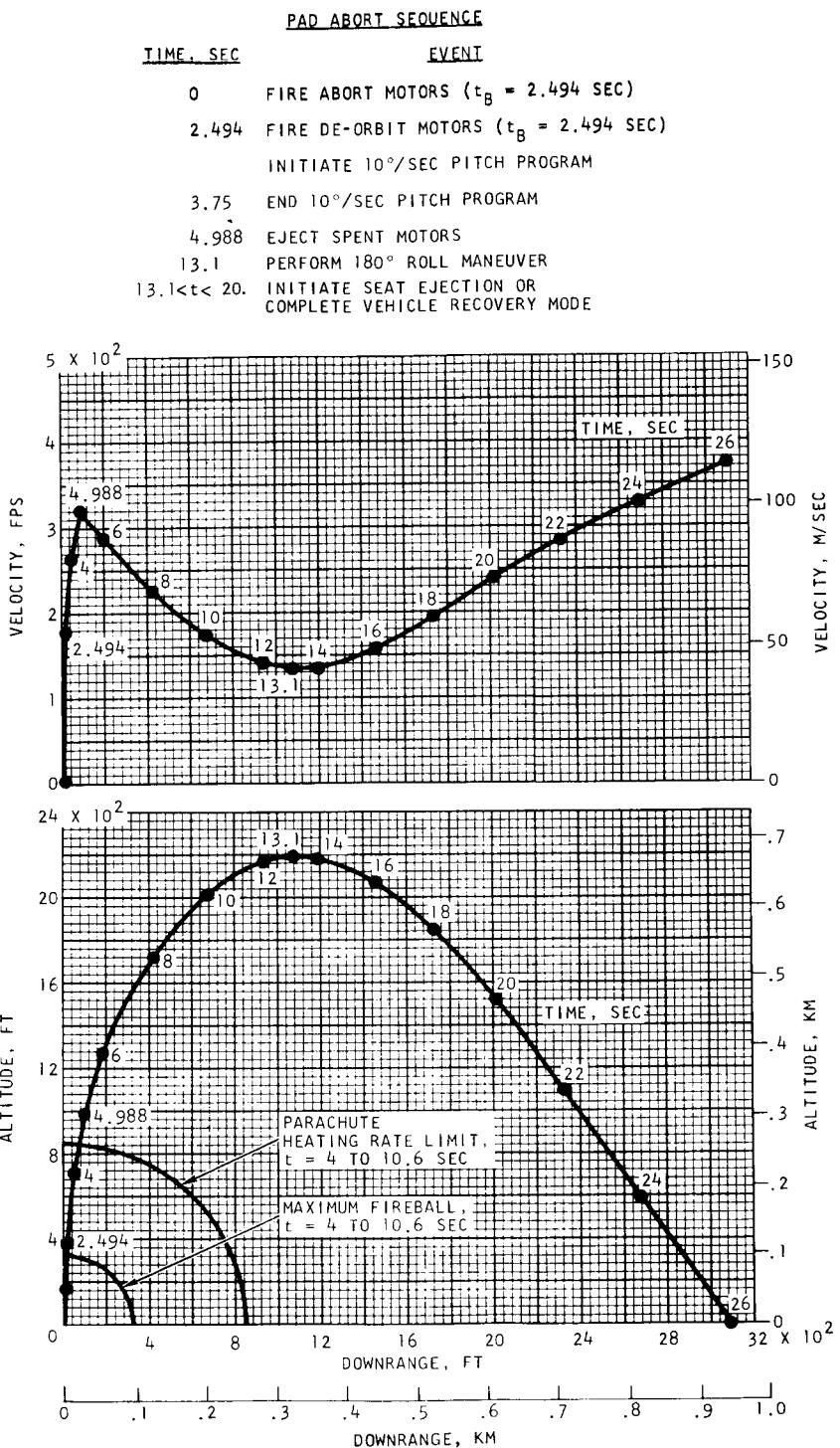


FIGURE 47. TYPICAL PAD ABORT TRAJECTORY

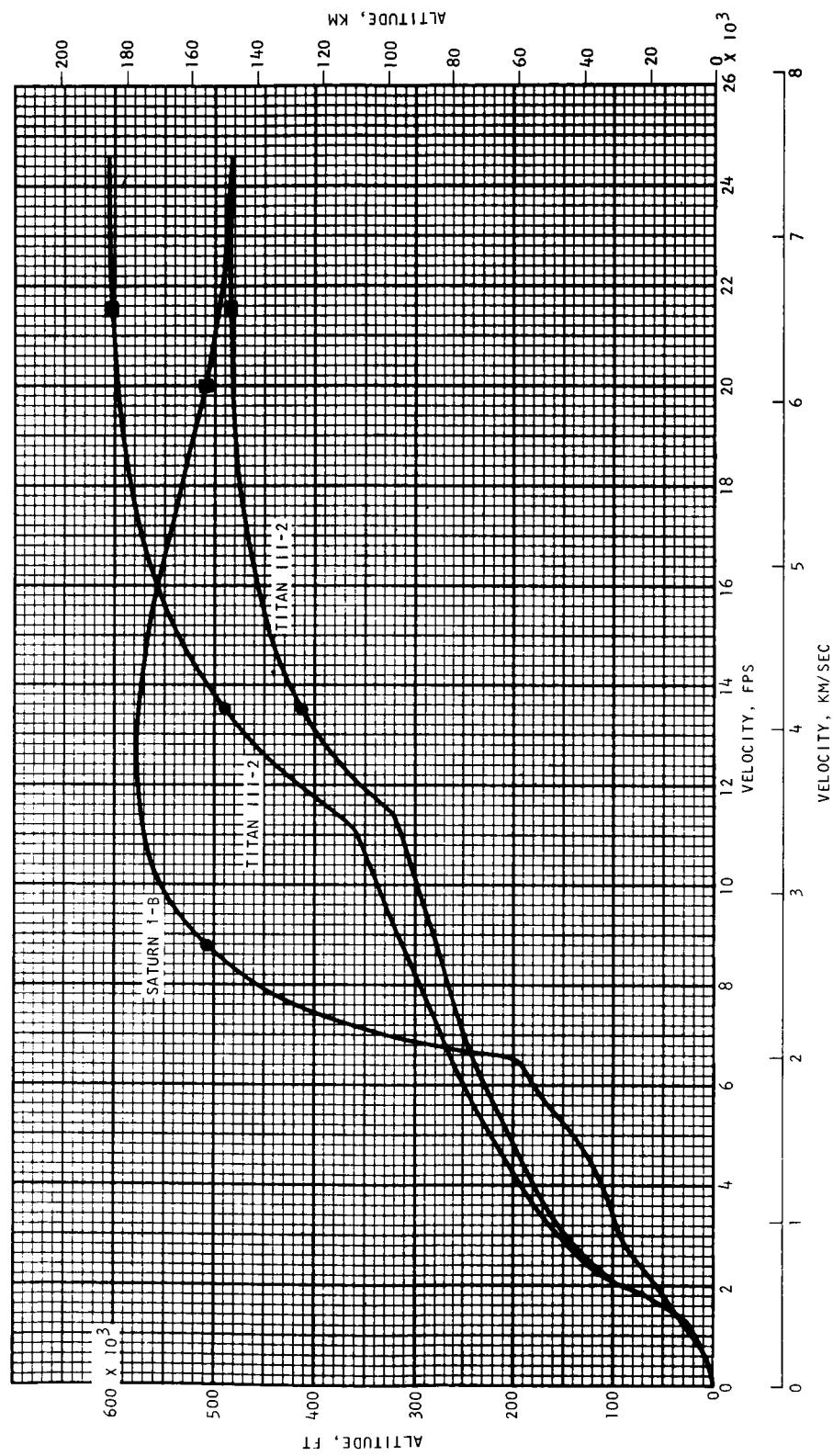


FIGURE 48. ABORT ANALYSIS LAUNCH TRAJECTORIES

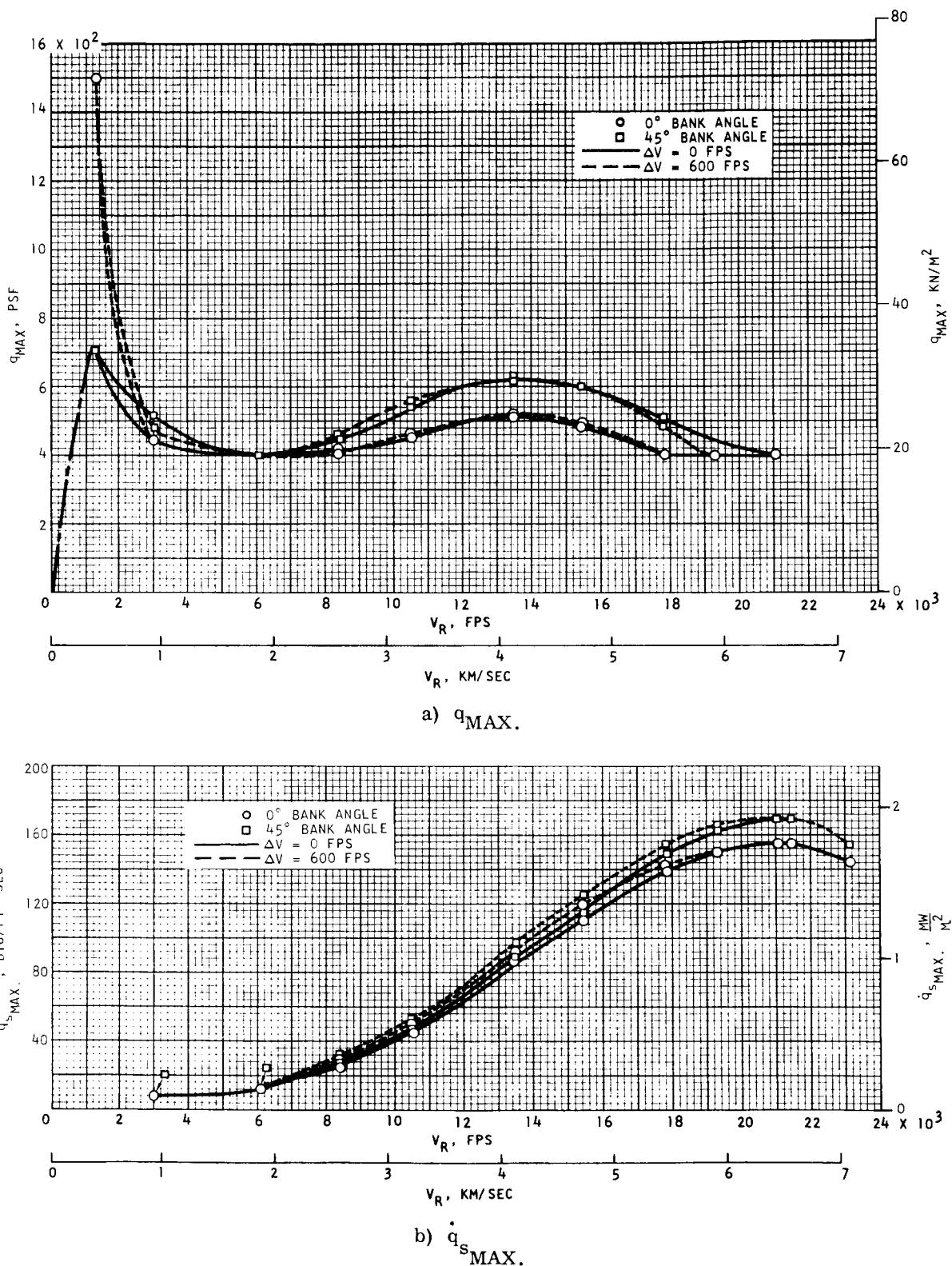
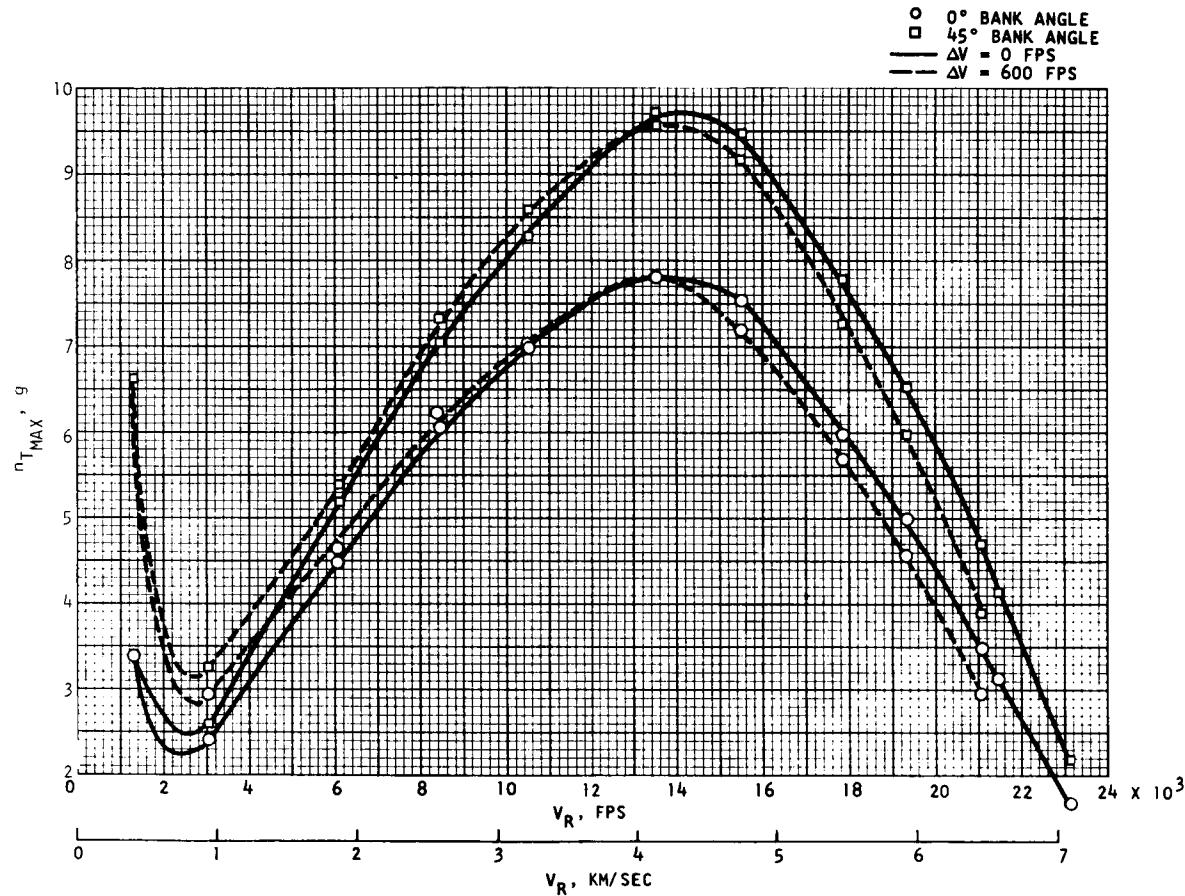
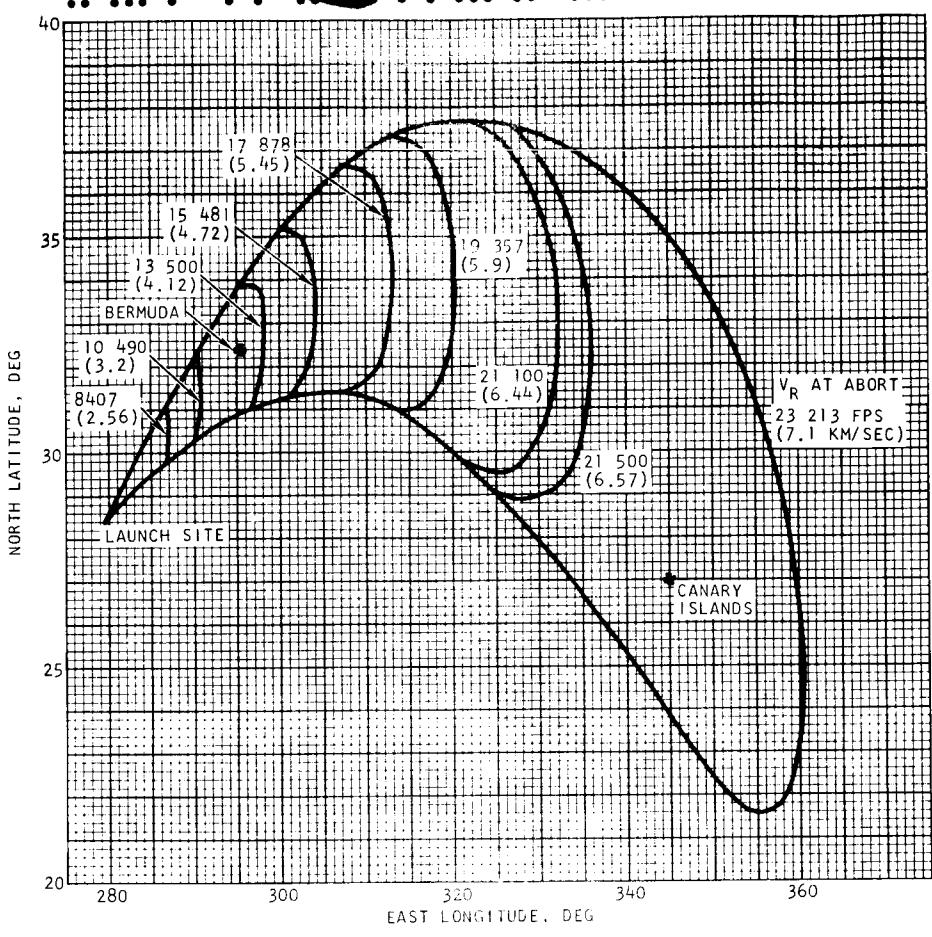


FIGURE 49. ABORT ENVIRONMENT PARAMETERS

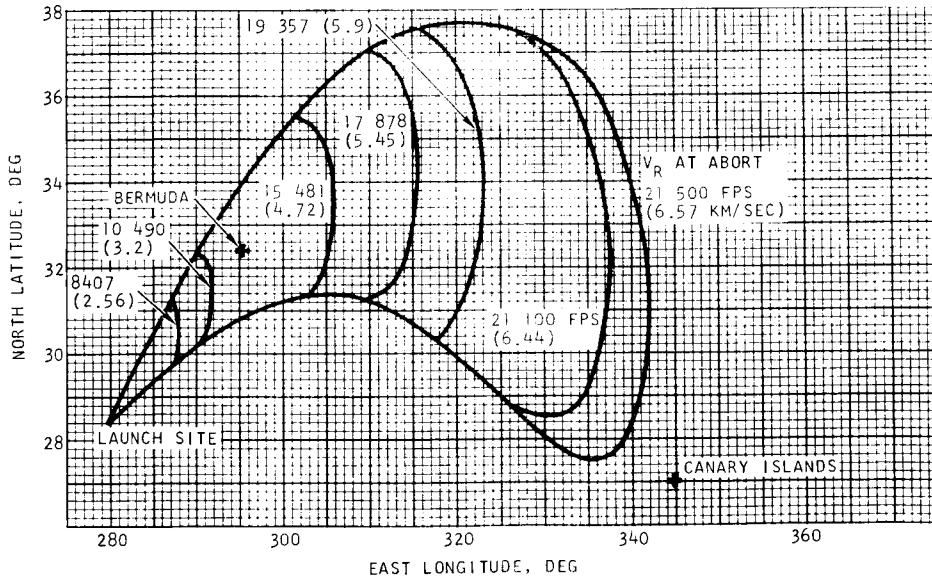


c) n_T MAX.

FIGURE 49. --CONCLUDED

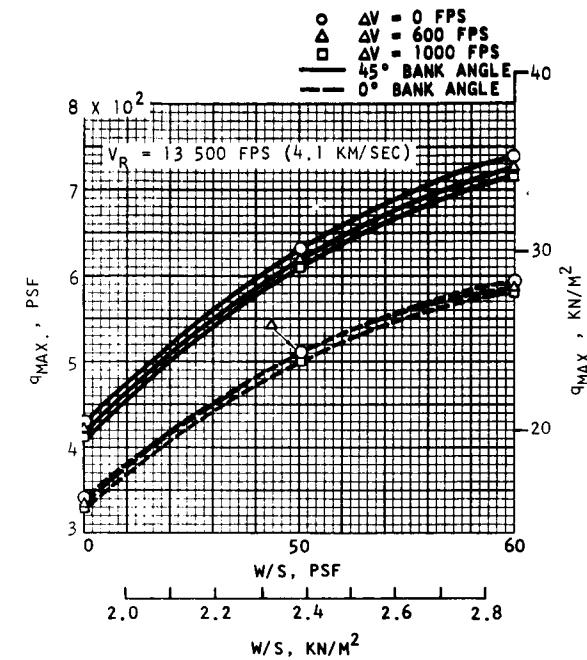


a) $\Delta V = 0$ FPS (0 M/SEC)

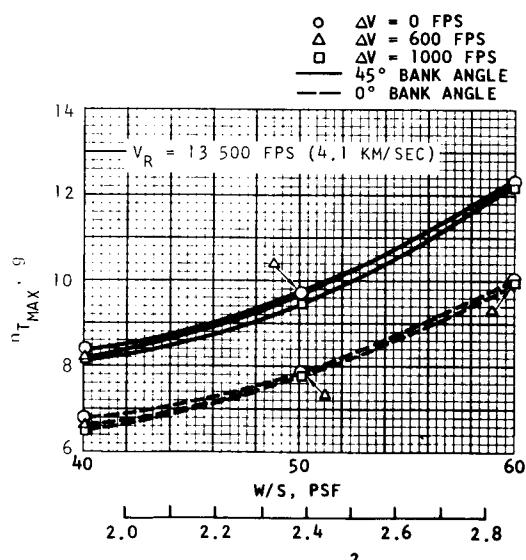


b) $\Delta V = 600$ FPS (183 M/SEC), POSIGRADE

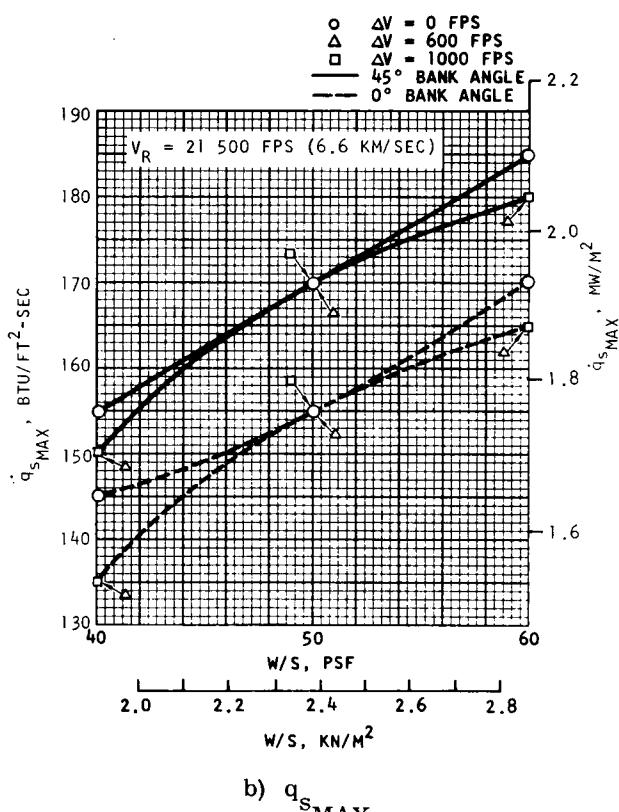
FIGURE 50. LANDING ENVELOPE



a) q_{MAX} .

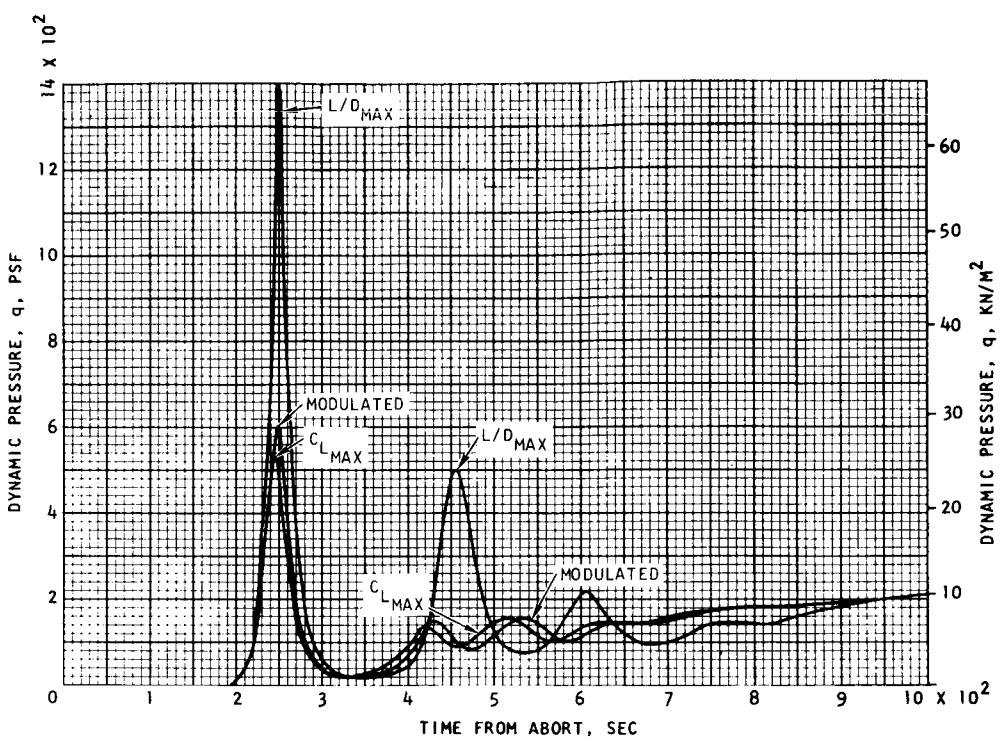


c) n_T_{MAX} .

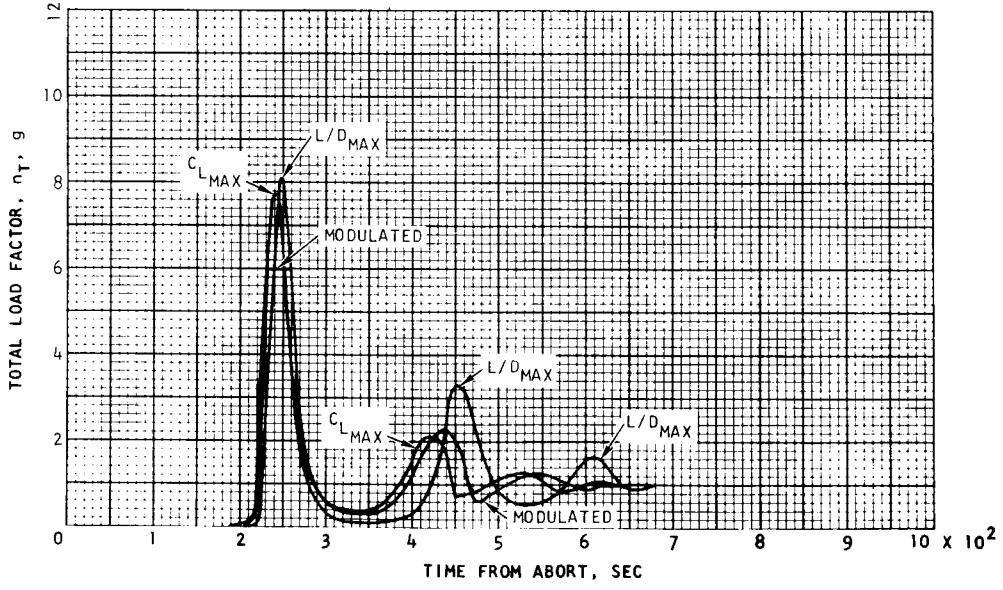


b) q_s_{MAX} .

FIGURE 51. EFFECT OF WING LOADING ON ABORT PARAMETERS

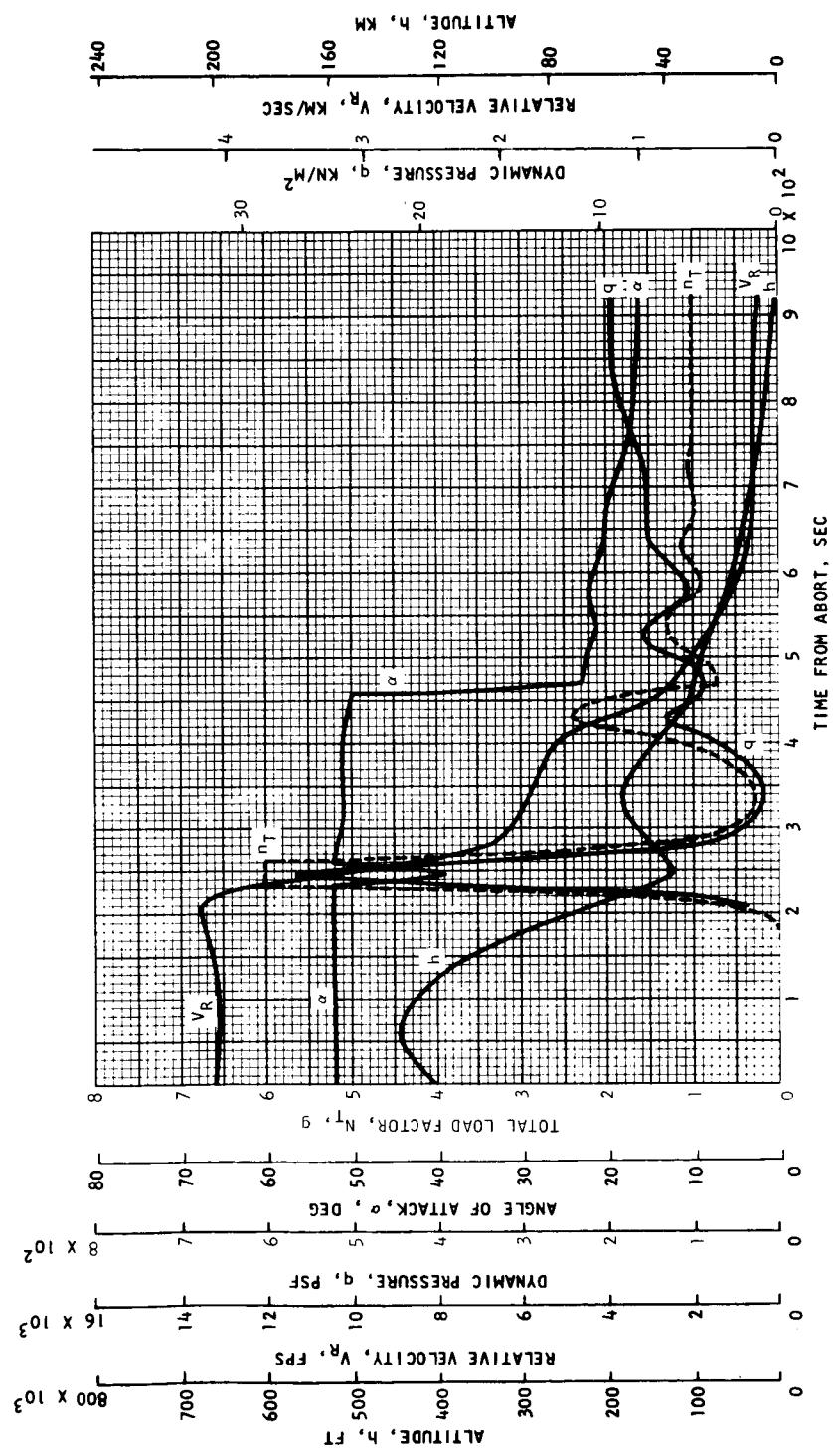


a) DYNAMIC PRESSURE



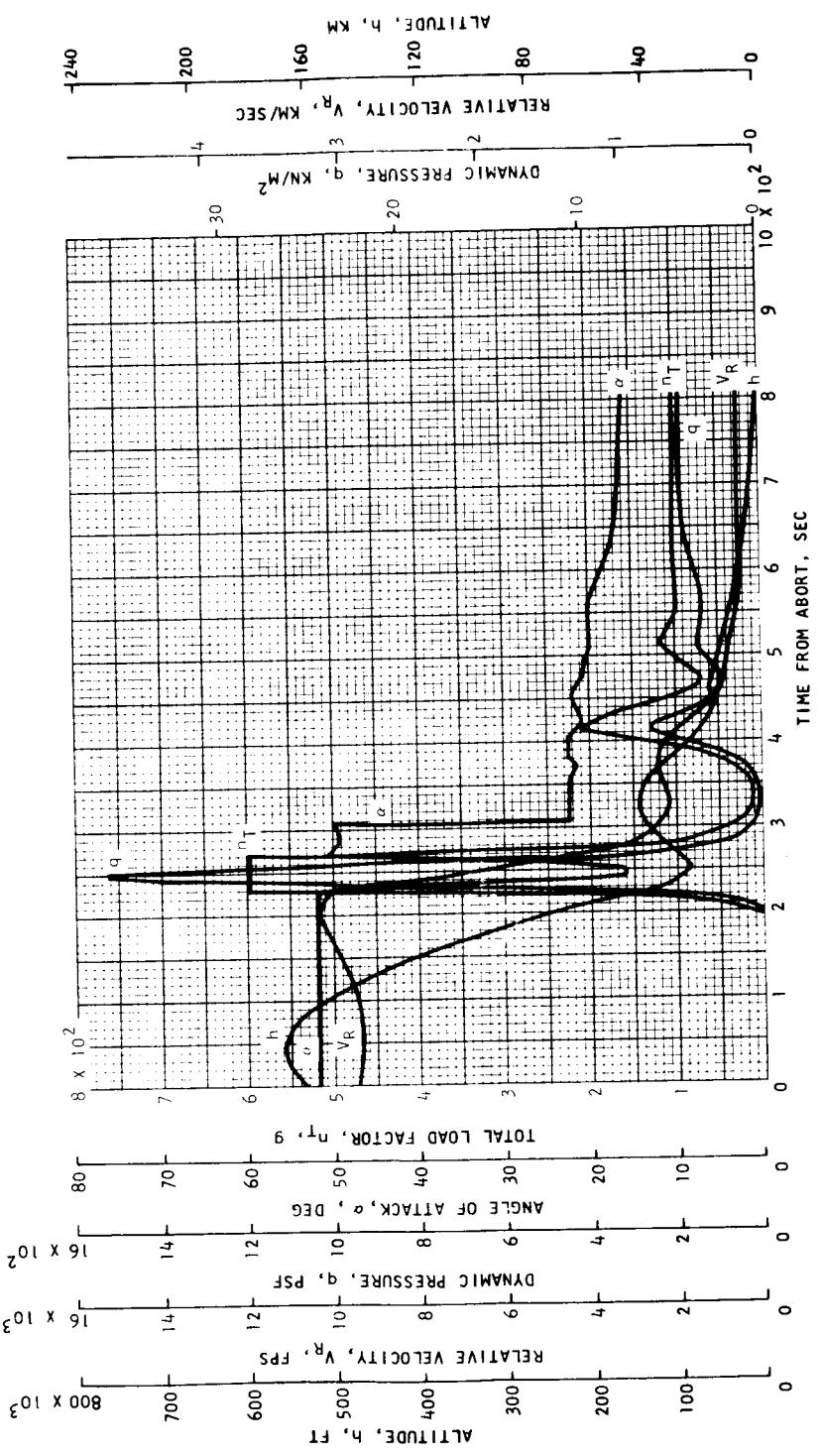
b) TOTAL LOAD FACTOR

FIGURE 52. ABORT ENTRY TIME HISTORIES



a) TITAN III-2

FIGURE 53. ABORT ENTRY TRAJECTORIES FOR MAXIMUM LOAD FACTOR



b) SATURN 1-B

FIGURE 53. --CONCLUDED

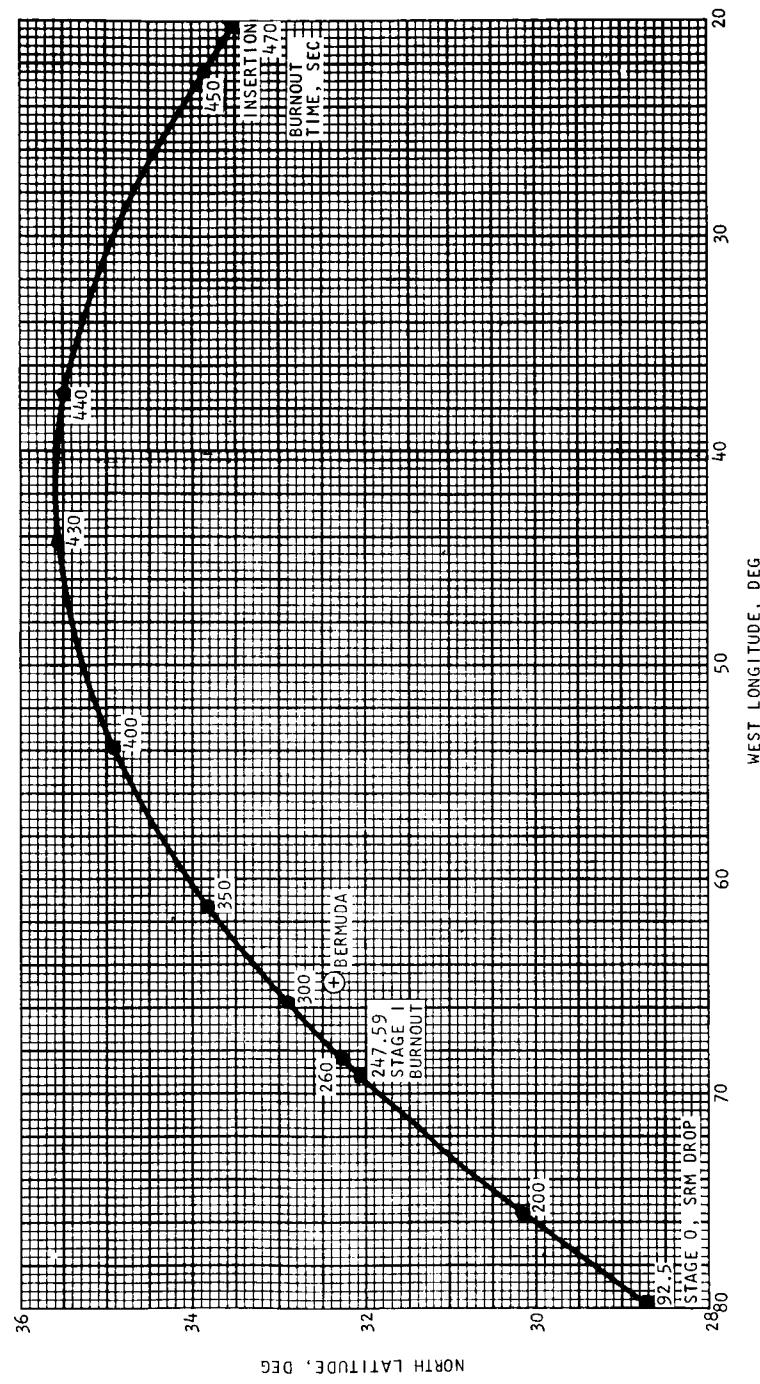


FIGURE 54. INSTANTANEOUS IMPACT POINTS, TITAN III-2

00000000000000000000